
Theses and Dissertations

Fall 2017

Applications, performance analysis, and optimization of weather and air quality models

Negin Sobhani
University of Iowa

Follow this and additional works at: <https://ir.uiowa.edu/etd>

 Part of the [Chemical Engineering Commons](#)

Copyright © 2017 Negin Sobhani

This dissertation is available at Iowa Research Online: <https://ir.uiowa.edu/etd/5996>

Recommended Citation

Sobhani, Negin. "Applications, performance analysis, and optimization of weather and air quality models." PhD (Doctor of Philosophy) thesis, University of Iowa, 2017.
<https://doi.org/10.17077/etd.gzcokjty>

Follow this and additional works at: <https://ir.uiowa.edu/etd>

 Part of the [Chemical Engineering Commons](#)

**APPLICATIONS, PERFORMANCE ANALYSIS, AND OPTIMIZATION
OF WEATHER AND AIR QUALITY MODELS**

by

Negin Sobhani

A thesis submitted in partial fulfillment
of the requirements for the Doctor of Philosophy
degree in Chemical and Biochemical Engineering in the
Graduate College of
The University of Iowa

December 2017

Thesis Supervisor: Professor Gregory R. Carmichael

Copyright by

Negin Sobhani

2017

All Rights Reserved

Graduate College
The University of Iowa
Iowa City, Iowa

CERTIFICATE OF APPROVAL

PH.D. THESIS

This is to certify that the Ph.D. thesis of

Negin Sobhani

has been approved by the Examining Committee for
the thesis requirement for the Doctor of Philosophy degree
in Chemical and Biochemical Engineering at the December 2017 graduation.

Thesis Committee:

Gregory R. Carmichael, Thesis Supervisor

Charles O. Stanier

Scott N. Spak

Thomas Peters

Patrick O'Shaughnessy

To my lovely parents, who made all of this possible,
for their love and support.
and
To all who believe in the power of kindness and peace.

“One doesn't discover new lands without consenting to lose sight,
for a very long time, of the shore.”

André Gide

ACKNOWLEDGEMENTS

There have been many people who walked alongside me during the past years. They have supported me, guided me, provided me with opportunities, and kept me going when I wanted to give up. I would like to thank each and every one of them. First and foremost, I would like to acknowledge my thesis advisor Dr. Gregory Carmichael for taking me as his student and for his endless support, encouragements, and patience. He thought me how to have a big picture vision for solving scientific problems. I would also like to express my sincere thanks to my supportive Ph.D. committee members: Dr. Charles Stanier, Dr. Patrick O'Shaughnessy, Dr. Thomas Peters, and Dr. Scott Spak for their support and interest in my research. They taught me many invaluable lessons in atmospheric science, modeling, air quality control technologies, and environmental regulations. I would also like to thank Dr. Sarika Kulkarni for her support and teaching me data analysis and writing scientific papers.

I would like to express my sincerest appreciations towards my knowledgeable mentor at NCAR, Dr. Davide Del Vento, for his constant support, encouragement, and assistance. I have learned a great deal from him and I am extremely grateful for his guidance throughout my research. I would also like to thank Dave Gill for his time and patience in teaching me all WRF details and for his contagious enthusiasm for weather modeling. I would like to especially acknowledge Dr. Rich Loft and SIParCS program for the support and providing me with an opportunity to learn more about high performance computing. SIParCS was truly a rewarding and insightful experience and a turning point in my graduate studies and perhaps in my life. I also wish to thank all NCAR CISL staff, Dave Hart, Siddhartha Gosh, Rory Kelly, Dan Nagle, Patrick Nicholas, Richard Valent,

and Brian Vanderwende who were always ready to train, support, and encourage me. I would also like to extend my sincerest appreciations to all NCAR staff who makes working at NCAR such a pleasant experience.

Special thanks to the Department of Chemical and Biochemical Engineering faculty and staff for giving me the opportunity to be part of their graduate program. I would also like to thank CGRER students and staff, especially Jane Frank, Jeremie Moen, and Amy Parker for administrative and technical support.

I would like to acknowledge all the people who guided and helped me through thick and thin of my Ph.D. years including all my friends. Most importantly, my thanks go to Nariman Jahani and Maral Razmand for their constant encouragement and emotional support. I would also like to thank Maryam Abdi for her unbelievable support, motivation, and patience during my Ph.D. years. I could not have finished this Ph.D. without her unfailing support and continuous encouragement.

There are no words to explain my gratitude towards my wonderful parents. I am forever grateful and indebted to my parents for giving me the opportunities and experiences that have made me who I am. Everything that I have achieved in my life is because of them. They have always encouraged me to explore new directions in life and put me through the best education system possible. Finally, I would like to thank my brother: Amin Sobhani for his constant love and support and for always being there for me as a friend. Being away from home and not visiting him during the past years was the biggest sacrifice I have made for this PhD.

ABSTRACT

Atmospheric particulate matter (PM) is linked to various adverse environmental and health impacts. PM in the atmosphere reduces visibility, alters precipitation patterns by acting as cloud condensation nuclei (CCN), and changes the Earth's radiative balance by absorbing or scattering solar radiation in the atmosphere. The long-range transport of pollutants leads to increase in PM concentrations even in remote locations such as polar regions and mountain ranges. One significant effect of PM on the earth's climate occurs while light absorbing PM, such as Black Carbon (BC), deposits over snow. In the Arctic, BC deposition on highly reflective surfaces (e.g. glaciers and sea ices) has very intense effects, causing snow to melt more quickly. Thus, characterizing PM sources, identifying long-range transport pathways, and quantifying the climate impacts of PM are crucial in order to inform emission abatement policies for reducing both health and environmental impacts of PM.

Chemical transport models provide mathematical tools for better understanding atmospheric system including chemical and particle transport, pollution diffusion, and deposition. The technological and computational advances in the past decades allow higher resolution air quality and weather forecast simulations with more accurate representations of physical and chemical mechanisms of the atmosphere.

Due to the significant role of air pollutants on public health and environment, several countries and cities perform air quality forecasts for warning the population about the future air pollution events and taking local preventive measures such as traffic regulations to minimize the impacts of the forecasted episode. However, the costs associated with the complex air quality forecast models especially for simulations with

higher resolution simulations make “forecasting” a challenge. This dissertation also focuses on applications, performance analysis, and optimization of meteorology and air quality modeling forecasting models.

This dissertation presents several modeling studies with various scales to better understand transport of aerosols from different geographical sources and economic sectors (i.e. transportation, residential, industry, biomass burning, and power) and quantify their climate impacts. The simulations are evaluated using various observations including ground site measurements, field campaigns, and satellite data.

The sector-based modeling studies elucidated the importance of various economical sector and geographical regions on global air quality and the climatic impacts associated with BC. This dissertation provides the policy makers with some implications to inform emission mitigation policies in order to target source sectors and regions with highest impacts. Furthermore, advances were made to better understand the impacts of light absorbing particles on climate and surface albedo.

Finally, for improving the modeling speed, the performances of the models are analyzed, and optimizations were proposed for improving the computational efficiencies of the models. Theses optimizations show a significant improvement in the performance of Weather Research and Forecasting (WRF) and WRF-Chem models. The modified codes were validated and incorporated back into the WRF source code to benefit all WRF users. Although weather and air quality models are shown to be an excellent means for forecasting applications both for local and hemispheric scale, further studies are needed to optimize the models and improve the performance of the simulations.

PUBLIC ABSTRACT

Atmospheric particulate matter (PM) such as Black Carbon (BC) has dual roles impacting both public health and climate. BC is the particulate matter produced during incomplete combustion of organic materials such as wood, coal, crop residue. According to the World Health Organization (WHO) PM contributes to approximately 7 million premature deaths annually. An important impact of PM on the earth's climate occurs while light absorbing particle (such as BC) deposits on snow. Atmospheric currents transport BC over large ranges and accumulate them on mountain tops and the Arctic glaciers. BC deposition on snow and ice increases the solar radiation absorption of snow and ice; hence, increase the temperature of snow and accelerate the snow melting process.

Considering the health and environmental impacts of PM, there is a great need for air quality modeling tools for forecasting air quality and informing emission reduction policies. Since there are many physical and chemical processes occurring in the atmosphere, modeling weather and air quality is a computational challenge.

This dissertation focuses on applications, performance analysis, and optimization of meteorology and air quality forecasting models. This dissertation presents several modeling studies with various scales to better understand transport of PM from different geographical sources and economic sectors (i.e. transportation, residential, industry, biomass burning, and power) and quantify their adverse impacts on climate. Finally, for improving the modeling speed, the performances of the models were analyzed, and optimizations were proposed for improving the computational efficiencies of the models.

TABLE OF CONTENTS

LIST OF TABLES	xii
LIST OF FIGURES	xiii
CHAPTER 1: GENERAL INTRODUCTION	1
Background and Significance	1
Research Objectives and Thesis Outline.....	4
Thesis Organization	11
CHAPTER 2: SOURCE SECTOR AND REGION CONTRIBUTIONS TO BC AND PM _{2.5} IN CENTRAL ASIA	12
Abstract.....	12
Introduction.....	13
Method and Data.....	15
Meteorological Model.....	15
Chemical Transport Model	16
Modeling Domain	17
Emissions	18
Observations	27
Simulations Analyzed	29
Model Evaluation.....	31
Results and Discussion	33
Regional Perspective.....	33
Model Evaluation with AOD and PM measurements.....	34
Source Contributions to PM _{2.5}	45
Seasonal Variations in AOD and PM at the Observation Sites	49
Source Contributions to BC	55
Vertical Distributions.....	59
Future Scenarios.....	60
Summary	64
CHAPTER 3: THE INTERCONTINENTAL TRANSPORT PATHWAYS OF PARTICLES THROUGH CENTRAL ASIA.....	66
Introduction.....	66
Method	67
Air Mass Trajectories Calculations.....	67
Results and Conclusion.....	70

Transport into CA	70
Long-range Transport Outside of CA Sources	73
Summary	78
CHAPTER 4: SOURCE SECTOR AND REGION CONTRIBUTIONS TO BLACK CARBON (BC) AND PM_{2.5} IN THE ARCTIC.....	80
Introduction.....	80
Method and Data.....	83
Modeling System	83
Observations	87
Sensitivity Analysis	89
Results and Discussions.....	90
Model Evaluations	90
Spatial Distribution of PM Species.....	102
Sources of Arctic PM.....	105
Transport Pathways.....	116
Conclusions and Future Works.....	119
CHAPTER 5: QUANTIFYING DEPOSITION OF BLACK CARBON AND DUST ON THE ARCTIC SNOW AND THE RESULTING ALBEDO REDUCTION.....	122
Abstract.....	122
Introduction.....	123
Model Description and Offline Calculations	126
Dry and Wet Deposition Algorithm.....	126
BC and Dust Content in Snow and Induced Albedo Reduction	128
Results and Discussions.....	131
BC and Dust Deposition in the Arctic	131
BC and Dust in Snow Concentration.....	137
Source Attribution of Arctic snow BC and Dust	142
Snow Albedo Reduction	147
Conclusions and Future Work	149
CHAPTER 6: PERFORMANCE ANALYSIS, PROFILING AND OPTIMIZATION OF WEATHER RESEARCH FORECASTING (WRF) AND WRF-CHEM MODELS	151
Abstract.....	151
Introduction.....	152
The WRF Description.....	153
Data and Method.....	159

Benchmarking Case	159
Utilized Tools.....	160
Results and Discussions.....	161
Scalability Analysis	161
Hybrid Parallelization	163
Hotspot Analysis.....	165
Performance Optimizations	168
Conclusions and Future Work	172
CHAPTER 7: GENERAL CONCLUSIONS AND FUTURE DIRECTIONS	173
REFERENCES	177

LIST OF TABLES

Table 2-1: Summary of changes in Central Asia region emissions and concentration under the future emission scenarios.....	62
Table 4-1: NASA ARCTAS Flight Categories for Spring and Summer 2008.....	91
Table 4-2- Statistical summary of comparison of observed and modeled meteorological parameters for NASA ARCTAS spring and summer flights. Obs and Mdl denote observation and model data.....	94
Table 5-1: Summary of snow and ice density adapted from Paterson 1994.....	140
Table 6-1- The performance speed-up for the optimized code for various compilers...	170

LIST OF FIGURES

Figure 2-1 : WRF-STEM modeling domain set up source region definition used in the simulations. (b) shows the topography around the observation sites.....	18
Figure 2-2: Spatial distribution of a) BC b) SO ₂ c) Natural dust d) Biomass burning PM _{2.5} emissions averaged over the simulation period in Gg/yr/grid.	21
Figure 2-3: Seasonal variability in spatial distribution of biomass burning PM _{2.5} emissions in Gg/month/grid (a) April 2008, (b) August 2008, (c) November 2008, and (d) May 2009.....	22
Figure 2-4: Spatial distribution of a) base year 2005 BC emissions (Gg/yr/grid) along with percent change (w.r.t to base year 2005) in (b) Reference 2030 BC emissions c) 2030 BC emissions with BC measures (low) and d) 2030 BC emissions with BC (lowest) and greenhouse gases measures aimed at keeping CO ₂ levels below 450ppm.....	25
Figure 2-5: Spatial distribution of a) base year 2005 PM _{2.5} emissions (Gg/yr/grid) along with percent change (w.r.t to base year 2005) in (b) Reference 2030 PM _{2.5} emissions c) 2030 PM _{2.5} emissions with BC measures and d) 2030 PM _{2.5} emissions with BC BC and greenhouse gas measures aimed at keeping CO ₂ levels below 450ppm.....	26
Figure 2-6: Spatial distribution of a) base year 2005 SO ₂ emissions (Gg/yr/grid) along with percent change (w.r.t to base year 2005) in (b) Reference 2030 SO ₂ emissions c) 2030 SO ₂ emissions with BC measures and d) 2030 SO ₂ emissions with BC and greenhouse gas measures aimed at keeping CO ₂ levels below 450ppm.	27
Figure 2-7: Spatial distribution of (a) MODIS and (b) modeled AOD along with (c) Comparison of MODIS, AERONET and Simulated AOD shown as box whisker plots averaged over the simulation period. The box plots are based on data that are paired in time and space. The triangle and circle markers on the spatial plots denote the location of LST and Bishkek sites. The numbers on the map denote contour values at sharp gradients. In each box whisker panel, the middle line denotes the median value, while the edges of the box represent 25th and 75th percentile values respectively. The whiskers denote the maximum and minimum values.....	34
Figure 2-8: Spatial distribution of simulated a) BC (µg/m ³), b) Dust (µg/m ³), c) PM _{2.5} (µg/m ³), and d) PM _{2.5} /PM ₁₀ ratio averaged over the simulation period. The values on the map denote contour values at sharp gradients.	36

Figure 2-9: Comparison of regional average AOD from MODIS with simulated AOD shown as box plots over the simulation period for selected source regions including Central Asia, China, Europe, Middle East, Russia and South Asia.....	38
Figure 2-10: Comparison of regional average AOD from MODIS with simulated values shown as monthly box plots over the simulation period for selected source regions (a) Central Asia (b) Middle East and (c) Europe.....	39
Figure 2-11: Comparison of predict PM_{10} with monthly observations from the European Monitoring and Evaluation Programme (EMEP available at http://www.nilu.no/projects/ccc/emepdata.html) and the Acid Deposition Monitoring Network in East Asia (EANET, data available at http://www.eanet.asia/product/index.html).....	41
Figure 2-12: Comparison of predicted meteorological variables from WRF model with observations shown as box and whisker plots over the simulation period (a) Temperature (K), (b) Relative Humidity RH (%), (c) Wind Speed (m/s), (d) Wind Direction ($^{\circ}$), and (e) PBL height (m).	42
Figure 2-13: Comparison of predicted aerosols with observations shown as box and whisker plots over the simulation period at a) LST and b) Bishkek sites. SP and LE denote the AOD from the sun-photometer (SP) and integrated from the vertical extinction profiles (LE). OBS and TEOM denote filter and TEOM measurements while the MDL denotes the modeled values respectively.	43
Figure 2-14: Comparison of observed and predicted PBL heights (m) at the LST site. Observed PBL heights were determined from the Lidar profiles.	45
Figure 2-15: Spatial Distribution of predicted species contributions (%) to AOD averaged over the simulation period a) Carbonaceous aerosols (BC+OC), b) SO_4 , c) Other $PM_{2.5}$, and d) Dust.	46
Figure 2-16: Spatial distribution of predicted species contributions (%) to $PM_{2.5}$ averaged over the simulation period a) Carbonaceous aerosols (BC+OC), b) SO_4 , c) Other $PM_{2.5}$, and d) Dust.	47
Figure 2-17: Summary of period mean contributions by source regions and sectors for AOD, $PM_{2.5}$, dust, non-dust $PM_{2.5}$, sulfate and BC in % for the grid cells containing the Bishkek and LST observation sites, and spatially averaged over the Central Asia region.	48

Figure 2-18: Temporal variability in simulated AOD compared with observations at the LST site. The box-plots of monthly values are shown. AOD from the sun-photometer (SP) and integrated from the vertical extinction profiles (LE) are shown.	50
Figure 2-19: Comparison of simulated PM mass with filter-based observations at Central Asia sites (a) $PM_{2.5}$ (LST) along with TEOM non-volatile measurements, (b) $PM_{2.5}$ (Bishkek), (c) PM_{10} (LST), and (d) PM_{10} (Bishkek) in ($\mu\text{g}/\text{m}^3$).	51
Figure 2-20: Temporal variability in simulated (a) Temperature (K) and (b) Relative Humidity RH (%) from WRF model compared with observations at the LST and Bishkek sites.....	53
Figure 2-21: Simulated composition of $PM_{2.5}$ at the LST site by a) Species ($\mu\text{g}/\text{m}^3$), b) Fine dust source regions($\mu\text{g}/\text{m}^3$) c) Anthropogenic $PM_{2.5}$ source regions ($\mu\text{g}/\text{m}^3$) d) Anthropogenic $PM_{2.5}$ source ($\mu\text{g}/\text{m}^3$) e) Biomass $PM_{2.5}$ source regions($\mu\text{g}/\text{m}^3$).The contributions from source region and sectors denote the non – dust portion of $PM_{2.5}$ mass.....	54
Figure 2-22: Summary of period mean contributions by source regions and sectors for OC in % for the grid cells containing the Bishkek and LST observation sites, and spatially averaged over the Central Asia region.	56
Figure 2-23: Simulated composition of BC at the LST site by a) Source regions ($\mu\text{g}/\text{m}^3$), b) Source sector ($\mu\text{g}/\text{m}^3$), and c) Biomass burning source regions ($\mu\text{g}/\text{m}^3$).	57
Figure 2-24: Percent change in simulated period mean surface BC and $PM_{2.5}$ concentrations for future 2030 emission scenarios relative to the base year (2005) a),d) reference 2030, b),e) BC measures (low) and c),f) BC (lowest) and greenhouse gas measures aimed at keeping CO_2 levels below 450 ppm.....	63
Figure 3-1: Time altitude cross sections of weekly averaged predicted BC, dust and $PM_{2.5}$ for the simulation period at the LST site.	69
Figure 3-2: Ten-day air mass back trajectories for August 2008 (events 1 and 2 as denoted in Figure 3-1) color coded by source regions. The blue diamond and green square hatched areas denote the natural dust and biomass burning emission sources while the number in black denote MODIS AOD contours averaged over the event time period and ten-day prior time window. The trajectories are color coded by source regions including Africa (blue), Middle East (green), Central Asia (yellow), North Asia biomass ($> 50^\circ \text{N}$, black), Europe (brown), China (red) and South Asia (orange).....	71

Figure 3-3: Same as Figure 3-2 but for November 2008, January 2009 and April 2009 (events 3, 4, 5 denoted in Figure 3-1).	73
Figure 3-4: Ten-day air mass forward trajectories illustrating the seasonality in transport pathways out of CA for a) June 2008, b) December 2008, and c) April 2009. The blue diamond, green square hatched areas denote the natural dust and biomass burning emission.	75
Figure 3-5: Seasonally averaged surface total dust (PM ₁₀) concentrations from Central Asia dust emissions. DJF (top left panel) denotes the average for the months of December, January and February.	76
Figure 3-6: Time series of predicted surface concentration at 6 h time step (top panel) and weekly averaged time altitude cross sections (bottom panel) of total dust (PM ₁₀) from Central Asia dust emissions at Mt. Bachelor, Oregon.	78
Figure 4-1: Spatial distribution of annual a) anthropogenic BC emission and b) wild fire BC emission in Gg/yr/grid.	85
Figure 4-2: Spatial distribution of percentage of economic sector (%) in annual total BC anthropogenic emission.	86
Figure 4-3: NASA ARCTAS DC-8 flight tracks during a) Spring 2008 and b) Summer 2008.	89
Figure 4-4: Comparison of key meteorological variables for NASA ARCTAS spring and summer flights.	93
Figure 4-5: Comparison of BC, SO ₄ , and SO ₂ for NASA ARCTAS spring and summer flights.	97
Figure 4-6: Vertical profile and comparison of STEM model aerosols with ARCTAS DC-8 aircraft observations.	98
Figure 4-7: Vertical profiles and comparisons of Model and Observation BC and SO ₄ by altitude for all ARCTAS flights.	98
Figure 4-8: Comparison of simulated BC with observations shown as box-and-whisker lots over the simulations period at Alert and Barrow site.	100
Figure 4-9: Annual average surface BC concentration over the U.S. The circles indicate IMPROVE sites with the color representing the BC concentration in µg/m ³	102

Figure 4-10: Spatial distribution of simulated a) BC ($\mu\text{g}/\text{m}^3$), b) Dust ($\mu\text{g}/\text{m}^3$), c) $\text{PM}_{2.5}$ ($\mu\text{g}/\text{m}^3$), and d) $\text{PM}_{2.5}/\text{PM}_{10}$ ratio averaged over the simulation period. The values on the map denote contour values at sharp gradients.	105
Figure 4-11: Source sector contributions (%) to annual BC surface concentration over the entire domain.	107
Figure 4-12: Time-series concentration and contribution of a) different sector to BC concentration b) different sectors to anthropogenic $\text{PM}_{2.5}$ concentration and c) different $\text{PM}_{2.5}$ species.	109
Figure 4-13: Source region contributions (%) to annual BC surface concentration over the entire domain.	114
Figure 4-14: Time Series of BC major geographical contributor to the Arctic average surface concentration.	115
Figure 4-15: Summary of annual mean contributions by source regions and sectors for BC SO_4 and Anthropogenic $\text{PM}_{2.5}$	115
Figure 4-16: Cross Section at 64.8 N for different seasons. The first and last rows show the BC and dust concentrations at the cross-section. The other rows show the contributions of major regional sources and BB burning to BC at 64.8 °N.	116
Figure 4-17: Ten-day backward trajectories released at various locations on longitude of 65°N.	119
Figure 5-1: Seasonal spatial plot of total BC deposition flux for MAM(March, April and May) , JJA(June, July and August) , SON(September, October, and November), and DJF(December, January and February).	132
Figure 5-2: Seasonal spatial plot of total BC dry deposition flux for MAM(March, April, and May) , JJA(June, July, and August) , SON(September, October, and November), and DJF(December, January, and February).	134
Figure 5-3: Seasonal spatial plot of total BC wet deposition flux for MAM (March, April, and May) , JJA (June, July, and August) , SON (September, October, and November), and DJF (December, January, and February).	135
Figure 5-4: Seasonal spatial plot of total dust (fine+ coarse dust) deposition for MAM(March, April and May) , JJA(June, July and August) ,	

SON(September, October, and November), and DJF(December, January and February).....	136
Figure 5-5: Spatial distribution of BC concentration of top layer snow (ng/g) for different months.....	138
Figure 5-6: Spatial distribution of BC content of top layer snow in ng/g for a) April 2008 and b) May-2008. The circles on the plots demonstrate the observation value from Doherty et al. 2010.	139
Figure 5-7: Spatial distribution of Dust content of top layer snow in ng/g for a) April 2008 and b) May-2008.....	141
Figure 5-8: Seasonal variations of various sectors contributions to Alert and Barrow BC deposition.	144
Figure 5-9: Seasonal Variation of contributions of various sectors to Alert and Barrow BC deposition.....	145
Figure 5-10: Seasonal Variation of contributions of various sectors to Alert and Barrow dust deposition.	146
Figure 5-11: Seasonal Variation of contributions of various sectors to Alert and Barrow dust deposition for both fine and coarse dust particles.....	146
Figure 5-12: Modeled snow albedo decrease (%) due to BC deposition for April and May 2008.	147
Figure 5-13: Source sector contribution (%) to BC albedo perturbation for April 2008.....	149
Figure 6-1: WRF system components. (Figure from Skamarock et al., 2008).....	155
Figure 6-2: WRF ARW model integration procedure. (Image source: WRF Tutorial January 2014).....	156
Figure 6-3: Positive definite and monotonic limiters in WRF-ARW for a 1-D advection. (Image source: WRF Tutorial January 2014).....	159
Figure 6-4: WRF scalability assessment for WRF 500x500 Hurricane Sandy case.	162

Figure 6-5: Percentage of total time spent on computation, MPI communication, and I/O.	163
Figure 6-6: Simulation speed for different combinations of tasks and threads per node.....	165
Figure 6-7: The processing time for WRF code as measured by Intel VTune XE.	166
Figure 6-8: Simplified flowchart for hotspot analysis and optimization.....	168
Figure 6-9- Single node performance of original and modified positive definite advection kernel for Intel 16.0.2 compiler.....	171
Figure 6-10- Single node performance of original and modified positive definite advection kernel for GNU 6.1.0 compiler.	171

CHAPTER 1: GENERAL INTRODUCTION

Background and Significance

There is growing awareness that air pollution is one of the major “global” problems faced by people all over the world. The intercontinental transport of pollutants leads to episodic increases in air pollution concentration in remote locations. Air pollutants including particulate matter (PM) have dual roles impacting public health and climate. PM is associated with a variety of detrimental health impacts including increased mortality rate. According to the World Health Organization (WHO) PM contributes to approximately 7 million premature deaths annually. (Pope et al., 2009) In 2012, ambient (outdoor air pollution) in both cities and rural areas was estimated to cause 3.7 million premature deaths worldwide with an additional 3.3 million deaths linked to indoor air pollution. (Lim et al., 2012) In general, air pollution is the world’s largest single environmental health risk. (WHO, 2016) Considering the broad range of health effects, many countries perform air quality forecasts to have preventive policies and to warn public to take cautions measure to reduce their exposure to the human health.

PM change the earth-atmosphere’s radiative balance by absorbing or scattering solar radiation while suspended in the atmosphere. (Ramanathan et al., 2001) Furthermore, these particles change the precipitation patterns, reduce visibility, and cause surface dimming. (Bond et al., 2013) Another important impact of PM on the earth’s climate occurs while light absorbing particles (such as Black Carbon (BC)) deposit on snow. BC particles are be transported over large ranges and accumulate on mountain tops and the Arctic glaciers.(Ramanathan and Carmichael, 2008; Jacobson, 2004) BC

deposition on snow and ice increases the solar radiation absorption of snow and ice; hence, increases the temperature of snow and accelerates the snow melting process.(Ramanathan and Carmichael, 2008; Wang et al., 2011) BC has been identified as the second largest contributor to global warming after carbon dioxide (CO₂). (Ramanathan and Carmichael, 2008)

Studies suggest that BC caused 25% of 20th century warming over the Arctic. (Bond and Sun, 2005; Koch and Hansen, 2005; Ramanathan and Carmichael, 2008) Arctic temperature has been elevated approximately twice the global average temperature increase rate over the last decade. The temperature increase has been up to 4°C during the winter months from 1954 to 2003. (Solomon et al., 2007; Stocker, 2014) Also the Arctic sea ice shrank to the lowest satellite records in September 2007. (Bond and Sun, 2005; Wang et al., 2011) The Arctic glaciers melting will affect the sea level rise, ocean salinity, and extinction of some animal species. (Bond and Sun, 2005) The effect of snow cover reduction has a positive feedback leading to further climate warming. The snow and sea ice melting causes the snow cover reduction over the Arctic and exposes the underlying dark surfaces of ocean water which then increases the absorption of solar radiation. The atmospheric lifetime of BC is estimated to be between 4 to 12 days. (Ramanathan and Carmichael, 2008) BC lifetime is considered very short in comparison with the Greenhouse Gases (GHGs) such as CO₂ with approximate atmospheric lifetime of 100 years, N₂O with atmospheric lifetime of 114 years, and CFC-115 with atmospheric lifetime of 1700 years. (Liu et al., 2011; Ramanathan and Carmichael, 2008) Therefore, by starting a policy for reducing or mitigating the emissions of BC, rapid changes in the

atmospheric concentration and the associated environmental and health impacts of BC will occur in the short term. (Quinn et al., 2008)

Considering the health and climate impacts of aerosols there is a great need for air quality modeling tools for forecasting air quality and formulating emission abatement policies. Due to the significant role of aerosols on climate and public health, several tools have been developed in the past few decades for predicting aerosols concentrations and their effects. Due to the importance of assessing the impacts of GHG and particle emissions on climate and significant public health impacts of air quality, forecasting future air quality and atmospheric modeling draw scientists' attention.(AMAP, 2011) Chemical Transport Models (CTMs) provide mathematical tools for a better understanding atmospheric system including chemical and particle transport, pollution diffusion, and deposition. CTMs are categorized into two main categories – Lagrangian and Eulerian. The Lagrangian models consider an air parcel with no mass transfer with surrounding atmosphere. However, the Eulerian CTMs assume the frame fixed in space and allows mass transfer between the grid cells. The continuity equations for Lagrangian models and Eulerian models are discussed in details in Jacobson 1998, Brasseur and Jacob, 2017, and Jacob, 1999.

CTMs are usually multi-layer, multi-pollutant, and Eulerian models. All the CTMs start with input data including: meteorological data, emission data, and initial and boundary conditions.(Jacobson, 2004) Solving sophisticated physical and chemical processes in the atmosphere coupled with transport of air pollutants makes CTMs

computationally expensive. (Brasseur and Jacob, 2017; Martín et al., 2004; Parada et al., 2002) High-performance computing is the only practical solution for making the large-scale, expensive, multi grid regional and global forecasts feasible. Parallel computing is defined as the utilization two or more processing unit simultaneously to solve one single problem. Parallelization of the numerical models and optimization of the codes are essential to simulate the numerical simulations at a reasonable speed. (Scott et al., 2005)

Several countries perform air quality forecasts for warning the population about the future air pollution events. Furthermore, there is an increasing need to higher resolution meteorological forecast and parallel programs to process big volumes of satellite data. However, the costs associated with the complex Numerical Weather Prediction Models (NWP) and CTMs especially for models with higher resolutions makes the “forecasting” a challenge. Small performance gains from optimization of NWP and CTMs have high impact on the overall costs associated with severe weather or air pollution event forecasts.

Research Objectives and Thesis Outline

This thesis is focused on the application, evaluation, performance assessment, and optimization of the Weather Research and Forecasting (WRF) model, Sulfur Transport and dEposition Model (STEM), and WRF-Chem. The specific aims and organization of this research are outlined below. In each objective, a brief introduction describing the background, significance, and motivation of each specific aim is included.

Objective 1: Determine the source sector and region contributions to BC and PM_{2.5} in Central Asia.

Central Asia (CA), a region of republics located between Europe and Asia, faces severe environmental problems, with origins dating back to the 1960s and best symbolized by the Aral Sea catastrophe (Whish-Wilson, 2002). CA and the surrounding areas are developing quickly and air pollution emissions are projected to increase significantly for the next several decades (Shindell et al., 2012). In recognition of the need to improve the environmental conditions in the region, five CA countries have formulated the Framework Convention on Preservation of Environment for Sustainable Development of CA (UNEP, 2006).

Despite the awareness of the environmental conditions, CA remains an understudied region and there is a general lack of air pollution observations within CA. Furthermore the recent assessment of the intercontinental transport of pollution (HTAP, 2010) has indicated that the major transport pathway of pollution from Europe to Asia is via low altitude flows passing through CA. The magnitude of the pollution transport from Europe to Asia is highly uncertain in large part due to the lack of observations of pollutants along this pathway. To help better characterize the air pollution levels and the transport pathways in the region a study was undertaken between Russia, Kyrgyz Republic, and USA scientists to observe and model aerosols in the region. Measurements of PM mass and composition were taken at two locations in the Kyrgyz Republic (Lidar Station Teplokluchenka (LST) and Bishkek) and modeling analysis was performed to

assess the contributions of local, regional and distant sources to the PM concentrations in the region (Miller-Schulze et al., 2012, Chen et al., 2012, 2013). For this objective, we present a modeling analysis of PM_{2.5}, PM₁₀, (PM_{2.5} refers to particles in the size range of less than 2.5 µm aerodynamic diameter (AD) and PM₁₀ refers to particles in the size range of less than 10 µm AD), black carbon (BC) and organic carbon (OC) mass concentrations and aerosol optical depth (AOD) over the time period of April 2008 to July 2009.

Chapter 2 of this dissertation is focused on determining the source sector and region contributions to BC and PM_{2.5} in Central Asia. Here, we used STEM, a regional scale CTM with a coarse resolution over a long period (16 month). This chapter is based on the results published on Kulkarni et al. (2015).

Objective 2: Quantify the intercontinental transport pathways of particles through Central Asia.

Intercontinental transport of air pollutants from one source continent (e.g. Europe) to another continent (e.g. North America) has major effects in increasing the background pollutant concentrations.(Kulkarni, 2009; Yienger et al., 2000) Central Asia is located among significant emission sources. Understanding the transport pathways of PM through CA will help us explain the seasonality of surface PM concentration in the CA region. The transport of aerosols into CA is explored through three-dimensional backward trajectory analysis. Transport from CA and their impacts on downwind areas are also analyzed via forward trajectory analysis. This chapter is based on the results published on Kulkarni et al. (2015).

Objective 3: Estimate the source sector and region contributions to BC and PM_{2.5} in the Arctic.

The episodic high concentration of the Arctic PM during spring and winter has been studied extensively. The composition of these haze events is mainly sulfate, OC, BC, sea salt and dust. Previous studies show that BC caused 25% of 20th century temperature increase over the Arctic. (Bond and Sun, 2005; Koch and Hansen, 2005; Ramanathan and Carmichael, 2008) BC concentration in the Arctic is highly dependent on the long range transport of natural and anthropogenic emissions from outside of the Arctic region (both mid latitudes and high latitudes).(AMAP, 2011; Law and Stohl, 2007) For making the global BC emission abatement policies the contribution of each geographical source region and source sector should be quantified.

There are limited emission sources of pollution in the Arctic itself and most of the pollutants are transported over long ranges from mid-latitudes where there are higher emissions. (AMAP, 2011; Bond et al., 2013) The minimum potential temperature in the Arctic boundary layer forms the arctic dome causing very stable air near the surface. (Klonecki et al., 2003; Stohl, 2006; Stohl et al., 2006) The strong atmospheric inversion reduces the vertical transport between boundary layer and free troposphere and limits the BC deposition to the ground. The Arctic front acts a transport barrier for Arctic lower troposphere in the more southerly latitudes reducing the low level transport of pollutants to the Arctic dome. (Barrie, 1986).

Previously, Northern America, Europe, and Asia have been identified as the major source region contributor to the Arctic BC. However, there is a significant uncertainty associated with the contribution of each source sector and region area to the Arctic BC concentration. (Koch and Hansen, 2005; Sharma et al., 2013a; Wang et al., 2011) In this study the effects of BC emissions from different source sectors (e.g. transportation, power, industry, residential and biomass burning) and source regions (e.g. Europe, North America, China, Russia, Central Asia, South Asia and Middle East) to the Arctic BC concentration were investigated. For this purpose, we used WRF-STEM modeling framework. The simulations were validated the data using surface observation over North America and aircraft observations over the Arctic during spring and summer 2008. This objective will help us understand the sources of emission during different seasons over the Arctic.

Objective 4: Estimate the BC and dust deposition on the arctic snow and the resulting albedo reduction.

Long-range transport of atmospheric particles from mid-latitude sources to the Arctic is the main contributor to the Arctic aerosol loadings and deposition. BC, Brown Carbon (BrC) and dust are considered of great climatic importance and are the main absorbers of sunlight in the atmosphere.(Bond et al., 2013; Koch et al., 2007) Furthermore, wet and dry deposition of light absorbing particles on snow and ice causes reductions of snow and ice albedo. BC and dust have significant radiative forcing and

effect on snow albedo causing snow and ice to absorb more solar energy because of their dark color and melt more quickly.

In this study, the potential impacts of BC and dust deposition from different emission source regions and sectors on snow albedo in the Arctic are studied. WRF-STEM framework is used to simulate the seasonality and transport of light absorbing particles from different geographical sources and sectors (i.e. transportation, residential, industry, biomass burning and power) to the Arctic. For assessing the effect of BC deposition on snow, albedo reduction caused by BC deposition from various emission sources on the Arctic snow is calculated. There are large uncertainties in estimating the sources and impacts of light absorbing particles on the Arctic snow.(Wang et al., 2011) Several factors including uncertainties in global emissions, transport pathways, snow effective grain size, snow again, and post-depositional process of light absorbing particles are the large sources of uncertainties in quantifying the impacts of BC and dust deposition on the Arctic snow. (Bond et al., 2013; Flanner et al., 2007; Jiao et al., 2014; Stier et al., 2013) To evaluate the simulated values, we compared the BC concentration in snow with observed values from previous studies including Doherty et al. 2010.

This chapter is focused on quantifying deposition of BC and dust on the Arctic snow and calculating the albedo reduction caused by deposition of BC on snow. The sector-based analysis provides implications for policy makers to inform policies targeting emission sectors and regions with highest impacts on the Arctic climate.

Objective 5: Improve the computational efficiency of models by performance analysis, profiling and optimization of WRF Model and WRF-Chem.

Numerical weather prediction (NWP) and air quality forecasting models involves solutions to a large system of differential equations based on transport, physical and chemical processes in the atmosphere. (Brasseur and Jacob, 2017; Naik Bhadreshbhai and Thomas, 2016) During the recent years, there is a growing demand for detailed and high resolution weather and air quality forecasts for various applications.

WRF model is an open source mesoscale NWP system extensively used in atmospheric research, operational forecasting and educational settings with more than 36,000 users from over 150 countries. (Elliott and Del Vento, 2015; Powers et al., 2017; Skamarock et al., 2008) The high computational costs associated with higher resolution and more complex forecasts besides the large community of users makes the optimization of WRF and WRF-Chem of high priority for the WRF code developers. This objective is focused on a variety of performance optimizations to improve the WRF and WRF-Chem performance. The four primary milestones for this objective are: (1) performance analysis and profiling of WRF in order to identify major performance hotspots and bottlenecks; (2) modifying and optimizing the identified hotspots to improve the performance; (3) validating the numerical accuracy and results of the modified kernel; (4) integrating these changes back into the WRF repository.

Thesis Organization

For accomplishing the above research objectives different modeling frameworks are used. Each of the modeling approach and methods is described in the related chapter. Chapter 2 of this thesis addresses the research objective 1 mentioned above to study source sector and region contributions to BC and $PM_{2.5}$ in Central Asia. Chapter 3 of this thesis is focused on the intercontinental transport pathways of $PM_{2.5}$. Chapter 4 addresses the research objective 3 to discuss the source sector and region contributions to BC and $PM_{2.5}$ to the Arctic. In chapter 5, the impacts BC and dust deposition from various emission source sectors and regions on the Arctic snow surface albedo. Chapter 6 is focused on the last research objective to assess performance and optimize performance of NWP and CTMs. The final chapter is a summary of this dissertation and discussion of future research directions.

CHAPTER 2: SOURCE SECTOR AND REGION CONTRIBUTIONS TO BC AND PM_{2.5} IN CENTRAL ASIA

Abstract

Particulate matter (PM) mass concentrations, seasonal cycles, source sector and source region contributions in Central Asia (CA) are analyzed for the period April 2008-July 2009 using the Sulfur Transport and dEposition Model (STEM) chemical transport model and modeled meteorology from the Weather Research and Forecasting (WRF) model. Predicted Aerosol Optical Depth (AOD) values (annual mean value ~0.2) in CA vary seasonally with lowest values in the winter. Surface PM_{2.5} concentrations (annual mean value ~10 µg/m³) also exhibit a seasonal cycle, with peak values and largest variability in the spring/summer, and lowest values and variability in the winter (hourly values from 2 – 90 µg/m³). Surface concentrations of black carbon (BC) (mean value ~0.1 µg/m³) show peak values in the winter. The simulated values are compared to surface measurements of AOD, and PM_{2.5}, PM₁₀, BC, organic carbon (OC) mass concentrations at two regional sites in the Kyrgyz Republic (Lidar Station Teplokluchenka (LST) and Bishkek). The predicted values of AOD and PM mass concentrations and their seasonal cycles are fairly well captured. The carbonaceous aerosols are underpredicted in winter, and analysis suggests that the winter heating emissions are underestimated in the current inventory.

Dust, from sources within and outside CA, is a significant component of the PM mass and drives the seasonal cycles of PM and AOD. On an annual basis, the power and industrial sectors are found to be the most important contributors to the anthropogenic

portion of $PM_{2.5}$. Residential combustion and transportation are shown to be the most important sectors for BC. Biomass burning within and outside the region also contributes to elevated PM and BC concentrations. The analysis of the transport pathways and the variations in particulate matter mass and composition in CA demonstrate that this region is strategically located to characterize regional and intercontinental transport of pollutants. Aerosols at these sites are shown to reflect dust, biomass burning and anthropogenic sources from Europe, South, East and CA, and Russia depending on the time period.

Simulations for a reference 2030 emission scenario based on pollution abatement measures already committed to in current legislation show that $PM_{2.5}$ and BC concentrations in the region increase, with BC growing more than $PM_{2.5}$ on a relative basis. This suggests that both the health impacts and the climate warming associated with these particles may increase over the next decades unless additional control measures are taken. The importance of observations in CA to help characterize the changes that are rapidly taking place in the region are discussed.

Introduction

Central Asia (CA), a region of republics located between Europe and Asia, faces severe environmental problems, with origins dating back to the 1960s and best symbolized by the Aral Sea catastrophe (Whish-Wilson, 2002). The Aral Sea has shrunk to only about 30 percent of its 1960 volume and roughly half its geographical size due to diversion of water for crop cultivation and other purposes. The resulting desertification of

the lake-bed has resulted in extensive dust storms from the region, which have impacted the surrounding agriculture, ecosystem, and the population's health.

The 2012 Environmental Performance Index (EPI), which tracks performance of 132 countries across a variety of environmental and ecosystem vitality indicators, ranked CA countries among the weakest performers (Kazakhstan 129, Uzbekistan 130, Turkmenistan 131, Tajikistan 121, and Kyrgyzstan 101) (Emerson et al., 2012). CA and the surrounding areas are developing quickly and air pollution emissions are projected to increase significantly for the next several decades (Shindell et al., 2012). In recognition of the need to improve the environmental conditions in the region five CA countries have formulated the Framework Convention on Preservation of Environment for Sustainable Development of CA (UNEP, 2006).

Despite the awareness of the environmental conditions, it remains an understudied region and there is a general lack of air pollution observations within CA. Furthermore the recent assessment of the intercontinental transport of pollution (HTAP, 2010) has indicated that the major transport pathway of pollution from Europe to Asia is via low altitude flows passing through CA. The magnitude of the pollution transport from Europe to Asia is highly uncertain in large part due to the lack of observations of pollutants along this pathway. To help better characterize the air pollution levels and the transport pathways in the region a study was undertaken between Russia, Kyrgyz Republic, and USA scientists to observe and model aerosols in the region. Measurements of particulate matter (PM) mass and composition were taken at two locations in the Kyrgyz Republic

(Lidar Station Teplokluchenka (LST) and Bishkek) and modeling analysis was performed to assess the contributions of local, regional and distant sources to the PM concentrations in the region (Miller-Schulze et al., 2012, Chen et al., 2012, 2013).

In this paper, we present a modeling analysis of PM_{2.5}, PM₁₀, (PM_{2.5} refers to particles in the size range of less than 2.5 µm aerodynamic diameter (AD) and PM₁₀ refers to particles in the size range of less than 10 µm AD), black carbon (BC) and organic carbon (OC) mass concentrations and aerosol optical depth (AOD) over the time period of April 2008 to July 2009. The Sulfur Transport and dEposition Model (STEM), a hemispheric chemical transport model (D'Allura et al., 2011), is used to estimate spatial and temporal variations in PM in CA, and to assess the contributions to PM from wind-blown dust, open biomass burning, and anthropogenic sources, and different geographical source regions and source sectors (transportation, power, industry and residential). The simulated values are compared to surface measurements of AOD, PM_{2.5}, PM₁₀, BC, OC mass concentrations at the two regional sites in CA. Finally, we present results of how the PM concentrations may change in the future using emission scenarios for 2030 that reflect possible air quality and climate policies.

Method and Data

Meteorological Model

The Weather Research and Forecasting (WRF) model (Skamarock et al., 2008) version 3.2 was used to generate the meteorological fields needed for simulating the transport patterns in the STEM model (D'Allura et al., 2011). The WRF simulations for

each day were initialized using the meteorological boundary conditions obtained from National Centers for Environmental Prediction (NCEP) Final Analysis (FNL, <http://rda.ucar.edu/datasets/ds083.2/>). A daily 24 hour spin up time for WRF was used (i.e. WRF was run for 48 hours each day and the first 24 hours were treated as spin up and were discarded). The STEM model simulation time period was from April 2008 to July 2009.

Chemical Transport Model

The STEM model (Carmichael et al., 2009) was used to simulate the mass of sulfate, BC, OC, other primary emitted PM_{2.5}, and other primary emitted PM₁₀ (i.e., non-carbonaceous PM such as fly ash, road dust, and cement), which were simulated as a single mass component with aerodynamic diameters less than or equal 2.5 μm , and between 2.5 and 10 μm (denoted as coarse fraction), respectively and referred to in this paper as OPM_{2.5} and OPM₁₀, dust (fine and coarse) and sea salt (fine and coarse). Nitrate and secondary organic aerosols (SOA) were not included in the model for this application. The nitrate aerosol is estimated to be a minor component of the PM mass in CA (Bauer et al., 2007). The importance of SOA will be discussed later in the paper. The dry deposition of aerosols was modeled using the “Resistance in Series Parameterization” (Wesely and Hicks, 2000) and wet deposition was calculated as a loss rate based on the hourly precipitation calculated from the WRF model. Further details of the wet scavenging can be found in Adhikary et al., 2007. The modeled AOD at 550 nm wavelength was calculated using the simulated three dimensional aerosol distributions and species specific extinction coefficients as described in Chung et al., 2010.

Modeling Domain

The STEM and WRF computation domains were identical, with a 60 ×60 km horizontal resolution (249 ×249 horizontal grid cells) and 22 vertical layers up to 10 hPa. The domain (Figure 2-1a) covered much of the northern hemisphere in a polar stereographic projection, centered over the Arctic region and extended to 35° N to include the major emission regions of North America, Europe, and Asia. This modeling system has been applied to simulate aerosol distributions for ARCTAS field campaign as described in D’Allura et al., 2011 and further details describing the model can be found there. STEM was initialized with a one month spin up using March 2008. Much of the analysis for this paper is focused on the domain denoted by the rectangle centered over CA shown in Figure 2-1-a. This domain has large gradients in topography (shown in Figure 2-1-b), which significantly impact the transport patterns in the region.

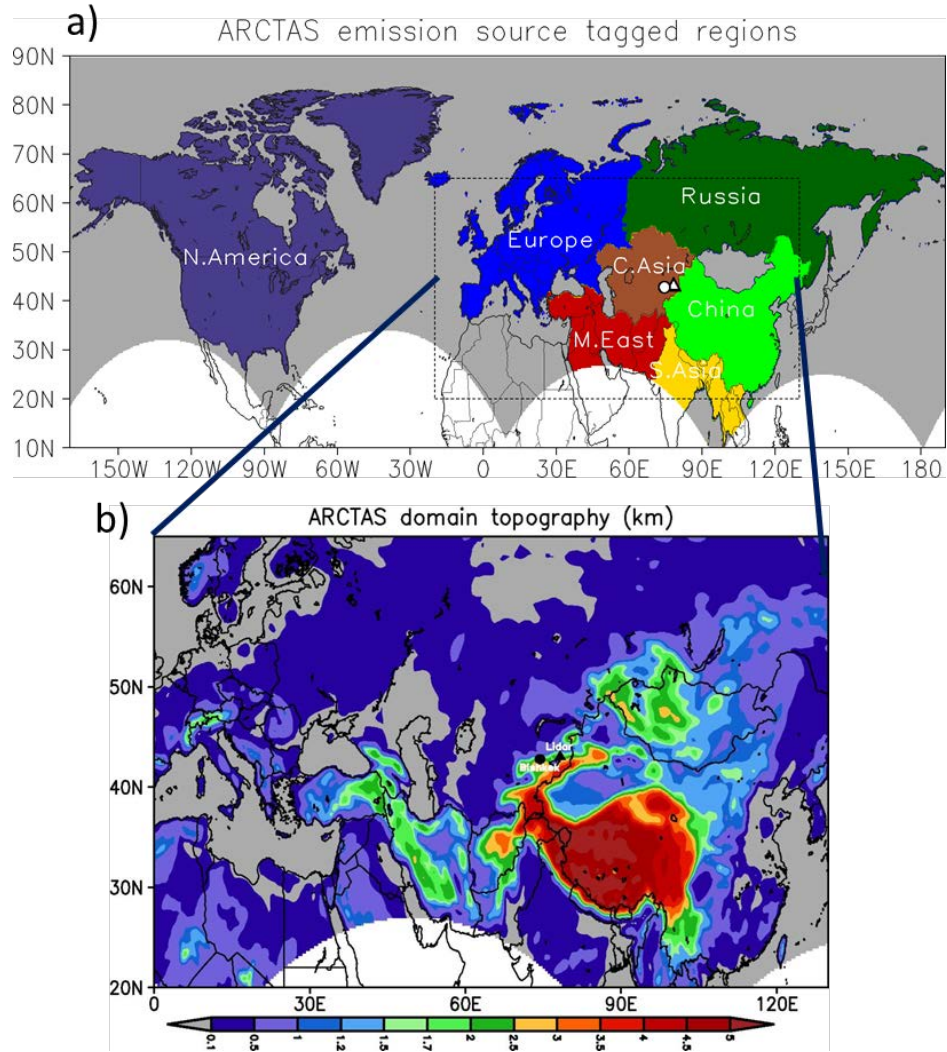


Figure 2-1 : WRF-STEM modeling domain set up source region definition used in the simulations. (b) shows the topography around the observation sites.

Emissions

Base Emissions

Anthropogenic emissions of BC, OC, PM_{2.5}, PM₁₀, and SO₂ were based on the ARCTAS emissions described in D'Allura et al., 2011, but updated with newly available information. For India and China BC, OC, and SO₂ emissions from Lu et al., 2011 were

utilized, and INTEX-B emissions were used for the rest of Asia (Zhang et al., 2009). For Europe, the EMEP 2008 (<http://www.ceip.at/webdab-emission-database/officially-reported-emission-data>) emissions were used for SO₂, PM_{2.5}, and PM₁₀, and the EUCAARI 2005 inventory was used for the carbonaceous particles (BC and OC) (Denier van der Gon et al., 2009; Visschedijk et al., 2009). The shipping emissions came from the IIASA base year 2005 inventory (UNEP and WMO, 2011). Mass conservative regrinding tools including MTXCALC and MTXCPL from the IOAPI m3tools suite (<http://www.baronams.com/products/ioapi/AA.html#tools>) were used to interpolate the input raw emissions described above on to the model grid.

Anthropogenic emissions for SO₂, BC and OC were available by major economic sectors; i.e., transportation, residential, industry, and power. The industry and power sectors were treated as small and large point sources, respectively, and emitted into the first 6 model levels (lowest 2 km). The residential and transportation emissions were treated as near surface area sources and partitioned into the first two model levels from surface to ~ 100m (i.e. AGL altitude of level 2) with a 90 – 10 percent split. Monthly emission allocation factors were applied over India and China for the economic sectors from (Lu et al., 2011). The rest of the domain (i.e. excluding India and China) used same emission rates for all months due to unavailability of monthly emission allocation factors.

The Fire Inventory from NCAR (FINN v1) was used for BC, OC, CO, SO₂, PM_{2.5} and PM₁₀ biomass burning emissions from forest, grassland and crop residual fires. The FINN database, which is based on MODIS fire detection as thermal anomalies, provides

global coverage of fire emissions at a spatial resolution of ~ 1km on a daily timescale (Wiedinmyer et al., 2011). The WRF-Chem fire utility (<http://bai.acd.ucar.edu/Data/fire/>) was employed to interpolate the speciated FINN emissions to the WRF model grid. The gridded two-dimensional FINN emissions were used as input to the WRF-Chem (Grell et al., 2005) plume rise model (Grell et al., 2011), which implements the Freitas et al., 2007 and Freitas et al., 2010 algorithm to compute injection heights and to calculate the vertical distribution of fire emissions at an hourly time step, which were further utilized as input to STEM model simulations.

Sea salt and dust emissions were calculated using the WRF meteorological fields based on the methods described in Gong, 2003 and Uno et al., 2004, respectively. The dust emissions were further constrained with snow cover (SNOWC variable from WRF output) and only grid cells with snow cover < 1% were used for dust emission calculations.

Figure 2-2 shows the annual gridded anthropogenic SO₂ and BC, dust, and biomass burning PM_{2.5} emissions in Gg per grid in and around CA. Large BC emission hotspots can be seen over the Indo-Gangetic plain and eastern China. Significant BC emissions are also seen over Europe, but are relatively lower in intensity than the Asian sources. The SO₂ emissions show Eastern China as the largest source region followed by regions of South Asia, Europe, and Russia. The major natural dust emission sources (Figure 2-2c) include Africa, the Middle East, CA, Western India boundaries, and

Western China. The major sources of biomass burning are Eastern Europe, portions of Siberian (between 40 – 60° N), Southeast Asia, Southern China and India (Figure 2-2d).

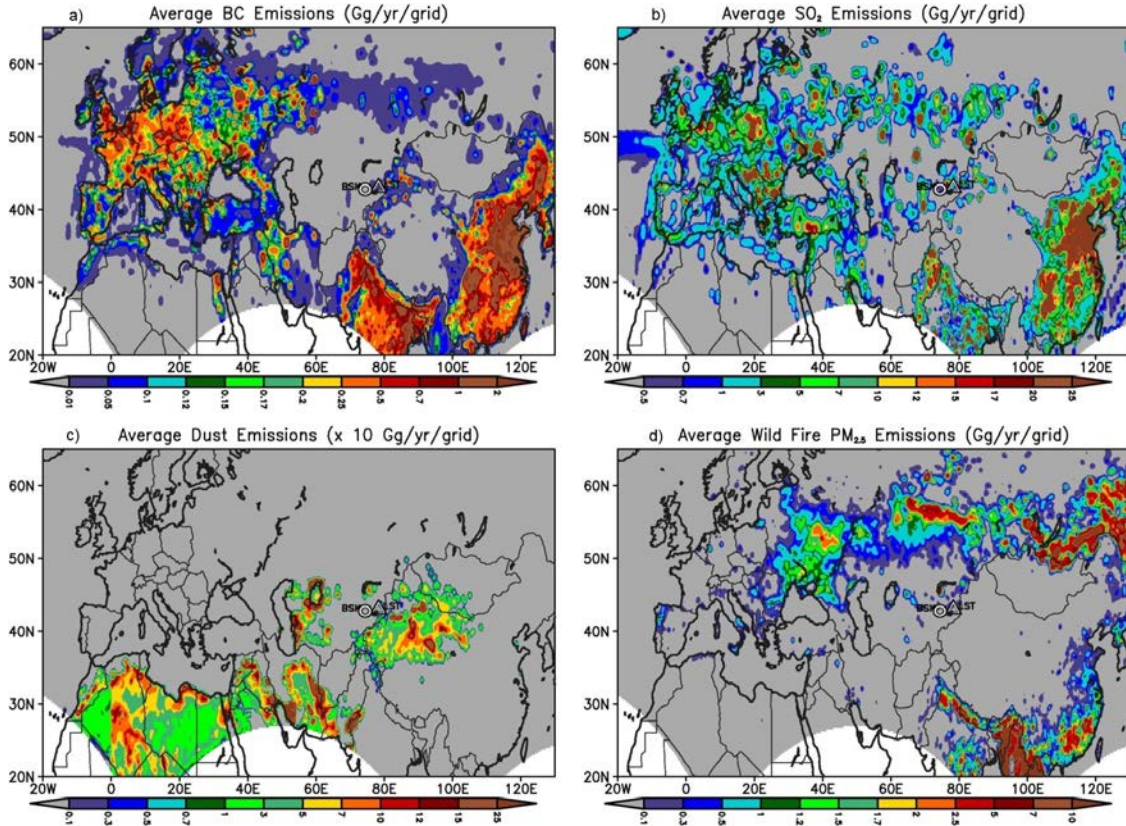


Figure 2-2: Spatial distribution of a) BC b) SO₂ c) Natural dust d) Biomass burning PM_{2.5} emissions averaged over the simulation period in Gg/yr/grid.

Dust emissions have a strong seasonal cycle. The major dust sources in the region are located to the east, west and south of the observation sites and include the cool winter deserts around the Aral and Caspian seas and those in western China and northern Pakistan as well as the sub-tropical deserts in western India, around the Persian Gulf and northern Africa. The emissions from the cool winter deserts occur when the surfaces are

free of snow cover (from March through October). Emissions from the sub-tropical deserts can occur throughout the year.

The open biomass burning emissions that impact CA also have a strong seasonality with minimum impact in winter. (Figure 2-3) Fires typically begin in the spring in Siberia along 50° N latitude and in northern India and South East Asia and in summer the high latitude burning shifts to the west. In October, the fire activity decreases and remains low until spring, with the most active fire regions associated with agricultural burning in northern India and southeast China.

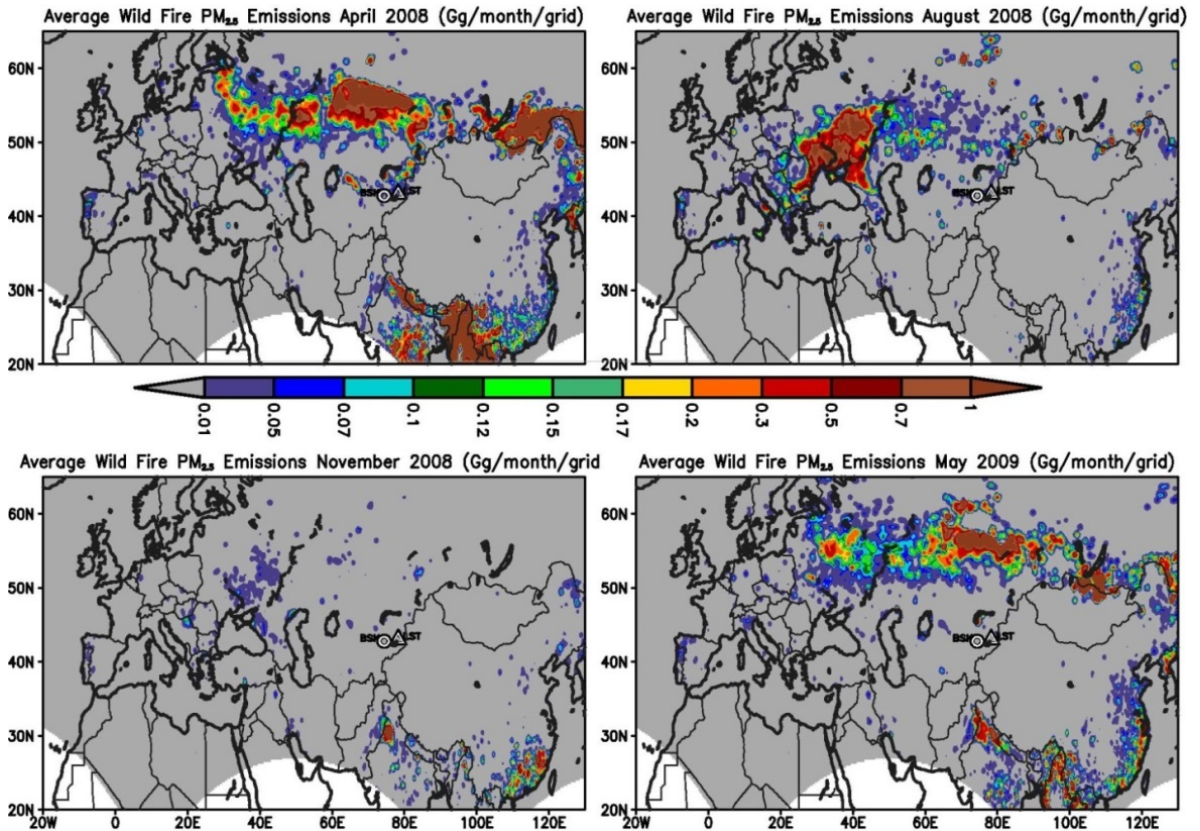


Figure 2-3: Seasonal variability in spatial distribution of biomass burning PM_{2.5} emissions in Gg/month/grid (a) April 2008, (b) August 2008, (c) November 2008, and (d) May 2009.

Future Emissions Scenarios

In addition to the base emissions, a series of simulations were analyzed using emission scenarios for 2030. These scenarios were developed for the WMO/UNEP report that looked at short lived climate pollutants as described in Shindell et al., 2012 and Anenberg et al., 2012. The reference scenario for 2030 was based on the implementation of control measures currently approved in the various regions and assumed their perfect implementation. The 2030 reference scenarios were developed from a reference global emissions inventory with a 2005 reference year, and assumed significant growth in fossil fuel use relative to 2005, leading to increases in estimated CO₂ emissions (45%). Abatement measures prescribed in current legislation were projected to lead to reductions in air pollutant emissions, which varied by pollutant and region. In the 2030 reference scenario, total primary PM_{2.5} emissions remain approximately constant, while BC and OC decline by a few percent. However, in the study domain emission changes varied widely. BC emissions increased by 10 – 100% in CA, South and Southeast Asia and in western China, and decreased in East Asia and Europe. The PM_{2.5} emissions showed similar regional changes but grew at smaller rates (10 – 40%). SO₂ emissions generally increased throughout the region by 10 – 20%. Spatial maps of emission changes for the 2030 reference scenario are presented in Figure 2-4b , Figure 2-5b, and Figure 2-6b.

A series of emission control scenarios for 2030 were developed to evaluate the impact of additional abatement measures designed to reduce the levels of short lived climate pollutants (e.g., BC). The BC measures in the scenarios included two different sets of assumptions (low and lowest). The first focused on reductions from incomplete

combustion sources. These included implementation of Euro 6 equivalent vehicle emission standards (requiring installation of diesel particulate filters) and improving traditional biomass cook stoves in developing countries (assuming 25% decrease in BC and 80–90% decreases in OC, CO, non-methane volatile organic compounds (NMVOC), methane, and direct $PM_{2.5}$, relative to emissions from traditional stoves). Under this scenario BC and $PM_{2.5}$ emissions in the study region are projected to decrease throughout most of the domain, with SO_2 emissions showing almost no change (see Figure 2-4c, Figure 2-5c, and Figure 2-6c).

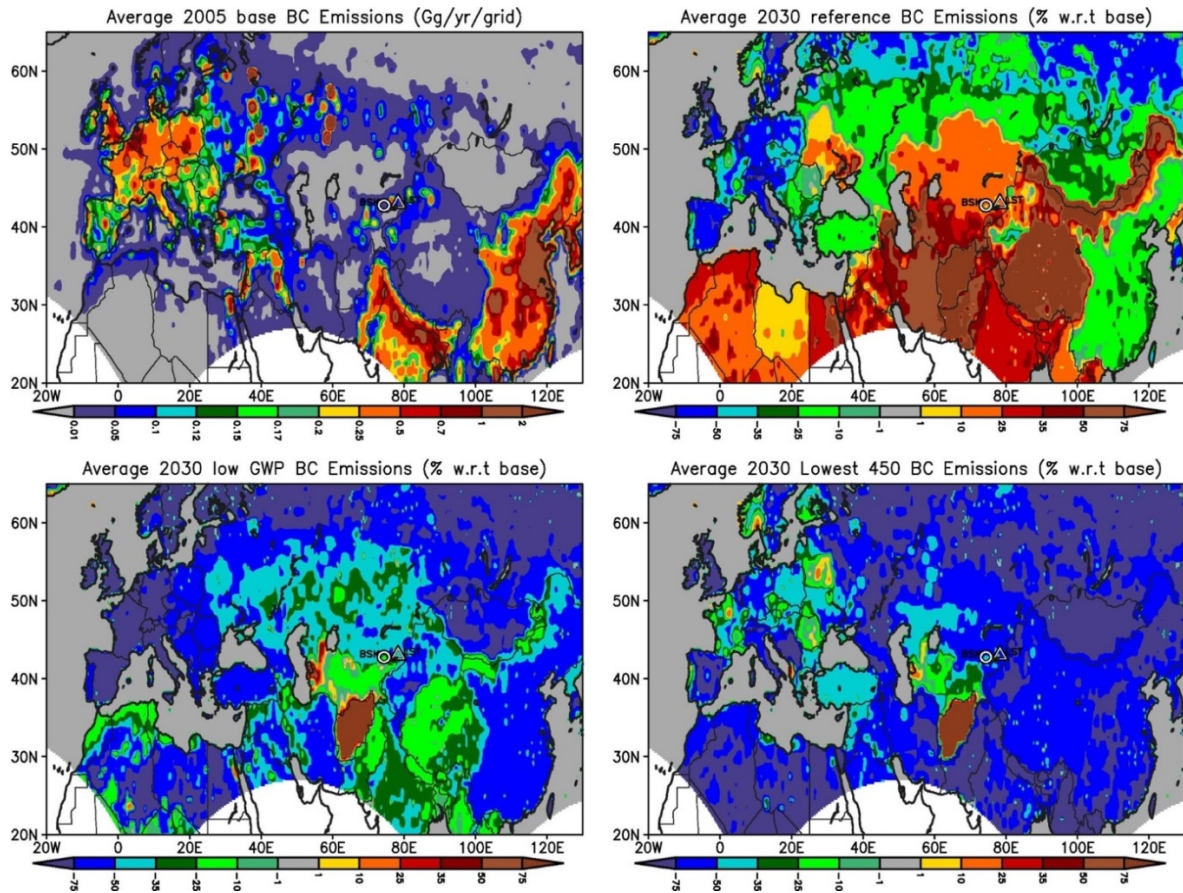


Figure 2-4: Spatial distribution of a) base year 2005 BC emissions (Gg/yr/grid) along with percent change (w.r.t to base year 2005) in (b) Reference 2030 BC emissions c) 2030 BC emissions with BC measures (low) and d) 2030 BC emissions with BC (lowest) and greenhouse gases measures aimed at keeping CO₂ levels below 450ppm.

The lowest option assumed the additional elimination of high-emitting vehicles, biomass cook stoves (in developing countries), and agricultural waste burning. These BC measures in the lowest scenario reduced global anthropogenic BC emissions by 75%. Measures targeting BC also substantially reduced total primary PM_{2.5} (-50%), OC (-79%), NO_x (-27%), and CO (-44%). These BC measures have little impact on SO₂

emissions. Projected emissions of BC and OC under these scenarios are reduced most in Asia, followed by Africa. North America, and Europe.

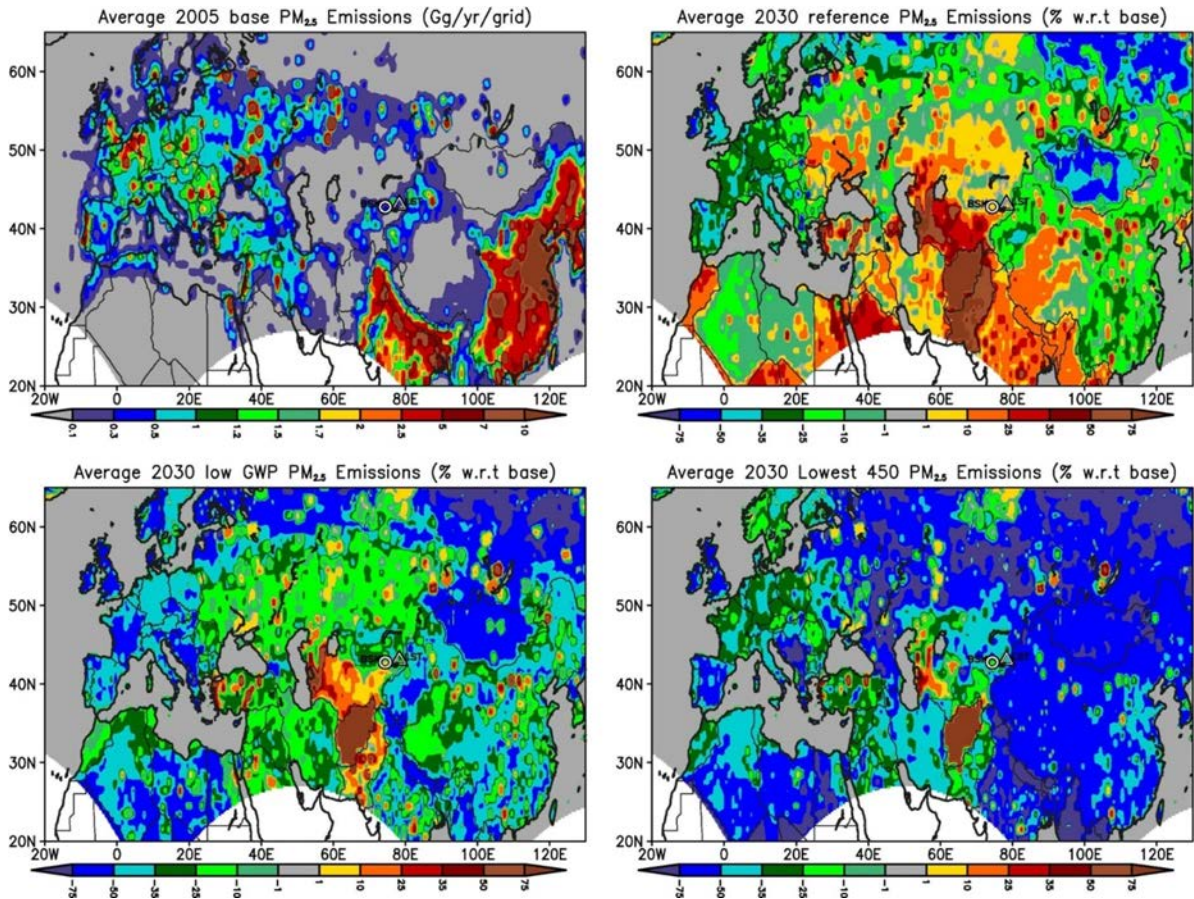


Figure 2-5: Spatial distribution of a) base year 2005 $PM_{2.5}$ emissions (Gg/yr/grid) along with percent change (w.r.t to base year 2005) in (b) Reference 2030 $PM_{2.5}$ emissions c) 2030 $PM_{2.5}$ emissions with BC measures and d) 2030 $PM_{2.5}$ emissions with BC and greenhouse gas measures aimed at keeping CO_2 levels below 450ppm.

These measures were also combined with a scenario designed to stabilize greenhouse gases at 450 ppm of CO_2 equivalent (lowest+450ppm scenario), consistent with a global average temperature increase of $\sim 2^\circ C$. These CO_2 measures reduced SO_2 (-30%) (Figure 2-6d) and NO_x (-20%), but had little further impact on BC ($\sim 5\%$ decline,

Figure 2-4d) since the major sources of CO₂ differ from those of BC. PM_{2.5} emissions were substantially further reduced under this scenario (Figure 2-5d).

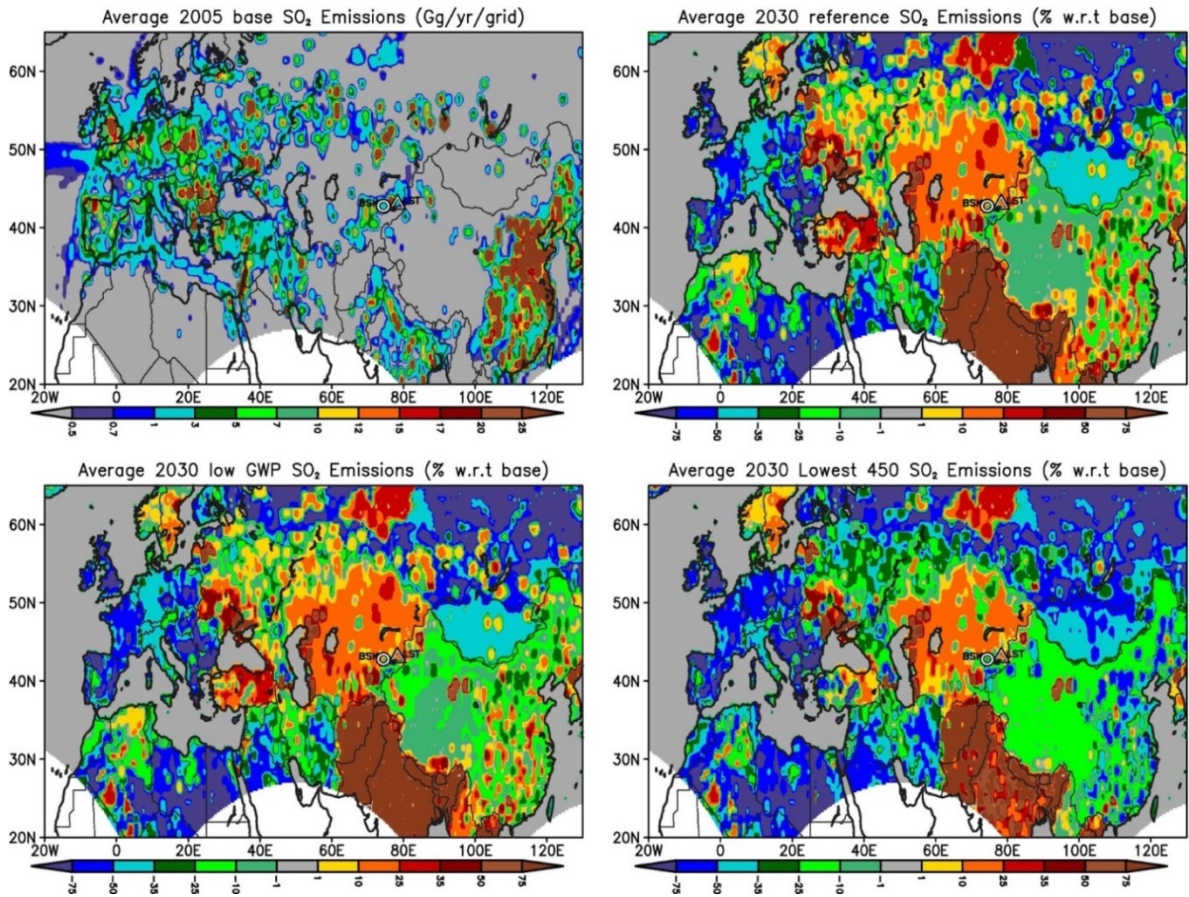


Figure 2-6: Spatial distribution of a) base year 2005 SO₂ emissions (Gg/yr/grid) along with percent change (w.r.t to base year 2005) in (b) Reference 2030 SO₂ emissions c) 2030 SO₂ emissions with BC measures and d) 2030 SO₂ emissions with BC and greenhouse gas measures aimed at keeping CO₂ levels below 450ppm.

Observations

Surface observations from two sites established in the Kyrgyz Republic to measure PM concentrations and AOD in CA are used in the analysis. The locations of the Bishkek (42°40'46.65"N, 74°41'38.13"E, elevation 1743 above sea level (ASL)) and LST

(42°27'49.38"N, 78°31'44.17"E, elevation 1921 m ASL) sites are denoted by circle and triangle markers, respectively, in Figure 2-1a. Both sampling sites are in mountain ranges with valleys to the north, with mountains that reach elevations greater than 3500 m ASL south of the Bishkek site and 4600 m ASL south of the LST site, and essentially no population to the south. At each site, PM_{2.5} mass was measured continuously with tapered element oscillating microbalance (TEOM) instruments and PM_{2.5}, PM₁₀, BC, and OC were obtained using filter-based sampling with samples collected for 24 h every other day. AOD was measured every day at 10:30 am local time (LT) using Microtops-II sun-photometers (SP). A stationary three wavelength aerosol Lidar measured vertical profiles of extinction and depolarization on an event basis at the LST site. The Lidar vertical profiles provide information on vertical distribution of the particles, and were also used to calculate AOD from the Lidar Extinction (LE) profiles and to estimate the height of the planetary boundary layer (PBL) as described in Chen et al., (2013). These observations sites are now part of the UNEP project ABC measurement network (<http://www.rrcap.ait.asia/abc/index.cfm>). Further details of the study can be found in Miller-Schulze et al., 2011. Observations from these sites were obtained for the period April 2008 to July 2009 (the TEOM measurements were available from April 2008 and filter measurements began from July 1, 2008).

In addition, the model prediction skill in simulating the aerosols is evaluated using the AOD observations from the AERosol RObotic NETwork (AERONET available at <http://aeronet.gsfc.nasa.gov/>) located within the domain and the time period used in this study along with PM₁₀ measurements from the European Monitoring and Evaluation

Programme (EMEP available at <http://www.nilu.no/projects/ccc/emepdata.html>) and the Acid Deposition Monitoring Network in East Asia (EANET available at <http://www.eanet.asia/product/index.html>) surface site networks.

The Moderate Resolution Imaging Spectroradiometer (MODIS) collection 5.1 Level 2 AOD products (~ 10 km horizontal resolution) at 550 nm wavelength from Terra and Aqua satellites were used to compare the observed and simulated AOD. The MODIS Level 2 data were used and included land and ocean AOD retrieved via the dark target algorithm (Remer et al., 2005), (Levy et al., 2007), and the Deep Blue AOD over land (Hsu et al., 2004), (Hsu et al., 2006), which can retrieve AOD over bright and desert surfaces. This is particularly relevant for the CA region, which contains major dust sources in western China, South Asia, the Middle East, and Africa (Ginoux et al., 2001). The MODIS Level 2 to Level 3 averaging procedure outlined in Hubanks et al., 2008 was employed to interpolate the 10 km Level 2 AOD products to the 60 km horizontal model resolution on a daily basis. Level 2 QA flag weightings were used to reduce the uncertainty associated with the MODIS retrievals. In grid cells where both the MODIS dark target and Deep Blue AOD were retrieved, the mean value of the two was used.

Simulations Analyzed

The CA region is strategically located and aerosols at these sites are shown to reflect impact of varied dust (including CA, Western China, Africa and Middle East), biomass burning (including Europe, Siberia, South Asia and North America) and anthropogenic sources (including Europe, South, East and Central Asia, and Russia)

depending on the time period. Therefore, we choose different regions for the anthropogenic, dust and biomass burning in order to capture the impact and the associated seasonality of these main regions on the regional distribution of aerosols in this region. We have more anthropogenic regions to better understand how regional changes in emissions may impact CA PM levels.

Several simulations were analyzed for this paper. The base simulation included all sources and used the meteorology from the WRF model for the period April 2008 – July 2009. To investigate the contributions from specific source sectors, additional simulations were performed where emissions from one sector were set to zero everywhere. The contribution from each sector was calculated as the difference between the base simulation and the simulation with emissions from that particular sector set to zero. This was repeated for each sector and for biomass burning. Additional simulations were performed to assess the source contribution from specific regions to the particle levels in CA. The specific regions used are shown in Figure 2-1. In these simulations, all anthropogenic emissions were set to zero in that region. In a similar manner, regional dust and fire sources were also studied and the source regions are also shown in Figure 2-1. Finally, simulations were performed using the reference 2005 and 2030 emissions and the low and lowest + 450 CO₂ 2030 scenarios (described above). For these runs, the meteorology, open biomass burning, and dust emissions were the same as in the base run (i.e., 2008/2009).

Model Evaluation

We have evaluated this model framework in other regions outside CA including arctic region and continental US previously, which are summarized below. The domain configuration and settings of the WRF/STEM modeling system used in this study have been applied to provide meteorology and air quality forecasting during the ARCTAS field campaign in 2008 (D'Allura et al., 2011) as mentioned earlier in previous sections. The study by D'Allura et al., used WRF v2.2 and pre-emission ARCTAS emissions data (http://mic.greenresource.cn/arctas_premission), real time biomass burning emissions from the RAQMS modeling group (<http://raqms-ops.ssec.wisc.edu/>) and evaluated the performance of the WRF-STEM modeling framework (used in this study) through the case study of the ARCTAS mission DC-8 flight conducted on July 9 2008. The WRF model compared well with observed meteorological variables (including temperature, pressure, wind speed and wind direction) along the flight and correctly simulated the various meteorological processes (i.e. cyclonic circulation, low pressure system, anticyclones and geostrophic wind flows) that facilitate transport of pollutants into the Arctic region. This study also compared CO along the flight and found that the simulated values were able to capture the magnitude and temporal variability seen in observed values. The study also found that the fires from North Asia and anthropogenic CO from China were the major sources contributing to observed CO levels along the flight suggesting that the mid-latitude pollution and summertime forest fires/biomass burning transport events were well represented in this modeling system.

Huang et al., 2012 used a subset of this domain (covering the region of continental North America) to simulate summertime sectoral and regional contributions to BC over continental US using the WRF/STEM modeling framework. Note that the Huang et al., 2012 study used the same WRF meteorology, ARCTAS emissions and RAQMS biomass burning emissions used in the D'Allura et al., 2011 study, but used the full-chemistry version of the STEM model. The comparison of the simulated aerosol BC from the STEM tracer model with corresponding BC values from the full chemistry version of the STEM model showed that the simulated tracer BC was able to capture trend and the same relative variability seen in the full chemistry predictions. Huang et al., 2012 evaluated the model performance aloft and at surface using measurements from ARCTAS mission DC8 flights conducted on June 20 and 22 and 24 that sampled over California and IMPROVE surface site network. Huang et al., 2012 found that the predicted BC values captured many of the vertical features seen in the flight observations with a tendency to over predict surface BC and $> 4\text{km}$. The comparison of predicted BC with observed values from the IMPROVE network showed that the model was able to capture the gradients in BC values with high concentrations in western and eastern NA regions with slight positive and negative biases over the mountain regions and the eastern US/California. In this paper, we further evaluate the performance of the model over the selected domain in this study (Figure 2-1) using MODIS and AERONET AOD and PM_{10} surface observations as described in the following sections.

Results and Discussion

Regional Perspective

CA is a region with high aerosol loadings as shown in the mean MODIS retrieved AOD at 550 nm for the time period of study (April 2008 – July 2009) (Figure 2-7a). AOD (period mean) throughout CA (~ 45-90° E, 35-50° N) are greater than 0.25, with the highest regional values around the desert areas near the Caspian and the Aral seas. There are also high values (>0.6) along CA's eastern border, which reflect the deserts and rapidly developing cities in western China, and to the south over Pakistan and northern India.

The period-mean predicted surface concentrations of PM_{2.5}, BC, total dust (fine and coarse) and PM_{2.5}/PM₁₀ ratio are shown in Figure 2-8. The BC levels in CA are typically less than 0.3 µg/m³ and its spatial pattern reflects contributions from both anthropogenic and biomass burning sources (Figure 2-8-a). The simulation period mean PM_{2.5} concentrations in CA (10 to 35µg/m³) (Figure 2-8-c) have a similar geographical distribution as AOD (Figure 2-7-a). Dust is the major component of predicted PM₁₀ in CA as seen from the high dust concentrations (25-100 µg/m³) in Figure 2-8-b and low values (0.3 – 0.4) of the predicted PM_{2.5}/PM₁₀ ratio (Figure 2-8-d). The natural dust source regions including Western China, Middle East, Africa and western India have similar PM_{2.5}/PM₁₀ ratio values (0.3-0.4) reflecting the major contribution of dust to PM over these regions. The high predicted PM_{2.5}/PM₁₀ ratio values (>0.6) are seen over southern and eastern China indicate that the non-dust sources are the dominant contributors to PM in this region.

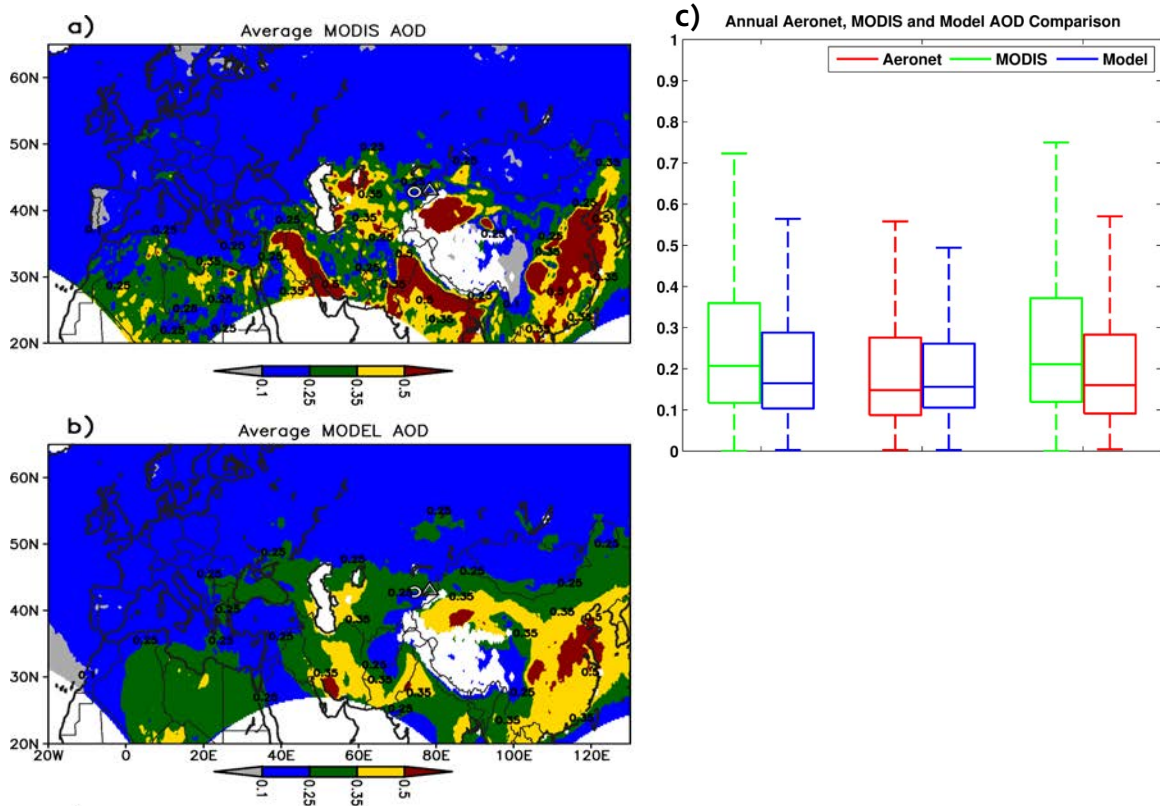


Figure 2-7: Spatial distribution of (a) MODIS and (b) modeled AOD along with (c) Comparison of MODIS, AERONET and Simulated AOD shown as box whisker plots averaged over the simulation period. The box plots are based on data that are paired in time and space. The triangle and circle markers on the spatial plots denote the location of LST and Bishkek sites. The numbers on the map denote contour values at sharp gradients. In each box whisker panel, the middle line denotes the median value, while the edges of the box represent 25th and 75th percentile values respectively. The whiskers denote the maximum and minimum values.

Model Evaluation with AOD and PM measurements

Comparison with MODIS and AERONET AOD

The predicted period mean AOD spatial distribution is shown in Figure 2-7-b (using only data from grid cells where MODIS AOD was available. The white colored areas denote regions where MODIS AOD data was not available). The simulated AOD values

capture the main observed spatial features including enhanced AOD over desert regions of Asia including East Asia, West Asia and along the western border of India, Eastern China, Northern India covering the Indo Gangetic Plain and Southeast Asia that are known to have large impacts of anthropogenic and wildfire emissions. However, the period mean AOD values are biased low relative to MODIS AOD over the regions of Northern India and Eastern China. This could be in part related to uncertainty associated with anthropogenic emissions over these regions and the 60km model resolution used in this study. The simulated AOD values are over-predicted relative to MODIS AOD over regions surrounding CA including parts of Eastern Europe, Russia, Northern China, Western Asia and Africa. These biases could be partly attributed to the uncertainty associated with regional transport of dust shown in spatial patterns of simulated dust and $PM_{2.5}/PM_{10}$ ratio (Figure 2-8).

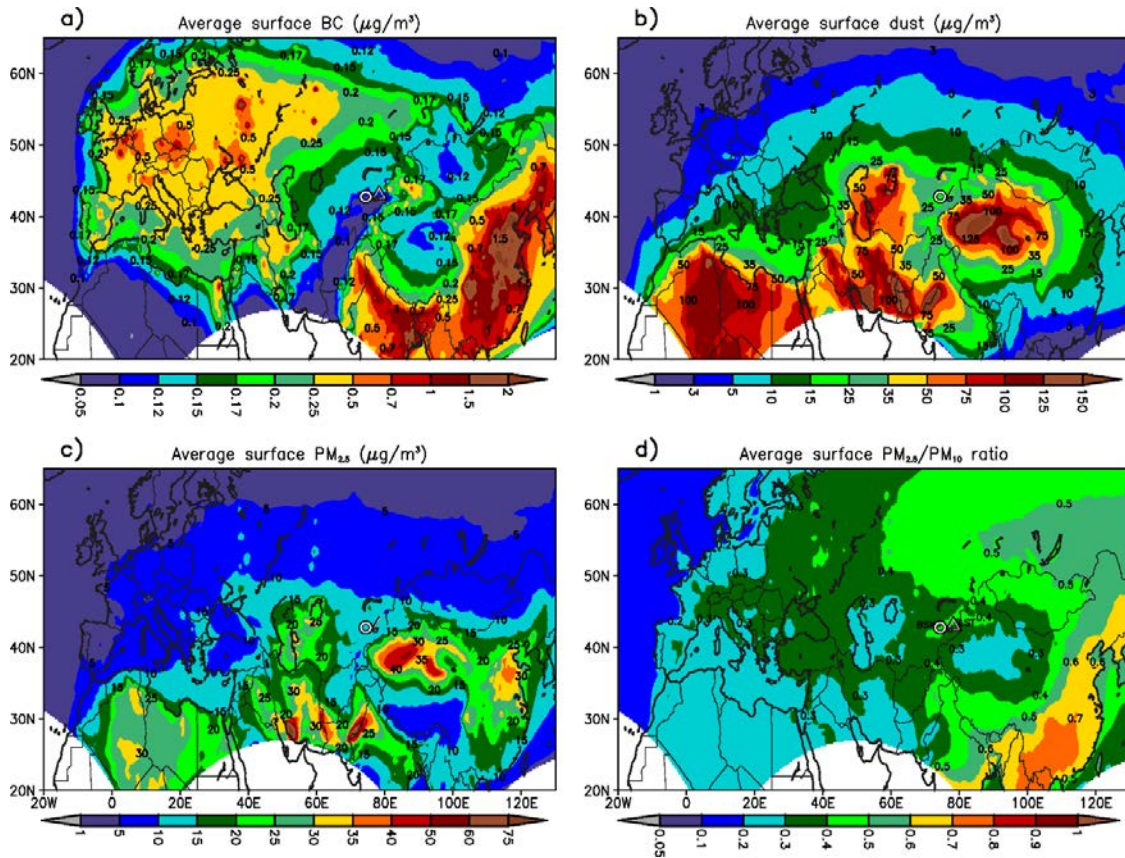


Figure 2-8: Spatial distribution of simulated a) BC ($\mu\text{g}/\text{m}^3$), b) Dust ($\mu\text{g}/\text{m}^3$), c) $\text{PM}_{2.5}$ ($\mu\text{g}/\text{m}^3$), and d) $\text{PM}_{2.5}/\text{PM}_{10}$ ratio averaged over the simulation period. The values on the map denote contour values at sharp gradients.

The model prediction skills in simulating the temporal and spatial patterns in AOD was evaluated by comparing the predicted daily AOD with the corresponding measured values at 142 sites from the AERONET program located within the domain and for the time period used in this study. We have also compared the AERONET AOD with MODIS on a daily time scale by extracting the daily MODIS retrieved AOD corresponding to the AERONET site locations for the simulation time period. The comparison of the predicted daily AOD with the available MODIS retrievals ($n = 29680$

using MODIS and simulated AOD extracted at the AERONET site locations, which are paired in space and time) is shown in Figure 2-7-c. The model values show a similar mean value (average simulated and MODIS AOD are 0.24 and 0.31 respectively), with a negative bias and an under-prediction in the variability. The comparison of model predictions with respect to AERONET AOD data (n = 22875) shows much closer agreement with mean modeled and AERONET values of 0.21 and 0.23 respectively; (note the comparison is based on paired data for the times only when AERONET data was available so the means are different than the MODIS/model comparison). Also shown is the comparison between MODIS and AERONET (for times/locations with paired AERONET measurements; n = 12719) with AERONET and MODIS mean values of 0.24 and 0.29 respectively. The comparison results of AERONET with respect to MODIS are similar to corresponding values of the MODIS/MODEL comparison, indicating that MODIS retrievals are biased high in the study domain. A more detailed analysis of the AOD comparison by region and season is included in the Figure 2-9 and Figure 2-10.

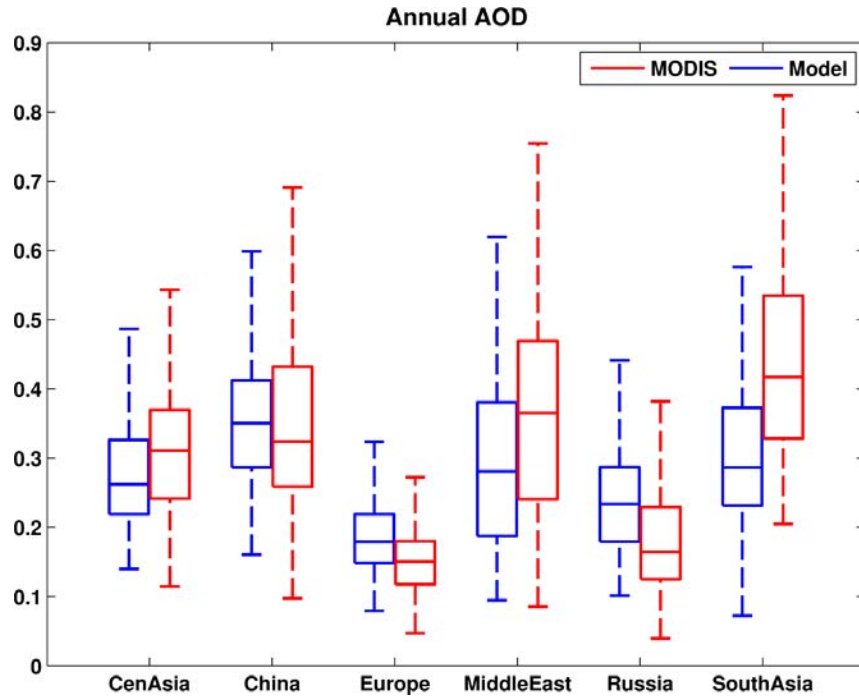


Figure 2-9: Comparison of regional average AOD from MODIS with simulated AOD shown as box plots over the simulation period for selected source regions including Central Asia, China, Europe, Middle East, Russia and South Asia.

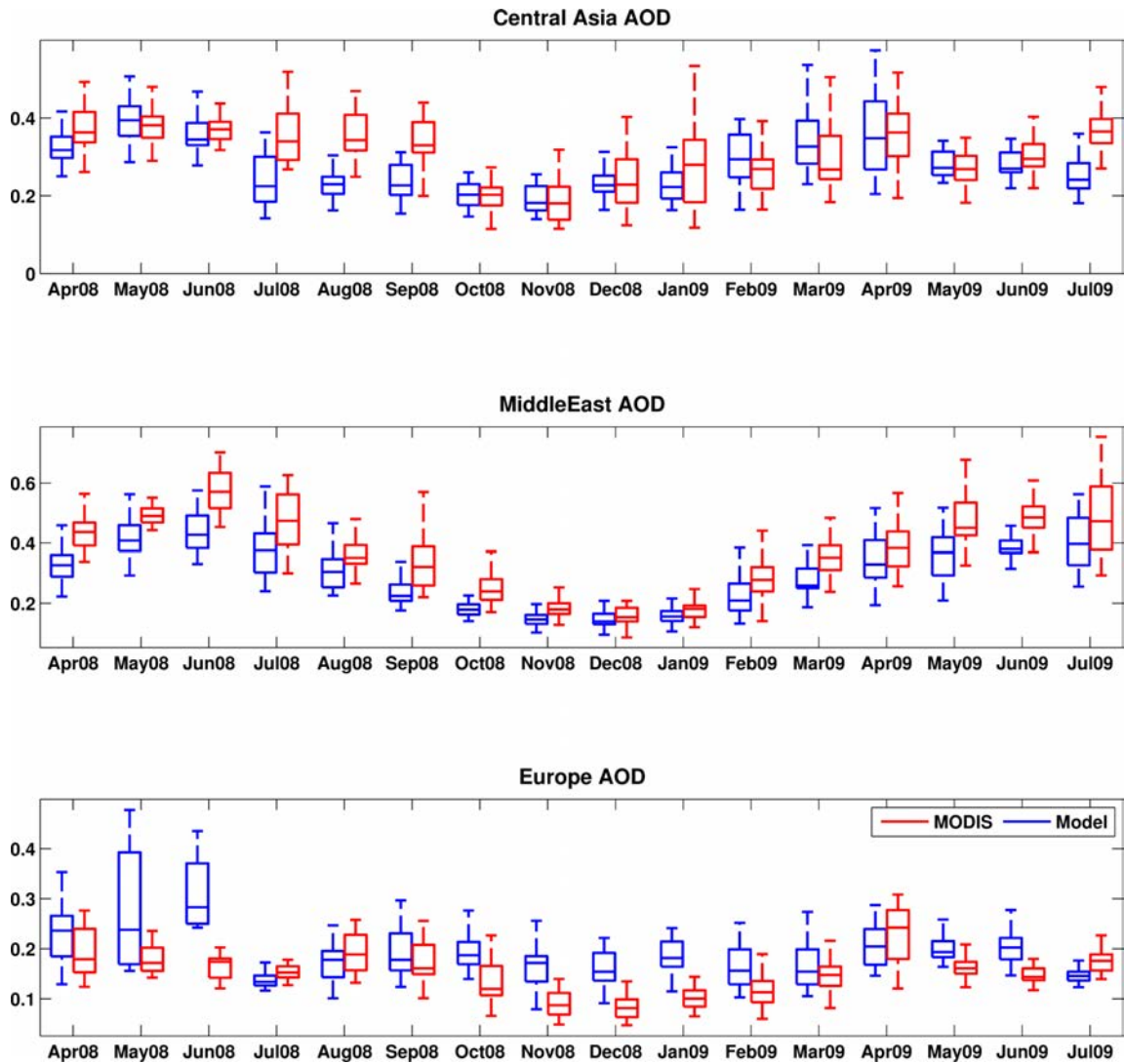


Figure 2-10: Comparison of regional average AOD from MODIS with simulated values shown as monthly box plots over the simulation period for selected source regions (a) Central Asia (b) Middle East and (c) Europe.

Comparison with PM_{10} Observations from EMEP and EANET Network

We also evaluated the simulated PM_{10} values with monthly mean observed data for the simulation time period from the EANET network over Asia (Figure 2-11). The modeled values are under-predicted as evident from the mean observed and modeled

PM₁₀ values of 32.2 and 22 $\mu\text{g m}^{-3}$ (n = 314). The normalized mean bias and error are ~ -32% and 44 % respectively. This could be partly attributed to the uncertainty associated with dust emissions that have a significant impact on the EANET site locations. We also evaluated the simulated PM₁₀ values over Europe using the available monthly mean observations from EMEP for the 2002-2003 time period. The mean observed and modeled values of PM₁₀ are 23.9 and 22.2 $\mu\text{g m}^{-3}$ (n = 130). The normalized mean bias and error for the EMEP PM₁₀ are -7 and 43 % respectively suggesting an overall under-prediction by the model.

The evaluation of this model framework in other regions outside CA including arctic region and continental US (described earlier) along with the comparison of regional distribution and temporal variability in simulated AOD using corresponding MODIS and AERONET measurements indicates that the predictions of aerosol mass and composition at the hemispheric scales are able to capture important aspects of horizontal gradients and variability, but have considerably higher uncertainties associated with emission estimates (in particular forest fires/biomass burning and natural dust emissions) and wet removal processes (Bates et al., 2006).

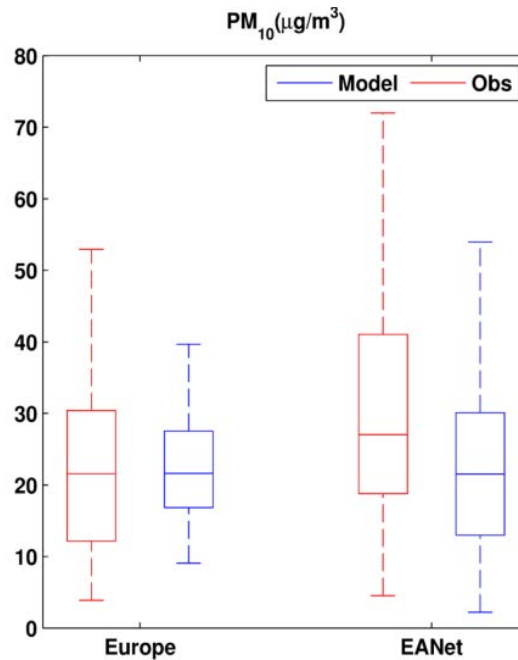


Figure 2-11: Comparison of predict PM_{10} with monthly observations from the European Monitoring and Evaluation Programme (EMEP available at <http://www.nilu.no/projects/ccc/emepdata.html>) and the Acid Deposition Monitoring Network in East Asia (EANET, data available at <http://www.eanet.asia/product/index.html>).

Comparison with Surface Observations in CA

The surface observations at the two CA sites provide the opportunity for the first time to evaluate the performance of chemical transport models in estimating the distribution of aerosols in CA and to assess the emission estimates in the region. A comparison of the predicted and observed meteorology is presented in Figure 2-12, where the distributions of key meteorological parameters for the entire measurement period are shown as box-plots. The model accurately predicted the magnitude and variability in temperature and relative humidity. For example, the model mean value of temperature and relative humidity are 279.3K and 61.6% in comparison to the observed values of

280.3K and 59.2% at the LST site. The model wind speeds were biased high by about 30% (mostly in winter) and the direction had a southwest bias. These biases are due in part to the 60 km model grid size, which is too coarse to capture the steep gradients in topography in and around the observation sites, and to the site placement in small N-S oriented valleys.

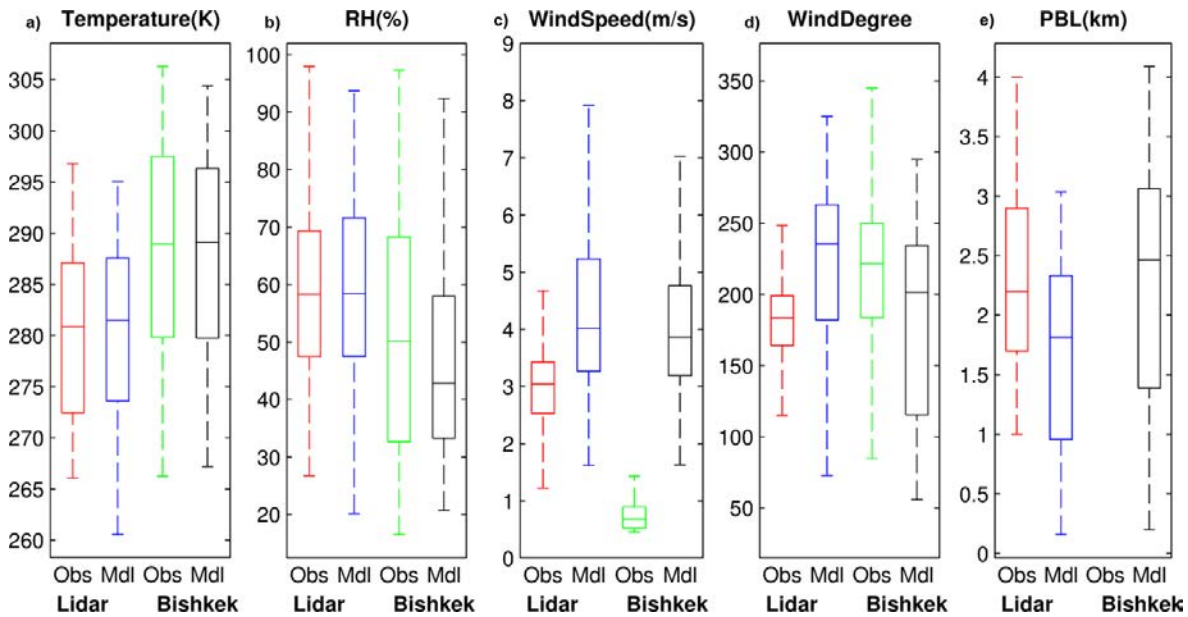


Figure 2-12: Comparison of predicted meteorological variables from WRF model with observations shown as box and whisker plots over the simulation period (a) Temperature (K), (b) Relative Humidity RH (%), (c) Wind Speed (m/s), (d) Wind Direction ($^{\circ}$), and (e) PBL height (m).

The observed and modeled distributions of AOD and PM are compared in Figure 2-13. The AOD observations based on the LE on average are $\sim 50\%$ larger than those from the SP. Modeled AOD on average are $\sim 20\text{-}30\%$ higher when compared to SP at the Bishkek and LST sites and $\sim 1\%$ lower when compared to the LE values. The variability in the predictions is slightly under-estimated. $\text{PM}_{2.5}$ is over predicted ($\sim 50\%$)

and the spread is accurately captured, while PM_{10} is over predicted by ~70%. This leads to an underestimation of the $PM_{2.5}/PM_{10}$ (0.4 predicted versus 0.5 observed) and also helps account for the overestimation in modeled AOD (by ~20-30%).

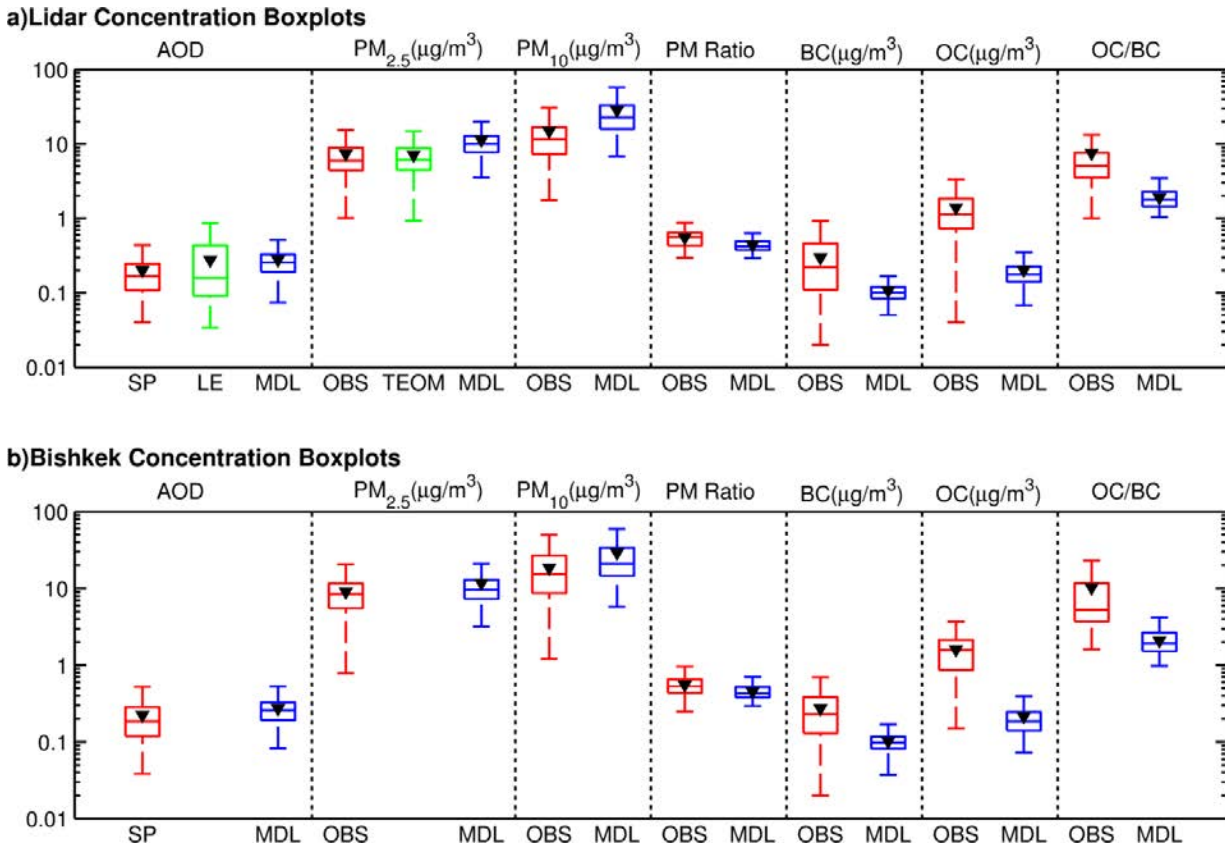


Figure 2-13: Comparison of predicted aerosols with observations shown as box and whisker plots over the simulation period at a) LST and b) Bishkek sites. SP and LE denote the AOD from the sun-photometer (SP) and integrated from the vertical extinction profiles (LE). OBS and TEOM denote filter and TEOM measurements while the MDL denotes the modeled values respectively.

Chemical analysis of the filter and soil samples in the CA dust regions have been used to estimate the dust contribution to measured PM at the two sites and to help identify source regions of importance (Park et al., 2014). The emission regions within

CA, including around the Aral Sea, and western China were identified as the most important dust sources, which is consistent with the regions identified in the simulations. Dust was estimated to comprise between 5-40% of $PM_{2.5}$ mass at the LST site and to vary by season (minimum values in winter). The observation-based estimates of dust percentage contribution suggest that modeled dust is over predicted by ~2 times. Thus it appears that dust is a main reason for the over prediction of $PM_{2.5}$ and PM_{10} , and that dust emission models need to be refined for CA applications.

The overestimation in PM mass at the surface could also be impacted by errors in the modeled PBL heights. The PBL height as determined by the Lidar aerosol profiles varies seasonally and is highest in the summer (from 2-4 km AGL) and lowest in the winter (Nov-Feb, 0.5-1.5 km AGL). The predicted PBL heights show a similar seasonal cycle with a tendency to under-predict the heights in all seasons as indicated by the comparison of the distributions of the observed and predicted values, and this occurs in all seasons. (Figure 2-14) The lower PBL height in the model contributes a systematic high bias in surface concentrations driven by near surface emissions.

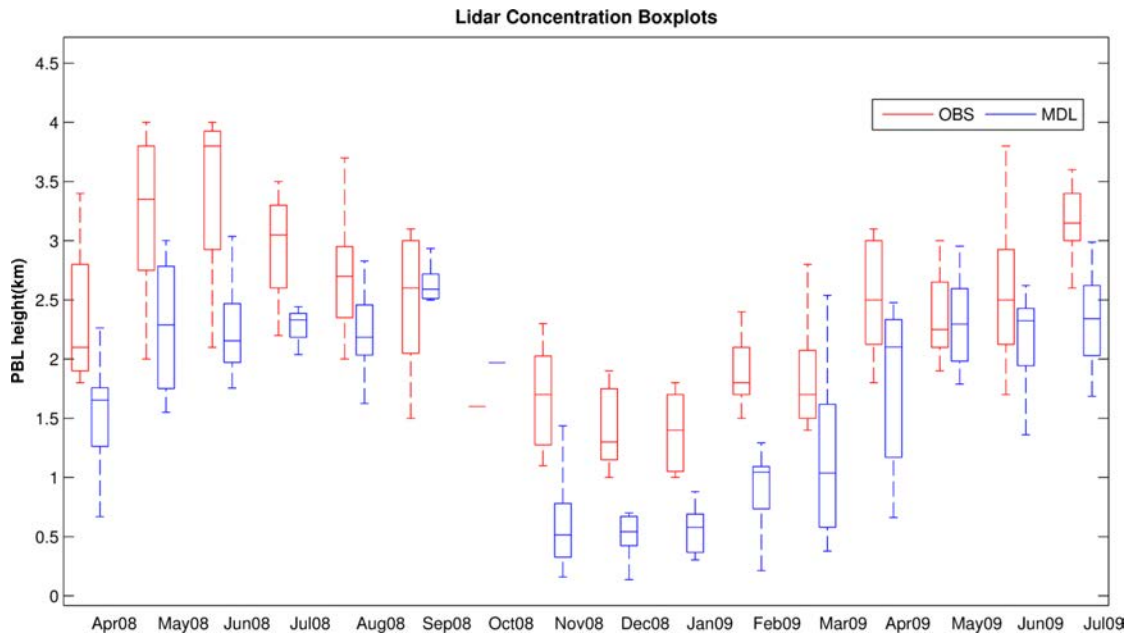


Figure 2-14: Comparison of observed and predicted PBL heights (m) at the LST site. Observed PBL heights were determined from the Lidar profiles.

Source Contributions to $PM_{2.5}$

Model simulations were performed to identify the component, source region and emission sector contributions to $PM_{2.5}$ mass. Period means for the spatial average over the entire CA region and for the grid cells for the Bishkek and LST observation locations are presented in Figure 2-17, and their comparison provides insights into the spatial variability of PM and its sources within CA, and how representative the observation sites are at characterizing CA PM. The component contribution to AOD at the sites and for the CA average are similar, with the major contributions coming from fine dust, sulfate, and OC. Spatial maps of mean percent contributions of the various components (i.e., BC, OC, sulfate, OPM, dust, and sea salt) to AOD and $PM_{2.5}$ mass are presented in Figure 2-16 and Figure 2-16, respectively.

Coarse particles contribute ~10% to mean AOD. Dust accounts for >60% of the calculated $PM_{2.5}$ mass at the observation sites and for the CA region. The dust source regions contributing to $PM_{2.5}$ vary within CA. Dust from the CA source regions has the largest influence on the region mean dust- $PM_{2.5}$ mass. At the LST site, which is located in the far east of CA, western China dust sources have their largest influence (~40%). African and Middle East source regions have their largest influence on the Bishkek site (20 and 15%, respectively), and collectively contribute ~25% to regional CA dust $PM_{2.5}$.

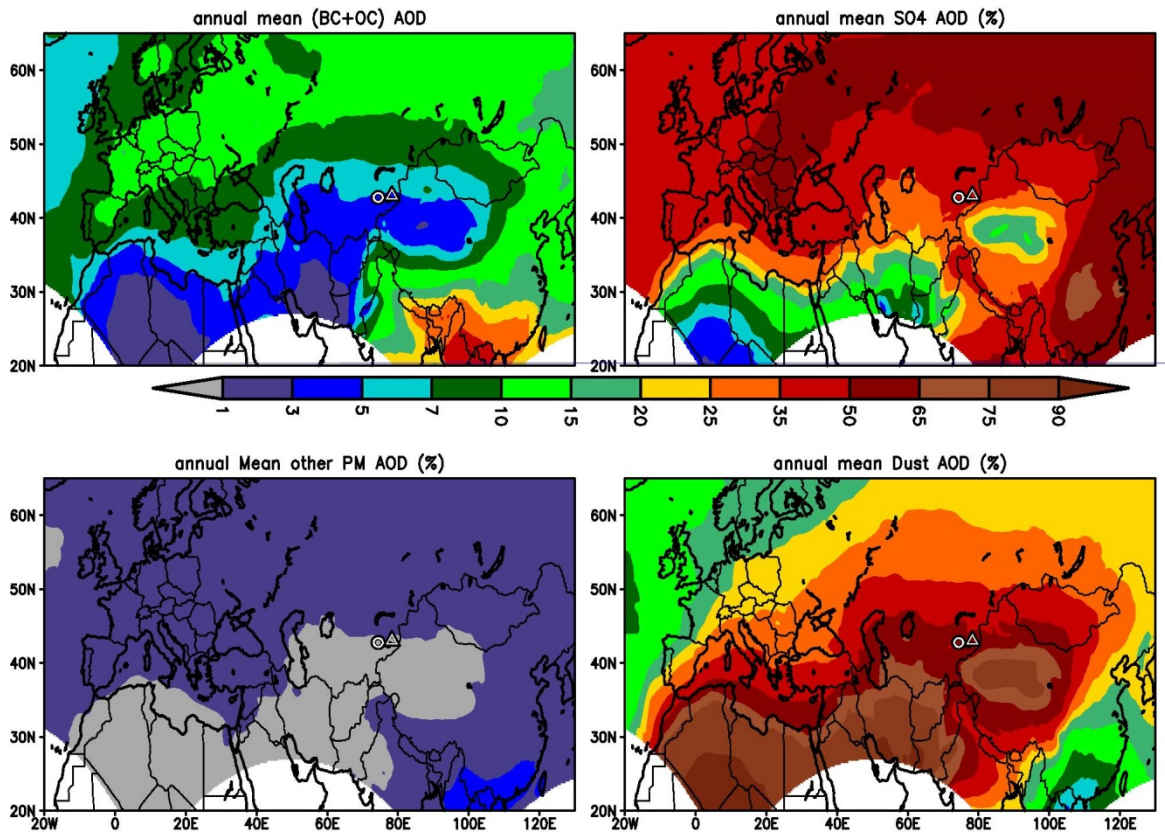


Figure 2-15: Spatial Distribution of predicted species contributions (%) to AOD averaged over the simulation period a) Carbonaceous aerosols (BC+OC), b) SO_4 , c) Other $PM_{2.5}$, and d) Dust.

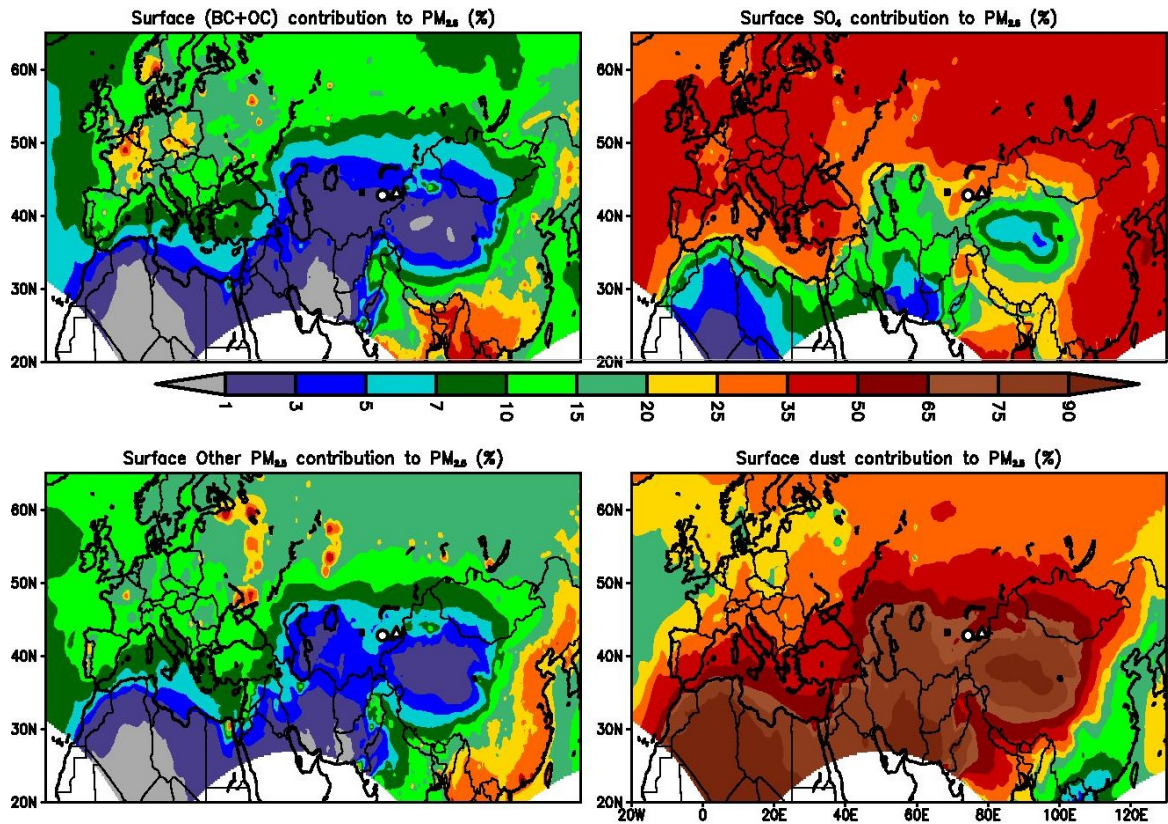


Figure 2-16: Spatial distribution of predicted species contributions (%) to $PM_{2.5}$ averaged over the simulation period a) Carbonaceous aerosols (BC+OC), b) SO_4 , c) Other $PM_{2.5}$, and d) Dust.

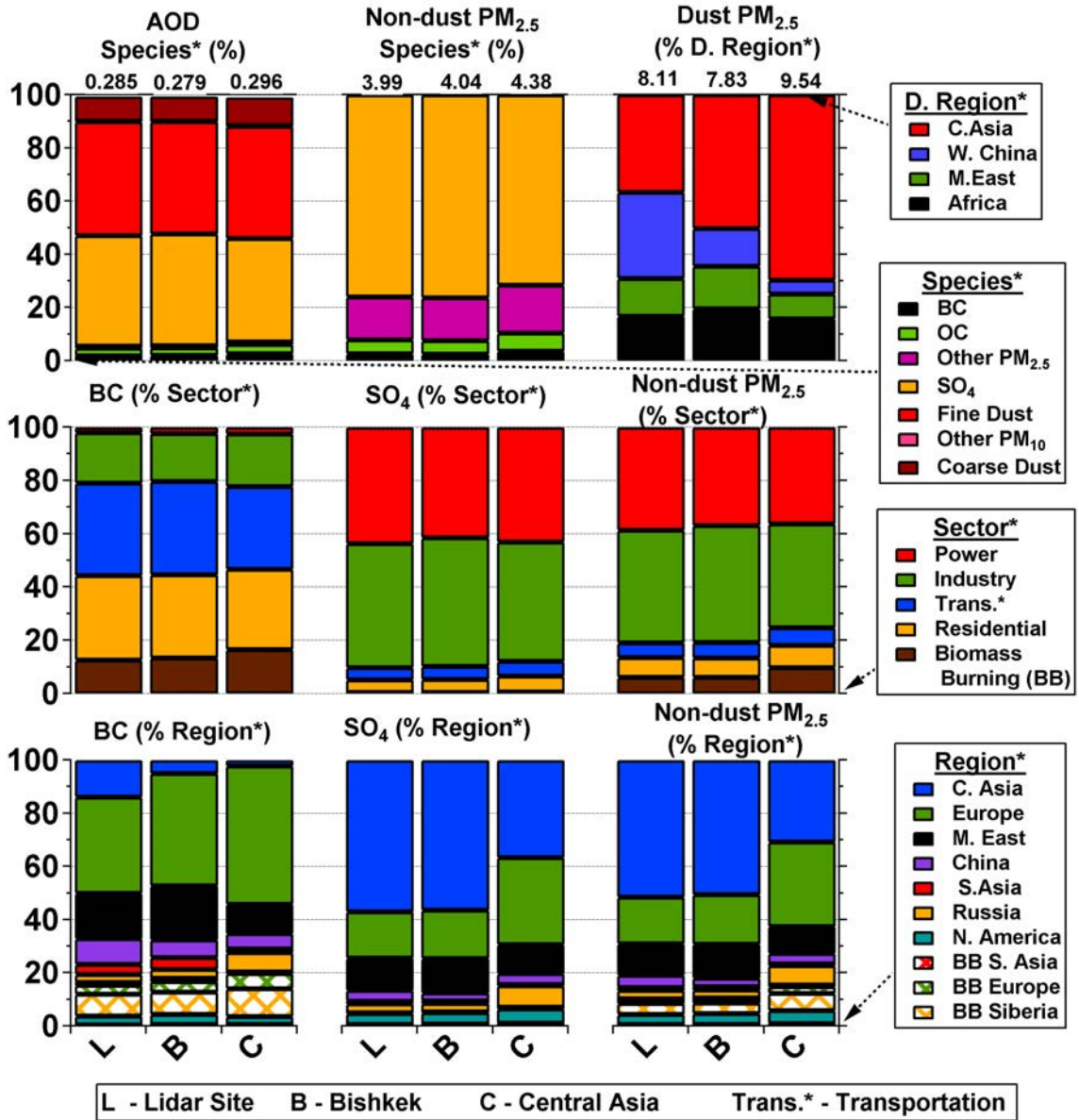


Figure 2-17: Summary of period mean contributions by source regions and sectors for AOD, PM_{2.5}, dust, non-dust PM_{2.5}, sulfate and BC in % for the grid cells containing the Bishkek and LST observation sites, and spatially averaged over the Central Asia region.

The source region contributions to the non-dust PM_{2.5} are very similar for the Bishkek and LST sites, with CA sources making the largest contribution (~50%)

followed by Europe (~20%), the Middle East (~15%), and biomass burning (~15% from all sources). For the entire CA region, the European source contribution is as large as the CA sources (~30% each), with larger contributions from biomass burning and Russia sources and smaller contributions from Middle East emissions than at the observation sites. The significant contribution from Europe sources reflects their large anthropogenic emissions and the general westerly transport patterns. On average the impact from South Asia sources are small. North America sources contribute between 3 to 7% to $PM_{2.5}$ in CA. Of the biomass burning contribution to $PM_{2.5}$, the Siberian and European fires contribute 63 and 25%, respectively, with contributions from South/Southeast Asia and North America fires each contributing ~5%. The power and industrial sectors are identified by the simulations as the largest contributors (~40% each) to non-dust $PM_{2.5}$ mass in CA.

Seasonal Variations in AOD and PM at the Observation Sites

AOD has a seasonal cycle with the lowest values in winter and highest values in spring and summer as shown in Figure 2-18 by the AOD observations at the LST site from both the SP and the LE profiles. A similar seasonal cycle was observed at the Bishkek site (not shown) and in the MODIS AOD retrievals. The modeled AOD captures this seasonal variation, with a tendency to over predict the values during the periods with the lowest observed AOD.

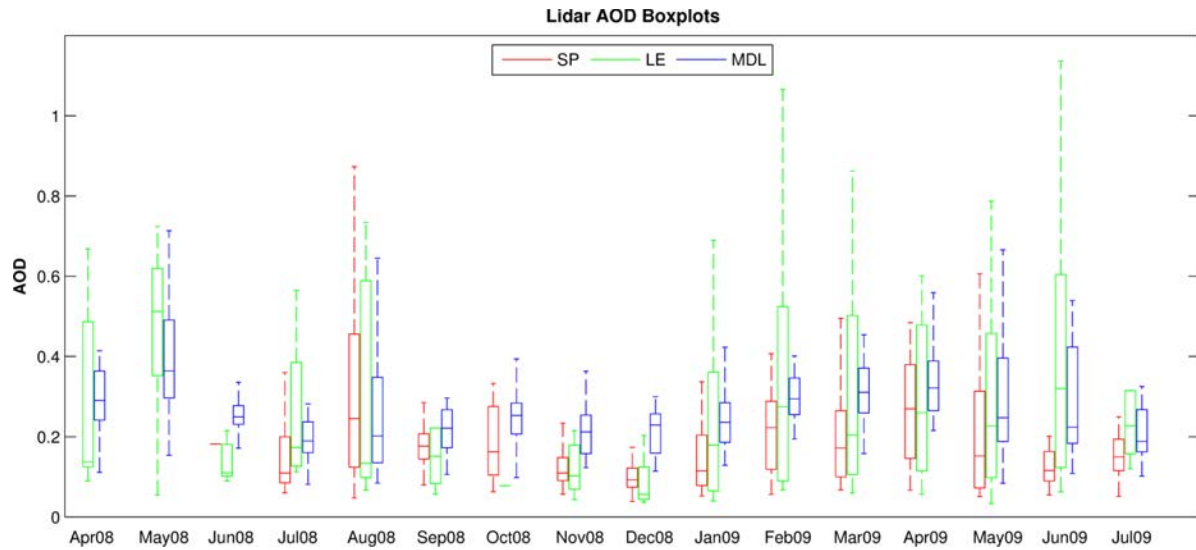


Figure 2-18: Temporal variability in simulated AOD compared with observations at the LST site. The box-plots of monthly values are shown. AOD from the sun-photometer (SP) and integrated from the vertical extinction profiles (LE) are shown.

The seasonal cycles in $PM_{2.5}$ and PM_{10} are similar to those for AOD, with minimum values in October – February. At the LST site $PM_{2.5}$ from both the filter based and the non-volatile TEOM measurements are plotted. Both the observations and the model find a strong similarity in the time series at the two sites.

There is also a clear seasonality in the surface meteorology in the region as shown by the time series in surface temperature and relative humidity at the two sites (Figure 2-20). There are distinct temperature minima in the winter and relative humidity minima in the summer. However, there is not a clear seasonality in wind speed and direction, and the winds are generally from the south and less than 4m/s throughout the year at the LST site.

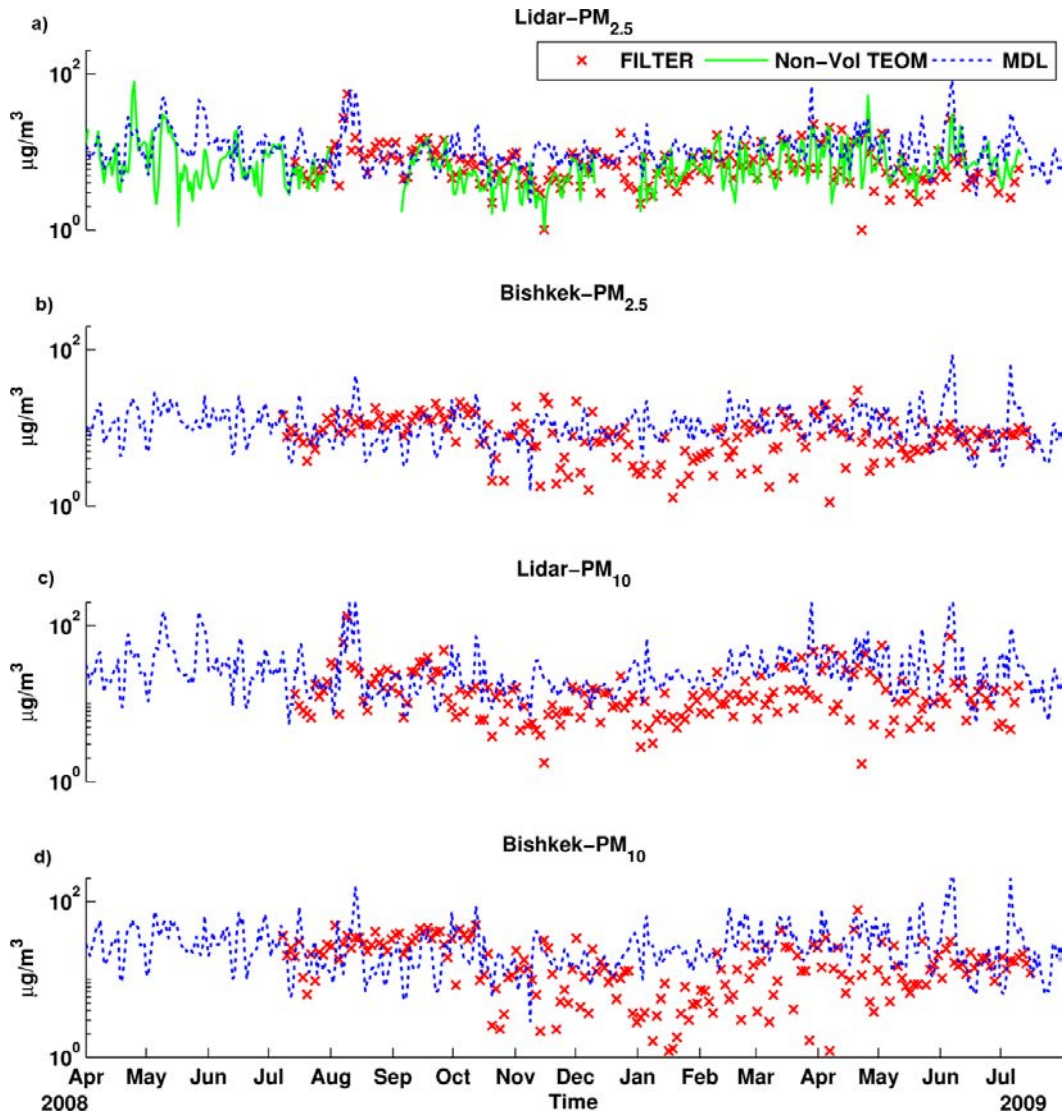


Figure 2-19: Comparison of simulated PM mass with filter-based observations at Central Asia sites (a) $PM_{2.5}$ (LST) along with TEOM non-volatile measurements, (b) $PM_{2.5}$ (Bishkek), (c) PM_{10} (LST), and (d) PM_{10} (Bishkek) in ($\mu\text{g}/\text{m}^3$).

The source region and component contributions exhibit seasonal variability as shown by the modeled contributions to $PM_{2.5}$ mass in Figure 2-21. Dust is found to be the main driver of the seasonal cycle of $PM_{2.5}$. The dust contribution to $PM_{2.5}$ is peak in spring and minimum in winter (<20%). During this time period the transport of air

masses to the sites are from the west and the southwest. When the transport is from the east then dust sources from western China can impact the stations. This transport pattern occurs episodically throughout the year, with contributions from western China sources as large as 20 to 50%. The dust seasonal cycle is in turn influenced by the seasonal variations in meteorology that drives the dust emissions and transport. The seasonal changes in the dust source regions can be seen in the seasonal spatial maps of AOD. Throughout the domain, AOD in the dust regions are highest in March–October and lowest in winter as the nearby desert regions are snow covered.

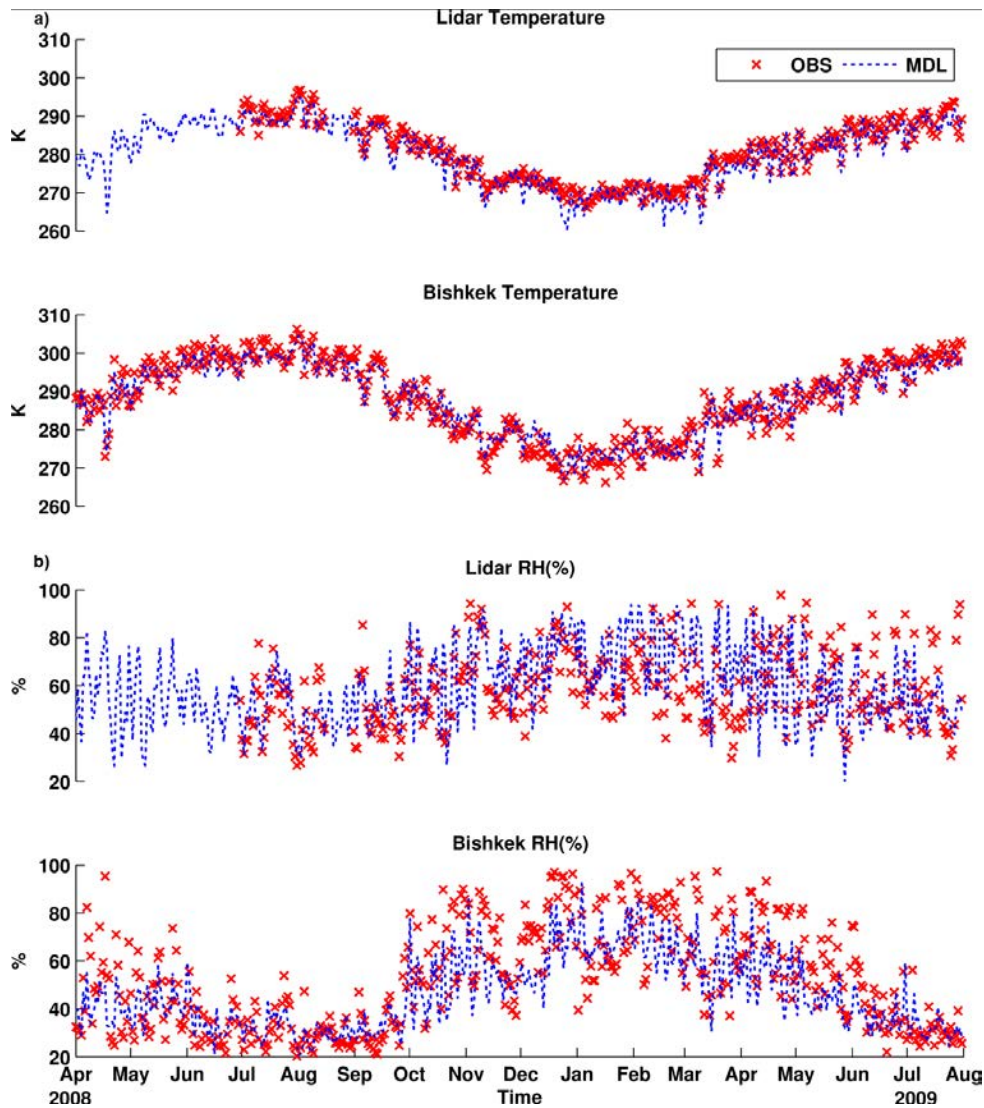


Figure 2-20: Temporal variability in simulated (a) Temperature (K) and (b) Relative Humidity RH (%) from WRF model compared with observations at the LST and Bishkek sites.

Biomass burning also adds to the seasonal cycle, and its contribution is minimum in the winter. South Asia sources can impact the sites in the winter time. The periods when North America sources impact the site are associated with strong transport events across the Atlantic and subsequent subsidence towards the surface associated with high pressure systems as they move towards CA.

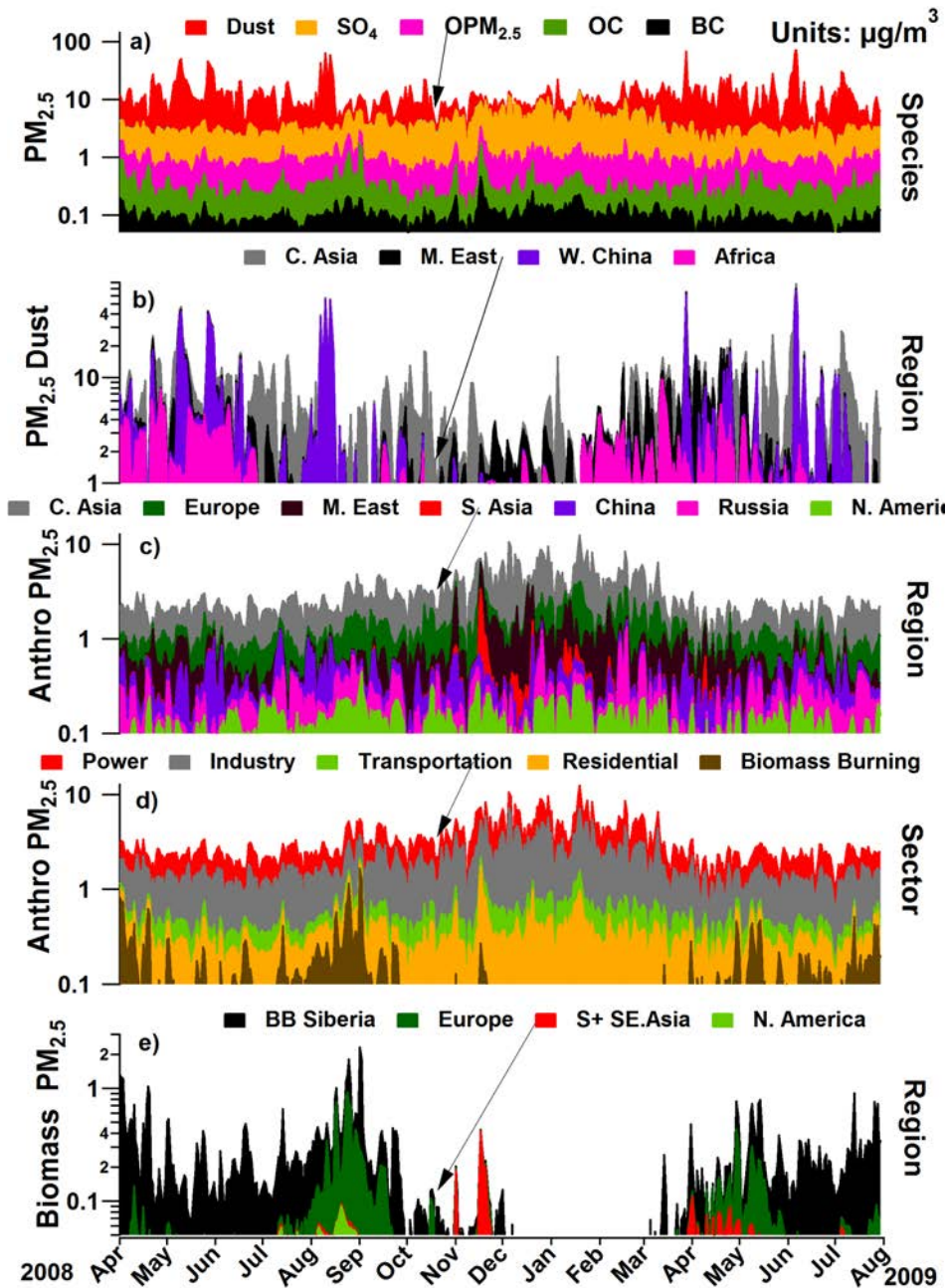


Figure 2-21: Simulated composition of PM_{2.5} at the LST site by a) Species (µg/m³), b) Fine dust source regions(µg/m³) c) Anthropogenic PM_{2.5} source regions (µg/m³) d) Anthropogenic PM_{2.5} source (µg/m³) e) Biomass PM_{2.5} source regions(µg/m³).The contributions from source region and sectors denote the non – dust portion of PM_{2.5} mass.

Source Contributions to BC

Because of its dual role as an air pollutant and as a climate warming agent there is special interest in understanding the regional and sector contributions to BC (Ramanathan and Carmichael, 2008). BC comprises on average only about 1-2% of PM_{2.5} mass in CA. The period mean predicted BC surface concentrations are ~0.1 µg/m³ at the two observation sites and 0.15 µg/m³ for the CA regional average. As shown in Figure 2-17, European emissions contribute ~50% to the mean BC concentrations in CA, while Middle-eastern and biomass burning sources each contribute ~15-20%. Residential and transport are the most important sectors each contributing ~30% to BC in CA, followed by industry (~20%), and with power the least important. This is in contrast to the sector contributions to non-dust PM_{2.5} mass, where power and industry are the most important sectors. On average biomass burning contributes ~10% to BC mass, with Siberian and European fires accounting for 61% and 33%, respectively. The source contributions to OC are shown in Figure 2-22.

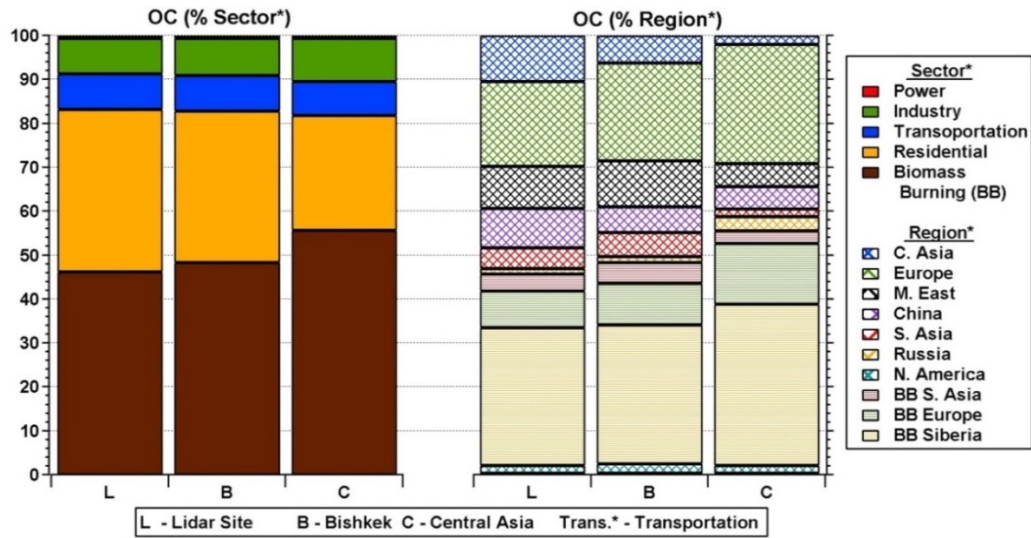


Figure 2-22: Summary of period mean contributions by source regions and sectors for OC in % for the grid cells containing the Bishkek and LST observation sites, and spatially averaged over the Central Asia region.

There is also large seasonal variability in BC concentrations and source sector/region contributions (Figure 2-23). BC surface concentrations show the highest values in fall/winter (as do the observations), when there is maximum contribution from the residential sector, reflecting the wide-spread use of biofuels and coal for heating in the region. The source region contributions vary by season, with maximum contributions from Europe and China. South Asia sources contribute in the winter. Biomass burning also is an important source of BC and plays an important role in influencing daily and seasonal variability in BC concentrations.

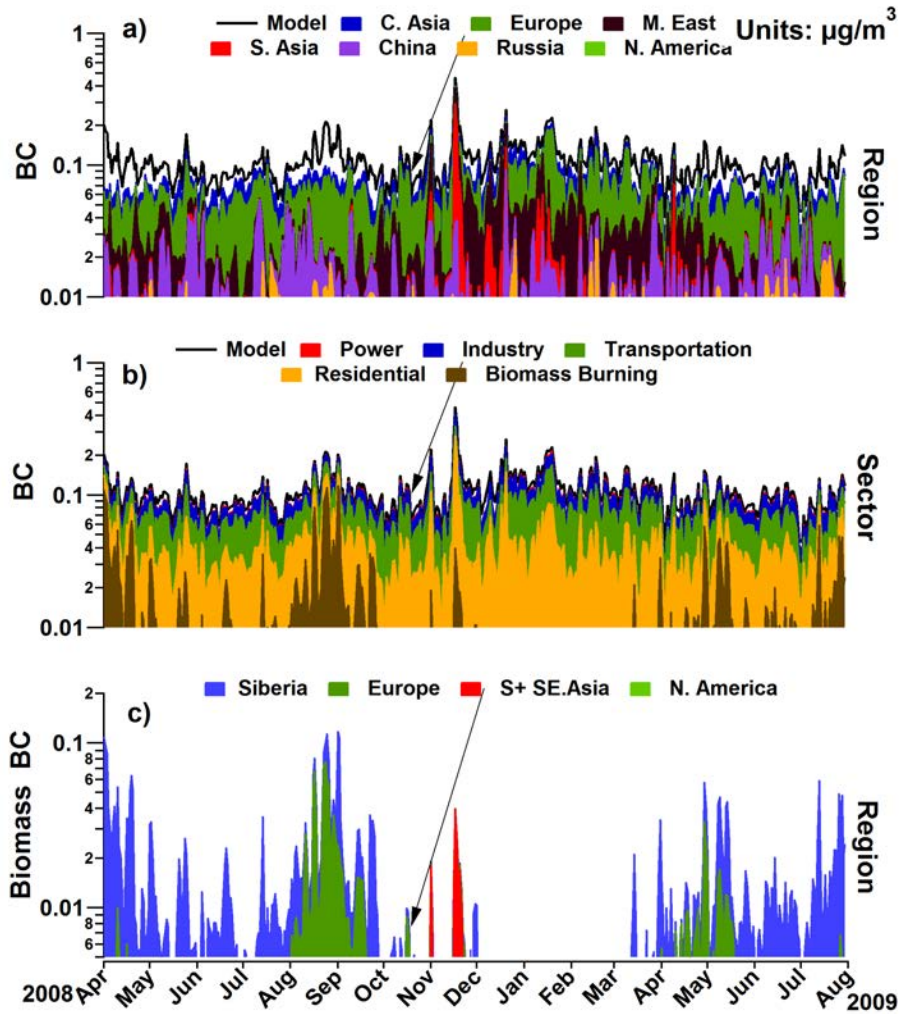


Figure 2-23: Simulated composition of BC at the LST site by a) Source regions ($\mu\text{g}/\text{m}^3$), b) Source sector ($\mu\text{g}/\text{m}^3$), and c) Biomass burning source regions ($\mu\text{g}/\text{m}^3$).

Predicted BC captures the seasonality and the magnitude of the spring and summer values as observed, but concentrations are biased low in the fall/winter. Median BC concentrations (and variability) are underestimated by a factor of 2 at both observation sites (Figure 2-13). The high wind speed bias in winter (\sim factor of 2), should result in too rapid dispersion and could contribute to the negative bias, but the negative

bias in the PBL heights should lead to higher predicted concentrations. Thus this negative bias is likely related to emissions (an indication of an underestimation of the heating fuel use).

The OC concentrations follow a similar seasonal cycle as BC and are also under predicted (Figure 2-13). Furthermore, the OC/BC ratio is under predicted by a factor of ~3. The observed OC/BC ratio follows a seasonal cycle with values >15 in summer and ~5 in September through April. Part of this under prediction in OC and the OC/BC ratio is due to the fact that SOA is not estimated in the model. However a source contribution of OC using the filter data and chemical mass balance (CMB) approach found that SOA sources were very low in winter and only ~ 20% in summer (Miller-Schulze et al., 2011). Thus SOA cannot account for the model under prediction of winter values. There appears to be an underestimation of regional OC primary emissions. SOA can however help account for the large values of OC/BC observed in the summer and not predicted.

Biomass burning emissions cannot account for the underestimation in winter BC and OC. The largest impact of fires at the observation sites is in the late summer, when the fires are concentrated in western Russia and the wind direction is such that the smoke is transported into CA. Fires from South Asia can impact the sites associated with the fires and high pollution levels in northern India and with winds from the south, which can occur in late fall, but not frequently.

The fact that BC and OC are systematically under predicted in the winter suggests that local/regional emissions during the heating season may be underestimated. This is

supported by the results of the CMB analysis of OC discussed above that found the contribution from biofuel combustion increased 2-3 times in the fall and winter periods. The uncertainty in emissions can also be partly caused by the lack of seasonal emissions over this region as described earlier.

Vertical Distributions

Figure 3-1 shows the predicted weekly averaged vertical distributions of PM_{2.5}, dust, and BC for the entire simulation period at the LST site. These plots show more clearly that much of the variability in the PM loadings is associated with dust and biomass burning episodes (as represented by the enhancements in BC). Typically the high PM episodes show elevated PM mass that extend from the surface to 2 to 4 km. The vertical extents show a seasonality associated with seasonal variations in the PBL heights. These vertical distributions indicate that much of the transport of aerosols in CA occurs via low altitude pathways. In some cases, there are large amounts of dust and biomass burning aerosol in the 3-6 km altitude range that are decoupled from the surface (e.g., dust in early May 2009), reflecting that some aerosols are lifted out of the boundary layer and are transported at high altitude over CA, enhancing AOD but not contributing to ground-level mass concentrations at the observation sites. These vertical features are confirmed by the aerosol extinction profiles observed at the LST site as discussed in (Chen et al., 2013). The variation in weekly averaged AOD can be significant (Figure 3-1 bottom panel) and is driven by variations in dust and biomass burning emissions.

Future Scenarios

How might PM levels change in the northern hemisphere over the next few decades? To address this question, simulations were repeated for various emission scenarios developed and used in the WMO/UNEP assessment on short-lived climate pollutants (Shindell et al., 2012). Dust and biomass burning emissions and meteorology were the same as those used in the 2008/2009 simulations. The period mean changes in surface BC and PM_{2.5} concentrations in 2030 for the reference scenario are shown in Figure 2-24 a and d, respectively. This scenario reflects all present agreed policies affecting emissions and assumes that they are fully implemented. Under this scenario PM_{2.5} increases significantly in South Asia and western China (>50%) and in parts of CA, including the area where the sampling sites are located. PM_{2.5} decreases in Western Europe and Eastern China (< 10%). BC surface concentrations show a similar pattern to PM_{2.5}, although covering larger portions of CA with relatively larger increases in BC than in PM_{2.5}. These results suggest that health impacts and climate warming due to BC and PM_{2.5} may increase in coming decades unless additional emission control measures are implemented.

Results for two other scenarios are also presented in Figure 2-24. One scenario specifically targets BC emission reductions in recognition that BC is also a major contributor to atmospheric warming (Ramanathan and Carmichael, 2008). These additional measures significantly reduce 2030 BC concentrations by greater than 35% throughout most of the domain, with only a few regions (e.g., Myanmar and eastern Afghanistan) showing increases in BC relative to 2005 levels. This scenario assumes that

all BC emission reduction measures are perfectly implemented and 100% effective. BC measures also impact emissions of co-emitted pollutants (e.g., OC and SO₂). PM_{2.5} concentrations under this scenario (Figure 2-24e) are reduced, but by much smaller amounts, and concentrations still increase relative to 2005 over large regions of South Asia and western China, and parts of CA. These results suggest that health impacts in these regions may increase due to the PM_{2.5} increases whereas positive radiative forcing and health effects due to BC may decrease. When the BC measures are used along with greenhouse gas measures aimed at keeping CO₂ levels below 450 ppm, the PM_{2.5} levels in South Asia are lower than 2005 levels (Figure 2-24f), with few exceptions (one being Myanmar region). This is due to the large decreases in SO₂ and NO_x emissions under this scenario, resulting in significant reductions in particulate nitrate and sulfate (e.g., a ~30% increase in particulate sulfate in CA).

Table 2-1: Summary of changes in Central Asia region emissions and concentration under the future emission scenarios

Emission Scenario	Emissions Gg yr ⁻¹			Emissions change (%) w.r.t to base 2005		
	BC	SO ₂	PM ₂₅	BC	SO ₂	PM ₂₅
Base 2005	39	1130	197			
Reference 2030	47	1326	224	22.1	17.3	13.9
Low GWP 2030	27	1325	177	-31.1	17.3	-10.1
Lowest GWP + 450	21	1058	115	-46.9	-6.4	-41.5

Emission Scenario	Concentration (µg m ⁻³)			Concentration change (%) w.r.t to base 2005		
	BC	SO ₄	PM ₂₅	BC	SO ₄	PM ₂₅
Base 2005	0.17	3.04	4.26			
Reference 2030	0.16	2.65	4.03	-4.2	-12.6	-5.3
Low GWP 2030	0.11	2.64	3.85	-36.6	-13	-9.5
Lowest GWP + 450	0.10	2.04	3.06	-38.5	-32.9	-28

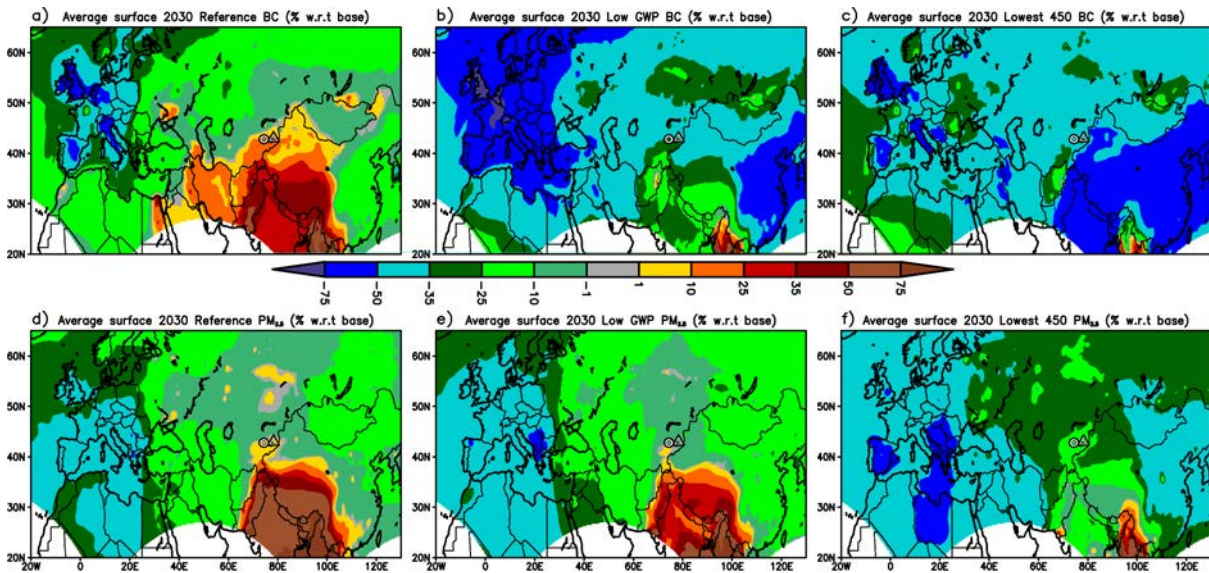


Figure 2-24: Percent change in simulated period mean surface BC and PM_{2.5} concentrations for future 2030 emission scenarios relative to the base year (2005) a),d) reference 2030, b),e) BC measures (low) and c),f) BC (lowest) and greenhouse gas measures aimed at keeping CO₂ levels below 450 ppm.

To get a regional perspective of how the future emission changes would specifically impact the CA region, we have summarized the changes in emissions and the corresponding concentrations in Table 2-1. The reference 2030 emissions scenario reports an increase in emissions of BC, SO₂ and PM_{2.5} over Central Asia by ~22, 17 and 14% respectively w.r.t to base 2005 levels. However, the corresponding BC, SO₄ and anthropogenic portion of PM_{2.5} decrease by ~ 5, 12 and 5% respectively. This suggest that on average the concentration levels go down even though CA emissions increase due to long range transport of pollutants into CA region from the surrounding regions, but locations within CA still increase when dominated by local sources. The Low GWP emission scenario predicts decrease in BC and PM_{2.5} emissions by 31% and 10%

respectively with the corresponding decrease in concentrations by ~ 37% and 10% respectively, while SO₂ emissions remained same as the reference 2030 scenario. The lowest +450 ppm scenario shows a consistent decreasing trend in emissions and concentration of all the species. This analysis suggests that the impact of the changes in major source region emissions and their subsequent transport to Central Asia will play a major role in determining the future aerosol levels in CA.

Summary

AOD in CA during the period April 2008 through July 2009 averaged ~0.3 and displayed a seasonal cycle with the lowest values in the winter and highest values in spring to mid-summer with observed values of AOD > 0.6 and even > 0.8. Surface PM_{2.5} measured at two sites in eastern CA averaged ~10 µg/m³ but with large variability (hourly values from 2 - 90 µg/m³). Surface concentrations of PM also showed a seasonal cycle with peak values and largest variability in the spring/summer, and lowest values and variability in the winter. BC at these sites averaged ~0.1 µg/m³ with peak values (~ 1 µg/m³) in the winter.

The seasonal cycles and source sector and source region contributions to PM in CA were analyzed using the STEM chemical transport model. Dust was the largest component of the PM_{2.5} and PM₁₀ mass in the region in all seasons except winter, whereas sulfate was the largest anthropogenic component of the PM_{2.5} mass. Dust was also found to be the major driver of the seasonal cycles of AOD and PM concentrations. On an annual basis, the power and industrial sectors were the most important contributors to PM_{2.5}, while residential and transportation were the most important sectors for BC.

Open biomass burning within and outside the region also contributed to elevated PM and BC concentrations and to the temporal variability.

The model simulations showed a systematic over prediction of PM mass. This is most likely due in large part to the over prediction in dust. Carbonaceous PM was underpredicted and it is speculated that the winter emissions associated with residential heating may be underestimated in the current emissions inventory. The predicted wind speeds were biased high (by ~30%) and the direction had a southwest bias. The high bias in wind speeds may also contribute to the over-prediction in PM₁₀, as dust emissions depend strongly on wind speed. Efforts to improve the dust emissions and to improve the wind speed and direction predictions using a finer model resolution are planned. Additional efforts are needed to improve the anthropogenic emissions estimates for CA.

Observations of PM and its composition in this region are of growing importance as it is estimated that PM_{2.5} levels are likely to increase significantly in Central and South Asia and western China over the next few decades. Simulations for a reference 2030 emission scenario showed that BC concentrations had a larger relative increase than PM_{2.5} concentrations. This suggests that health impacts and climate warming associated with these pollutants may increase over the next decades unless additional control measures are implemented. Continued pollutant observations in CA will help to characterize the changes that are rapidly taking place in the region.

CHAPTER 3: THE INTERCONTINENTAL TRANSPORT PATHWAYS OF PARTICLES THROUGH CENTRAL ASIA

Introduction

Semi-arid Central Asia (CA) countries face many severe environmental problems; however, very little is known about the air pollution levels in this region. CA and the surrounding regions have witnessed a significant increase in air pollution emission due to the fast economic growth and industrialization in the past few decades. Shindell et al., 2012 reports Central Asian region is developing quickly and air pollution emissions are projected to increase significantly for the next several decades.

Aerosols have negative impacts on both health and environment, but the magnitude of the impacts are still uncertain. (Koch et al., 2007) Previous modeling studies showed that the air pollutants concentration at a particular location is impacted by local emissions and inter-continental transport of aerosols. Furthermore, the recent assessment of the intercontinental transport of pollution (HTAP, 2010) has indicated that the major transport pathway of pollution from Europe to Asia is via low altitude flows passing through CA. The magnitude of the pollution transport from Europe to Asia is highly uncertain in large part due to the lack of observations of pollutants along this pathway.

In this chapter, the transport of aerosols into CA is explored through three-dimensional backward trajectory analyses. Transport from CA and their impacts on downwind areas are also analyzed via forward trajectory analysis. The analysis of the transport pathways and the variations in particulate matter mass and composition in CA

demonstrate that this region is strategically located to characterize regional and intercontinental transport of pollutants. Aerosols at these sites are shown to reflect dust, biomass burning and anthropogenic sources from Europe, South, East and CA, and Russia depending on the time period. (Kulkarni et al., 2015)

Method

Air Mass Trajectories Calculations

The CA observation sites as discussed in Chapter 2 are impacted by dust, anthropogenic pollution, and biomass burning emissions from various source regions. To further understand the transport pathways and source region influences on the PM distributions at these sites, three-dimensional ten-day air mass trajectories (both forward and backward in time) from each site were calculated for the entire time period (April 2008 – July 2009). In this trajectory analysis, we utilized the three dimensional wind fields (including u, v and w components) along with the above ground level (AGL) altitude simulated by the WRF meteorological model consistent with D’Allura et al., 2011 study. These trajectories describe the general flow patterns based on wind fields alone and provide useful information about the history of air mass transport, particularly the influence of source regions over which the air mass has resided before arriving at the site of interest. Note that these trajectories do not account for any other atmospheric processes such as diffusion or chemical evolution along its path (Guttikunda, 2005; Kurata et al., 2004).

To understand the differences in transport patterns at the surface and aloft, and to study the impact of topographic gradients in the vicinity of the sites, trajectories were

initialized at different altitudes (0.1 (100m), 0.3 (300m) 0.5 (500m), 1, 2, 3, and 5 km) a.g.l at the site locations (i.e. latitude and longitude) every 3 hours for a ten-day period both backward and forward in time for the identified periods. The trajectories were terminated when they touched the ground, or went out of the model domain or exceeded the ten-day calculation period. The trajectories (at or below 1 km) were used to characterize transport pathways impacting the surface concentrations at these sites, which are discussed later in this chapter.

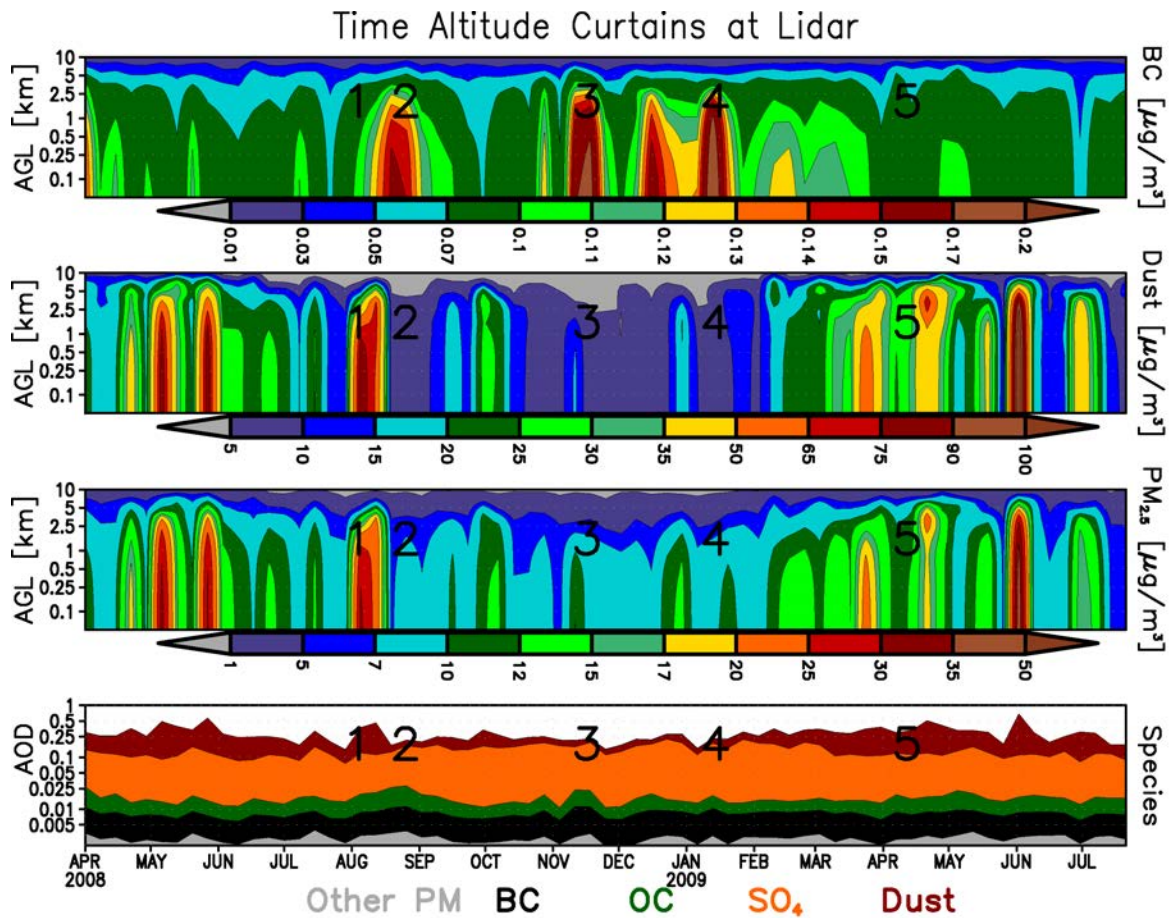


Figure 3-1: Time altitude cross sections of weekly averaged predicted BC, dust and PM_{2.5} for the simulation period at the LST site.

The three-dimensional ten-day air mass trajectories were utilized to further understand the transport pathways of air masses entering into and exiting out of the CA region and its subsequent impact of source regions on the aerosol distributions at the CA sites.

Results and Conclusion

Transport into CA

The air mass transport into CA is discussed through back trajectories associated with the five events labeled on Figure 3-1. These five events represent transport episodes with elevated surface PM_{2.5} (averaged over the 3h time window consistent with trajectory time step) with varying contributions from biomass burning, anthropogenic pollution, and dust sources. In each trajectory figure (Figure 3-2 and Figure 3-3), the regions with active dust (blue diamond hatches) and biomass burning emissions (green square hatches) for the event time period and prior ten days are identified and MODIS AOD (values printed in black) overlaid. The trajectories are color coded by region to distinguish the source impacts. The regions include: Africa (blue), Middle East (green), CA (yellow), North Asia biomass (>50° N, black), Europe (brown), China (red) and South Asia (orange).

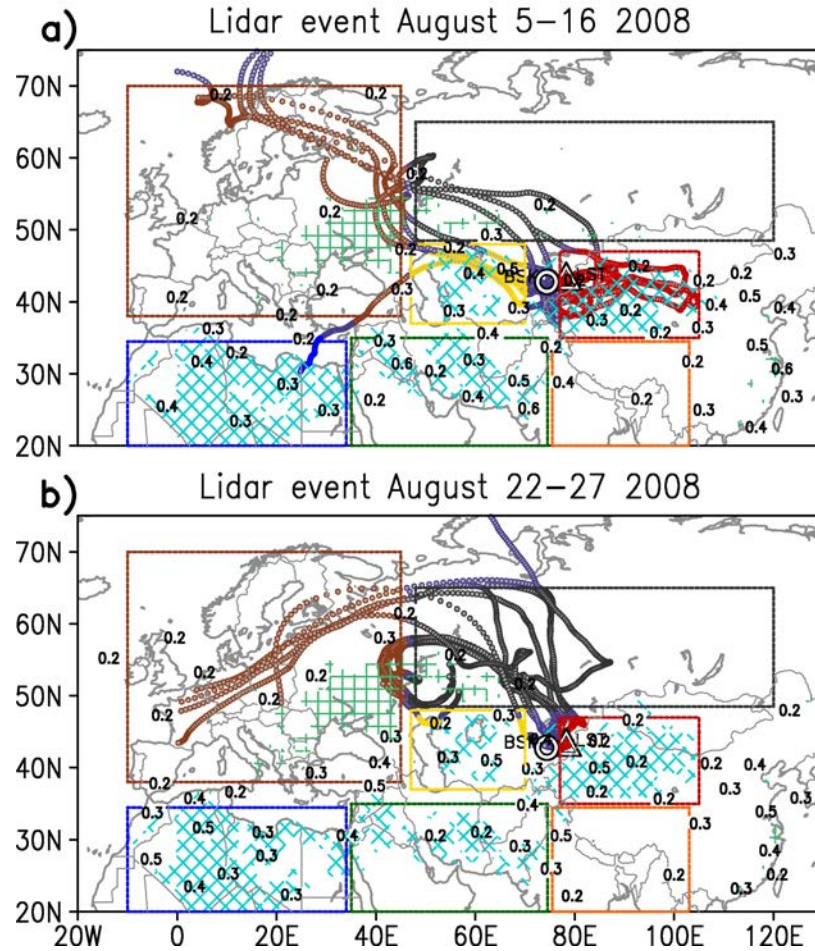


Figure 3-2: Ten-day air mass back trajectories for August 2008 (events 1 and 2 as denoted in Figure 3-1) color coded by source regions. The blue diamond and green square hatched areas denote the natural dust and biomass burning emission sources while the number in black denote MODIS AOD contours averaged over the event time period and ten-day prior time window. The trajectories are color coded by source regions including Africa (blue), Middle East (green), Central Asia (yellow), North Asia biomass (> 50° N, black), Europe (brown), China (red) and South Asia (orange).

Figure 3-2 shows the first two events for August 2008. The first event in early August (Figure 2-23, event labeled 1) is a high dust event associated with trajectories from the west passing over the dust regions of the Aral Sea (~45° N, 55° E) and eastern

trajectories passing over the Taklimakan region of western China (90-100° E, 40° N). These were both regions with active dust emissions as indicated by the elevated MODIS AOD values. Thus the PM increases during this event were due largely to dust emitted from CA and western China deserts. The second event in the latter half of August is characterized by high levels of BC without dust. During this episode, the transport to the site was under the influence of a high pressure system located to the northwest and air masses were transported over the active fire region in western Russia.

Figure 3-3 shows winter and spring events. The November episode (event 3) is a period with elevated BC and PM_{2.5} from pollution sources from South Asia (including some fires) and western China and low fire and dust emission activity. The January episode (event 4) is a period of elevated BC with air masses coming from Europe, indicating the influence of anthropogenic pollution coming from this industrialized region, and from CA sources. Dust emissions from CA and Africa were low during this period. The final illustrative episode is for April 2009 (event 5), a period with both elevated levels of dust from western China, CA and Africa and BC from both fire and anthropogenic pollution from Europe, CA and Russia sources.

These examples provide insights into the source region contributions to PM mass in CA. CA is an ideal location to observe a variety of source regions as it is at the crossroad of transport patterns with air masses impacted from dust, anthropogenic activity and biomass burning from different geographical regions.

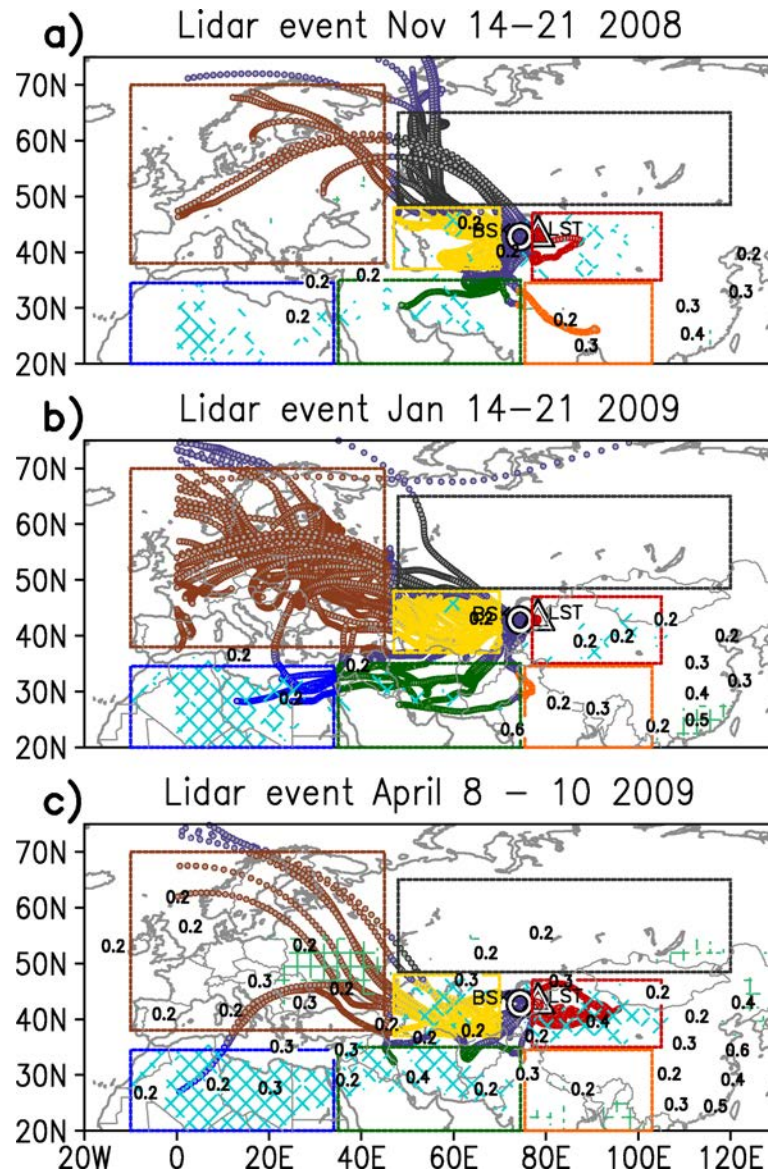


Figure 3-3: Same as Figure 3-2 but for November 2008, January 2009 and April 2009 (events 3, 4, 5 denoted in Figure 3-1).

Long-range Transport Outside of CA Sources

The transport pathways out of CA were also evaluated by calculating forward trajectories from the observation sites. Selected forward trajectories initialized at or below 1 km are used to represent the transport of boundary layer PM from CA and these

are shown for summer, winter and spring periods in Figure 3-4. In these plots the MODIS AOD, dust, and fire emissions plotted for each event represent values averaged over the subsequent ten days and trajectories were stopped if they impacted the surface. During the summer, outflow from CA is towards the north in association with the summer monsoon system. Figure 3-4-a shows the subset of forward trajectories that reside for at least 3 days over the region 48 - 65° N during June 2008. Trajectories typically pass over Russia and reach into the Arctic and also can be caught in westerly storm tracks and reach the higher latitudes of the northern hemisphere. During the winter, air mass transport out of CA is associated with the winter monsoon system and the transport pathway is over Mongolia and then over eastern China as seen in Figure 3-4-b. In this figure, forward trajectories that pass over the region west of 130° E during late December 2008 are shown. Figure 3-4-c illustrates transpacific transport of CA air masses. Plotted are the forward trajectories that stay within the 30 – 50° N region for at least 3 days during the month of April 2009. During the spring transport from CA is dominated by strong westerly flows and air masses are transported over China, Korea, and Japan and then across the Pacific, reaching North America in 7 – 10 days.

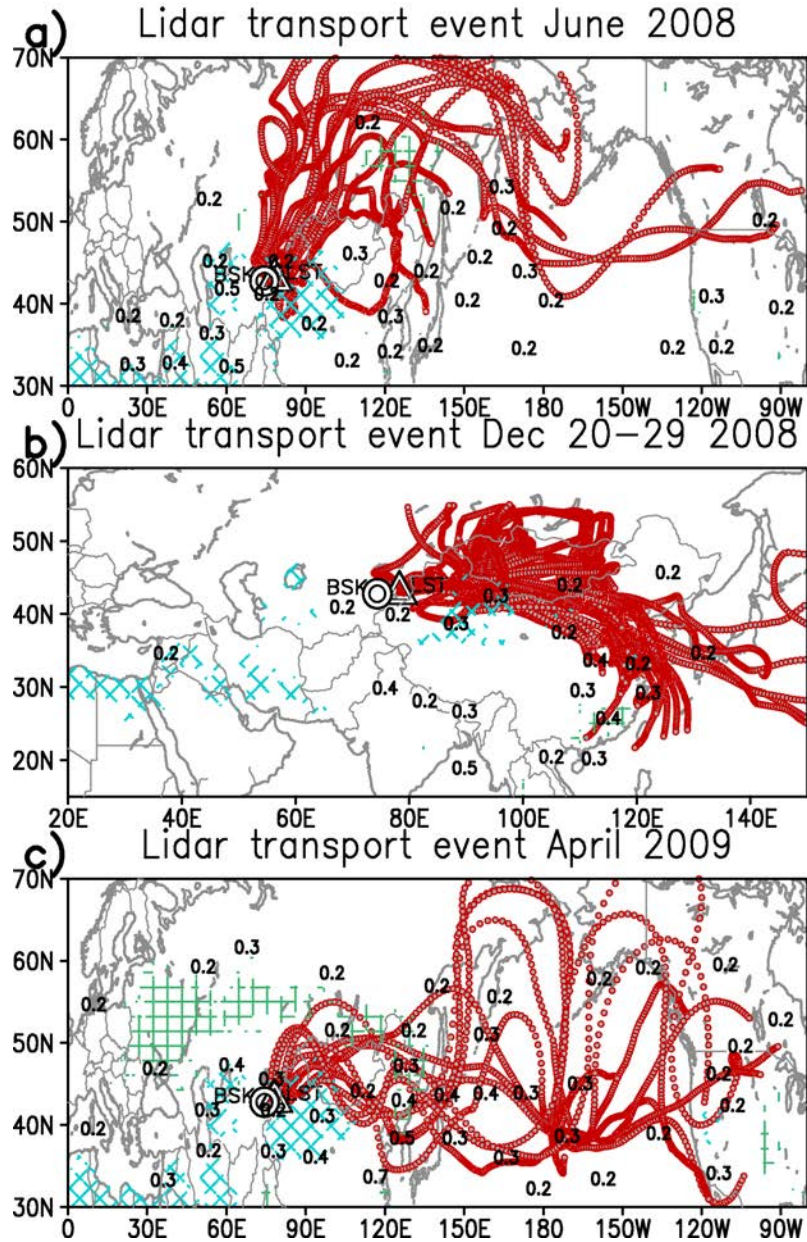


Figure 3-4: Ten-day air mass forward trajectories illustrating the seasonality in transport pathways out of CA for a) June 2008, b) December 2008, and c) April 2009. The blue diamond, green square hatched areas denote the natural dust and biomass burning emission.

PM arising from dust and anthropogenic emissions from CA impact the entire northern hemisphere as illustrated in the hemispheric maps of seasonal average surface

dust concentrations due to CA emissions only (Figure 3-5). The predominant westerly flows in all seasons in the northern hemisphere result in the bulk of the CA emissions being transported to the west. The contribution of CA sources to surface PM concentrations of $0.35 \mu\text{g}/\text{m}^3$ or greater covers large portions of the northern hemisphere, including the Arctic, all of Asia, much of Europe, and portions of the continental US.

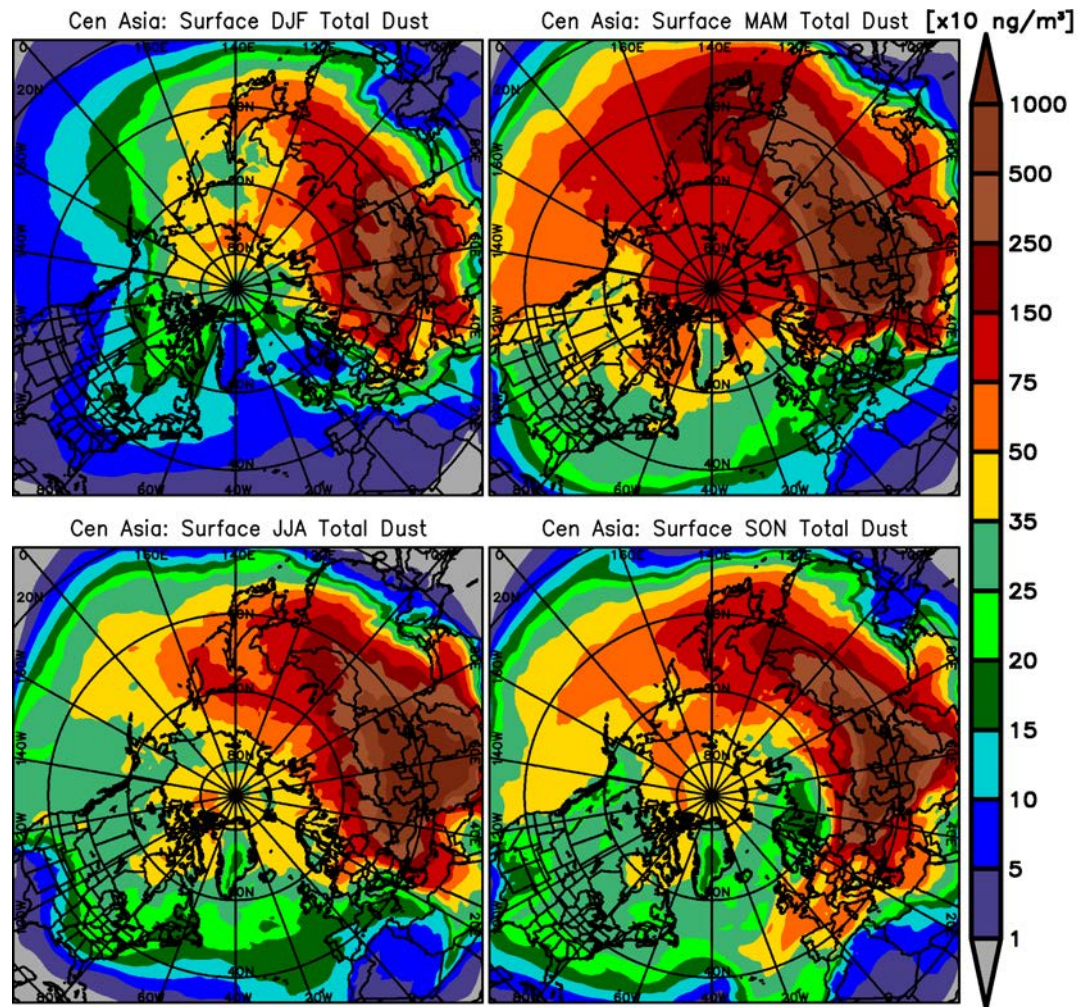


Figure 3-5: Seasonally averaged surface total dust (PM_{10}) concentrations from Central Asia dust emissions. DJF (top left panel) denotes the average for the months of December, January and February.

There are episodic and seasonal components to the intercontinental transport as shown in the time series of the vertical profiles of PM_{2.5} at Mt. Bachelor, Oregon (43.97° N, 121.69° W, 2700 m AGL) (Figure 3-6). The bulk of the CA particle transport takes place in the free troposphere and impacts surface concentrations in the US as the boundary layer grows and entrains “plumes” aloft. This occurs most frequently in spring, summer and fall. The episodic contributions of CA sources to surface concentrations can exceed 1.5µg/m³. In the fall, there is also strong transport of dust from CA across Europe and out into the Atlantic.

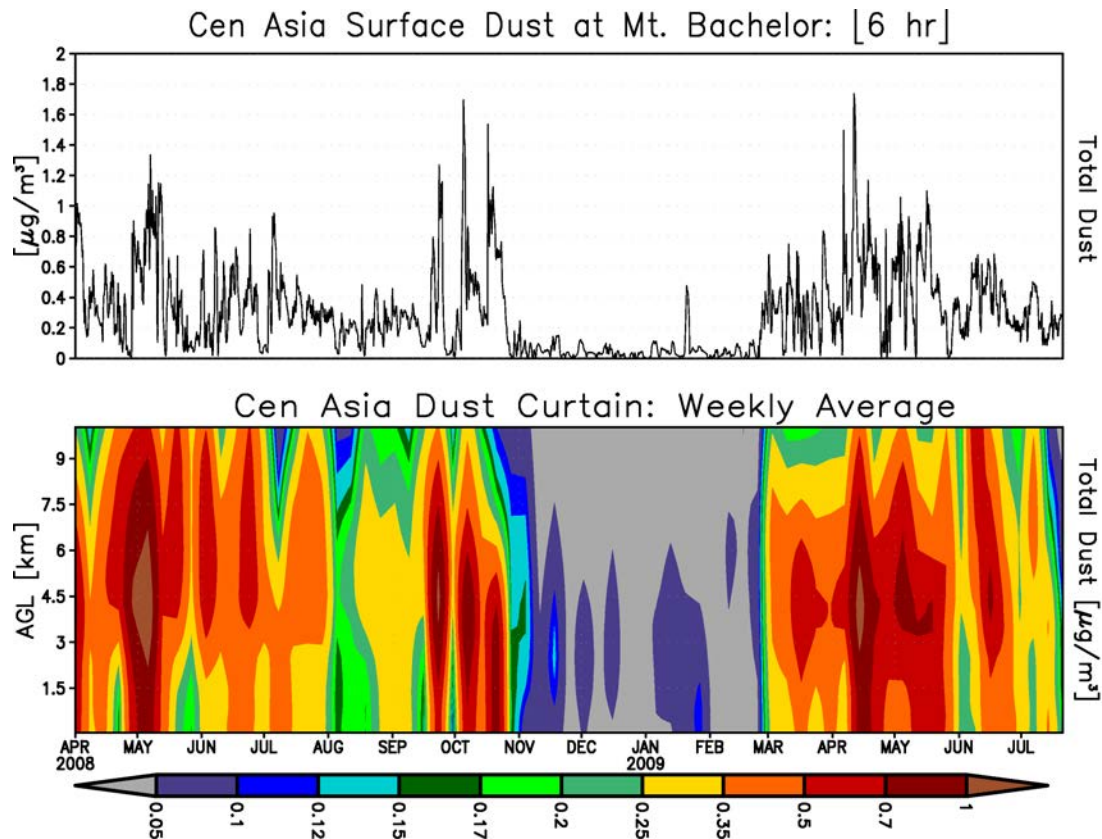


Figure 3-6: Time series of predicted surface concentration at 6 h time step (top panel) and weekly averaged time altitude cross sections (bottom panel) of total dust (PM_{10}) from Central Asia dust emissions at Mt. Bachelor, Oregon.

Summary

There is a rising awareness regarding long range transport of air pollutions and its effects on the global air quality. Currently, there are few measurements in CA that can be used to quantify the intercontinental transport of pollution from Europe to Asia. The analysis of the transport pathways and variations in PM mass and composition observed at the two sites in CA demonstrate that this region is strategically located to characterize regional and intercontinental transport of pollutants. Aerosols at these sites were shown to reflect dust, biomass burning, and anthropogenic sources from South, East, and CA,

Europe, and Russia depending on the time of year. For example, during the spring fine particles from Europe and Africa were transported to CA, on to eastern Asia, and then across the Pacific to North America.

CHAPTER 4: SOURCE SECTOR AND REGION CONTRIBUTIONS TO BLACK CARBON (BC) AND PM_{2.5} IN THE ARCTIC

Introduction

Arctic temperature has increased more than the mean global surface air temperature over the past century due to various positive feedbacks and amplification mechanisms such as black carbon (BC) deposition and albedo reduction. (Cohen et al., 2012; Screen and Simmonds, 2010; Solomon et al., 2007; Stocker, 2014) Long-range transport of atmospheric particulate matter (PM) from mid-latitudes to the Arctic is the main contributor to the Arctic aerosol load. (AMAP, 2011; Law and Stohl, 2007; Quinn et al., 2007) Several studies, as early as the late 1980s, reported a distinctive seasonal cycle in the Arctic aerosol concentration and visibility. (Barrie, 1986; Quinn et al., 2007; Wang et al., 2011) The so-called Arctic Haze phenomenon in the winter-spring period has been attributed to increased levels of transported PM from anthropogenic emission sources at lower latitudes and slower wet deposition removal processes. (Law and Stohl, 2007; Quinn et al., 2002, 2007)

Sulfate particles, one of the main components of Arctic PM, scatter solar radiation and modify cloud properties. (AMAP, 2011; Quinn et al., 2007) Another critical component of the Arctic haze is BC, which influences global climate and water cycles in various ways. (AMAP, 2011; Bond et al., 2013; Shindell et al., 2008) BC particles in the atmosphere absorb solar radiation and warm the surrounding air. When deposited to snow and ice, BC reduces the surface albedo and absorbs more solar radiation; hence, increases the temperature of snow and accelerates the snow melting process. (Clarke and Noone,

1985; Flanner et al., 2007; Hansen and Nazarenko, 2004; Koch et al., 2007; Wiscombe and Warren, 1980) Although BC is a minor contributor to aerosol loading (~10%), it has been identified as the second largest contributor to global warming after carbon dioxide (CO₂). (Ramanathan and Carmichael, 2008) Studies suggest that BC has caused 25% of the 20th century warming over the Arctic.(Bond and Sun, 2005; Koch and Hansen, 2005; Ramanathan and Carmichael, 2008) Although BC has a significant role in the global climate, there is a high uncertainty in assessing the magnitude of BC effect on radiative forcing in climate. (Bond et al., 2013) Considering the short atmospheric lifetime of BC and its significant impacts on the Arctic climate, mitigating BC emissions provides us with an opportunity to decrease the BC concentration in the atmosphere immediately and a reduction in near-term climate impacts of BC. For making effective global BC emission abatement policies, it is necessary to quantify the contribution of each geographical source region and source sector and identify the major transport pathways to the Arctic. (AMAP, 2011)

BC in the Arctic has both natural (e.g. biomass burning) and anthropogenic sources, but there are few emission sources in the Arctic itself. Hence, the main contributor to BC in the arctic atmosphere is long-range transport of particles from both mid-latitudes and high-latitude regions. (AMAP, 2011; Bond et al., 2013) Several studies have shown that transport of aerosols from mid-latitudes is the most significant transport mechanism to the Arctic pollution. (AMAP, 2011; Law and Stohl, 2007) Earlier studies have identified Europe as the major source region contributor to Arctic BC concentrations. (Barrie, 1986; Quinn et al., 2007, 2008) However, during the past two

decades emissions from East Asia have increased rapidly due to the vast economic growth and the emissions from the Europe have declined.(Streets et al., 2009) Recent studies show significant contribution of Asian emission to the Arctic, especially during winter-spring. (Koch and Hansen, 2005; Shindell et al., 2008; Stohl, 2006) However, there is significant uncertainty associated with these estimates.(Koch and Hansen, 2005; Sharma et al., 2013b; Wang et al., 2011) Several factors including the uncertainties in emissions, and the complicated transport pathways from mid-latitudes to the Arctic, contribute to the uncertainties in calculating the impacts of emission sources. (Bian et al., 2013; Fuelberg et al., 2010)

There is also a major seasonal cycle in transport pathways of BC to the Arctic, and the contribution of each emission sectors and regions to Arctic BC changes during the year. (AMAP, 2011) The minimum potential temperature in the Arctic boundary layer forms the Arctic dome causing very stable air near the surface.(Klonecki et al., 2003; Stohl, 2006) The strong atmospheric inversion reduces the vertical transport between the boundary layer and free troposphere and limits BC deposition to the ground. (AMAP, 2011) The Arctic front acts as a transport barrier for the Arctic lower troposphere reducing the low-level transport of pollutants to the Arctic dome. (Barrie, 1986) The Arctic front reaches as far south as 40° N in January, which includes all European and Siberian emissions. (Barrie, 1986; Heidam et al., 2004; Stohl, 2006) Hirdman et al., 2010 study shows that BC concentration at Alert and Barrow are highly sensitive to the emissions from higher latitudes, especially during the winter, but less sensitive to the South Asian emission.

During the summer, the Arctic front is located further north, causing less Eurasian emissions to transport to the Arctic. (Stohl, 2006) In general, the seasonality of BC in the Arctic is attributed to the seasonal variations of transport pathways, precipitation seasonality and emission changes in the mid-latitudes. (AMAP, 2011; Garrett et al., 2010; Stohl, 2006)

In this study, we designed a modeling framework (WRF-STEM) for analyzing BC, organic carbon (OC), SO₄, PM_{2.5}, and PM₁₀ concentrations over the Arctic. We utilize this system to study the seasonal variations in the contributions of emissions from different source sectors (e.g. transportation, power, industry, residential and biomass burning) and source regions (e.g. Europe, North America, China, Russia, Central Asia, South Asia and Middle East) on Arctic PM mass concentration. Backward trajectories are used for assessing transport pathways to the Arctic.

Method and Data

Modeling System

Meteorological Model

The Weather Research and Forecasting model (WRF) version 3.5 is used for producing necessary meteorological inputs for the STEM model. The ice sheet coverage, initial and boundary conditions for the model are provided by the National Center for Environmental Prediction (NCEP) Final Analysis (FNL, <http://rda.ucar.edu/datasets/ds083.2/>). The meteorological factors affecting chemical

distribution and concentration were imported into the STEM model every 6 hours as described in Kulkarni et al. 2015.

Emissions

The emission setup used for this modeling study is similar to Kulkarni et al. 2015. The base emission set up is used previously for ARCTAS campaign as described in D'Allura et al., 2011b and Huang et al., 2011. However, the emissions are updated with EUCARRI 2005 for BC and OC and EMEP 2008 emission data for SO₂, PM_{2.5} and PM₁₀ for the Europe region. For shipping emissions, data from IIASA 2005 is used. Also for Asia, the INTEX-B emission data is used but it is updated with BC, OC, and SO₂ emission data from Lu et al. 2011. (Kulkarni et al. 2015) For carbonaceous aerosols and PM emission from biomass burning sector, FINNv1 is used. Dust and sea salt emissions are estimated using Uno et al 2004 method for grids with snow cover <1%. The emissions are further described in Kulkarni et al. 2015. The emission also includes new source category of emission from open waste burning from Wiedinmyer et al., 2014.

Figure 4-1 shows the regional distribution of anthropogenic and wildfire BC emissions for the modeling domain. The major anthropogenic BC emission hotspots are over China and India. Also there are significant emissions from Eastern CONUS, Europe and Northern Middle East regions. The main hotspots of wild fire BC emissions are over South East Asia, Siberia, and Europe. There are also less intense wild fire emission sources from Southeastern and Western CONUS.

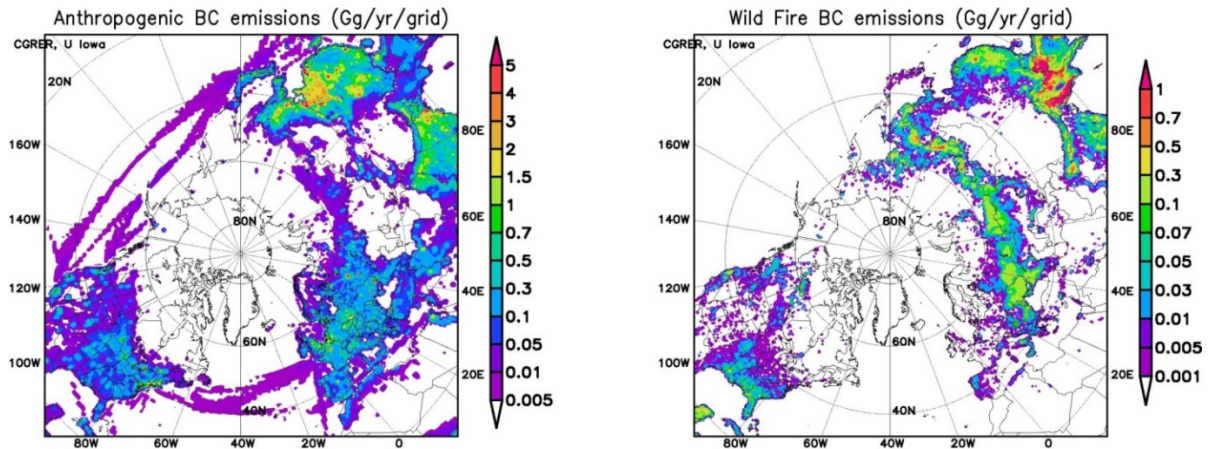


Figure 4-1: Spatial distribution of annual a) anthropogenic BC emission and b) wild fire BC emission in Gg/yr/grid.

Figure 4-2 shows the anthropogenic BC emission from the different economic sectors. Based on this figure, residential BC emission is the major source sector from China, India, Southeastern Asia, and Central Asia. However, the most significant source sector for BC emissions over North America is Transportation, with values between 45% to 95% of total anthropogenic BC emissions. The Industry sector contributes between 35% to 50% of total BC emission over Central Asia and Siberia.

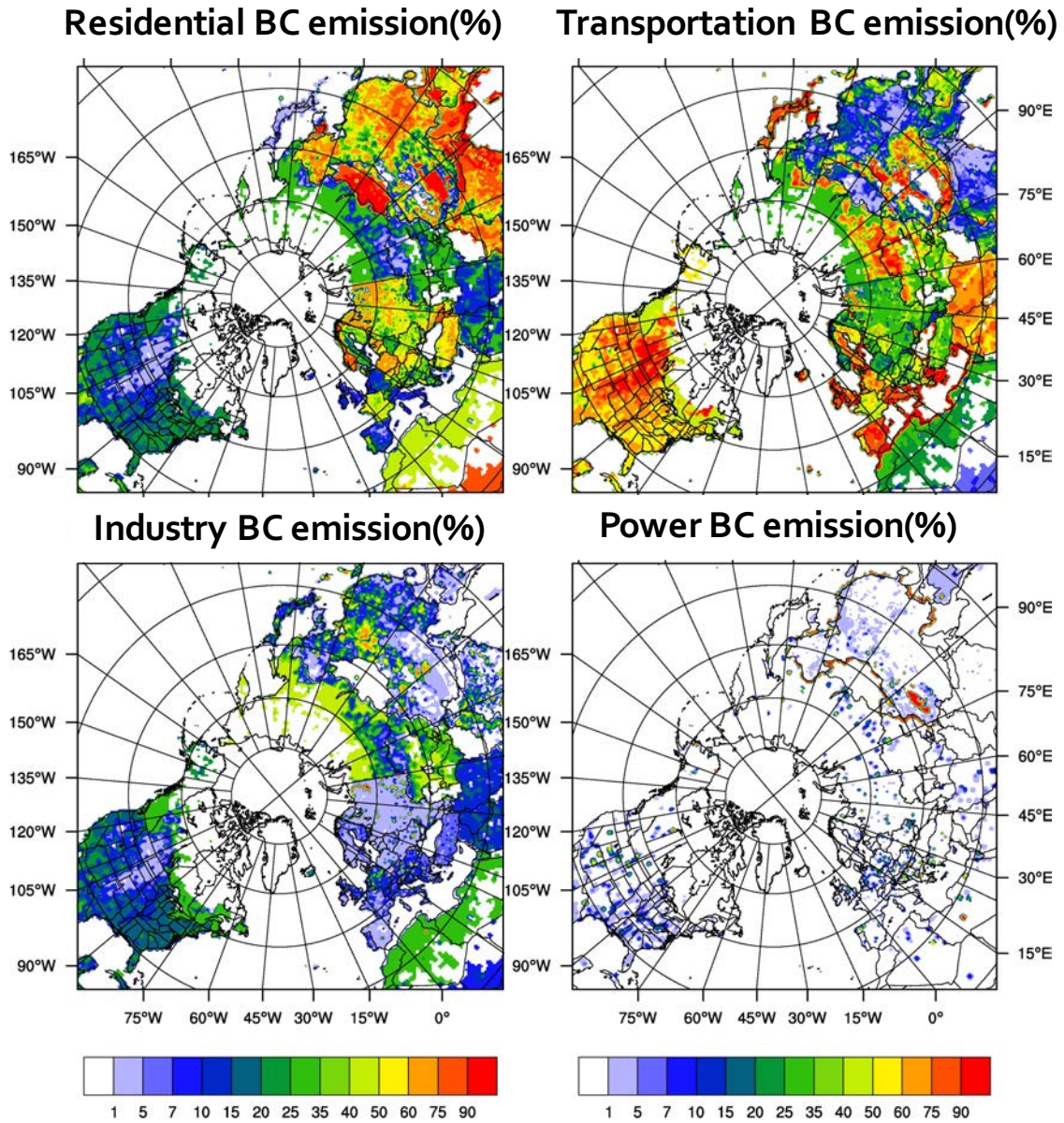


Figure 4-2: Spatial distribution of percentage of economic sector (%) in annual total BC anthropogenic emission.

Chemical Transport Model

The WRF-STEM modeling framework is similar to that used in Kulkarni et al. 2015. The STEM model is a regional scale CTM developed at the University of Iowa in

the 1980's and has continuously developed since then. The STEM model includes the emission, transport (convective and diffusive), and deposition of particles and chemicals with a Eulerian approach.

The modeling domain for both WRF and STEM models covered most of the Northern hemisphere including the significant emission sources such as Asia, Russia, Europe and North America. Also the model extends over the Northern Africa, Middle East and South Asia to include the dust emissions from the arid regions and anthropogenic emissions from the population-dense regions. The models used polar stereographic map projection with 60 km horizontal resolution (249x249 grid cells). This modeling system is described in further details in Kulkarni et al. 2015 and D'Allura et al. 2011.

Observations

For evaluating the modeling system performance, the model's outputs are compared with aircraft data from the National Aeronautics and Space Administration (NASA) ARCTAS field campaign. The ARCTAS field campaign measurements included observations from DC-8, P-3 and B-2000 research aircrafts and data analysis and forecasts by different global and regional modeling teams. The ARCTAS field campaign took place as a part of the international POLARCAT during the 2007-2008 International polar year, with the goal to better understand the factors causing changes in the Arctic atmospheric composition and radiative forcing. (Jacob et al., 2010) (www.polarcat.no) The spring phase (ARCTAS-A) which happened during April 2008, were concurrent with

unusually higher number of Siberian fires, which subsequently caused higher concentrations of carbonaceous aerosols. Figure 4-3 a and b show the flight pathways of all ARCTAS flights during spring (ARCTAS-A) and summer 2008 (ARCTAS-B) respectively.

For evaluating the model performance during different seasons, we compared our simulated concentrations with the surface observations at two sites located in the Arctic: Barrow Alaska (156.6° W, 71.3° N, 11 m a.s.l.) and Alert (Nunavut), Canada (62.3° W 82.5° N, 210 m. a.s.l.). The Barrow site is located northeast of the Barrow town at the northern edge of the Alaska. Observations at Barrow are retrieved from NOAA Global Monitoring Division (GMD), where a particle soot absorption photometer (PSAP) is used for measuring BC light absorbing coefficient at three wavelengths (476, 530, and 660 nm). (Data is available at <https://esrl.noaa.gov/gmd/aero/net/>) The Alert station in the Qikiqtaaluk region is located in the northernmost place in Canada and is more isolated from both local and continental source regions. Alert BC concentrations are calculated using light absorption coefficients data measured by Environment and Climate Change Canada using a PSAP (Radiance Research, Inc.) at three wavelengths (476, 530, and 660 nm). (Sharma et al., 2017) (Data available at <http://ebas.nilu.no/>). The light absorption coefficients are converted to Equivalent Black Carbon (EBC) using mass absorption cross-section (MAC). In this study for calculating EBC concentration, light absorption coefficient at 530nm was used with a MAC value of 9.5 m²/g as recommended by McNaughton et al., 2011; Wang et al., 2011.

For further validating the model's performance outside the Arctic's circle, BC surface concentration data was evaluated using annual average data from 168 IMPROVE (Interagency Monitoring of Protected Visual Environment) sites over North America.

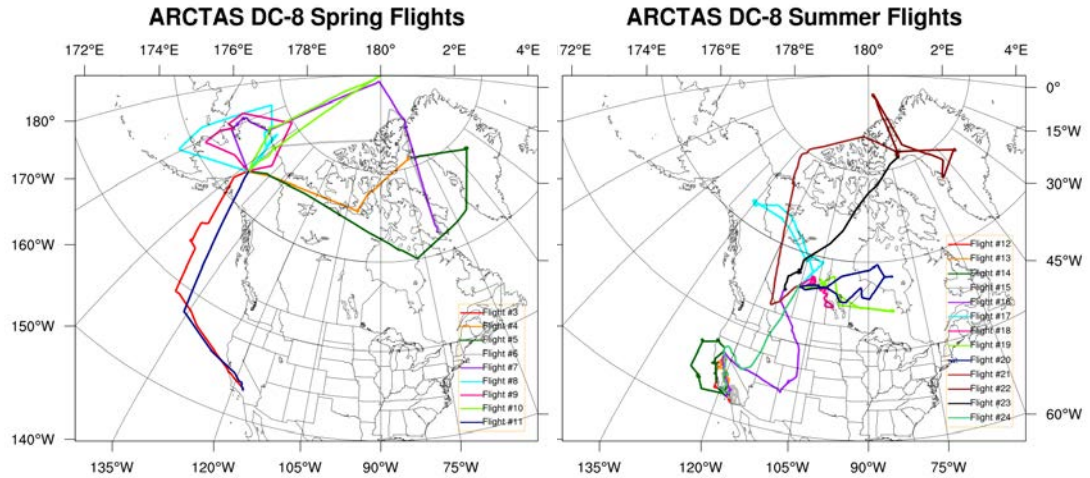


Figure 4-3: NASA ARCTAS DC-8 flight tracks during a) Spring 2008 and b) Summer 2008.

Sensitivity Analysis

For making effective emission mitigations policies, it is essential to assess the impacts of source sectors and source regions on global air quality and climate. For assessing the impacts of various emission sectors and regions to the concentrations of PM in Arctic, the base simulations and sensitivity analysis with perturbed emissions are used. The sector contributions were calculated using a series of models runs by eliminating the emissions of a particular sector each time. The base simulation included emissions from all sectors and used meteorology from the WRF model for the study period. The

contributions of each sector to the concentrations are calculated as the difference between the base case and a simulation including all emission but zeroing out the specific sector. Additional simulations were performed to calculate the source contribution from specific regions to PM concentration over the Arctic.

Results and Discussions

Model Evaluations

Meteorological Model Evaluation

The spring and summer 2008 ARCTAS flight tracks are illustrated in Figure 4-3 a and b respectively. All the flights were categorized based on the location of the flight path into 7 categories: 1- Spring Alaska Local Flights 2- Spring Greenland Flights 3- Spring Transit Flights 4- Summer California Flights 5- Summer Canada Local Flights 6- Summer Canada Greenland Flights and 7- Summer Transit flights. Table 4-1 shows the different flight categories and the date of the flights corresponding for each category. The model data were evaluated for each individual flight and each flight category.

Figure 4-4 boxplots compare the model vs. observation meteorological data for each of the flights. Each flight category is shaded with a different color and the spring and summer transitional flights are not shaded. The meteorological variables are compared against observational data along the DC-8 flight pathways and each are summarized into one box/whisker plot. Further statistics are also summarized in Table 4-2.

Table 4-1: NASA ARCTAS Flight Categories for Spring and Summer 2008

Flight Season	Flight Categories	Flight Date	Flight Number
Spring Flights	Spring Alaska Local Flights	04/12/2008	08
		04/16/2008	09
	Spring Greenland Flights	04/04/2008	04
		04/05/2008	05
		04/08/2008	06
		04/09/2008	07
		04/17/2008	10
	Spring Transit Flights	04/01/2008	03
		04/19/2008	11
	Summer Flights	Summer California Flights	06/18/2008
06/20/2008			13
06/22/2008			14
06/24/2008			15
Summer Canada Flights		06/29/2008	17
		07/01/2008	18
		07/04/2008	19
		07/05/2008	20
Summer Canada Greenland Flights		07/08/2008	21
		07/09/2008	22
		07/10/2008	23
Summer Transit Flights		06/26/2008	16
		07/13/2008	24

The results show that the WRF model captured the meteorological model accurately at different altitudes and locations for each flight. Temperature shows a slight positive bias for summer flights and a negative bias at higher altitudes during spring. In addition, the model under-predicts RH during the spring and summer California flight, while it over-predicted it during the summer Canada Greenland flights. The RH under-prediction happens at lower latitudes for spring flights and over-prediction occurs in higher altitudes for summer flights. This is caused by the complicated ice and cloud formation mechanisms at higher altitudes over the Arctic region during spring. The

model tends to slightly over-predict wind speed by (~4%) at higher altitudes during spring flights. The model under-predicted the wind speed for all summer California flights. The model does reasonably well in capturing the RH vertical distribution in the lower troposphere but displays a large negative bias at altitudes above ~ 4km. This behavior is due to the complex ice and cloud formation properties at high altitudes in the polar region during spring time.

Table 4-2 summarizes the statistical summary of the major meteorological variables for both ARCTAS observation data and model output. Based on this table and box and whisker plots analysis the model captures the vertical profile and magnitude of meteorological values with good skill.

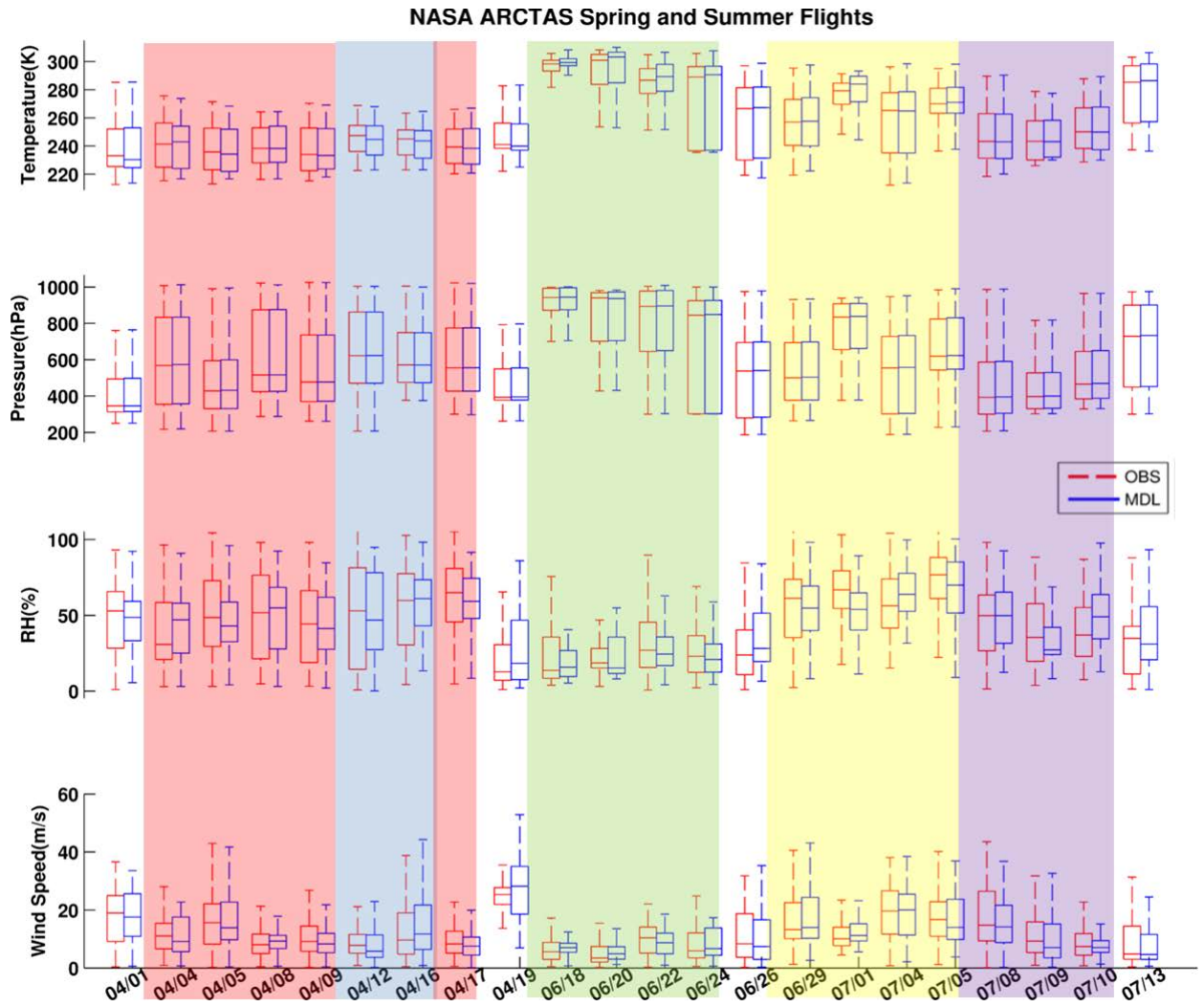


Figure 4-4: Comparison of key meteorological variables for NASA ARCTAS spring and summer flights.

Table 4-2- Statistical summary of comparison of observed and modeled meteorological parameters for NASA ARCTAS spring and summer flights. Obs and Mdl denote observation and model data

	Temperature (K)		Pressure (hpa)		Relative Humidity (%)		Wind Speed (m/s)	
	Obs	Mdl	Obs	Mdl	Obs	Mdl	Obs	Mdl
Mean	248.4	263.1	610.2	594.6	45.5	45.5	13.0	13.5
Standard Error	0.3	0.3	3.7	3.4	0.4	0.4	0.2	0.1
Median	245.4	265.7	554.9	569.0	43.4	43.4	9.7	11.5
Mode	225.0	231.4	1007.0	329.3	19.8	19.8	25.7	25.7
Standard Deviation	23.6	23.1	253.2	232.8	27.0	27.0	10.9	9.1
Range	94.8	93.6	818.9	817.2	117.1	117.1	56.2	43.4
Minimum	212.7	212.2	206.7	187.1	0.7	0.7	0.2	0.1
Maximum	307.4	305.8	1025.6	1004.2	117.8	117.8	56.4	43.5
R-Square	0.984		0.757		0.585		0.405	
Standard Error	32.463		314.263		34.059		12.553	

Concentration Evaluation

Modeling BC distributions and concentrations over the Arctic is considered a challenging task for chemical transport models. (Wang et al., 2011) Previous model inter-comparison shows order of magnitude differences between observation and model. (Bond and Sun, 2005; Wang et al., 2011) Shindell et al. 2008 and Koch et al. 2009 show negative bias between model and observation. (Koch et al., 2007; Shindell et al., 2008) However, Shwartz et al. 2010 shows positive bias comparing global models with observation. (Shwartz et al. 2010, Sharma et al., 2013) These differences between model performances are largely due to the high uncertainty in emissions and scavenging

efficiency for calculating wet deposition. Regional chemical transport models with a focus on the Arctic capture the BC concentration better over the Arctic. Koch et al. 2009 and Liu et al. 2011 studies captured the ARCTAS flights vertical profiles and seasonality well. (Koch et al., 2009a, 2009b; Liu et al., 2009)

Concentration Evaluation along ARCTAS DC-8 flights

The simulated air pollution concentration data were evaluated using NASA ARCTAS flight data. Table 4-1 shows the NASA ARCTAS flight categories and Figure 4-3 a and b shows the flight tracks. Figure 4-5 shows boxplots comparing concentrations of BC, SO₄, and SO₂ for model and observations for each ARCTAS flight. The flight categories are shaded similar to Figure 4-4. Figure 4-5 boxplots compare the simulated concentration values along the ARCTAS flights with observations for BC, SO₄ and SO₂. Furthermore, Figure 4-6 compares the vertical BC and SO₄ concentration profiles for different flight categories. In these plots, both modeled and observed values are binned by flight altitudes every 1 km. The model captured the vertical variability of BC and SO₄ concentration well. For BC, model has negative bias on lower altitudes (below 4km) and relatively lower positive bias for altitudes above 6km. The model under-predicted the BC values for spring transition flights between 1km and 5 km.

The spring Transit flights are from Alaska to California and over Pacific Ocean. The time series plots show that the model captured observed values along the transition flight pathways weakly. (The plots are not included here) However, the model slightly over-predicted BC and SO₄ at higher altitudes. (Figure 4-6) There is a BC plume at

~3500m over California region on the 04/01/2008 flight and the model did not capture this plume. Also, there is another high BC event over the Pacific region in the 04/19/2008 flight around 4800m that the model failed to capture. There is also a negative bias around 5km altitude in Spring Alaska local flights.(shaded green in Figure 4-5) The model constantly over-predicted SO₄ and SO₂ concentration during the Spring Alaska local flights. The model has significantly better performance for all other flight categories.

In general, the model captured SO₂ and SO₄ vertical variability and magnitude well for all flight categories. There is a constant over-prediction of SO₄ in higher altitudes. These higher altitudes positive bias could be due to under-prediction of RH and hence in-cloud scavenging at altitudes above 6km. Also, the negative bias of SO₄ at the surface might be due to low values of SO₂ emissions.

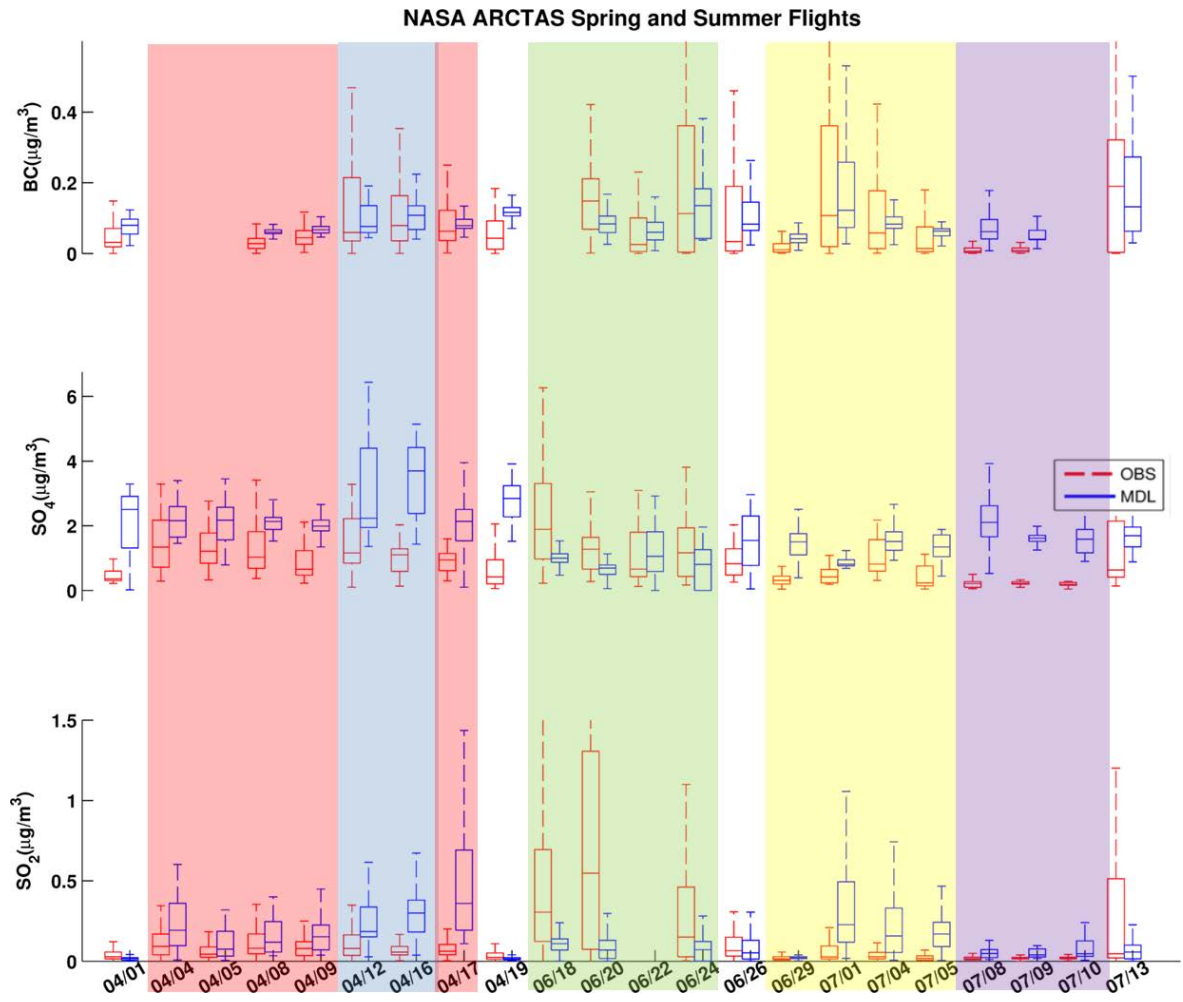


Figure 4-5: Comparison of BC, SO₄, and SO₂ for NASA ARCTAS spring and summer flights.

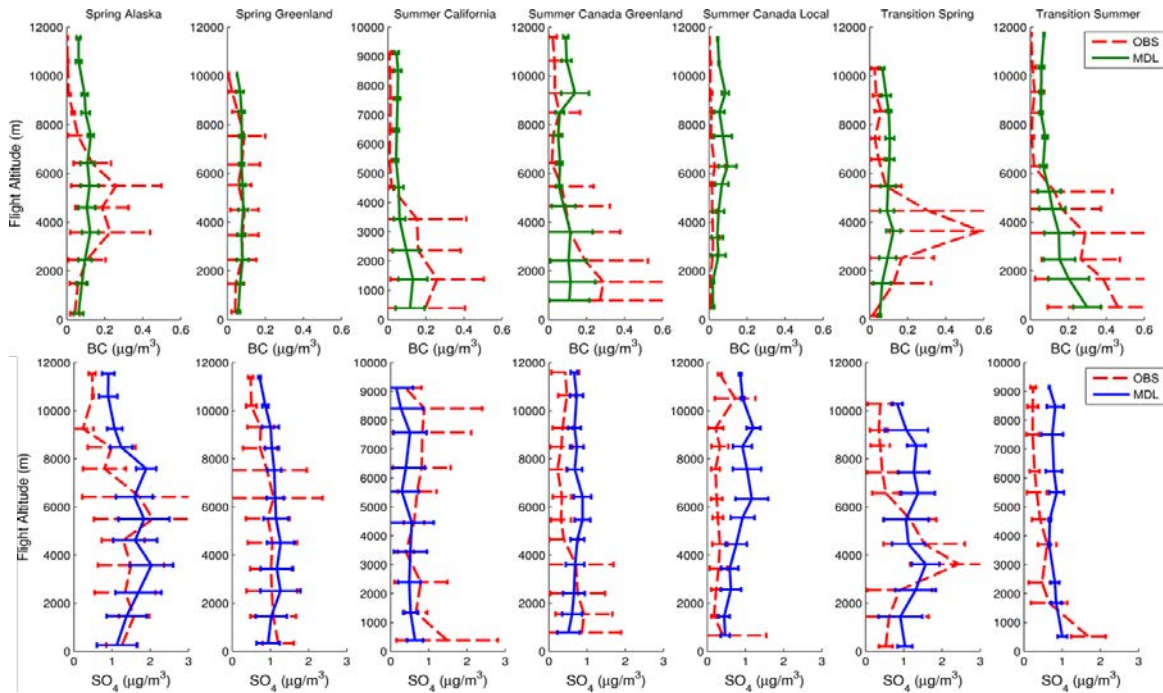


Figure 4-6: Vertical profile and comparison of STEM model aerosols with ARCTAS DC-8 aircraft observations.

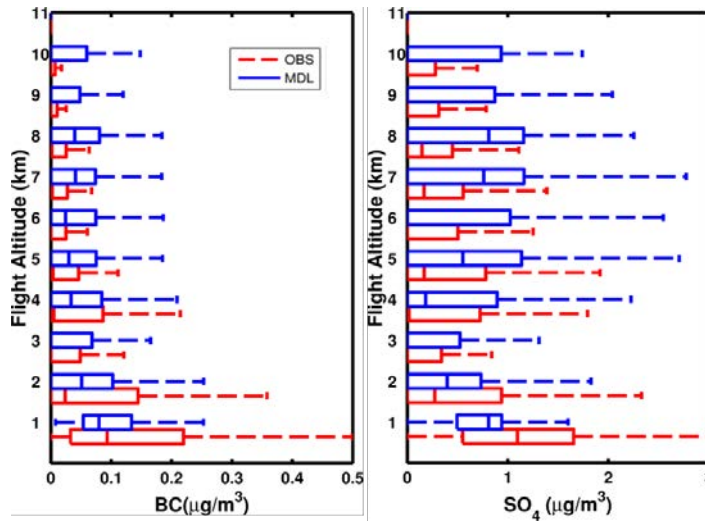


Figure 4-7: Vertical profiles and comparisons of Model and Observation BC and SO₄ by altitude for all ARCTAS flights.

BC Surface Concentration Evaluation at Barrow and Alert

For evaluating the model performance in capturing the seasonality of BC concentration in the Arctic region, we compared the simulated BC surface concentrations with BC data available at Barrow and Alert stations for the duration of study. (April 2008- March 2009) When using EBC values, it is very important to keep in mind that the MAC values used for estimating EBC has a very large range (from 5m²/g to 20m²/g) and EBC concentrations has at least a factor of two uncertainty. (Qi et al., 2017a; Sharma et al., 2013b; Stohl et al., 2013) Traditionally, a MAC value of 10 m²/g was used for EBC calculations for aged BC particles and (Sharma et al., 2013a) even uses MAC values of 19 m²/g for both Barrow and Alert sites. (Stohl et al., 2013) However, recent studies suggest much lower values for MAC compared to 9.5 m²/g used for this study. Sharma et al., 2017 suggest MAC values of 5 ± 2 m²/g for summer-time and Sinha et al., 2017 suggested MAC values as low as 8.5 m²/g for Barrow site.

Figure 4-8 shows the time-series boxplots of simulated BC vs observation BC concentration for the duration of the study at the surface for the Alert and Barrow sites. Both model and observation show higher values of BC during winter and spring, indicating the Arctic Haze. At the Alert site, the model especially captured the winter-time and spring-time peak values; however, it over-predicted the summer BC concentration. The model accurately predicted the seasonality of BC in both sites. However, for Barrow site the model consistently over-estimates the BC concentration during the year. The over-estimation of BC during summer can be due to the large contributions of biomass burning from Siberia and SA in the simulations caused by

overestimations of emissions and/or too little removal during transport. However, the Stohl et al., 2006 study discussed that the biomass burning contributions from remote locations were unintentionally removed in the Barrow measurements data processing. By removing the data cleaning for Barrow site, the observations were increased by a factor of 2-3 during summer.(Stohl et al., 2013, 2006) Other possible reasons for overestimation during the summer in both sites are excessive convective transports, the underestimation of wet scavenging in convective clouds, and errors in parametrizations of BC aging and wet scavenging.

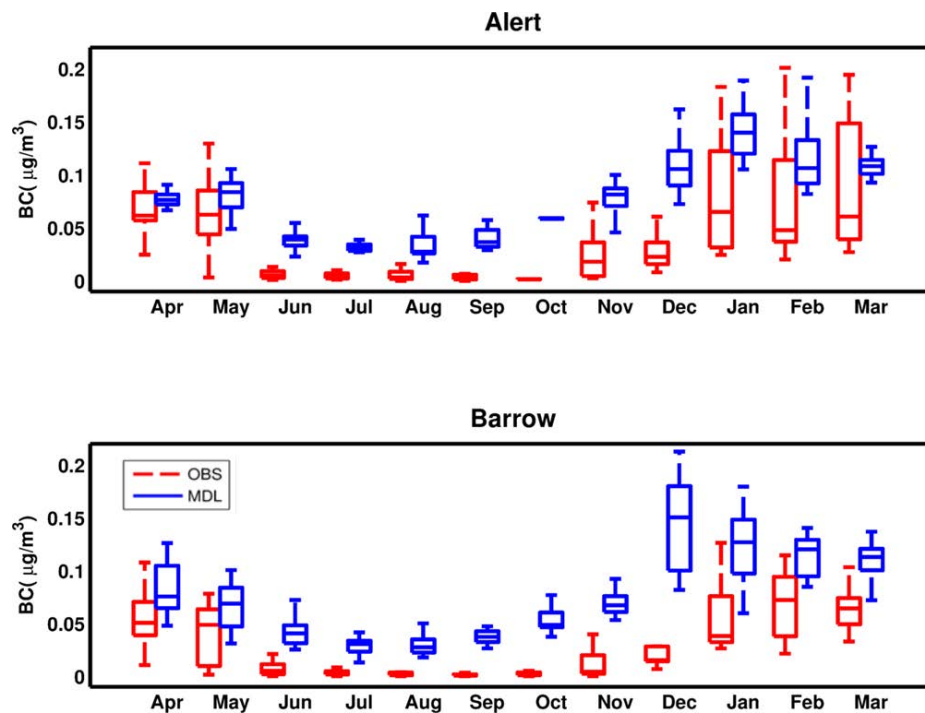


Figure 4-8: Comparison of simulated BC with observations shown as box-and-whisker lots over the simulations period at Alert and Barrow site.

BC Concentration Evaluation for IMPROVE sites

The simulated air pollution concentrations were further evaluated using data from 168 IMPROVE sites over the U.S. for the period of April 2008 to July 2009 (Data available from <http://vista.cira.colostate.edu/improve/Data/IMPROVE/AsciiData.-asp>). Figure 4-9 shows the annual mean surface BC concentration over the U.S. compared with observations at IMPROVE network sites. Each site is represented as a circle in the map. The average model BC over the U.S. is $0.16 \mu\text{g}/\text{m}^3$ while average IMPROVE data is $0.19 \mu\text{g}/\text{m}^3$. Further statistical analysis shows that the root-mean-square deviation (RMSE) between model and observation is 32% and the mean bias error (MBE) is $0.03 \mu\text{g}/\text{m}^3$. The mean simulated/modeled BC concentration is 1.2 while average global model simulated/modeled BC is 1.6 over North America. (Koch et al., 2007). The model evaluation over CONUS provides with a broader perspective and also give us some idea about the North American contributions to the Arctic has accuracy.

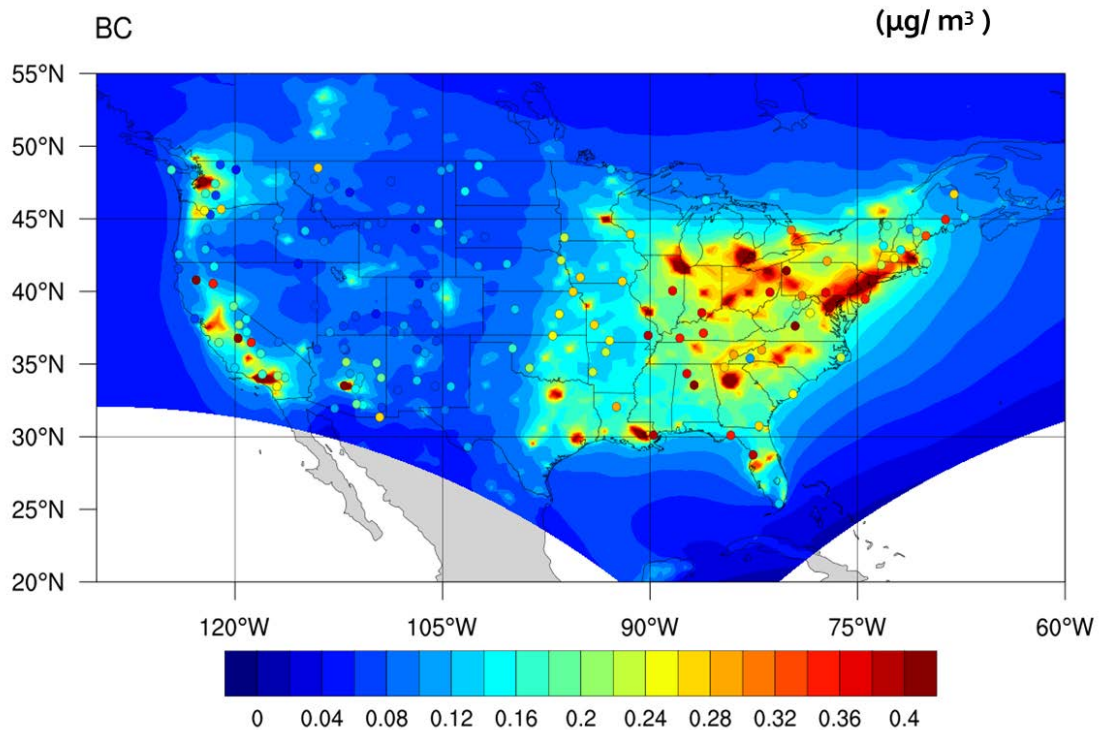


Figure 4-9: Annual average surface BC concentration over the U.S. The circles indicate IMPROVE sites with the color representing the BC concentration in $\mu\text{g}/\text{m}^3$.

Spatial Distribution of PM Species

BC and SO_4 are major parts of $\text{PM}_{2.5}$, and they can be transported over long-ranges and across the continents, and they both have various anthropogenic and natural sources emission sources. Figure 4-10a-d presents the annual average concentration of surface BC, SO_4 , $\text{PM}_{2.5}$ and PM Ratio over the entire modeling domain. Figure 4-10-a shows that the modeled BC surface concentration is in the range of ~ 0.25 to $3 \mu\text{g}/\text{m}^3$. The major BC hotspots are over southeast Asia, northern India and China with annual average concentration of $\sim 3 \mu\text{g}/\text{m}^3$. Furthermore, the seasonal and monthly results show that BC concentration peaks during wintertime since there are higher biomass and fossil fuel

burning for heating during the winter season. The annual average surface concentration over the U.S. is $0.16 \mu\text{g}/\text{m}^3$ with the maximum BC over the Eastern U.S. with average of $0.75 \mu\text{g}/\text{m}^3$. The annual average BC for the Arctic area (altitude higher than 60°N) is between $\sim 0.025 \mu\text{g}/\text{m}^3 - 0.075 \mu\text{g}/\text{m}^3$ with the minimum occurring over Greenland, Alaska and Northern Canada. This value is consistent with the average of $0.06 \mu\text{g}/\text{m}^3$ over the Arctic from Sharma et al. 2013.

SO_4 particles can be produced by sea spray or volcanos, but they are mostly from oxidation of SO_2 emitted during combustion of sulfur containing fossil-fuels SO_4 scatters solar radiation and has a negative direct radiative forcing. Figure 4-10-b shows that the major SO_4 levels are in Asia, northern India with less intense but significant concentrations over Europe and eastern CONUS. However, the concentration of SO_4 particles over the East Asia is approximately two times higher than over the eastern CONUS and Europe. This is due to higher SO_2 emissions in the Asian region and relatively faster SO_2 oxidation rates. (Chin et al., 2007)

Figure 4-10c shows the distribution of surface $\text{PM}_{2.5}$. Major $\text{PM}_{2.5}$ hotspots are over the Persian Gulf, Central Asia, northern India and northern Africa with annual average maxima as high as $\sim 80 \mu\text{g}/\text{m}^3$ around the Persian Gulf. The Arctic area (above 60°N) show values between $1 - 5 \mu\text{g}/\text{m}^3$ with maximum occurring over northern Europe and northern Russia. Greenland, Northern Canada and Alaska show average $\text{PM}_{2.5}$ concentrations of $\sim 2 \mu\text{g}/\text{m}^3$. Figure 4-10-d shows the $\text{PM}_{2.5}/\text{PM}_{10}$ ratio. The arid regions with high natural dust emissions such as northern African, the Persian Gulf, and Central

Asia show lower PM ratios indicating the major contributions of dust to PM over these regions. Over the oceans, the PM ratio is very low (0.1-0.2) caused by higher contributions of sea salt to PM₁₀ and low PM_{2.5} concentration. (~38mg/m³ SSC /45mg/m³ PM₁₀ = 84% contribution of coarse sea salt to PM 10 over the Atlantic Ocean and 75% over the Pacific Ocean.) Higher PM ratio values in eastern Asia and eastern CONUS indicate that the sources of PM in these regions are mostly anthropogenic and not dust.

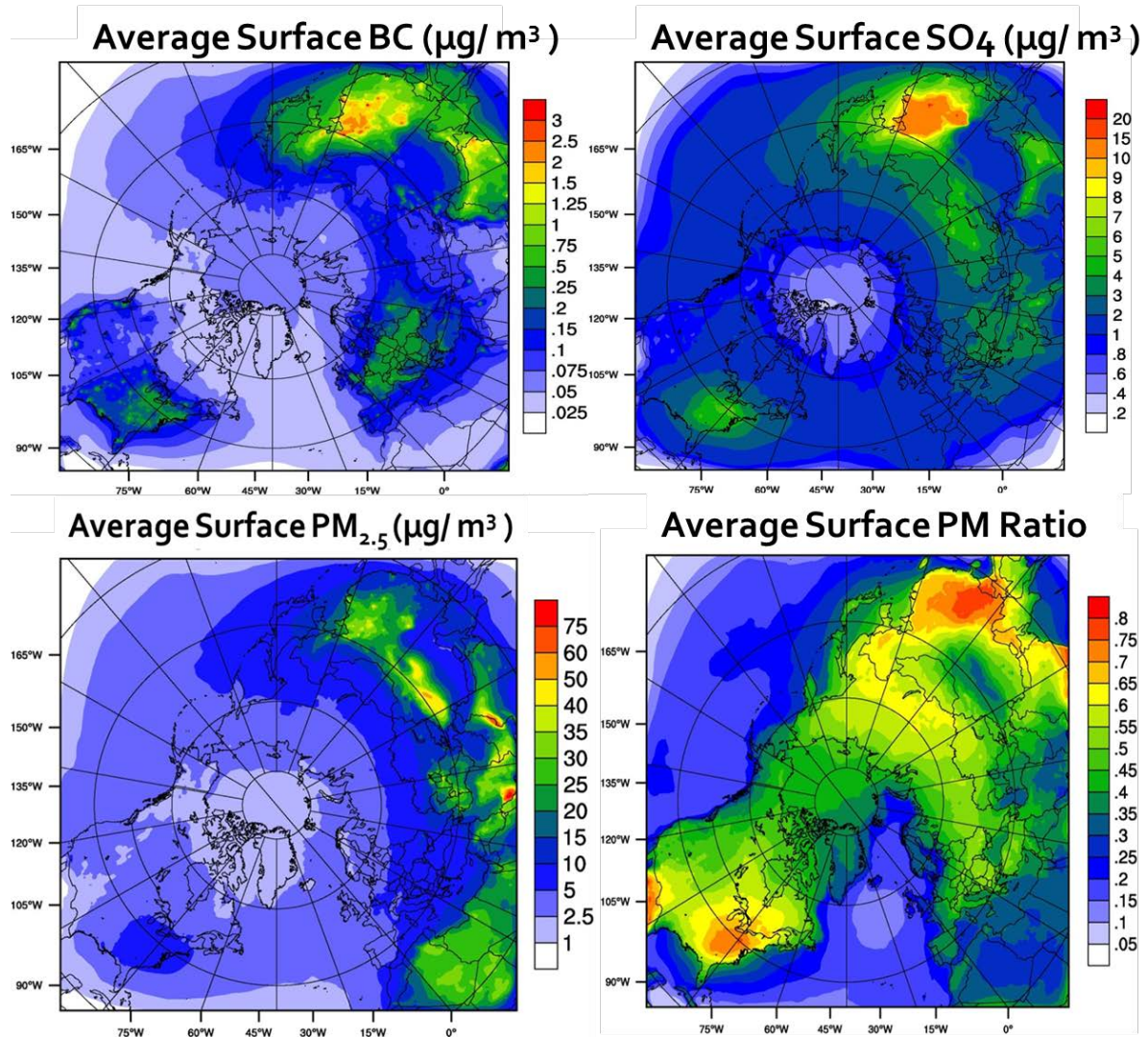


Figure 4-10: Spatial distribution of simulated a) BC ($\mu\text{g}/\text{m}^3$), b) Dust ($\mu\text{g}/\text{m}^3$), c) $\text{PM}_{2.5}$ ($\mu\text{g}/\text{m}^3$), and d) $\text{PM}_{2.5}/\text{PM}_{10}$ ratio averaged over the simulation period. The values on the map denote contour values at sharp gradients.

Sources of Arctic PM

Source sectors contributing to PM surface concentration

Due to the significant contribution of BC in global warming over the Arctic, it is extremely important to understand the influence of specific source regions and source

sectors of BC concentration over the Arctic. In this study, the impact of emission sector categories including residential, transportation, biomass burning, power, and industry is investigated using a series of sensitivity runs. For each sector sensitivity run the emission from the selected sector is zeroed out to calculate the impact of the source sector on concentrations. The percent change is calculated as (perturbed concentration-base case concentration)/ base case concentration x 100%. Figure 4-11 shows the 5 major source sector contributions (%) to BC surface concentrations. Transportation is the major sector contributor over North America with contributions between 35%-55%. However, the residential sector has a significant (~25%) contribution over Western U.S. The residential sector contributions show the outflow of Asian BC over Pacific Ocean and to the West Coast. The residential sector is the major contributor to BC over China, Southeastern Asia with maximum residential (%) contribution as high as ~70 %. Over Europe residential, transportation and industrial sectors are the major emission sources respectively. Over the Arctic area (over 60 °N) residential and transportation sectors show maximum contributions of ~40% and ~28% respectively. Biomass burning shows high contributions over Siberian Arctic with values as high as 40%, which indicates Siberian forest fire effects especially during springtime. Industrial and power emissions had the highest contributions on the Arctic SO₄ concentration, while biomass burning, power and industrial emissions have the highest contributions on the Arctic PM_{2.5}. The seasonality of sector contributions to the Arctic pollution is shown in Figure 4-12.

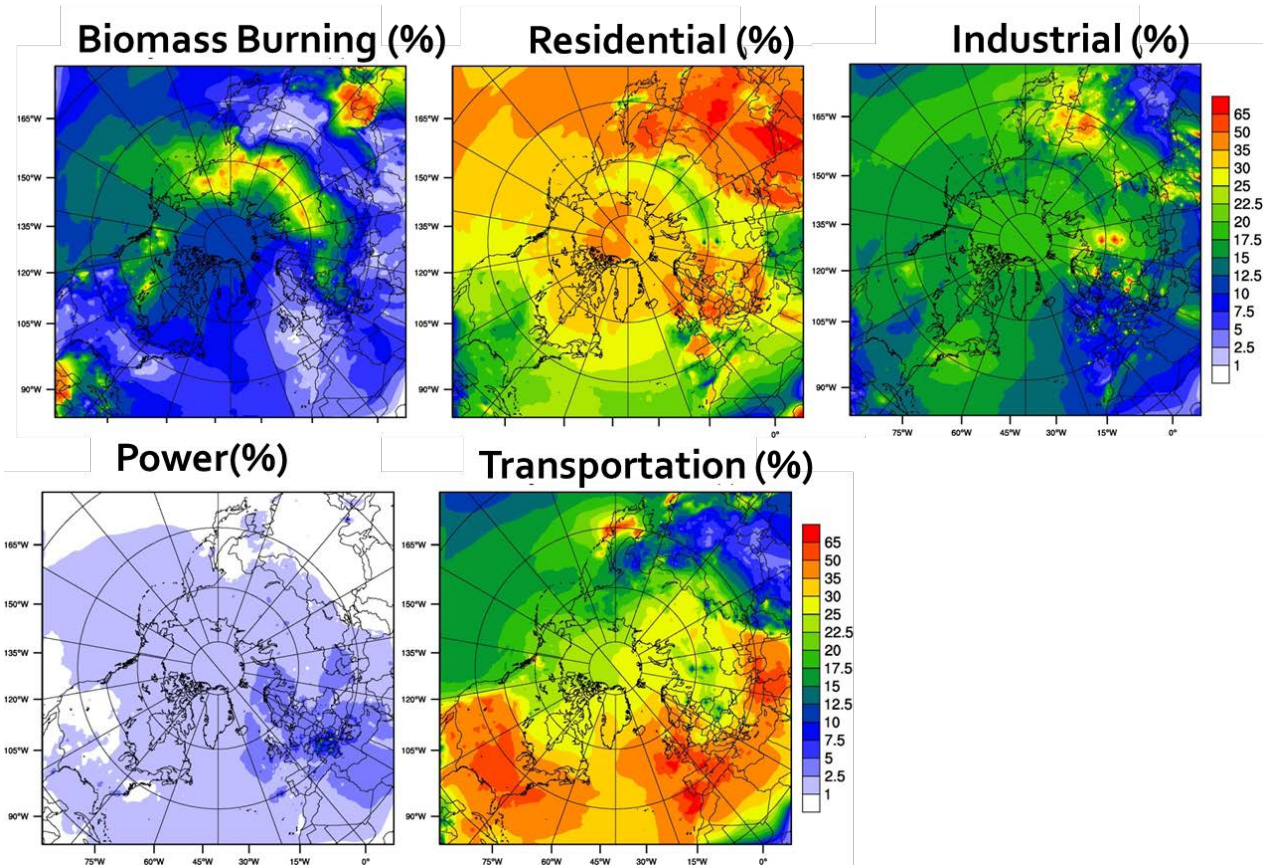


Figure 4-11: Source sector contributions (%) to annual BC surface concentration over the entire domain.

Figure 4-12- top panel shows the time series contribution from five emission sectors to BC surface concentration over the Arctic. For this plot, the area average surface concentration for latitudes 60°N and above is shown. The surface concentrations range from 0.05 $\mu\text{g}/\text{m}^3$ to 0.2 $\mu\text{g}/\text{m}^3$ over the Arctic. The maximum BC concentration occurred during wintertime, indicating the Arctic haze. The contribution from residential sector significantly increases during wintertime, since burning of biofuels and coal are the main heating resource at higher latitudes. Furthermore, there is a high seasonal variability in the contribution of biomass burning with the minimum occurring in the winter and

maximum occurring during the spring. In the spring, there are high numbers of agricultural burning in Russia and higher events of Siberian forest fires. (Bond et al., 2013) During spring 2008, biomass burning was reported unusually high. (AMAP, 2011) Furthermore, during the spring the arctic front is more southerly on the Eurasian side. (Bond et al., 2013) Hence, the BC emitted from agricultural burning and boreal forests from Europe and Russia transport easily, especially at lower altitudes. This results are similar to Warneke et al., 2009 and (Qi et al., 2017b) , which suggest that high altitude agricultural and boreal forest fire is one of the main contributors to amount of BC over the Arctic during spring 2008.

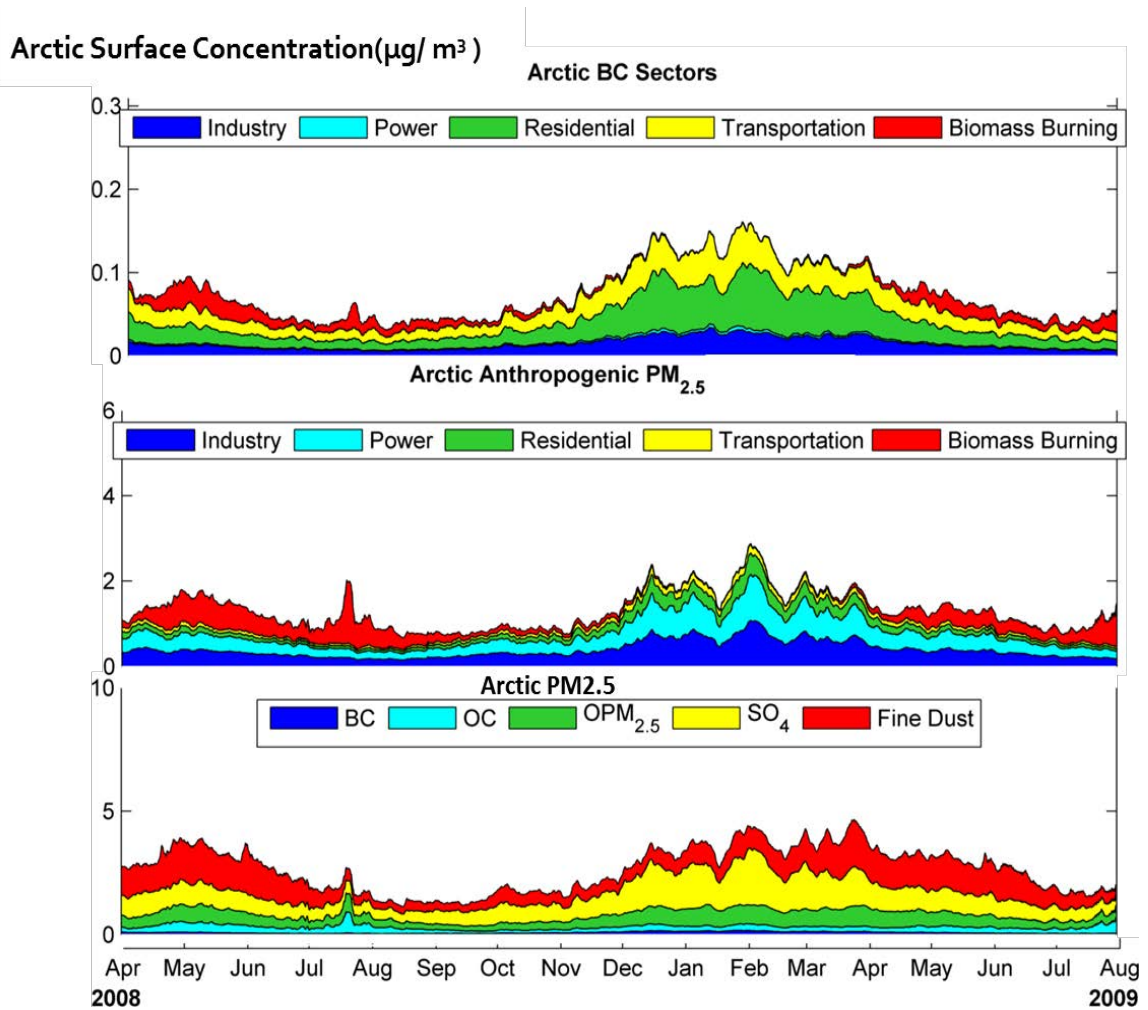


Figure 4-12: Time-series concentration and contribution of a) different sector to BC concentration b) different sectors to anthropogenic $PM_{2.5}$ concentration and c) different $PM_{2.5}$ species.

Figure 4-12 middle panel shows the time series of contributions from the emission sectors to Anthropogenic $PM_{2.5}$ over the Arctic region. Biomass burning contributes to the $PM_{2.5}$ seasonality with maximum contribution In Spring and summer. The power, industry, and transportation sectors are the highest contributors during winter-time, due to higher energy consumptions for both domestic and industrial heating.

Figure 4-12- bottom panel shows the contribution of different PM_{2.5} components to the Arctic total PM_{2.5} concentration. BC comprises an average of PM_{2.5} over the Arctic. Fine dust (defined as dust with aerodynamic diameter of less than 2.5 µm) is a major source of PM_{2.5} seasonal variation, with maximum contribution in spring (%40). SO₄ shows the highest contribution over the winter months with a peak of 60%. SO₄ maximum in winter shows the higher use of fossil fuel and coal burning and SO₂ emission in cold months. Annually, industry and power sectors have the highest contributions to the Arctic SO₄ concentration. (each ~40%) The transport pathways and seasonality are further described in the transport pathways section.

Geographical source contribution to PM concentration

Contributions of BC emissions from different source regions (i.e. Europe, China, North America, Central Asia, Middle East, South Asia, Central Asia and Siberia) were also analyzed using sensitivity analysis. Figure 4-13 shows the spatial plots of annual average contributions from different geographical regions to BC surface concentration. Europe and China have the largest contribution to BC surface concentration over the Arctic. China contributes up to 35% to the BC in the Northwestern CONUS and Alaskan regions. North American emissions have up to 20% contribution to Southern Europe surface concentration.

The source regions contributions to surface and column BC concentration also show seasonal variability. Figure 4-14 shows the contributions of different emission regions to BC surface concentration and column amounts. Anthropogenic emissions

from Europe and China have the highest impact on the Arctic surface concentration with annual averages of ~40% and ~25%. However, Europe only contributes to ~25% of the Arctic BC column and China contributes ~36% of column BC in the Arctic. During the winter and spring, air masses from colder and dryer regions can follow surfaces of constant potential temperature and cross the Arctic front barrier but emissions from moister and warmer regions such as North American and China cannot easily cross the Arctic front. However, these particles originating from warmer and moister regions can be lifted and transported to the Arctic in the middle and upper troposphere along the isentropes. (Bond et al., 2013) Therefore, emissions from northern latitudes such as (Europe and Russia) have higher contributions to the surface concentration but emissions from lower latitudes have higher contributions to the column aerosol load. Anthropogenic emissions from North America (Canada and United States) are also significant contributors to the BC column concentration with contributions of ~10%. However, anthropogenic emissions from North America contribute only ~4% of surface concentration over the Arctic. North American emissions are mostly from lower latitudes with higher potential temperature and higher humidity. Therefore, the major transport pathway of North American emissions to the Arctic following constant potential temperatures, which cause cloud formation and precipitation, hence higher wet scavenging of aerosols. Brock et al., 2011, Liu et al., 2015 and Xu et al., 2017 show similar low contributions of North American Anthropogenic emission to the arctic surface concentration. Less than 5% percent of emissions are transported from each of South Asia and the Middle East to the Arctic. During the winter, anthropogenic emissions

from Russia is accountable for ~12% of BC surface concentration and less than 5 % of column BC concentration over the Arctic. This is due to the thermal stable condition and lower vertical mixing during the winter over Russia. During the spring time, anthropogenic emissions from Europe, China, and Russia account for ~35%, 25%, and 10% of BC surface concentration. This study is consistent with Koch and Hansen 2005, who show that emissions from Russia, Europe and South Asia have contributions of 20-30% during springtime

The peak BC surface concentration occurs during the wintertime; however, the contribution of biomass burning in Siberia significantly increases during spring and summer period, when the biomass burning emissions are the highest. The contributions of Siberian biomass burning to the Arctic surface and column concentration almost doubled during spring 2008 compared to spring 2009. The spring 2008 peak concentrations are explained in the model by Siberian biomass burning plumes transported to the Arctic with little wet scavenging by precipitation and dilution. The anthropogenic emissions from Europe, China, and Russia are major contributors to peak BC surface concentration with contributions of 40%, 30% and 10% respectively. During the winter, anthropogenic emissions are accountable for ~97% of BC concentration over the Arctic, while during the summer biomass burning contributes ~50% of Arctic BC concentration. During the summer, the contributions of European biomass burning increase. The simulation results also show that the biomass burning plumes from South East Asia can reach the Arctic troposphere accounting for up to 10% of BC aerosol loading during April 2009.

Figure 4-15 shows the contributions percentage of various sectors and regions to BC, SO₄, and PM_{2,5} for Alert, Barrow, and Arctic site. This figure shows the major sector contributor to SO₄ is power and industry in both alert and Barrow observation sites and in the Arctic region. SO_x is produced during burning of sulfur containing materials such as fossil fuels. Burning sulfur containing fossil fuels such as oil and coal for electric power generation is the main emission source of SO_x in the atmosphere. Another important source of SO_x in the atmosphere is metal smelting and petroleum refining. (Cooper and Alley, 2011; Hand et al., 2012) Sulfate or SO₄ is a secondary aerosol produces during photochemical reaction of SO₂ in the atmosphere.(Hand et al., 2012) The major region contributor for SO₄ is China, Central Asia, and Europe. Although several control strategies reduced global SO₂ emissions in recent years, many countries such as India and Central Asian countries show an increase in their SO₂ emission. (Lu et al., 2010) In general, the contributions of various sectors and regions to the Arctic PM are similar for Alert, Barrow and the Arctic average. Therefore, we can safely assume that Alert and Barrow sites are good representations of the Arctic area average for future analysis.

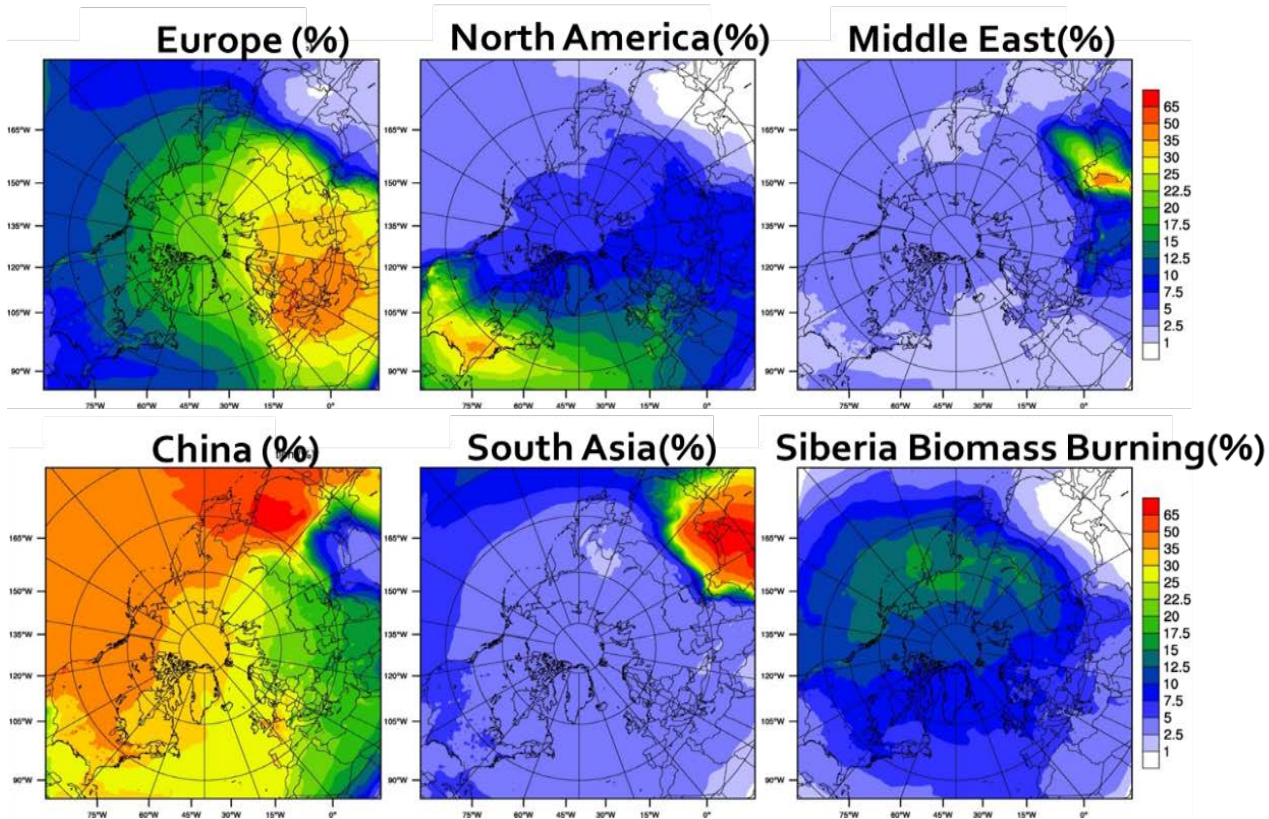


Figure 4-13: Source region contributions (%) to annual BC surface concentration over the entire domain.

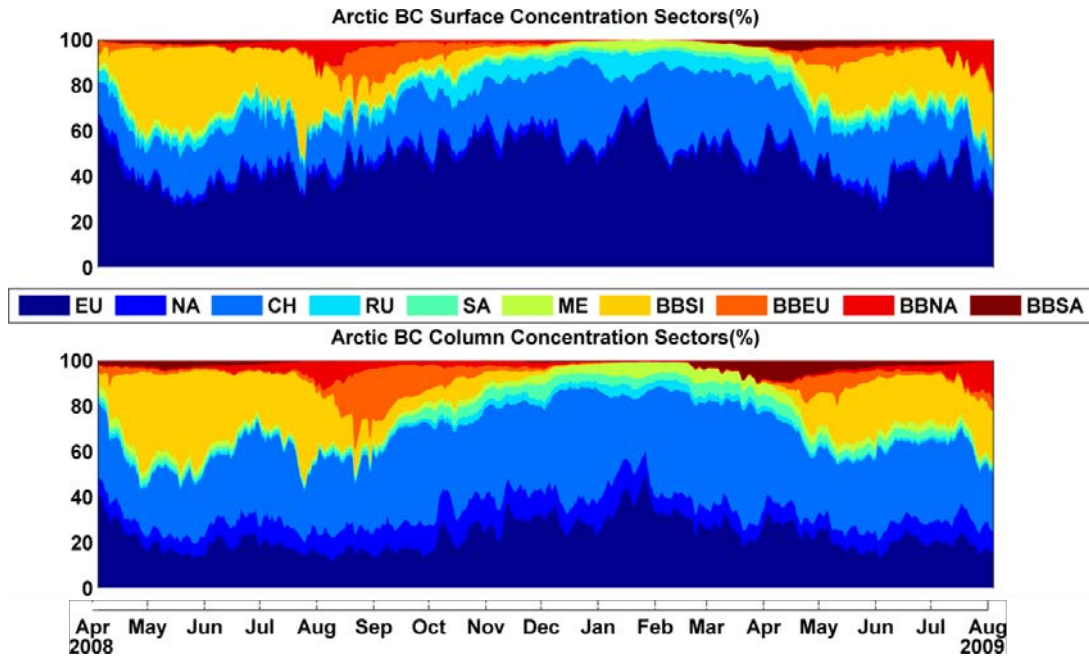


Figure 4-14: Time Series of BC major geographical contributor to the Arctic average surface concentration.

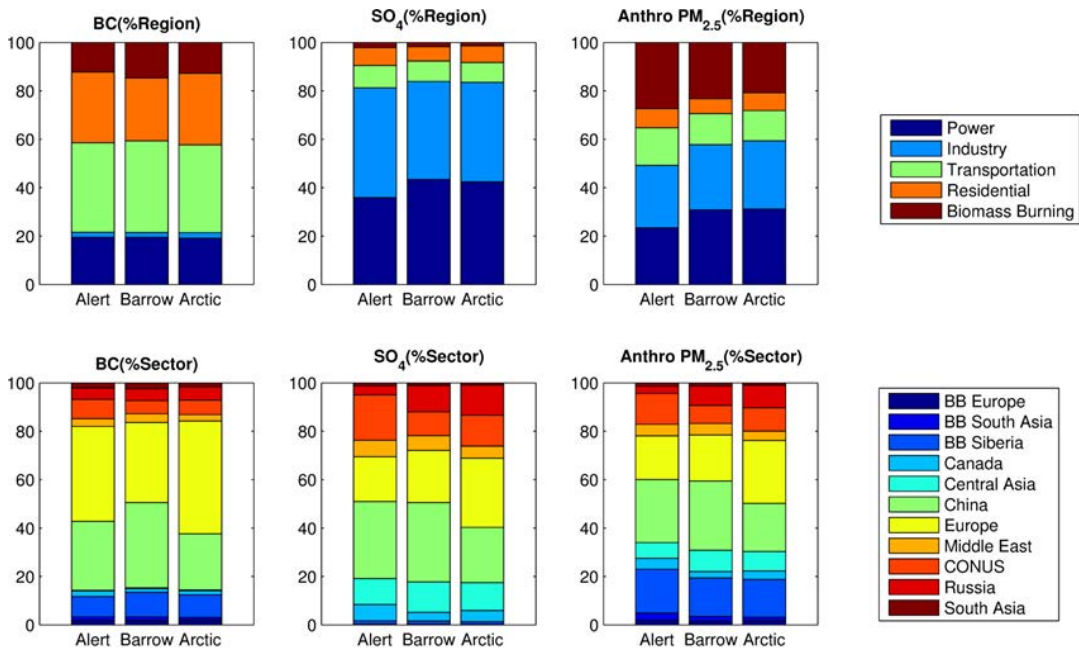


Figure 4-15: Summary of annual mean contributions by source regions and sectors for BC SO_4 and Anthropogenic $PM_{2.5}$.

Transport Pathways

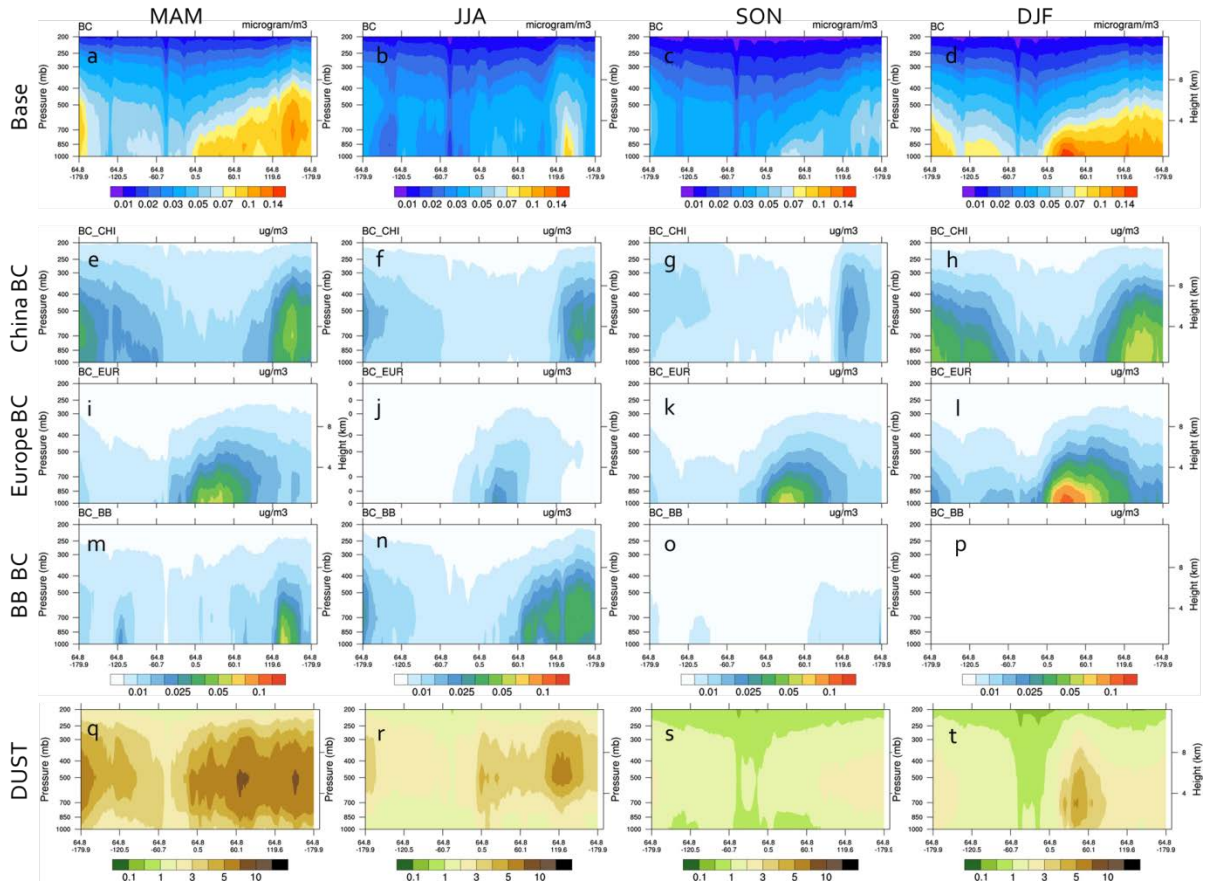


Figure 4-16: Cross Section at 64.8 N for different seasons. The first and last rows show the BC and dust concentrations at the cross-section. The other rows show the contributions of major regional sources and BB burning to BC at 64.8 °N.

To further study the seasonality and transport pathways of BC in the Arctic, the altitude- latitude cross sections are shown at 65 °N(entrance boundary for the Arctic) in Figure 4-16. During the spring, the magnitude of BC is relatively high in Eurasia and Siberia. This is partly due to southerly extent of the polar dome during spring especially over Eurasia, which facilitates the transport of BC emission from lower latitudes to the

Arctic. During spring, there are extensive agricultural fires and high number of forest fires in Northern Siberia. In addition, spring 2008 had exceptionally higher numbers of (almost double) Siberian forest fires compared to other years. (Liu et al., 2015)

During winter (Figure 4-16-d) ,we see higher concentration of BC up to 5km indicating the higher low-level transport of BC from the source regions including NA, Europe and Siberia. This shows the stable and low vertical mixing. During the cold months, Europe is the major contributor to the BC concentration, at lower altitudes as shown in Figure 4-16-i. This is due to thermally stable conditions over winter, which inhibits the upward transport and vertical mixing of emission plumes. However, China shows higher contribution at mid and upper troposphere, which indicates the transport pathways of Asian plumes to the Arctic. (Figure 4-16-h) The contribution of biomass burning to BC concentration is high during summer over Eurasian Arctic, Siberia, and North American Arctic. The contribution of BB is especially high over spring over Siberia during spring 2008 relative to the other years. Also, higher residential emission of BC in Europe and Asia during the winter is another factor contributing to the higher BC concentration over the Arctic. Siberian forest fires are the major cause of higher BC concentration in Siberian Arctic during summer. (Figure 4-16-n) The higher rate of wet scavenging during summer causes lower transport via low-level pathways. However, the convection caused by forest fires can inject BC in the free troposphere, which reduce the wet and dry deposition for that plume. Figure 4-16 (q-t) shows the dust concentration at the 65 N cross section. During spring we have higher altitude plumes of dust transporting to the Arctic. Dust emission sources are usually from lower latitudes dry and semi-arid

regions; hence dust transport to the Arctic is usually in higher troposphere. Summer also shows similar pattern but with less intensity compared to the spring.

For further analysis of transport pathways, 10-day back trajectory analysis was performed using FLEXPART-WRF (Brioude et al., 2013; Stohl et al., 1998). The backward trajectories were initiated at latitudes of 65 °N and longitudes of 170 °E, 150°E, 120°E, 75°E, 75°W and 120°W. These trajectory analyses provide us with useful information about the transport pathway of air masses and the regions the air mass has passed over while transporting to the Arctic. The back-trajectory analysis shows that Siberian Arctic is mostly affected by East Asian, Russian, and Central Asian emissions, while Eurasia is mostly affected by European and central Asian emission. The Canadian subarctic the source is mostly affected emissions from Asia and lower latitudes in Northern America. The backward trajectory at 65 °N and 120 °W shows the direct transport pathway of air parcels over large anthropogenic emissions in Asia. The backward trajectories show that the pollution from East Asia can reach Canadian subarctic via pacific route, while emissions from Europe affect Eurasian Arctic. North American Emission are also transported to European Arctic and Greenland by passing over the Atlantic Ocean.

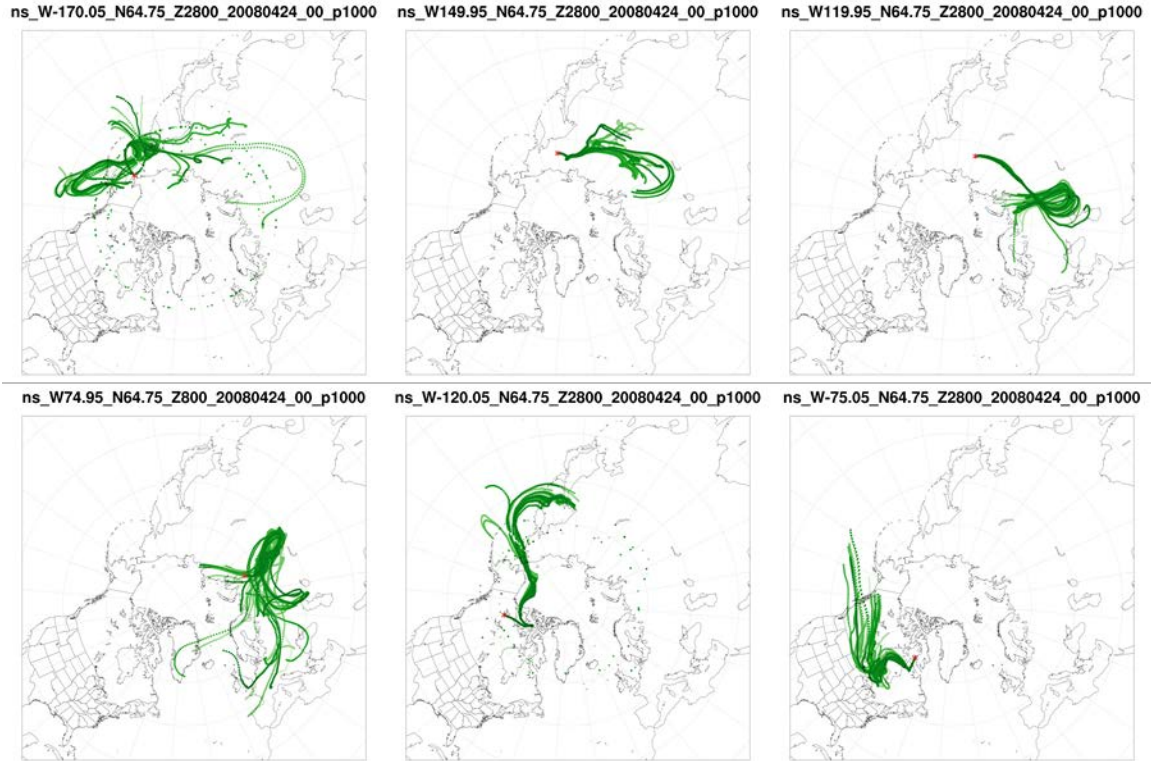


Figure 4-17: Ten-day backward trajectories released at various locations on longitude of 65°N.

Conclusions and Future Works

To help better understand the potential importance of emissions sources to the Arctic, it is beneficial to calculate the source regions and source sectors contributing to the Arctic particle loading. In this study, we used a chemical transport model (STEM) to investigate long-range transport of PM to the Arctic and calculate the contributions of various anthropogenic and biomass-burning emission sources to the Arctic surface and column PM concentration. The focus of this study is to quantify of the source sector and source regions contribution to the Arctic loading.

This study shows that emissions originating from residential and transportation sectors are the major contributors to the Arctic BC loading on annual basis with

contributions of ~35% and ~30% respectively. However, the results show that power industrial, and biomass burning emissions are the major contributor to the Arctic $PM_{2.5}$ (contributions of ~30%, 25%, and 20% respectively). Our simulations showed a distinctive seasonality for the contributions of sectors and regions to BC and $PM_{2.5}$ concentration over the Arctic. During the winter peak, the contributions from residential sector are maximized due to high-energy consumption for heating purposes. Biomass burning also shows a distinctive cycle with contributions to BC surface concentration as high as 50% during summer and less than 3% during winter. The contributions of anthropogenic sources to BC concentration near the surface was dominant varying from 55% -97% over the year. However, the contribution of BB from Siberia become significant during spring and the contributions of BB emission from Europe become significant over the summer accounting for up to 20% of Arctic BC loading.

Dust is one of the most important drivers of the Arctic $PM_{2.5}$ seasonality. Dust is the largest component of $PM_{2.5}$ in the region in all seasons except for cold months, when sulfate is the largest contributors to the $PM_{2.5}$.

The results show that the major source region contributor to BC surface concentration is Europe and China annually with contributions 40% and 25% respectively. In mid and upper troposphere, the contributions of Chinese emissions are higher due to the different transport pathway of lower latitude Asian emissions to the Arctic. Our model results show a distinctive temporal variability for regional

contributions to the Arctic. In general, the anthropogenic emissions from Europe are the most significant due to its large contributions over the winter (haze season).

We evaluated our metrological model performance (WRF) using metrological observations along the ARCTAS flights. The resulting simulations provide a good fit for the observations along the flight. For evaluating simulated BC, we also used BC concentration along the ARCTAS DC-8 Flights, BC surface concentration at IMPROVE sites, and EBC surface observations at Alert and Barrow sites. The model tends to over-predicts the BC concentration at the surface sites but captured the magnitude and vertical profile of ARCTAS flights.

There are many factors contributing to uncertainties associated with the contributions of each source sector and source regions to the Arctic PM loading. The most important uncertainties are transport pathways, emission inventories, and removal parametrizations. More observations at Arctic locations along with higher resolution modeling studies are necessary to evaluate model concentration. The future work is focused on the effect BC from different sectors on the RF change over the Arctic.

CHAPTER 5: QUANTIFYING DEPOSITION OF BLACK CARBON AND DUST ON THE ARCTIC SNOW AND THE RESULTING ALBEDO REDUCTION

Abstract

Long-range transport of atmospheric particles from mid-latitude sources to the Arctic is the main contributor to the Arctic aerosol loadings and deposition. Black Carbon (BC), Brown Carbon, and dust are considered of great climatic importance and are the main absorbers of sunlight in the atmosphere. Furthermore, wet and dry deposition of light absorbing particles (LAPs) on snow and ice reduce albedo. LAPs have significant radiative forcing and effect on snow albedo causing snow and ice to warm and melt more quickly.

There are high uncertainties in estimating radiative forcing of LAPs. In this chapter the potential effect of LAPs from different emission source regions and sectors on snow albedo in the Arctic is studied. A modeling framework including Weather Research and Forecasting Model (WRF) and the University of Iowa's Sulfur Transport and dEposition model (STEM) is used to predict the transport of LAPs from different geographical sources and sectors (i.e. transportation, residential, industry, biomass burning and power) to the Arctic. The main geographical source contributor to the Arctic BC flux is China. However, there is a distinct seasonal variation for the contributions of geographical source emissions to BC deposition. During the spring, when the deposition flux is highest, the contribution of biomass burning attributes for up to ~40% of total deposition at Alert and Barrow. However, during the winter, the anthropogenic sectors

contribute up to ~95% of total BC deposition. The simulated snow BC mixing ratios are evaluated using the observed BC snow concentration values from previous studies including Doherty et al., 2010. The simulations show the BC deposition cause ~0.6% snow albedo decrease during spring 2008.

Introduction

During the past century, the Arctic climate has undergone multiple changes. The Arctic surface air temperature has increased at almost twice the global mean rate, resulting in various regional and global impacts including sea ice loss, increase in wildfires, and sea level rise. (AMAP, 2011; Stocker, 2014) Light absorbing particles such as black carbon (BC), Brown Carbon (BrC), and dust are among the significant contributors to the Arctic warming. (AMAP, 2011) These particles are considered of great climatic importance and are the main absorbers of sunlight in the atmosphere. (Bond et al., 2013; Koch et al., 2007) Light absorbing particles also affect cloud distribution, lifetime, and microphysical properties through indirect and semi-direct effects. (AMAP, 2011) Light absorbing particles deposited on snow absorbs solar radiations, decrease surface albedo, and accelerate the warming and melting of snow and ice. (Haywood and Ramaswamy, 1998; Wiscombe and Warren, 1980) Snow covers most of the Arctic area land and ocean during winter and spring. In the Arctic region, the melting of snow and ice will expose the darker sea underneath, thereby further reducing the albedo and increasing the warming. (Hansen and Nazarenko, 2004)

Numerous modeling and observational studies have shown that the concentration of aerosols at a particular location is influenced by natural, anthropogenic and long-range

transport emissions of pollutants.(HTAP, 2010; Liu et al., 2009) BC is carbonaceous particles produced during incomplete combustion of biomass materials (e.g. wood, crop residue, dung, and etc.), and fossil fuels (e.g. coal, diesel fuel, natural gas, and etc.)(Jacobson, 2004; Ramanathan and Carmichael, 2008) There are currently limited BC emission sources in the Arctic itself.(Bond et al., 2013) Therefore, long-range transport of atmospheric particles from mid-latitude sources to the Arctic is the main contributor to the Arctic aerosol loadings and deposition. (AMAP, 2011; Law and Stohl, 2007)

Dust is another important light absorbing particle with 50 times less effect on snow albedo reduction compared to BC. (Doherty et al., 2010; Wiscombe and Warren, 1980) However, in some regions where dust deposition is strongly higher than BC deposition, dust becomes the dominant light absorbing impurity on snow.(Doherty et al., 2010) Painter et al., 2007 and Skiles et al., 2012 show that dust has significant effect on melting snow in Upper Colorado River Basin. Painter et al., 2012 and Huang et al., 2010 also show the significance of albedo reduction caused by dust deposition on snow in Northern China, close to arid and semi-arid regions and Himalayan glaciers respectively. Globally, natural dust emissions including wind-blown dust from arid and semi-arid regions are the major source of dust emission in the atmosphere. (Fan, 2013; Ginoux et al., 2012) Dust emissions have a strong seasonality; however, nearly 55% of the global annual dust emission is from Northern Africa alone. (Ginoux et al., 2012; Kulkarni et al., 2015) Dust emissions at higher altitude are strongly dependent on wind speed, snow cover, and vegetation type. (Groot Zwaafink et al., 2017)

The minimum potential temperature in the Arctic boundary layer forms the Arctic dome causing very stable air near the surface. (Klonecki et al., 2003; Stohl, 2006; Stohl et al., 2006) The strong atmospheric inversion reduces the vertical transport between boundary layer and free troposphere and limits the aerosol deposition to the ground. The Arctic front acts a transport barrier for Arctic lower troposphere in the more southerly latitudes reducing the low level transport of pollutants to the Arctic dome. (Barrie, 1986) However, the Arctic front reaches as south as 40°N in January which includes all European and Siberian emissions.

In general, the seasonality of particulate matter (PM) in the Arctic is attributed to the seasonal variation of transport pathways, precipitation, and emissions in the mid-latitudes. (AMAP, 2011; Law and Stohl, 2007) PM particles transported to the Arctic at low altitudes are more likely to deposit on snow and PM from higher altitudes are generally ventilated out of the Arctic depending on meteorological conditions.

There are high uncertainties in estimating radiative forcing of light absorbing particles. (AMAP, 2011; Clarke and Noone, 1985; Hansen and Nazarenko, 2004; Qian et al., 2014; Stocker, 2014) Several factors including uncertainties in emission estimates, transport pathways, and deposition mechanism contributes to the high uncertainty in calculating radiative forcing from LAP deposition. (Dou and Xiao, 2016)

In this paper, we used a Chemical Transport Model (CTM) to calculate the BC and dust deposition flux on snow and ice. The mixing ratio of BC and dust in snow is calculated. For assessing the effect of BC deposition on snow albedo, BC deposition on

snow is calculated. To evaluate the simulated values, we compared the BC concentration in snow with observed values from previous studies including Doherty et al. 2010. Furthermore, we estimated the sectoral and regional contributions to BC in snow over the Arctic.

Model Description and Offline Calculations

The sulfur Transport and Deposition Model (STEM) is a regional chemical transport model (CTM) that is used for this study. This model has been developed at the University of Iowa in the early 1980's and has been continuously developed and tested for various field campaigns. Weather Research Forecasting (WRF) is used to provide metrological input for STEM model. For this study, both WRF and STEM model has 60kmx60km resolution with 31 vertical layers up to 10 hpa. The emission input for this study is similar to the previous chapter.

Dry and Wet Deposition Algorithm

Liu et al. 2011 showed that the representation of wet and dry deposition removal in the model has a profound effect on the result of BC modeling over the Arctic. The removal processes of aerosol and gases from the atmosphere happen in the two main forms of dry and wet deposition. Dry deposition occurs when an aerosol particle diffuses to the surface or falls to the ground due to gravitational forces. The deposited gas or particle can stick to the surface or get resuspended in the atmosphere. Wet deposition occurs when atmospheric precipitation scavenges aerosol particles through in-cloud and below-cloud pathways.

For this study the dry deposition process of particles was modeled using the “Resistance in Series Parameterization” from Wesely and Hicks, 2000. Since particles are heavier than gases, the sedimentation speed is included for particles. (D’Allura et al., 2011a) Also we assumed that once particles stick to the surface they will not get resuspended into the atmosphere. The dry deposition of all particles are calculated using the sulfate dry deposition velocity and scaling with the deposition velocity ratio of corresponding particle. For hydrophobic BC and hydrophilic BC scaling s of 0.1 and 1 are used, respectively. (Uno et al., 2004) The wet deposition is calculated using precipitation output from WRF model on an hourly rate. The accumulated deposition fluxes are extracted as model output by the differences between concentrations at each transport time step between the original BC concentration and BC concentration output from the model when the deposition mechanisms are turned off for that specific time step. Equation 5-1 and Equation 5-2 show the method for calculating BC dry and wet deposition amount.

$$BC_DD = BC_{(DD\ rate = 0)} - BC_{(original)} \quad \text{Equation 5-1}$$

$$BC_WD = BC_{(WD\ rate = 0)} - BC_{(original)} \quad \text{Equation 5-2}$$

In the above equations, BC_DD and BC_WD denote BC dry and wet deposition values respectively. $BC_{(DD\ rate = 0)}$ and $BC_{(WD\ rate = 0)}$ are the BC concentration when dry and wet deposition rates are set to zero, respectively. $BC_{(original)}$ is the original BC concentration output from the model with non-zero BC dry and wet deposition rates. Dry and wet deposition variables are reset to the original values after each transport time step.

BC and Dust Content in Snow and Induced Albedo Reduction

For assessing the albedo change caused by BC and dust deposition on snow, first the mixing ratio of BC and dust in snow is calculated. BC concentration in the snow layer is the total amount of deposited BC wet deposition and BC dry deposition and snow processes including melting and sublimation. In this study, an adapted method from Jacobson et al. 2004 and Doherty et al., 2014 was used with meteorological parameters from WRF-V3.7 for offline calculation of snow BC mixing ratio. A similar algorithm using different dry deposition velocities from Uno et al. 2004 is used for dust and OC in snow calculation. The method is summarized below:

First, the total mass of BC due to dry and wet deposition during previous time steps (time step is 6hr) is calculated. Total mass of dry BC deposited is the sum of BC addition to snow (flux) over time (Δt). Equation 1 (adapted from equation 2 of Jacobsen 2004) is used for calculating mixing ratio of BC in snow due to dry deposition.

$$r_{d,BC,t} = \frac{r_{d,BC,t-h} + \frac{hF_{d,BC,t}}{D'_{s,t}}}{1 + \frac{hS_{f,BC}}{D'_{s,t}}} \quad \text{Equation 5-3}$$

In the above equation t denotes the time, h is the time step for calculation, $r_{d,BC,t}$ is the time dependent mixing ratio of BC due dry depositions. $S_{f,BC}$ is the diffusion speed (m/s) of the BC from the top of the snow layer to the bottom of it. Also $F_{d,BC,t}$ and $F_{p,BC,t}$ is the time dependent dry and wet deposition flux of BC respectively.

The fall speed of BC through snow is calculated as the ratio between snow depth and BC life time. For our calculations we set the fall speed of BC to 10^{-7} m/s. Jacobson, 2004 reports there are high uncertainties in estimating BC fall speed but due to its small value it is unlikely to cause high uncertainties in our calculations.

$D'_{s,t}$ is the modified snow layer thickness for our calculation(m). Actual snow depth (D_s , m) is related to the precipitation amount and melting of snow and is one of the WRF output variables (SNOWH in WRF files). The modified snow layer is assumed to be less than 0.1 m. ($D'_{s,max} = 0.1m$). Sunlight penetrates through the top ~10 cm of snow depending on snow density, grain size, zenith angle and light absorbing content of snow. Snow is a highly scattering medium and only 1% of sunlight absorbs by the snow layer can penetrate through 10 cm depth. For removing the very high or ∞ mixing ratio causing by division over very small values we only calculate $r_{d,BC,t}$ where snow depth is higher than 1mm. ($D'_{s,min} = 0.001m$)

Wet deposited BC is added to snow in the form of the mixing ratio of BC in snowfall by adding a new snow layer to the snow. Mass added to each time step is considered to be the flux of wet deposition x time step ($h \times F_{p,BC,t}$) and the time dependent mixing ratio of BC in snow is calculated with equation 2. This equation is adapted from equation 1 of Jakobsen et al. 2004 and equations 1 and 4 Doherty et al. 2014.

$$r_{w,BC,t} = r_{w,BC,t-h} \times (1 - \gamma_t) + \frac{h \times F_{p,BC,t}}{D'_{s,t}} \quad \text{Equation 5-4}$$

γ_t is the ratio of new snow depth added in each time step from precipitation over the current snow layer depth. ($D'_{s,t}$).

$$\gamma_t = \frac{D_{snowfall}}{D'_{s,t}} = \frac{h \times P_{s,t}}{D'_{s,t}} \quad \text{Equation 5-5}$$

In the above equation $P_{s,t}$ is the snowfall rate and *Dsnowfall* is the added snow layer from new snow fall. Please note that in the real world wet deposition only happens at time steps where there is a precipitation (added snow layer). However, the STEM model calculated both dry and wet deposition over each time step. In cases where the added snow layer is bigger than the current snow depth, the term $(1 - \gamma_t)$ becomes negative. In these cases, we simply substitute zero instead of $(1 - \gamma_t)$ for removing negative wet deposited BC in snow concentration. The total BC content in snow is the sum of dry and wet deposited mixing ratios:

$$r_{T,BC,t} = r_{w,BC,t} + r_{d,BC,t} \quad \text{Equation 5-6}$$

Mixing ratios of Dust (fine and coarse) and OC in top surface layer of snow is calculated with the similar method.

For calculating of snow albedo reduction due to BC deposition over the Arctic a method adapted from Flanner et al., 2007, Wiscombe and Warren, 1985 and Jacobson

2004 is used. The equation below using total BC in snow mixing ratio $r_{T,BC,t}$ is used to calculate the estimated albedo reduction percentage.

$$\Delta\alpha = 2 \times 10^{10} \left(r_{T,BC,t} \right)^2 - 7.3358 \times 10^4 \times r_{T,BC,t} - 0.0021 \quad \text{Equation 5-7}$$

The above equation is a second-order polynomial fit for figure 2 of Waren and Wiscombe, 1985 with $R^2=0.99$.

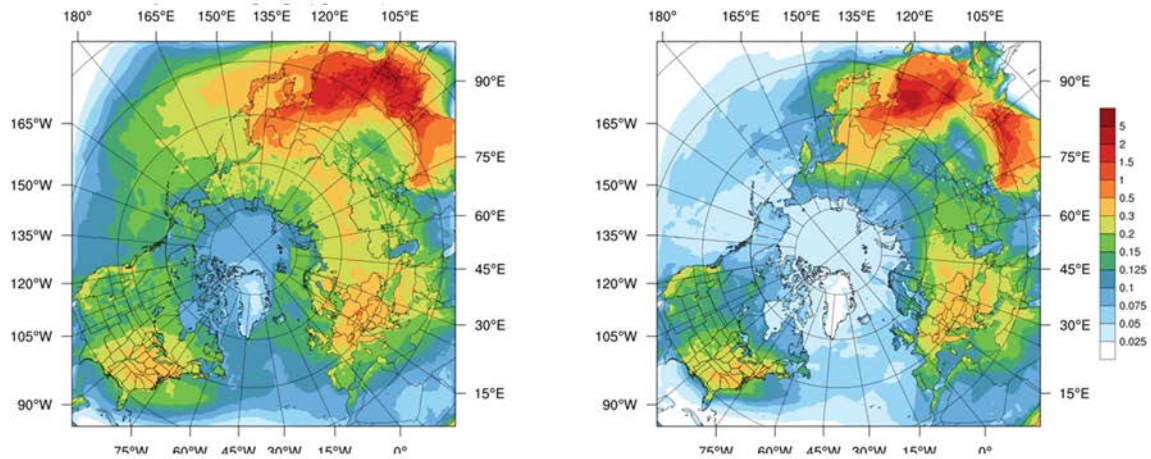
Results and Discussions

BC and Dust Deposition in the Arctic

Figure 5-1 shows the spatial distribution of total BC deposition flux for different seasons: winter (DJF), spring (MAM), summer (JJA), fall (SON) over our modeling domain. Wang et al. 2011 studied deposition over the Western Arctic during spring 2008 and found that the average BC dry deposition flux was $45 \mu\text{g}/\text{m}^2\cdot\text{month}$. (Wang et al., 2011) Spackman et al. 2010 estimated the BC dry deposition flux of $\sim 3\text{-}160 \mu\text{g}/\text{m}^2\cdot\text{month}$ for April 2008 during NOAA ARCPAC field experiment. This is consistent with our estimate of $25\text{-}120 \mu\text{g}/\text{m}^2\cdot\text{month}$ for dry deposition over Western Arctic and Alaska. (Figure 5-1) The maximum of BC deposition flux occurred over the Siberian Arctic and European Arctic with values as high as $0.5 \text{ mg}/\text{m}^2\cdot\text{month}$. The model results show relatively small total deposition of $\sim 0.05 \text{ mg}/\text{m}^2\cdot\text{month}$ for the Arctic sea ice. Jiao et al. 2014 summarized the results of 25 different modeling studies and reported the average BC deposition flux over the Arctic (latitude 60°N and above) is between $0.25\text{-}1.6 \text{ mg}/\text{m}^2\cdot\text{month}$ with high inter-model variability. (Jiao et al., 2014) However, the majority of models used in Jiao et al. 2014 study estimated the highest BC deposition flux

occurring during summer time with values less than $\sim 1\text{mg/m}^2\cdot\text{month}$. The large variations between different modeled fluxes can be attributed to different emission, transport scheme and deposition processes in the different models.

BC Deposition Flux_MAM_(mg/m².month) BC Deposition Flux_JJA_(mg/m².month)



BC Deposition Flux_SON_(mg/m².month) BC Deposition Flux_DJF_(mg/m².month)

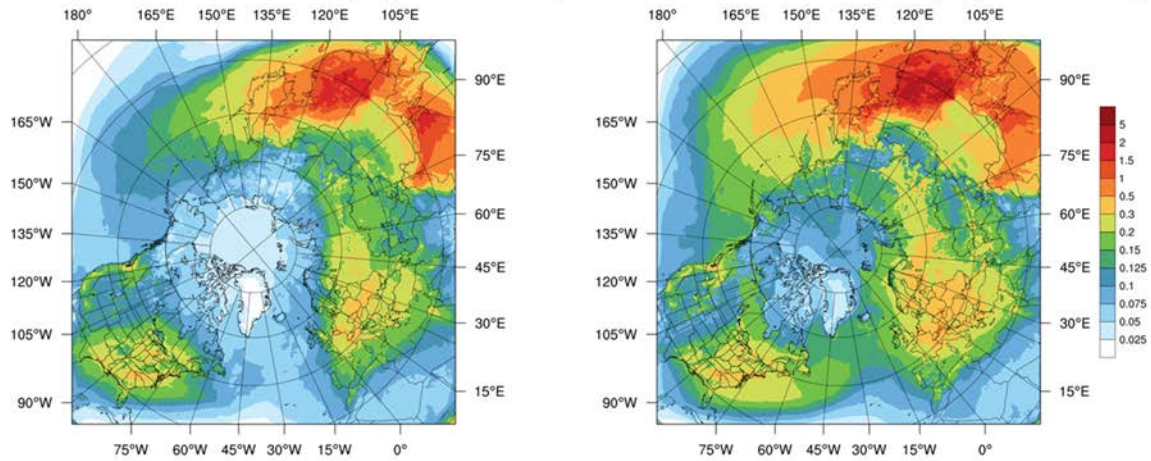
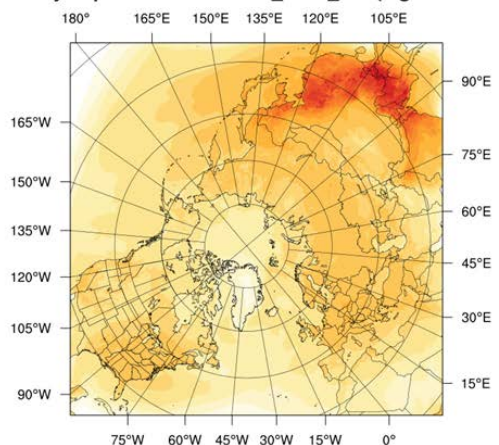


Figure 5-1: Seasonal spatial plot of total BC deposition flux for MAM(March, April and May) , JJA(June, July and August) , SON(September, October, and November), and DJF(December, January and February).

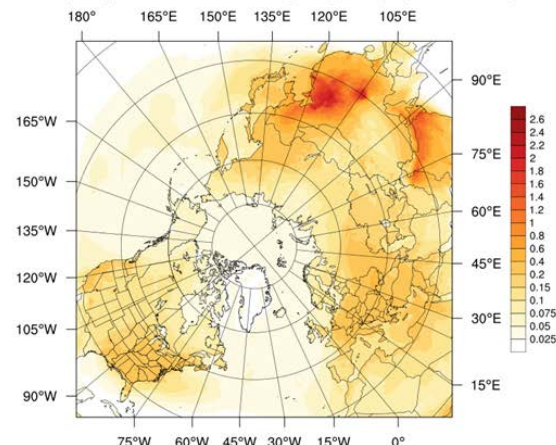
Wet and dry deposition fluxes of BC were investigated separately for different months to study the seasonality. The seasonal variations of BC deposition flux show maximum values during spring over the Russian Arctic and Siberia due to the increased BC emissions from natural emissions (forest fires.) However, during winter time there is higher contributions from Asian and European anthropogenic emissions.

Higher BC dry deposition occurs in springtime and wintertime. (Displayed in Figure 5-2) The wet deposition reaches its maximum during spring and summer due to higher precipitation in these seasons. BC seasonal wet deposition flux is displayed in Figure 5-3. Major hotspots of dry deposition are over China and Southern Asia since there is higher BC concentrations over these regions. Wet deposition is high in Northern India and Southeastern Asia due to higher precipitation during monsoon months.

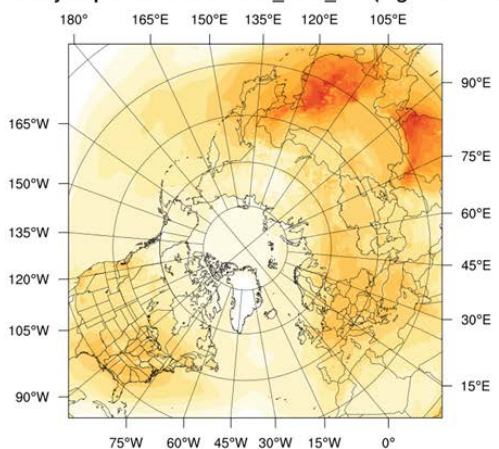
BC Dry Deposition Flux BCDD_MAM_ave (mg/m2.mont



BC Dry Deposition Flux BCDD_JJA_ave (mg/m2.month)



BC Dry Deposition Flux BCDD_SON_ave (mg/m2.mont



BC Dry Deposition Flux BCDD_DJF_ave (mg/m2.month)

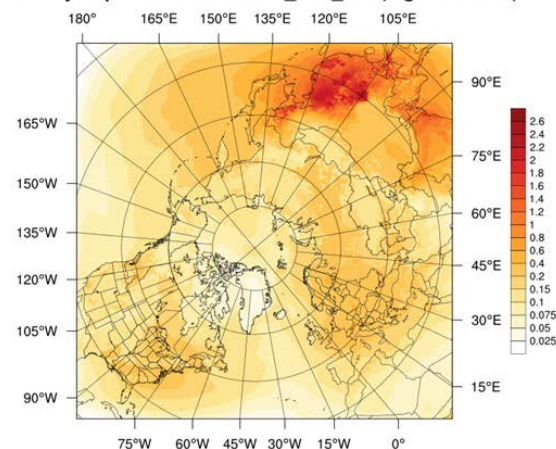


Figure 5-2: Seasonal spatial plot of total BC dry deposition flux for MAM(March, April, and May) , JJA(June, July, and August) , SON(September, October, and November), and DJF(December, January, and February).

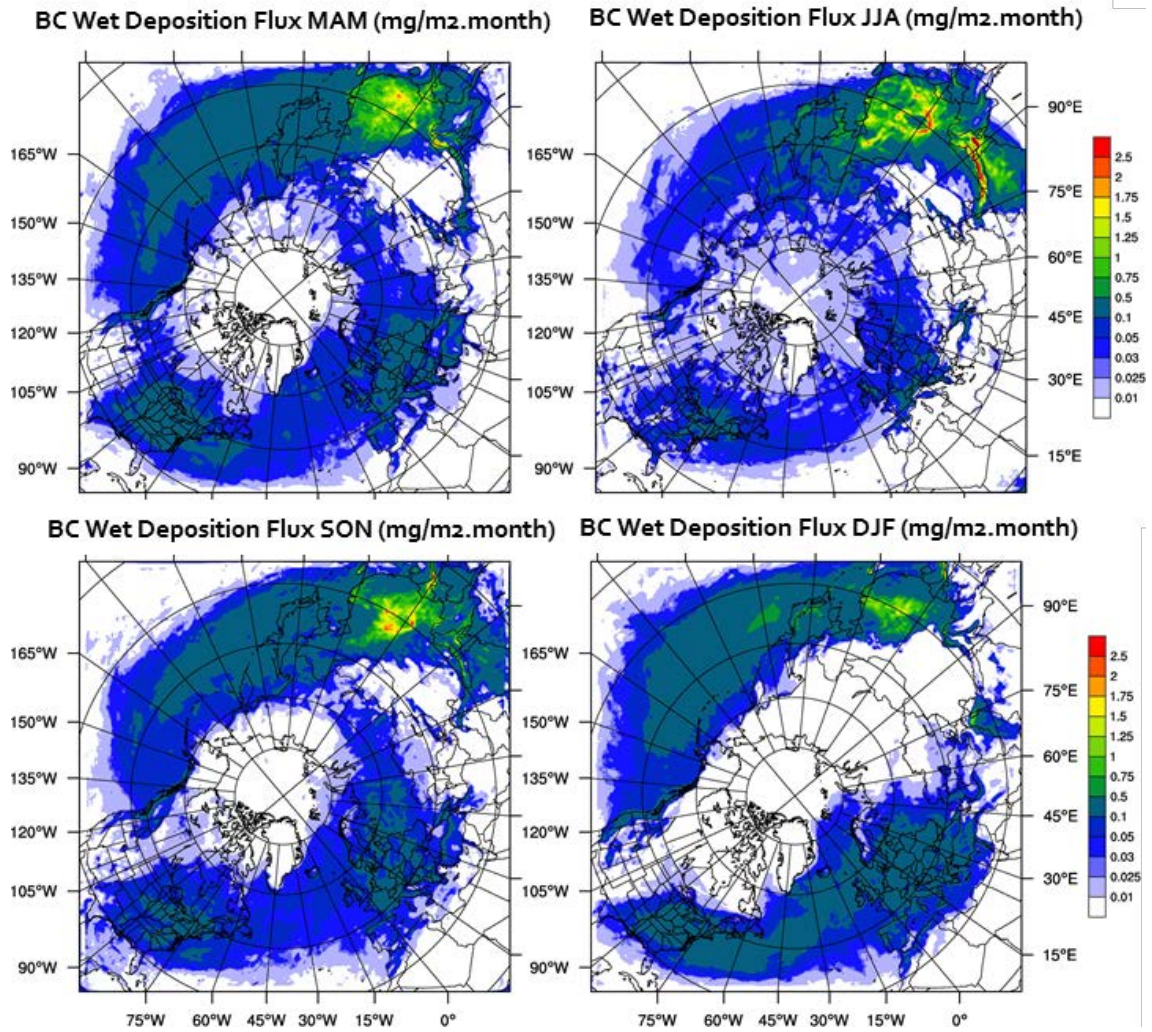


Figure 5-3: Seasonal spatial plot of total BC wet deposition flux for MAM (March, April, and May) , JJA (June, July, and August) , SON (September, October, and November), and DJF (December, January, and February).

Dust and OC also deposit on the snow and increase the absorption of solar radiation. Dry and wet deposition is calculated for both fine and coarse dust with a method similar to above. Figure 5-4 shows the spatial distribution of simulated dust flux deposition for different seasons. Dust deposition flux peaks at spring in the Arctic with an average of $\sim 35 \text{ mg/m}^2 \cdot \text{month}$. Dust deposition flux shows higher values over Siberia and

Eurasian Arctic and minimum values of less than 5mg/m².month occurring over Greenland and Svalbard. Figure 5-4 shows high values of both fine and coarse dust deposition flux over Tibetan Plateau and Tien Shen.

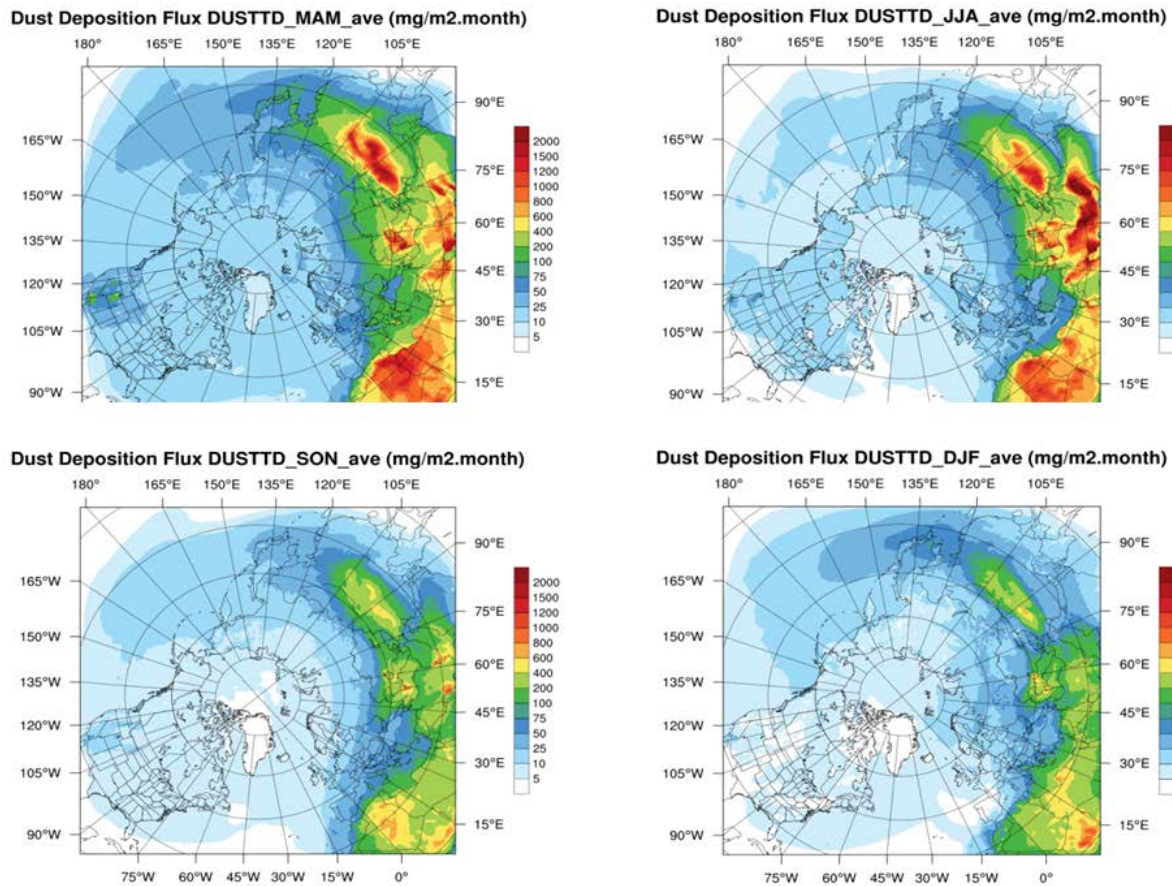


Figure 5-4: Seasonal spatial plot of total dust (fine+ coarse dust) deposition for MAM(March, April and May) , JJA(June, July and August) , SON(September, October, and November), and DJF(December, January and February).

BC and Dust in Snow Concentration

BC and dust particles accumulate on snow by precipitation and dry deposition. (Bond and Sun, 2005) The parameters that influence BC concentration in snow are snow melting, vapor deposition and size of the liquid or ice droplets falling to surface. (Wang et al., 2011) Dry deposition on snow is related to resistance to molecular diffusion and the settling speed of particles. (Wang et al., 2011) Figure 5-5 shows the monthly average results of simulated BC content of snow. The results are compared with Doherty et al., 2014. This study reports snow BC content for a network of observation in the Arctic Ocean, Canadian Arctic, Greenland, Russia and Svalbard and Norway for spring and summer of 2007 -2009. The observations show lower values compared to previous observational studies such as Clarke and Noone, 1985; which indicates the lower levels of atmospheric BC concentration compared to previous decades.

BC concentration in snow (ng/g)

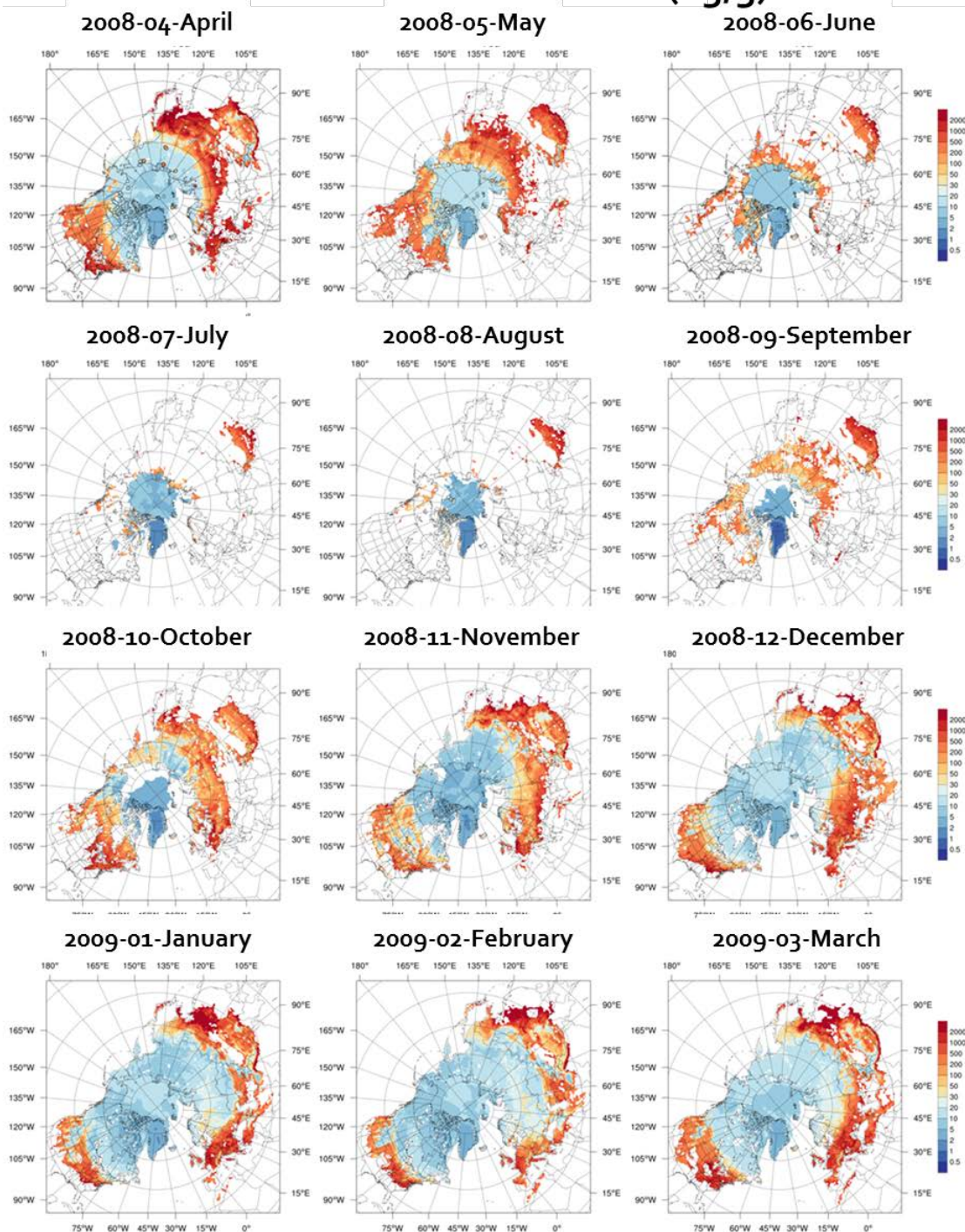


Figure 5-5: Spatial distribution of BC concentration of top layer snow (ng/g) for different months.

Figure 5-6 a and b shows the simulated BC in snow mixing ratio in April 2008 and May 2008 compared with results from observation data from of Doherty et al. 2010. Each point shows the station of sampling. Please note that the observational data are daily values while the model data used for this plots are monthly average.

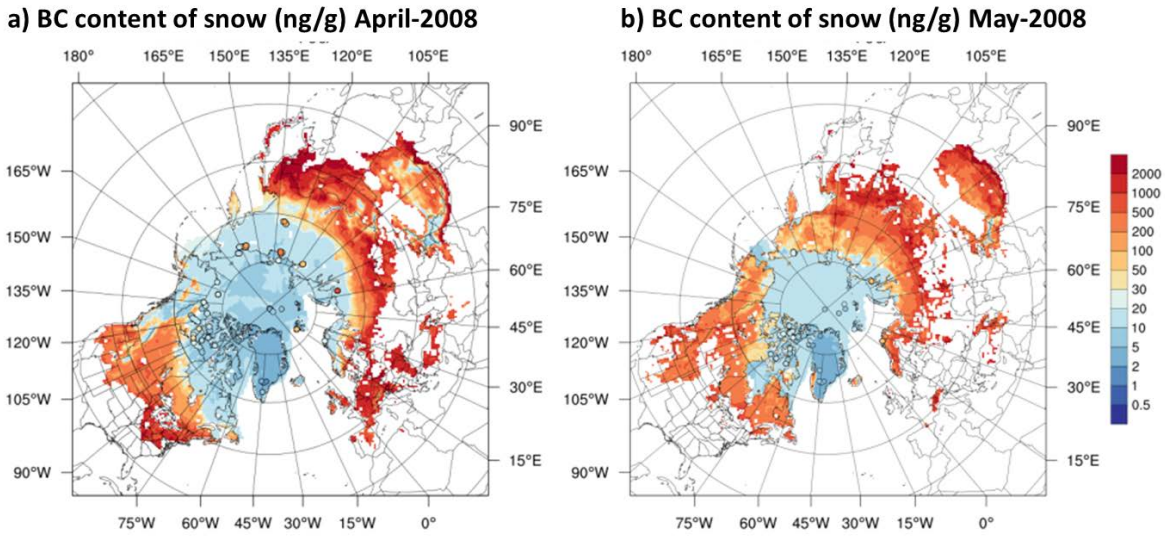


Figure 5-6: Spatial distribution of BC content of top layer snow in ng/g for a) April 2008 and b) May-2008. The circles on the plots demonstrate the observation value from Doherty et al. 2010.

Based on Figure 5-6 the model captures the observational values very well over the Arctic Ocean, Greenland, Northern Norway and Canadian Arctic and subarctic. The slight different can be attributed to the monthly averaged data and simplifications of the model. However over Eurasian Arctic, Siberia and Northwestern Russia the model tends to under-estimate the BC mixing ratio in snow. As discussed in previous objectives there are higher numbers of forest fires incidents during spring time. Also 2008 is one of the highest rates of forest fires. (Wang et al., 2011) One source of our under-estimation over

Russian Arctic can be because of the under-estimation of biomass burning emission. Most of the observations in Doherty et al. 2010 are remote areas in the Arctic far away from any regional emissions. In Figure 5-6 the location points show much higher values are in urban areas (Northern Russia) Therefore another underestimation of model at some of these observation sites can be due to contribution of local urban pollution over the Arctic (roads, industrial complexes in cities, and snowmobile). Snow pack density is assumed constant of 350 kg/m^3 in our model calculations following Meinander et al., 2013 and Kuusisto,1984. Table 5-1 summarizing different snowpack density based on Paterson, 1994 study.

Table 5-1: Summary of snow and ice density adapted from Paterson 1994

Typical densities of snow and ice (kg/m^3)	
New snow (immediately after falling in calm)	50-70
Damp new snow	100-200
Settled snow	200-300
Depth hoar	100-300
Wind packed snow	350-400
Firn	400-830
Very wet snow and firn	700-800
Glacier ice	830-917

Snowpack density has very high effect on the BC in snow calculations. For example, for a very fresh snow the density is 100kg/m^3 and for very wet snow, firn and glacier ice it can be up to 917 kg/m^3 . (Warren, 2013) Snow grain size is assumed to be constant. However, studies show that snow grain size changes when BC mixing ratio

increases. Snow aging and grain size change are two other important factors which we did not include in our calculations.

Figure 5-7 shows the spatial distribution of dust mass concentration in the top layer of snow over our modeling domain for April and May 2008. The average mixing ratio of dust in snow over the snow-covered Arctic (area over 60°N) is ~3 mg/g for April 2008 and ~5 mg/g for May 2008. Also, there are extremely high snow dust mixing ratio over Himalayas, Central Asia, and Turkey. (higher than 1500 mg/g) As displayed in Figure 5-7 shows, dust concentration in snow is higher closer to the arid and semi-arid region where the emission of dust is highest.

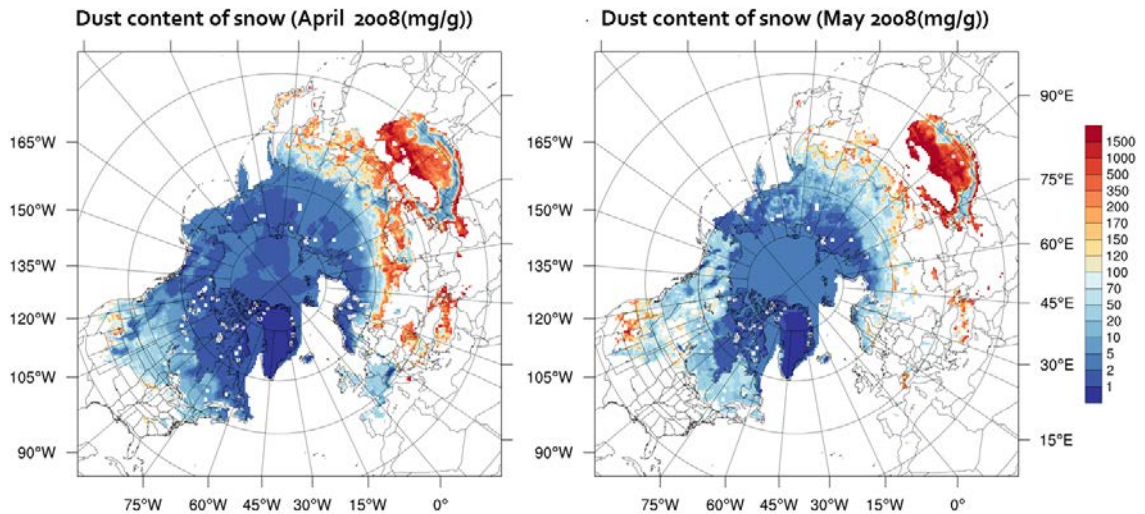


Figure 5-7: Spatial distribution of Dust content of top layer snow in ng/g for a) April 2008 and b) May-2008.

Source Attribution of Arctic snow BC and Dust

For making effective emission reduction policies to slow the Arctic sea ice loss, it is necessary to identify the source sectors and source regions contribution to the Arctic ice light absorbing impurities. There are few BC emission sources within the Arctic itself, therefore the BC present in Arctic snow must be transported from other regions to the Arctic. (Bond et al., 2013) Also, there is a significant seasonality in dust emission depending on snow cover, soil moisture, erosion, wind speed, vegetation type, and land use. The impacts of each source sector (i.e. industry, transportation, residential, biomass burning and power) and geographical source region on the Arctic snow BC concentration were estimated using sensitivity analysis. For dust emission, the sensitivity analyses are conducted for main regions contributing to the global dust emission, including Central Asia, western China, Arica, and Middle East. Figure 5-8 demonstrates the percentage of regional contributions to total top-layer snow BC concentration in two Arctic sites: Barrow, Alaska (71.3°N, 156.6°W, 0.01 km a.s.l) and Alert, Canada (82.3°N, 62.3°W, and 0.21 km a.s.l).

Figure 5-8 shows that for both sites, during the winter the % contributions from Europe increases. During the cold season, the Arctic front over the Arctic make it difficult for pollutions from lower latitude to enter the Arctic troposphere. This arctic front usually goes to lower latitudes over the Europe and Eurasia compared to the Canadian subarctic side. The emissions originated from the dryer and colder regions can typically follow the surfaces of constant temperature to enter the Arctic troposphere. However, the emissions from the warmer and moister regions such as from North

America and China are lifted and transported to the higher Arctic troposphere. Therefore, while BC emission from China has the highest contribution to the column BC in the Arctic, the lower plume of BC which has higher chance of depositing in the snow originates from Europe. (AMAP, 2011; Bond et al., 2013)

During the spring and summer, the contributions of biomass burning from Siberia to the BC in snow are maximized for both sites. (up to ~35% during May 2008) This is mainly caused by broad forest fires and extensive agricultural burning in Russia. Besides, the lower arctic front over Russia reduces the vertical mixing of this emission and facilitates the transport to higher latitudes and deposition on snow.

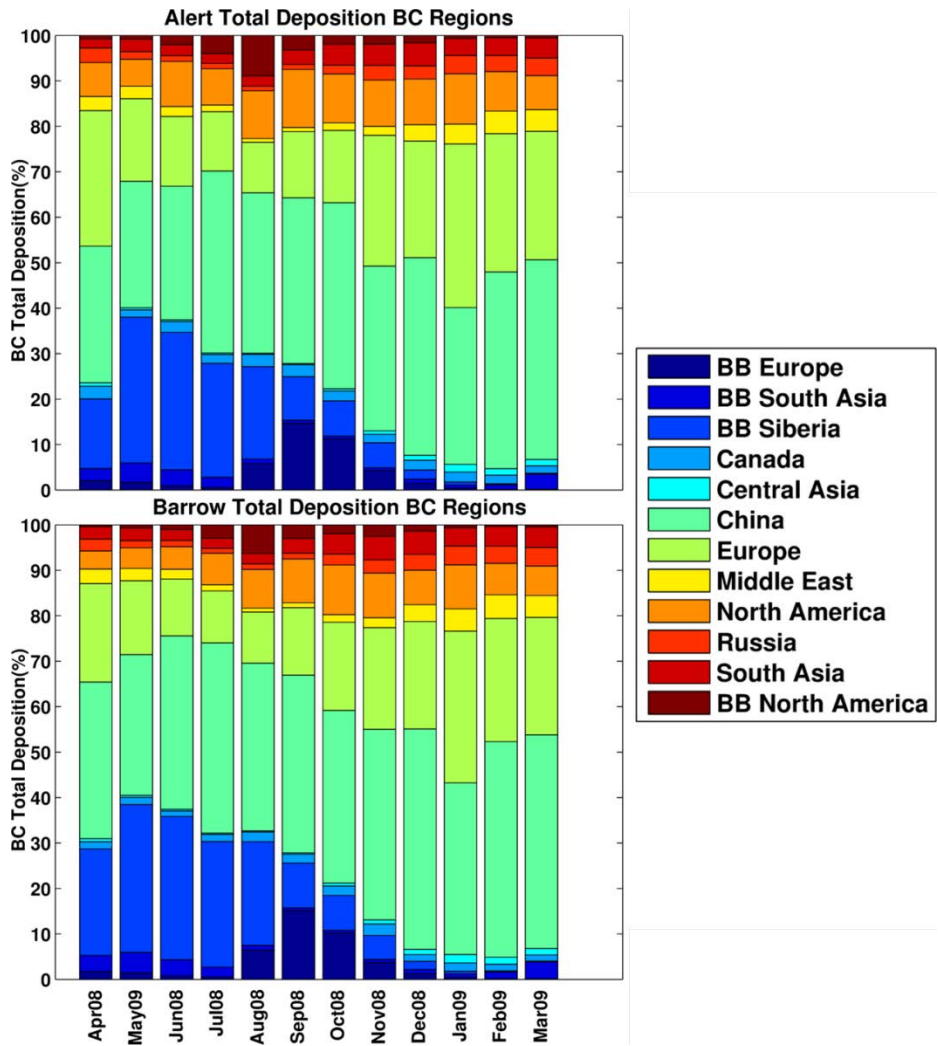


Figure 5-8: Seasonal variations of various sectors contributions to Alert and Barrow BC deposition.

Figure 5-9 shows the sector contribution (%) of various economic sectors to BC deposition and BC concentration in the surface snow layer for Alert and Barrow. During the summer months, the contributions of Biomass Burning from North America and Europe increases which subsequently has significant effects on snow BC in the Arctic.

During the colder months, the highly stable arctic dome prevents emissions from lower latitudes to be transported to the Arctic lower troposphere.

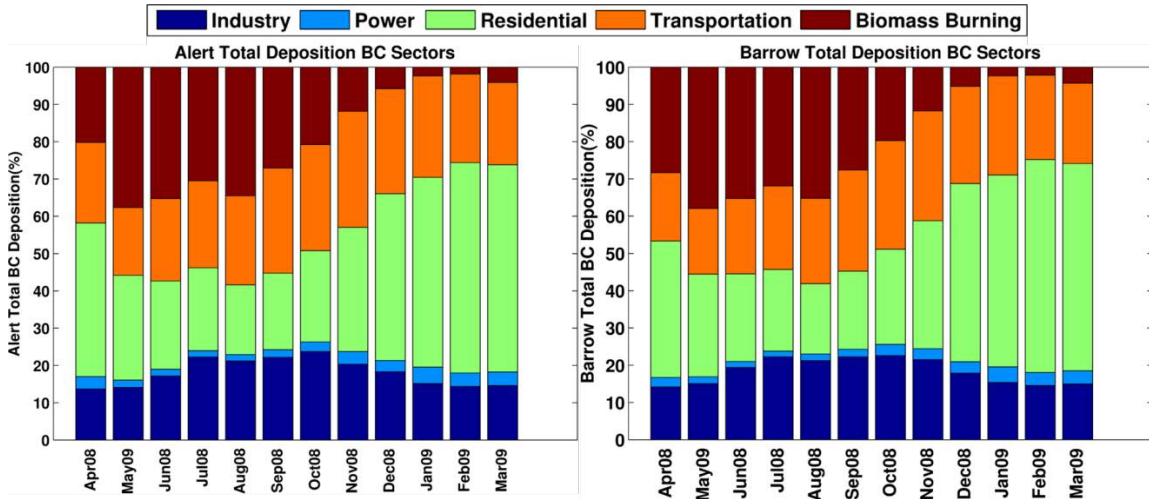


Figure 5-9: Seasonal Variation of contributions of various sectors to Alert and Barrow BC deposition.

Figure 5-9 shows the sector contributions of emissions from various economic sectors to BC deposition (snow BC mixing ratio) at Barrow and Alert sites. This figure shows the significance of biomass burning to the Arctic snow BC during spring and summer. Also, the seasonal cycle of Residential (%) of BC is displayed in Figure 5-9.

Figure 5-10 shows the seasonal variability of region contributions to the dust deposition on snow (dust mixing ratio) in the Arctic. In general, there are higher dust emissions (and concentrations) in summer over lower latitudes and during spring over Central Asia and Himalayas.

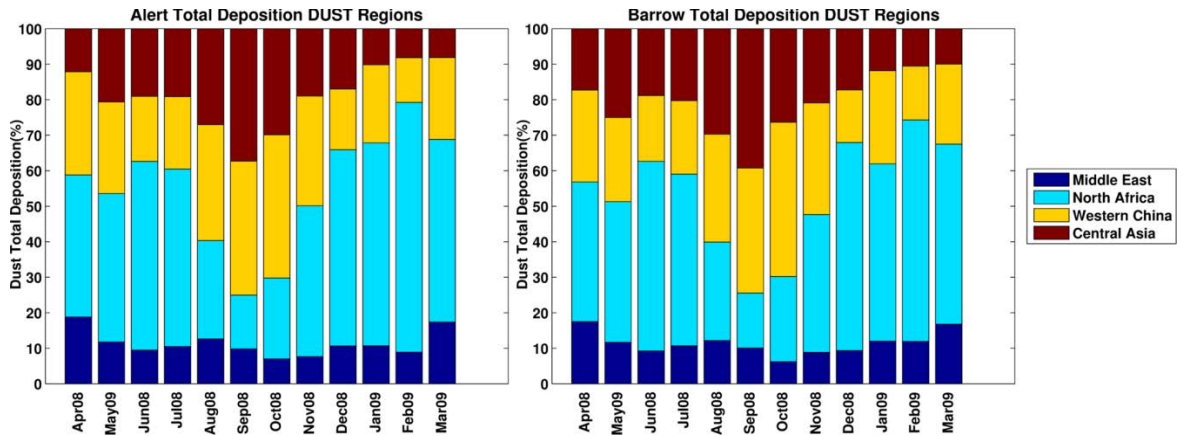


Figure 5-10: Seasonal Variation of contributions of various sectors to Alert and Barrow dust deposition.

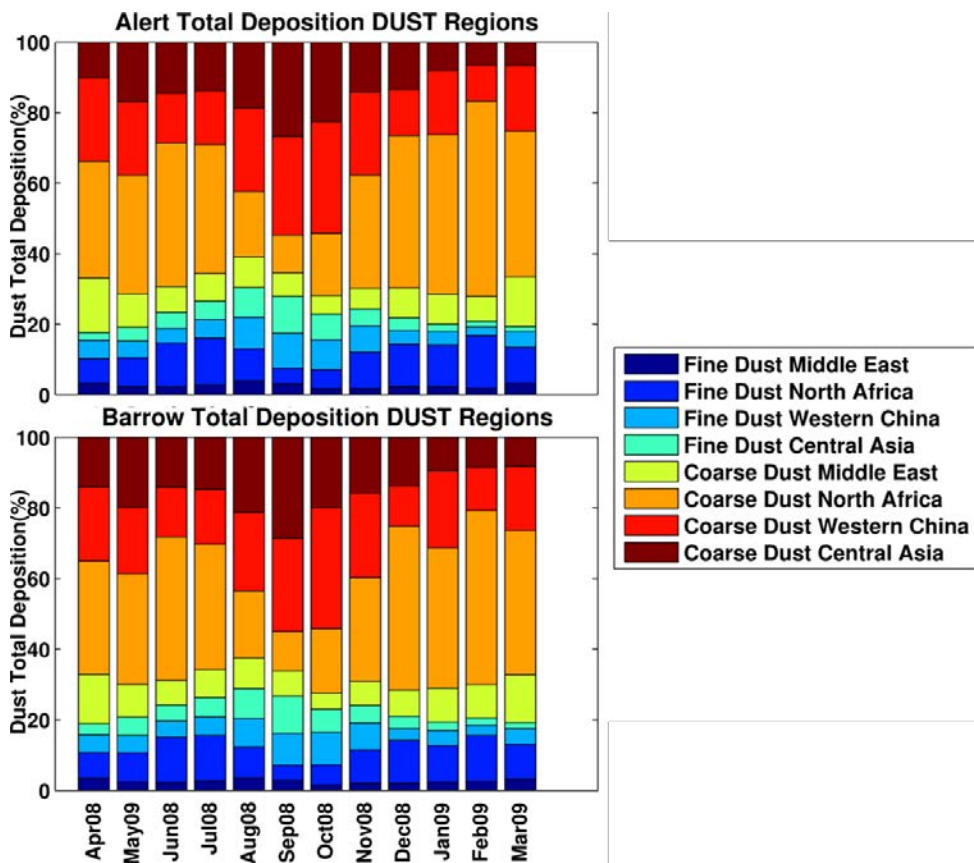


Figure 5-11: Seasonal Variation of contributions of various sectors to Alert and Barrow dust deposition for both fine and coarse dust particles.

Snow Albedo Reduction

Figure 5-12 displays simulated snow albedo reduction (%) caused by BC in snow for April 2008. In these calculations, the grain radius is assumed to be constant of 1mm. (McConnel 2007) These results show an average of 0.5 % albedo decrease over the Arctic with the minimum of less than 0.1% albedo reduction over the Greenland and maximum albedo reduction occurring over Russia (up to ~7% reduction). These results are in the range of previous studies of Wang et al. 2008 and lower than previous estimations of Flanner et al. 2007 and Koch et al. 2009a

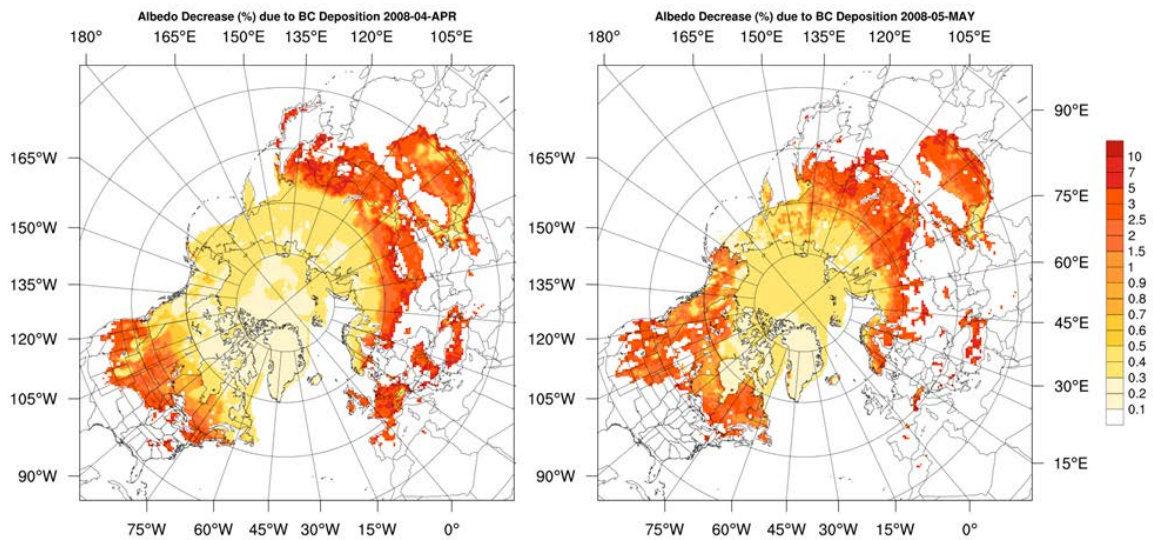


Figure 5-12: Modeled snow albedo decrease (%) due to BC deposition for April and May 2008.

For making effective emission mitigation policies to minimize impacts of BC on snow albedo, it is essential to quantify the impacts of emissions from each source sector and geographical region on snow albedo. Figure 5-13 shows the contributions of each

economical sector to snow albedo change during April 2008. Based on Figure 5-13, biomass burning causes between ~50% of albedo change caused in Russia during April 2008. Over Southern Russia, Tien Shen mountains, Central Asia, and Mongolia, emissions from biomass burning accounts for more than 80% of snow albedo perturbation during April 2008. Over Canadian subarctic and Greenland emissions from residential and transportation sectors are the dominant contributors (~35% and 20% respectively) to snow albedo perturbation during April 2008. Emissions from residential sector contribute to more than 50% of albedo perturbation over Himalayan glaciers. However, emissions from southeastern Asian forest fires also influence the snow albedo over southern Himalayas. Emissions from transportation, industrial, and residential sectors have significant impacts on Rocky Mountains snow albedo change during April 2008 with contributions of ~30%, 25% and 20% respectively. This sector-based analysis can provides us with valuable information to make policies to target source sectors with large impacts.

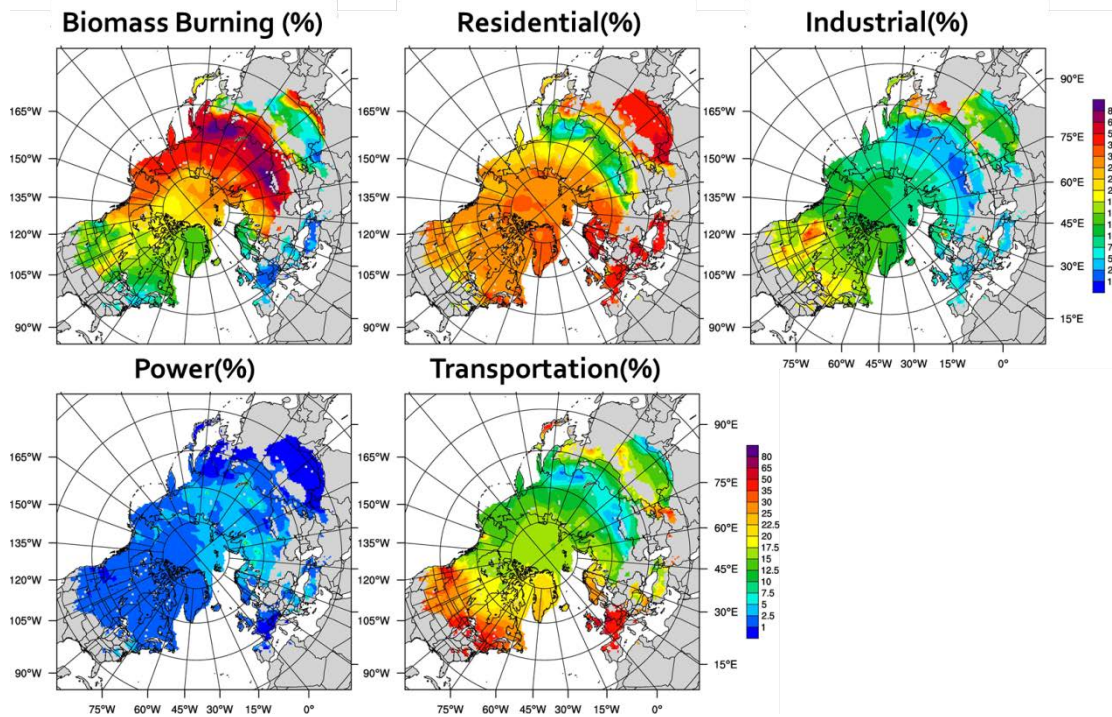


Figure 5-13: Source sector contribution (%) to BC albedo perturbation for April 2008.

Conclusions and Future Work

In this study, we used WRF-STEM to simulate BC and dust deposition fluxes, and concentration in top-layer snow and ice. BC and dust transports from different regions to the Arctic and eventually deposits on the Arctic snow and ice. Deposited BC and dust particles on snow and ice increases the absorption of solar radiation and accelerate the snow and ice melting. This chapter is focused on identifying the effects of BC on the snow and ice albedo and quantifying the contributions of each source sector and source region to BC and dust concentration in snow. Sensitivity analyses were performed to identify source sectors and source regions of snow BC and dust in the Arctic. Furthermore, the modeling results were validated with the BC measurement from observations networks from Doherty et al. 2010 study. The results show strong

seasonality in the contributions of regions and sectors to BC mixing ratio in the Arctic. Anthropogenic emissions contribute to up to ~95% of snow BC mixing ratio during the winter. However, biomass burning contributes to up to ~40% of snow BC mixing ratio during spring 2008. We should keep in mind that spring 2008 had unusually high number of forest fires especially over Siberia and eastern Russia. This study shows that BC deposition causes ~0.5-0.6% snow albedo decrease during spring 2008. The future work includes more sensitivity analysis to quantify the impacts of albedo change caused by BC and dust deposition on temperature, precipitation, soil moisture, snowpack, and runoff. The results of this chapter suggest that there is a strong need for more observational data of mixing ratios of BC and dust for both Arctic and lower latitudes glaciers. More observational measurements of snow LAP impurities in the Arctic region with more focus on snow aging and in-snow processes will help minimize the uncertainties for calculating the albedo change caused by BC deposition.

CHAPTER 6: PERFORMANCE ANALYSIS, PROFILING AND OPTIMIZATION OF WEATHER RESEARCH FORECASTING (WRF) AND WRF-CHEM MODELS

Abstract

The Weather Research and Forecasting (WRF) model is an open source mesoscale numerical weather prediction (NWP) system extensively used in atmospheric research, operational forecasting and educational settings. For profiling and identifying the bottlenecks of WRF code, we used Alinea MAP, TAU (Tuning and Analysis Utilities) and Intel Vtune Amplifier XE. The results show that advection is the most time-consuming routine in the ARW (Advanced Research WRF) dynamic solver. For further investigating the hotspots, the advection code is extracted from the WRF Fortran code as a separate kernel. WRF model uses the Runge-Kutta (RK) 3rd order for integrating the time, and 2nd through 6th order advection schemes in both horizontal and vertical directions. This basic RK scheme produces negative values and oscillations near sharp gradients due to the numerical dispersion errors. Positive definite and monotonic flux limiter schemes are used for reducing the negative values and spurious oscillations from the dispersion errors.

We designed a testing framework for optimizing, compiling, profiling, and evaluating the kernel with different FORTRAN compilers including Intel, GNU, and PGI compilers. Several optimization techniques including exposing more vectorization and improving the cache hit rates are utilized on the advection modules and the outputs are

verified. Reasonable speed-up (up to 4x) can be achieved on different compilers using the modified advection kernel.

Introduction

The Weather Research and Forecasting (WRF) model is an open source mesoscale Numerical Weather Prediction (NWP) model extensively used in atmospheric research, operational forecasting and educational settings.(Skamarock et al., 2008) WRF model has many applications in simulating various earth system phenomena with various scales from meters to thousands of kilometers, including: applications in air quality modeling, hurricanes forecasting, hydrological simulations, and regional climate modeling.(Powers et al., 2017; Skamarock et al., 2008; Wang et al., 2017) WRF model includes two dynamical cores (or solvers), a data assimilation system, and a software architecture facilitating parallel computing. (Wang et al., 2017) The WRF model is widely used code in the weather, climate and High Performance Computing (HPC) communities with more than 36,000 users from over 160 countries.(Elliott and Del Vento, 2015; Powers et al., 2017) WRF-Chem model is an online chemical transport model(CTM) which simultaneously simulate the transport, physical and chemical processes of chemicals and particles in the atmosphere. (Grell et al., 2005) In both scientific and operational communities, there is a significant ever-increasing need to have longer and larger simulations with higher resolutions and more sophisticated physical and chemical representation of the atmosphere.(Grell et al., 2005) Since WRF and WRF-Chem are computationally expensive and with such a large user base, performance optimization of the model is of high priority for the code developers.

As high performance computing is moving towards exascale era, it is essential to prepare legacy codes to enable them to take advantage of modern supercomputing architectures. (Elliott and Del Vento, 2015) WRF can be used with distributed, shared memory, and hybrid parallel architectures. However, the modern heterogeneous architecture is only used for WSM5 and Goddard microphysics schemes. (Mielikainen et al., 2014) It is also essential to study the performance of WRF on current systems to optimize our simulations using our current HPC resources. In this study, first we analyzed the performance of different components of WRF model to identify the hotspots of the code. The so-called hotspots are sections of the code which contributes the most to the application runtime. (Supalov et al., 2014) After identifying the model hotspots, the code is optimized to improve the model performance. The four primary milestones of this research are: (1) performance analysis and profiling of WRF in order to identify major performance hotspots; (2) modifying and optimizing the identified hotspots to improve the performance; (3) validating the numerical accuracy and results of the modified kernel; (4) integrating these changes back into the WRF repository and future WRF releases.

The WRF Description

The WRF software framework provides a highly modular, single source infrastructure for consistent implementation of WRF dynamic solvers, various physics packages, and WRF-Chem. (Wang et al., 2017) Figure 6-1 shows the modeling system flowchart for WRF model. The WRF model contains two different dynamic cores; the Advanced Research WRF (ARW) solver (previously known as the Eulerian mass solver) developed by NCAR, and the Non-Hydrostatic Mesoscale Model Solver (NMM)

developed by National Center for Environmental Prediction (NCEP). The ARW dynamical core solves the fully compressible non-hydrostatic equations with the hydrostatic option using a terrain following, dry hydrostatic pressure vertical coordinate and Arakawa C-grid staggering in horizontal direction. (Skamarock et al., 2008) WRF time integration uses a 2nd or 3rd order Runge-Kutta scheme with a smaller acoustic and gravity mode time steps. The ARW core use 2nd to 6th order advection options for both horizontal and vertical directions. Figure 6-2 summarizes the time-split RK3 integration technique. In this chapter, we only discuss the ARW solvers. WRF is written mostly in FORTRAN and can be compiled with various compilers. (Powers et al., 2017)

WRF Modeling System Flow Chart

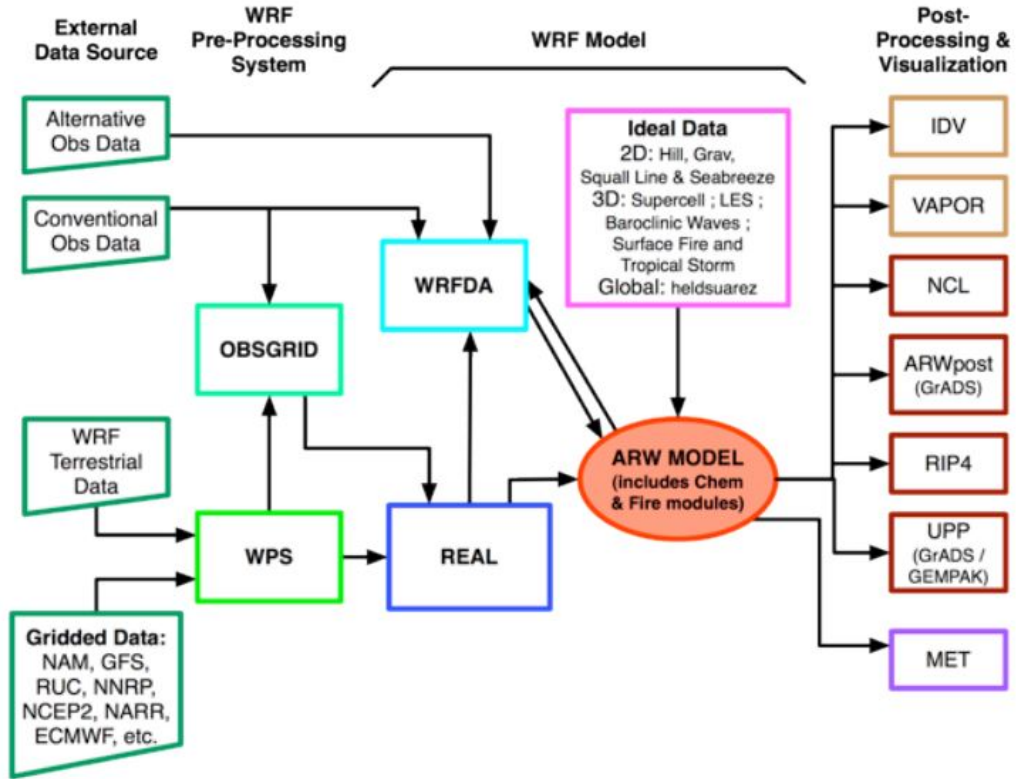
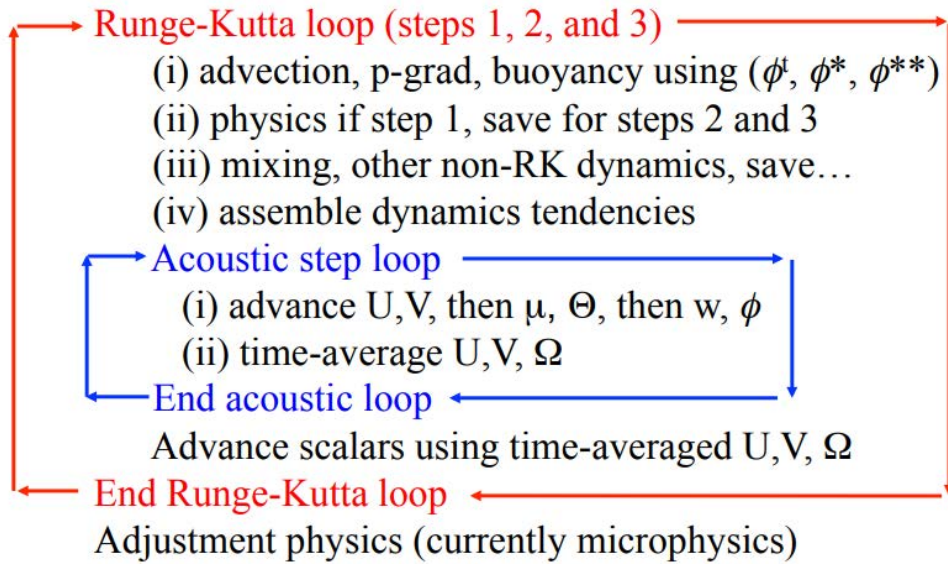


Figure 6-1: WRF system components. (Figure from Skamarock et al., 2008)

WRF physics includes various microphysics, cumulus, surface physics, planetary boundary layer physics, and radiation schemes. WRF-Chem is an online (inline) atmospheric chemistry model which has simultaneously solve the conservative transport of chemicals and tracers by metrological model and includes various gas-phase chemical reaction calculations and emission processing.(Fast et al., 2006; Grell et al., 2005)

Begin time step



End time step

Figure 6-2: WRF ARW model integration procedure. (Image source: WRF Tutorial January 2014)

WRF advection simulates the transport of tracers, chemical species, and/or scalars using wind forecast. Scalars are defined as variables with single-value, contrary to vector values. The advection of an atmospheric species (i.e. tracer) in a geophysical fluid can be written using the continuity equation as following:

$$\frac{\partial \rho \phi}{\partial t} + \nabla \cdot \rho V \phi = 0$$

Equation 6-1

Equation 6-1 is the Eulerian form of the advection equation, in which φ is the tracer mixing ratio, ρ is the density of the fluid (air for the atmospheric models) and V is the velocity vector. (Skamarock, 2006)

$$\frac{\partial \mu \varphi}{\partial t} + \frac{\partial \mu u \varphi}{\partial x} + \frac{\partial \mu v \varphi}{\partial y} + \frac{\partial \mu \omega \varphi}{\partial \eta} = \mu S_{\varphi} \quad \text{Equation 6-2}$$

In this equation φ is the tracer mixing ration, μ is the column mass of dry air, η is the vertical coordinates, and S_{φ} the represents the sources and sink terms. (Skamarock, 2006; Skamarock and Weisman, 2009; Wang et al., 2009; Wicker and Skamarock, 2002) This equation can be solved using RK3 scheme in the following three steps:

$$(\mu \varphi)^{t+\Delta t/3} = (\mu \varphi)^t - \frac{\Delta t}{3} \times \left(\sum_i \delta_{xi} F_{xi}^t - \mu S_{\varphi}^t \right) \quad \text{Equations 6-3}$$

$$(\mu \varphi)^{t+\Delta t/2} = (\mu \varphi)^t - \frac{\Delta t}{2} \times \left(\sum_i \delta_{xi} F_{xi}^{t+\Delta t/3} - \mu S_{\varphi}^t \right)$$

$$(\mu \varphi)^{t+\Delta t} = (\mu \varphi)^t - \Delta t \times \left(\sum_i \delta_{xi} F_{xi}^{t+\Delta t/2} - \mu S_{\varphi}^t \right)$$

In the above equations (Equations 6-3), the term $\delta_{xi} F_{xi}$ represents centered flux divergence at time step indicated by superscript and at the i th coordinate direction. (Skamarock and Weisman, 2009; Wang et al., 2009) For example a simplified 1-D direction of this term is:

$$\delta_x F_x = \frac{(F_{x+\Delta x/2} - F_{x-\Delta x/2})}{\Delta x}$$

Equation 6-4

We can write similar set of equations for 5th order RK scheme. The ARW dynamic solver uses 3rd order and 5th order RK scheme for solving the vertical and horizontal fluxes. (Skamarock and Weisman, 2009) Using RK integrations schemes as above equations results in accurate results and is mass-conservative. However it not positive definite or monotonic (shape-persevering), causing undesired negative mixing ratios (undershoots) and overshoots associated with them. (Brasseur and Jacob, 2017) Filtering to remove the negative concentration values will result in addition of mass to the system making it non-conservative.

In WRF, positive definite and monotonic flux renormalization is used to resolve this issue. In general a positive definite scheme does not generate any negative mixing ratio. (Skamarock, 2006) A monotonic is both positive definite and shape preserving meaning it does not generate spurious maxima or minima. (Thuburn, 1996) Both monotonic and positive definite flux limiter are implemented in the last RK time integration step. More details about the positive definite and monotonic flux limiters in WRF can be found in (Skamarock, 2006; Skamarock and Weisman, 2009). Figure 6-3 shows the effects positive definite and monotonic limiters for a simple 1-D top-hat advection.

1D Top-hat transport $Cr = 0.5$, 1 revolution, 200 steps

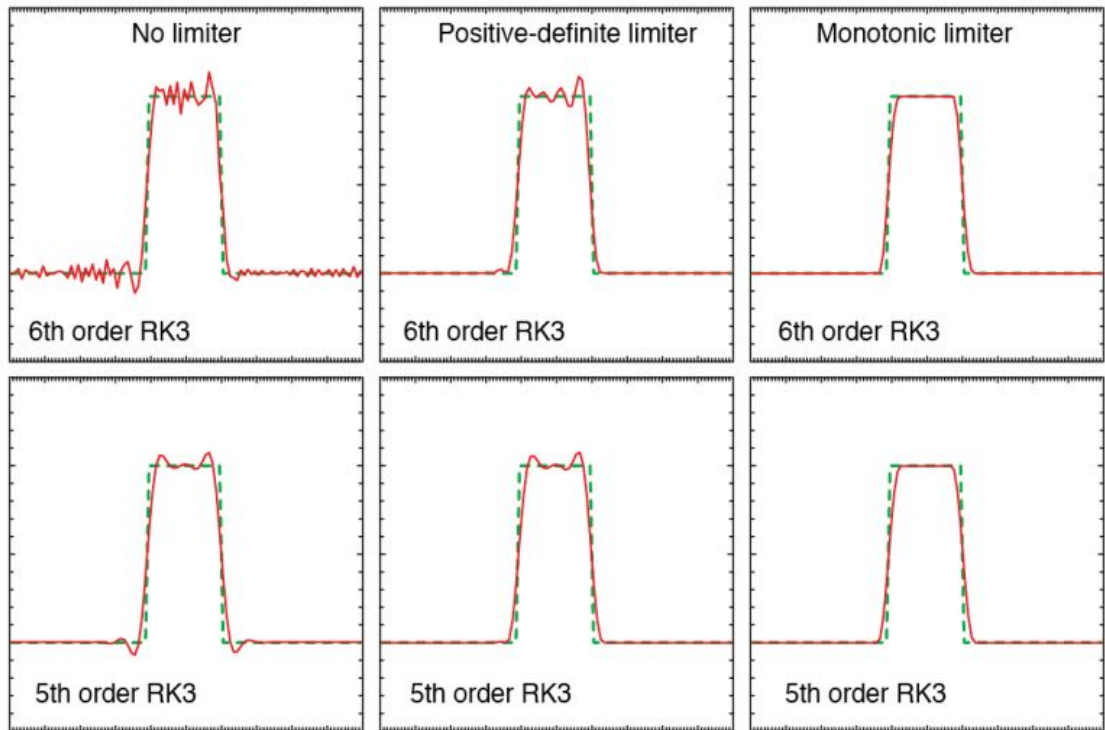


Figure 6-3: Positive definite and monotonic limiters in WRF-ARW for a 1-D advection. (Image source: WRF Tutorial January 2014)

Data and Method

Benchmarking Case

To demonstrate the computational performance and scaling of WRF on various architectures Hurricane Sandy benchmarks (Johnsen et al., 2013) were used. Two cases using a 50x50 coarse resolution (40-km) case and another 500x500 fine resolution (4km) case were used. Both simulations include 54 hour forecasts between 2012 Oct 27 12:00 UTC through 2012 Oct 29 18:00 UTC and has 60 vertical layers. We used 180 sec and 20 sec time step for coarser and finer resolutions respectively. More information on the benchmark cases are available at: <http://box.mmm.ucar.edu/wrf/WG2/bench/>.

Utilized Tools

Several performance analysis and profiling tools were used in this study. These tools provided us with dynamic program analysis including memory usage, calculation speed, function call graphs, load balance, and multithreading information. Below is a summary and overview of some of the tools utilized in this study. Each of these tools has their unique capabilities and limitations.

Intel VTune Amplifier XE

The Intel Vtune Amplifier XE is a commercial performance profiling tool which identifies major hotspots and bottlenecks of the code and provides information such as CPU usage, memory usage, and floating point operations for each section of both serial and parallel code. (<https://software.intel.com/en-us/intel-vtune-amplifier-xe>) The Intel VTune uses the Performance Monitoring Unit (PMU) to extract hardware event counters and collect information regarding the program and display this data in a user-friendly format. Intel Vtune hotspot analysis is used to locate the most time-consuming sections and functions of the code. (Klemm, 2011)

Tuning and Analysis Utilities (TAU)

The Tuning and Analysis Utilities (TAU) is a suite of performance evaluation and tracing tools that is developed for parallel profiling by the Oregon Performance Research Lab. (Shende and Malony, 2006) TAU can use both manual and automatic instrumentations, which add probes to the source code to gather performance information. (Lindlan et al., 2000) Program Database Toolkit (PDT) automatically adds

instrumentations to the source code. TAU also collect hard performance counters via PAPI. For evaluating the computational performance of an application, it is necessary to investigate CPU utilizations and caches misses besides simulation speed.

Allinea Tools (MAP/Performance Reports)

Allinea MAP is a GUI based commercial profiler used for both single threaded and multi-threaded codes to identify the bottlenecks and hotspots of the source code with minimal overhead. (<https://www.allinea.com/products/map>) Allinea MAP reports on memory usage, CPU memory access, MPI usage, CPU usage, CPU instruction, and I/O information. Allinea Performance report is an easy to use performance profiler which provides quick summary and effective review of the program performance.

Results and Discussions

Scalability Analysis

Previous scaling studies on WRF scalability, shows WRF scales well on different systems demonstrating both weak and strong scaling. (Christidis, 2015; Kruse et al., 2013) Figure 6-4 demonstrates the scalability assessment for Hurricane Sandy benchmark for up to 500 cores. For this case, WRF was compiled using Intel FORTRAN compiler 2015. For assessing the performance of the model, simulation speed parameter is used which is defined as duration of simulation per wall clock time. For this case, the WRF scales linearly up to 500 cores. However, after 500 cores the simulation speed becomes constant and finally decreases as the number of core increases. This shape demonstrates there will be a MPI communication overhead cost associated with the increase of the number cores. In the beginning region of the scaling plot (compute bound region) the

computation in each grid is the dominant cost of the total time spent. However, as the number of the cores increase the share of the MPI communication cost exceeds the computation inside each grid causing the performance to reduce in the MPI bound region of plot.

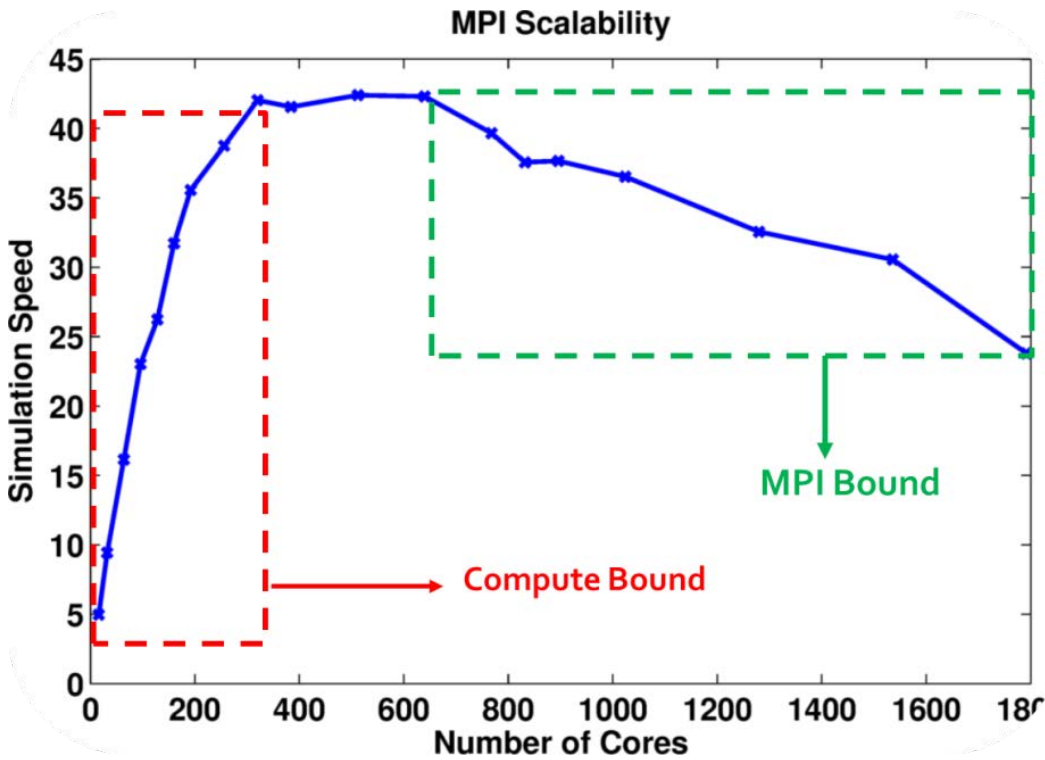


Figure 6-4: WRF scalability assessment for WRF 500x500 Hurrigan Sandy case.

For further clarification Allinea Performance Report are used. results show what percentage of time is spent on each main part of the code (i.e. compute, MPI, and I/O). As the number of cores increases the total time spent on the run decreases. While for 16 cores 87% of the total time is spent on computation while for 512 cores 79% of the total time is spent on MPI communication and only ~20% is spent on computation inside each grid. Please note that for this case the output is written in separate NetCDF file

(io_form_history=102 in WRF namelist). This option is the cheapest I/O option and needs further post-processing for modeling analysis.

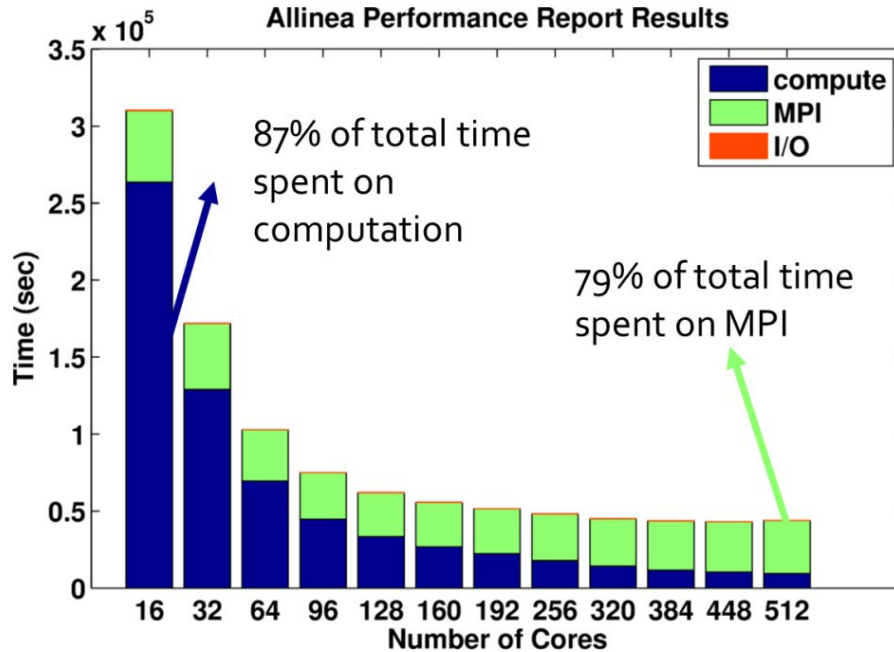


Figure 6-5: Percentage of total time spent on computation, MPI communication, and I/O.

Hybrid Parallelization

For the hybrid parallelization, WRF was compiled using distributed-memory (dmpar) and shared-memory parallelization (smpar). Distributed memory parallelism is implemented using Message Passing Interface (MPI) application programming interface (API) for communications between nodes. Open-MP is used for shared memory parallelism in WRF. Two-level domain decomposition is used in WRF to split the total simulation workload over parallel processes. (Michalakes et al., 2005; Michalakes and Gill, 2016; Powers et al., 2017) WRF model decomposes the modeling domain horizontally into patches and tiles. Patches are sections of the simulation domain assigned

to a distributed-memory node. Shared memory parallelism in WRF is between tiles, which are sections domain allocated to a shared-memory processor within a node. (Michalakes and Gill, 2016)

Figure 6-6 shows the results of hybrid parallelization simulation speeds. The number of the threads per node (top horizontal axis) and the number of tasks per node (bottom horizontal axis) are chosen so that the cores are not over-subscribed with threads or tasks. Therefore, as the number of threads per nodes increases the number of tasks per node decreases. (e.g. two threads and eight nodes or four threads and four nodes).

The results show that for a normal no binding case (blue cross) the simulation speed is increased with higher MPI tasks (and lower OpenMP threads). However, task/thread binding can improve the performance significantly for hybrid cases. (red circles in Figure 6-6) Intel compiler's OpenMP runtime library can be used for binding OpenMP threads to physical processing units. Threads spawned across sockets do not share L3 cache, causing issues such as higher rates of false sharing and reduced speed. For this case the performance increased by ~20% using thread binding. Furthermore, the hybrid parallelization shows better scaling in MPI bound workloads (relatively smaller workloads).

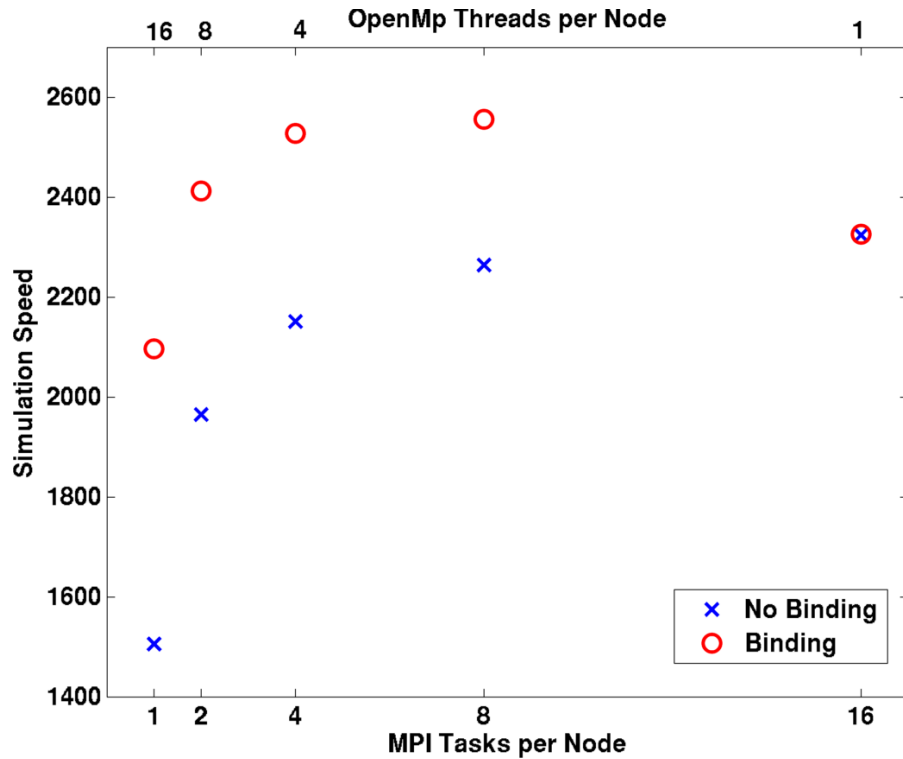


Figure 6-6: Simulation speed for different combinations of tasks and threads per node.

Hotspot Analysis

Although several runtime and compilation options can improve the performance of the code, it does not answer the question of what makes WRF runs expensive. Before putting any efforts in parallelization and optimization of the parallelized code, the serial performance of the code should be optimized. (Wellein, 2004) In this chapter, we focused on evaluating and optimizing the serial performance of the advection schemes. For analyzing different parts of the code, several software tools including Intel Vtune XE, TAU tools, and Alinea MAP are used. Figure 6-7 shows the results of the computation time spent in each part of the code categorized. The results show that the dynamic section of the code spent 48% of all the time spends on the code. In the dynamic section of the

code, advection related modules constitute 74% of all time spent. Several simulations using different microphysics and radiation schemes were performed to assess if advection takes significant time for different cases.

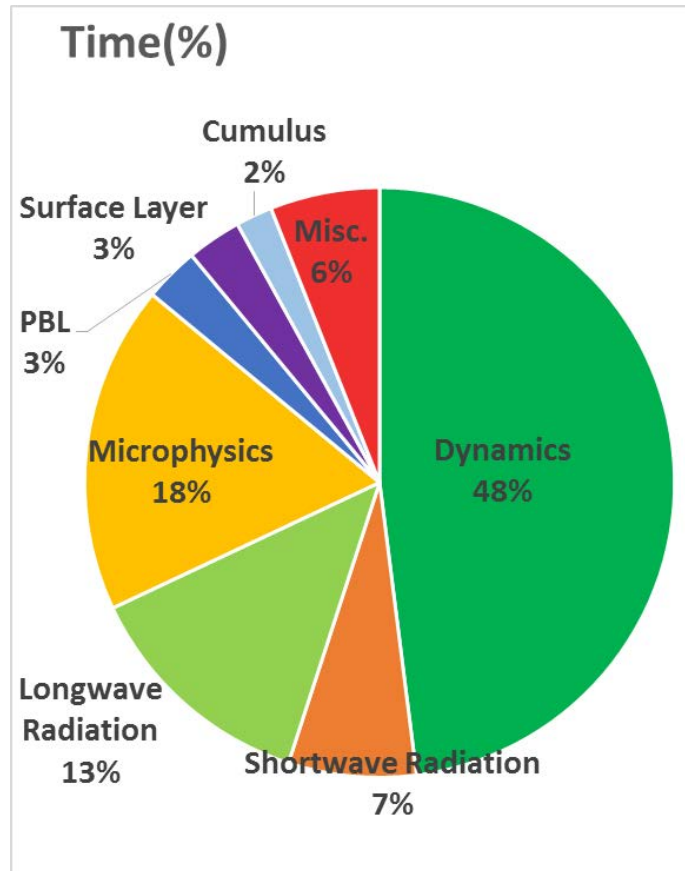


Figure 6-7: The processing time for WRF code as measured by Intel VTune XE.

For this case, advection is the most expensive subroutine. In a typical WRF with five moisture tracers, advection takes up to ~10% of the total run time on a single processor. The computational cost of tracer advection scales linearly with the number of tracers. (Michalakes and Vachharajani, n.d.) Therefore, for WRF-Chem cases with orders

of magnitude higher number of tracer (~100 tracers depending on the namelist options chosen), the computational cost of the advection subroutine becomes very significant.

For comprehensive investigation of the advection subroutines, TAU is utilized. PDT instrumentation of module_advect_em gives general performance statistics on the loop level. For higher granularity inspection, manual code instrumentation is used. The following TAU/PAPI variables were analyzed for both PDT and manual instrumentations.

- 1- Time
- 2- L1 and L2 Data Cache Misses (DCM)
- 3- Conditional branch instructions mispredicted
- 4- Floating point instruction and operations
- 5- Single and double precision vector/SIMD instructions

Using the above parameters two main hotspots of the advection modules are identified for further investigations and future study. The identified hotspots are summarized below:

- 1- Positive definite advection loop: This loop includes only 32 line of the whole WRF code but shows the highest time, L1 and L2 cache misses, and branch miss-predictions.
- 2- x, y and z flux 5 advection equation loops showing high time and high cache misses and repeated through the code for different advection schemes.

Performance Optimizations

For further investigation of the advection module, the advection kernel is extracted and tested separately. We designed a testing framework for optimizing, compiling, profiling, and evaluating the kernel with different FORTRAN compilers including Intel, GNU, and PGI compilers. In this framework, the measured processing times are an average of 10 runs. Figure 6-8 flowchart shows the simplified procedure of hotspot analysis and performance optimization process.

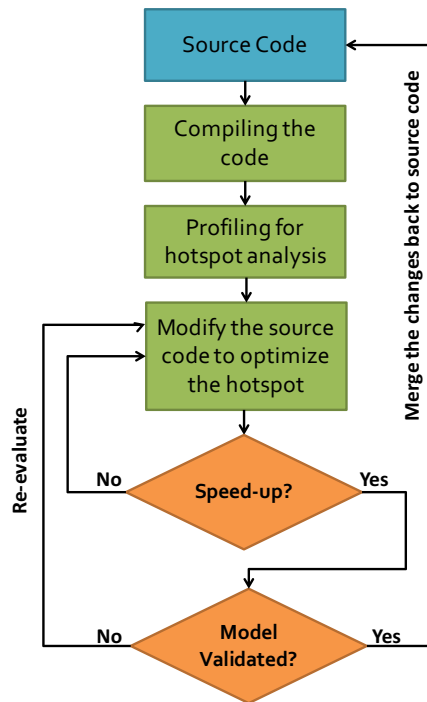


Figure 6-8: Simplified flowchart for hotspot analysis and optimization.

In general, various WRF modules have a low arithmetic intensity and operand reuse.(Mielikainen et al., 2014) Moreover, higher working loads overflow cache memories; hence, increasing the cache misses. (Mielikainen et al., 2014) Several

optimization techniques including exposing more vectorization and improving the cache hit rates are utilized on the advection modules and the outputs are verified for positive definite and monotonic advection schemes.

For example, for the first identified hotspot (positive definite delimiter loop), the optimization process is described below. The loop is composed of several stencils written in FORTRAN 90. Although the first two RK time steps run scalar advection and only the final RK time step runs positive definite advection, the profiling results show that positive definite delimiter loop (32 lines) account for more than 25% time spent on total advection steps for intel compiler.

By reconstructing and splitting the positive definite delimiter the vectorization of this loop increased; hence, the performance improved significantly. In this optimization step, the i-loop nested inside j- and k-loops was split into three separate i-loops. The speed-up results for various compilers are summarized in Table 6-1. This optimization increased the speed of whole advection for ~17% for Intel compiler. The results of the code modifications were validated by checking for bit-for-bit results. For a WRF-Chem case where moisture, several tracers, particles, species and scalars are advected, this speed-up has significant impact on overall performance. The code modifications and optimizations were merged back to the WRF source code, to benefit WRF community and users.

Table 6-1- The performance speed-up for the optimized code for various compilers

Compiler	Optimization Flag	Loop Speed-up	Kernel Speed-up
Intel(v16.0.2)	-O3	100%	~17%
GNU (v6.1.0)	-Ofast	105%	~11%
PGI (v16.5)	-O3	35%	~4%

Further studies and analysis is planned for increasing vectorization, reducing cache misses, and improving the code performance. Figure 6-9 and Figure 6-10 show the preliminary results of speed-up for developed versions for Intel and GNU compilers. The preliminary results show that up to 1.5x and 1.8x speed-up for positive definite advection scheme can be achieved for Intel and GNU compilers respectively.

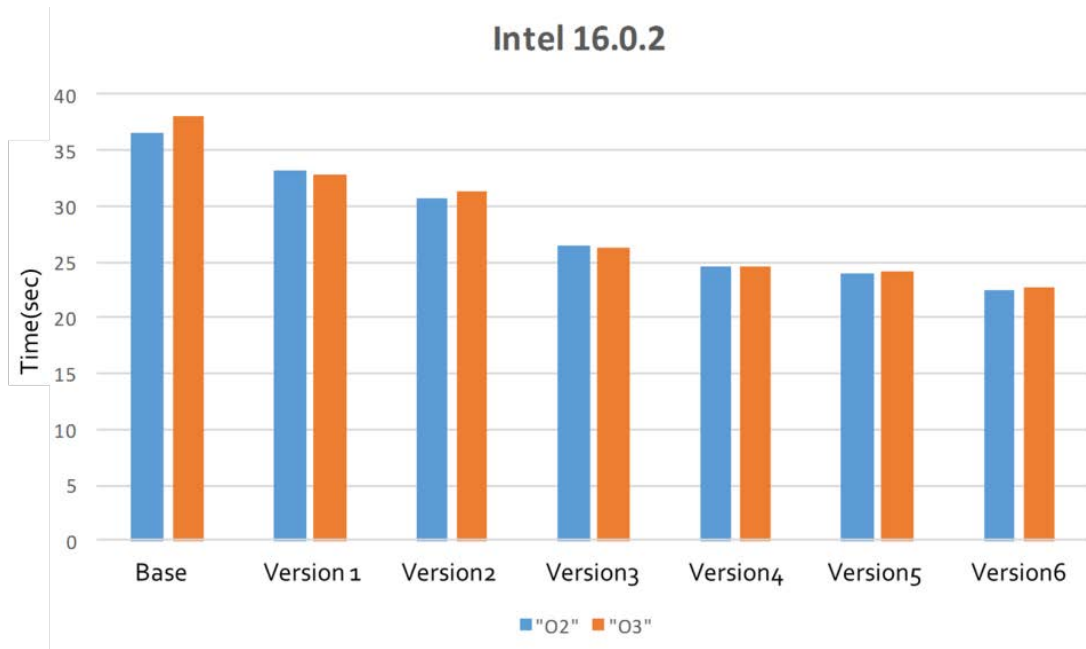


Figure 6-9- Single node performance of original and modified positive definite advection kernel for Intel 16.0.2 compiler.

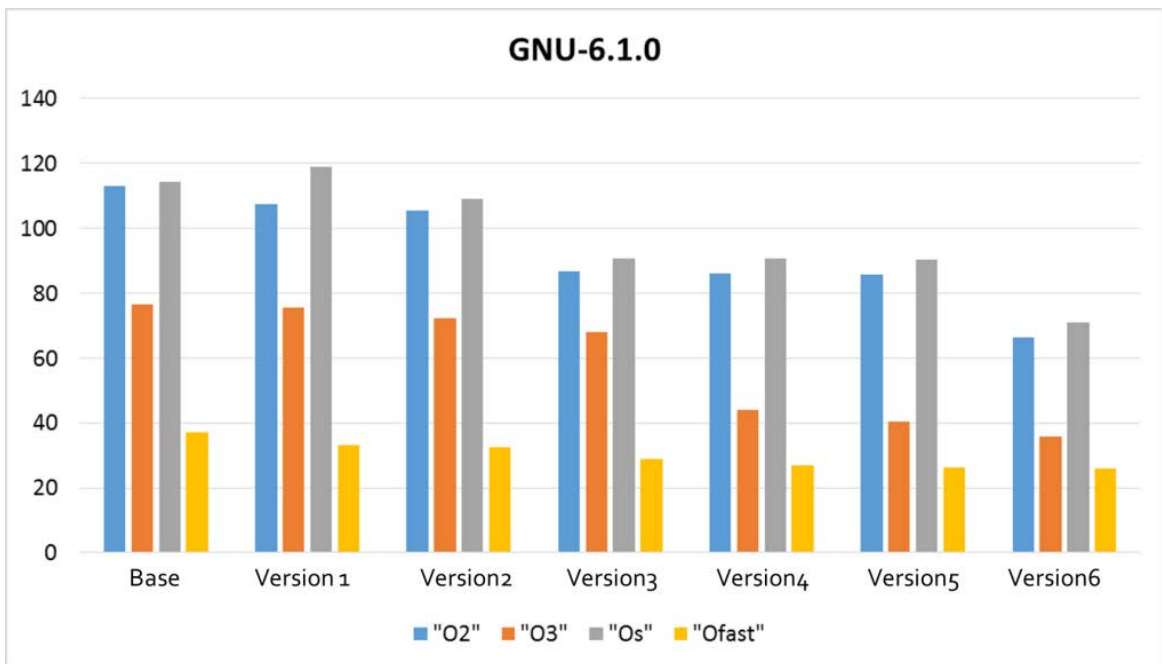


Figure 6-10- Single node performance of original and modified positive definite advection kernel for GNU 6.1.0 compiler.

Conclusions and Future Work

WRF is a computationally expensive program with a wide variety of application and such a vast user base. Therefore, any performance optimization of the model is of high priority for the WRF community and developers. In this chapter, we have evaluated the WRF performance and scalability. Furthermore, the hybrid parallelization using both MPI (dmpar) and OpenMP (smpar) is studied. While WRF code contains more than several hundreds of thousands of lines, small sections of the code are responsible for the majority of the simulation cost. Therefore, for focusing the WRF model optimization efforts on the major hotspots, WRF is profiled using various profilers such as Intel Vtune Amplifier and Allinea MAP. The profiling results show that advection is computationally expensive, especially in WRF cases where many tracers and chemicals are advected and transported. For example, for cases that transport dust and other particles and tracers transport with no chemistry the overall performance will increase significantly. In this chapter, several optimizations were proposed for the various advection schemes including monotonic and positive definite advection schemes. The results show that the modifications and optimizations improved WRF performance. These source code modifications were tested for bit-for-bit results and integrated back to the WRF main repository to benefit all the WRF users. Several different optimizations are currently in preparations which are not included in this thesis chapter. Future work includes analysis of hardware counters to fix branch mispredictions and cache misses, and reducing memory footprint by decreasing the number of variables.

CHAPTER 7: GENERAL CONCLUSIONS AND FUTURE DIRECTIONS

Understanding the impacts of different emission sources, identifying transport pathways in different seasons and optimizing the associated modeling techniques can assist policymakers in facilitating emission abatement policies for reducing negative health and environmental effects of pollutants globally. This Ph.D. research included several modeling studies to better understand transport of aerosols from different geographical sources and economic sectors (i.e. transportation, residential, industry, biomass burning and power) and quantify their climate impacts.

This thesis addressed the following five objectives. The first objective was to determine the source sector and region contributions to BC and PM_{2.5} in Central Asia. The contributions of emissions from various geographical regions and sectors including power, industry, transportation, residential, and biomass burning to Central Asia air quality were studied using a series of simulations. The simulations results showed that emissions from industry and power sectors are major contributors to CA anthropogenic PM_{2.5} (~35% each) but residential and biomass burning sectors are also significant (~10% each). Dust was identified as the major component of total PM_{2.5} during spring and summer seasons, and SO₄ is the major part of PM_{2.5} (~50%) especially during fall/winter. Dust accounted for more than 60% of simulated PM_{2.5} in Central Asia. Emissions from within Central Asia were the largest contributor to the non-dust PM_{2.5} in Central Asia (~50%). However, emissions from Europe and the Middle East contributed ~20% and ~10% to Central Asia non-dust PM_{2.5} respectively. BC accounted for ~1-2% of PM_{2.5} concentration in Central Asia with an average annual concentration of ~0.15 µg/m³.

Emissions from residential and transport sectors were the major contributors to the Central Asia BC (~30% each). Simulations for a reference 2030 emission scenario indicated that BC will increase at a higher rate compared to PM_{2.5} in Central Asia. This analysis indicates the importance of additional air pollution control measures and emission policies over Central Asia to reduce the health and environmental impacts of these pollutants in this region over the next decades

The second objective of this thesis was to quantify the intercontinental transport pathways of particles through Central Asia. To further understand the transport pathways and source region influences on the PM distributions at Central Asia, three dimensional ten day air mass trajectories (both forward and backward in time) from each observation site were calculated for the entire time period. The back-trajectory analysis and the seasonal contributions of emissions from various geographical regions to Central Asia air quality, indicate that this region is strategically located for studying hemispheric and intercontinental transport pathways of pollutants.

In the third objective, the source sector and region contributions to BC and PM_{2.5} in the Arctic were studied. This objective was addressed by a series of WRF-STEM simulations to identify the importance of each emission sector and geographical region emissions to the Arctic PM. The simulations show that the emissions from power, industrial, and biomass burning sectors are the main contributor to the Arctic PM_{2.5} with contributions of ~30%, 25%, and 20% respectively. However, residential and transportation sectors are the major contributors to the Arctic BC with contributions of

~35% and 30% respectively. Anthropogenic emissions were significant contributor to the surface concentration over the Arctic; however, the contributions from biomass burning become significant over the summer. (~ up to 20%) The transport pathways of pollutants to the Arctic during were studied using FLEXPART model for high aerosol loading episode during spring. More comprehensive backward trajectory analysis is needed to fully understand the transport pathways of pollutants to the Arctic for both cold and warm seasons.

The fourth objective was to quantify BC and dust deposition on the Arctic snow and ice and estimate the albedo reduction caused by BC deposition. For addressing this objective, the wet and dry deposition fluxes were extracted from STEM model at each time step. Using offline calculations the mixing ratio of BC and dust in snow and the effects of BC on albedo change was studied. The calculations show ~0.6 % albedo reduction over the Arctic region for spring 2008. For better assessing the BC deposition effects on climate, this study needs to be extended for other years. Dust and OC both are also light absorbing particles and cause albedo change when deposited on snow. Although these particles are orders of magnitude weaker than BC in absorbing sunlight, at higher snow concentration, they have significant impacts on albedo change. Further studies investigating the impacts of OC and dust deposition on radiative forcing of snow is required to better understand the climate impacts of light absorbing particles. Also more studies specifically on mountain ranges and high altitude glaciers can help us understand the albedo change and its impacts on hydrological cycle of mountain glaciers.

Weather and air quality prediction modeling has always been considered a demanding numerical and computational challenge. Better climate and weather simulations with higher resolution could save thousands of lives and prevent billions of dollars of damages to the economy each year. The impacts of weather and air quality forecasts on the world's population and economy drive the improvements of more advanced high performance computing systems. As high performance computing is moving towards exa-scale era, it is essential to prepare legacy weather and climate codes such to enable them to take full advantage of modern supercomputing architectures. The final objective of this study was to improve the computation efficiency of CTMs by performance analysis, profiling and optimization of WRF and WRF-Chem. For profiling and identifying the bottlenecks of WRF code, several profilers including Allinea MAP, TAU (Tuning and Analysis Utilities), and Intel Vtune Amplifier XE were used. The results show that advection is the most time-consuming routine in the ARW (Advanced Research WRF) dynamic solver. Several optimizations including exposing more vectorization and improving the cache hit rates are utilized on the various advection schemes to improve the model performance speed. Further studies are needed to improve the performance of other various sections of the WRF and WRF-Chem codes. These optimizations will widely benefit the large community of research and operational forecasters by reducing the computation costs.

REFERENCES

- Adhikary, B., Carmichael, G. R., Tang, Y., Leung, L. R., Qian, Y., Schauer, J. J., Stone, E. A., Ramanathan, V. and Ramana, M. V: Characterization of the seasonal cycle of south Asian aerosols: A regional-scale modeling analysis, *J. Geophys. Res.*, 112(D22), doi:10.1029/2006jd008143, 2007.
- AMAP: The Impact of Black Carbon on Arctic Climate. By: P.K. Quinn, A. Stohl, A. Arneth, T. Berntsen, J. F. Burkhardt, J. Christensen, M. Flanner, K. Kupiainen, H. Lihavainen, M. Shepherd, V. Shevchenko, H. Skov, and V. Vestreng., Arctic Monitoring and Assessment Programme (AMAP), Oslo, Norway. [online] Available from: <http://forskningbasen.deff.dk/Share.external?sp=S39b23054-f90c-4eb7-885a-846f62d83a76&sp=Sau>, 2011.
- Anenberg, S. C., Schwartz, J., Shindell, D., Amann, M., Faluvegi, G., Klimont, Z., Janssens-Maenhout, G., Pozzoli, L., Van Dingenen, R., Vignati, E., Emberson, L., Muller, N. Z., West, J. J., Williams, M., Demkine, V., Hicks, W. K., Kuylensstierna, J., Raes, F. and Ramanathan, V.: Global Air Quality and Health Co-benefits of Mitigating Near-Term Climate Change through Methane and Black Carbon Emission Controls, *Env. Heal. Perspect*, 120(6), 831–839, doi:10.1289/ehp.1104301, 2012.
- Barrie, L. A.: Arctic air pollution: an overview of current knowledge, *Atmos. Environ.*, 20(4), 643–663, 1986.
- Bates, T. S., Anderson, T. L., Baynard, T., Bond, T., Boucher, O., Carmichael, G., Clarke, A., Erlick, C., Guo, H., Horowitz, L., Howell, S., Kulkarni, S., Maring, H., McComiskey, A., Middlebrook, A., Noone, K., O'Dowd, C. D., Ogren, J., Penner, J., Quinn, P. K., Ravishankara, A. R., Savoie, D. L., Schwartz, S. E., Shinozuka, Y., Tang, Y., Weber, R. J. and Wu, Y.: Aerosol direct radiative effects over the northwest Atlantic, northwest Pacific, and North Indian Oceans: estimates based on in-situ chemical and optical measurements and chemical transport modeling, *Atmos. Chem. Phys.*, 6(6), 1657–1732, doi:10.5194/acp-6-1657-2006, 2006.
- Bauer, S. E., Koch, D., Unger, N., Metzger, S. M., Shindell, D. T. and Streets, D. G.: Nitrate aerosols today and in 2030: a global simulation including aerosols and tropospheric ozone, *Atmos. Chem. Phys.*, 7(19), 5043–5059, doi:10.5194/acp-7-5043-2007, 2007.
- Bian, H., Colarco, P. R., Chin, M., Chen, G., Rodriguez, J. M., Liang, Q., Blake, D., Chu, D. A., da Silva, A., Darnenov, A. S., Diskin, G., Fuelberg, H. E., Huey, G., Kondo, Y., Nielsen, J. E., Pan, X. and Wisthaler, A.: Source attributions of pollution to the Western Arctic during the NASA ARCTAS field campaign, *Atmos. Chem. Phys.*, 13(9), 4707–4721, doi:10.5194/acp-13-4707-2013, 2013.
- Bond, T. C. and Sun, H.: Can reducing black carbon emissions counteract global warming?, *Environ. Sci. Technol.*, 39(217), 5921–5926 [online] Available from: <http://pubs.acs.org/doi/abs/10.1021/es0480421> (Accessed 2 February 2015), 2005.

- Bond, T. C., Doherty, S. J., Fahey, D. W., Forster, P. M., Berntsen, T., DeAngelo, B. J., Flanner, M. G., Ghan, S., Kärcher, B., Koch, D., Kinne, S., Kondo, Y., Quinn, P. K., Sarofim, M. C., Schultz, M. G., Schulz, M., Venkataraman, C., Zhang, H., Zhang, S., Bellouin, N., Guttikunda, S. K., Hopke, P. K., Jacobson, M. Z., Kaiser, J. W., Klimont, Z., Lohmann, U., Schwarz, J. P., Shindell, D., Storelvmo, T., Warren, S. G. and Zender, C. S.: Bounding the role of black carbon in the climate system: A scientific assessment, *J. Geophys. Res. Atmos.*, 118(11), 5380–5552, doi:10.1002/jgrd.50171, 2013.
- Brasseur, G. P. and Jacob, D. J.: *Modeling of Atmospheric Chemistry*, Cambridge University Press., 2017.
- Brioude, J., Arnold, D., Stohl, A., Cassiani, M., Morton, D., Seibert, P., Angevine, W., Evan, S., Dingwell, A., Fast, J. D., Easter, R. C., Pisso, I., Burkhardt, J. and Wotawa, G.: The Lagrangian particle dispersion model FLEXPART-WRF version 3.1, *Geosci. Model Dev.*, 6(6), 1889–1904, doi:10.5194/gmd-6-1889-2013, 2013.
- Brock, C. A., Cozic, J., Bahreini, R., Froyd, K. D., Middlebrook, A. M., McComiskey, A., Brioude, J., Cooper, O. R., Stohl, A., Aikin, K. C., de Gouw, J. A., Fahey, D. W., Ferrare, R. A., Gao, R.-S., Gore, W., Holloway, J. S., Hübler, G., Jefferson, A., Lack, D. A., Lance, S., Moore, R. H., Murphy, D. M., Nenes, A., Novelli, P. C., Nowak, J. B., Ogren, J. A., Peischl, J., Pierce, R. B., Pilewskie, P., Quinn, P. K., Ryerson, T. B., Schmidt, K. S., Schwarz, J. P., Sodemann, H., Spackman, J. R., Stark, H., Thomson, D. S., Thornberry, T., Veres, P., Watts, L. A., Warneke, C. and Wollny, A. G.: Characteristics, sources, and transport of aerosols measured in spring 2008 during the aerosol, radiation, and cloud processes affecting Arctic Climate (ARCPAC) Project, *Atmos. Chem. Phys.*, 11(6), 2423–2453, doi:10.5194/acp-11-2423-2011, 2011.
- Carmichael, G. R., Adhikary, B., Kulkarni, S., D’Allura, A., Tang, Y., Streets, D., Zhang, Q., Bond, T. C., Ramanathan, V., Jamroensan, A. and Marrapu, P.: Asian Aerosols: Current and Year 2030 Distributions and Implications to Human Health and Regional Climate Change, *Environ. Sci. Technol.*, 43(15), 5811–5817, doi:10.1021/es8036803, 2009.
- Chen, B. B., Sverdlik, L. G., Imashev, S. A., Solomon, P. A., Lantz, J., Schauer, J. J., Shafer, M. M., Artamonova, M. S. and Carmichael, G.: Empirical relationship between particulate matter and aerosol optical depth over Northern Tien-Shan, Central Asia, *Air Qual Atmos Heal.*, 6(2), 385–396, doi:10.1007/s11869-012-0192-5, 2012.
- Chen, B. B., Imashev, S. A., Sverdlik, L. G., Solomon, P. A., Lantz, J., Schauer, J. J., Shafer, M. M., Artamonova, M. S. and Carmichael, G. R.: Ozone Variations over Central Tien-Shan in Central Asia and Implications for Regional Emissions Reduction Strategies, *Aerosol Air Qual. Res.*, 13, 555–562, 2013.
- Chin, M., Diehl, T., Ginoux, P. and Malm, W.: Intercontinental transport of pollution and dust aerosols: implications for regional air quality, *Atmos. Chem. Phys.*, 7(21), 5501–5517, doi:10.5194/acp-7-5501-2007, 2007.

- Christidis, Z.: Performance and Scaling of WRF on Three Different Parallel Supercomputers BT - High Performance Computing: 30th International Conference, ISC High Performance 2015, Frankfurt, Germany, July 12-16, 2015, Proceedings, edited by J. M. Kunkel and T. Ludwig, pp. 514–528, Springer International Publishing, Cham., 2015.
- Chung, C. E., Ramanathan, V., Carmichael, G., Kulkarni, S., Tang, Y., Adhikary, B., Leung, L. R. and Qian, Y.: Anthropogenic aerosol radiative forcing in Asia derived from regional models with atmospheric and aerosol data assimilation, *Atmos. Chem. Phys.*, 10(13), 6007–6024, doi:10.5194/acp-10-6007-2010, 2010.
- Clarke, A. D. and Noone, K. J.: Soot in the Arctic snowpack: a cause for perturbations in radiative transfer, *Atmos. Environ.*, 19(12), 2045–2053, doi:10.1016/0004-6981(85)90113-1, 1985.
- Cohen, J. L., Furtado, J. C., Barlow, M. A., Alexeev, V. A. and Cherry, J. E.: Arctic warming, increasing snow cover and widespread boreal winter cooling, *Environ. Res. Lett.*, 7(1), 14007 [online] Available from: <http://stacks.iop.org/1748-9326/7/i=1/a=014007>, 2012.
- Cooper, C. D. and Alley, F. C.: *Air Pollution Control: A Design Approach*, 4 edition., Waveland Pr Inc., 2011.
- D’Allura, A., Kulkarni, S., Carmichael, G. R., Finardi, S., Adhikary, B., Wei, C., Streets, D., Zhang, Q., Pierce, R. B., Al-Saadi, J. a., Diskin, G. and Wennberg, P.: Meteorological and air quality forecasting using the WRF–STEM model during the 2008 ARCTAS field campaign, *Atmos. Environ.*, 45(38), 6901–6910, doi:10.1016/j.atmosenv.2011.02.073, 2011.
- Denier van der Gon, H., Visschedijk, A., Droge, R., Mulder, M., Johansson, C. and Klimont, Z.: A high resolution emission inventory of particulate elemental carbon and organic carbon for Europe in 2005, 7th Int. Conf. Air Qual. – Sci. Appl. (Air Qual. 2009), 2009.
- Doherty, S. J., Warren, S. G., Grenfell, T. C., Clarke, A. D. and Brandt, R. E.: Light-absorbing impurities in Arctic snow, *Atmos. Chem. Phys.*, 10(23), 11647–11680, doi:10.5194/acp-10-11647-2010, 2010.
- Doherty, S. J., Bitz, C. M. and Flanner, M. G.: Biases in modeled surface snow BC mixing ratios in prescribed-aerosol climate model runs, *Atmos. Chem. Phys.*, 14(21), 11697–11709, doi:10.5194/acp-14-11697-2014, 2014.
- Dou, T.-F. and Xiao, C.-D.: An overview of black carbon deposition and its radiative forcing over the Arctic, *Adv. Clim. Chang. Res.*, 7(3), 115–122, doi:<http://dx.doi.org/10.1016/j.accre.2016.10.003>, 2016.
- Elliott, S. J. and Del Vento, D.: Performance Analysis and Optimization of the Weather Research and Forecasting Model (WRF) on Intel Multicore and Manycore Architectures, in *The International Conference for High Performance Computing, Networking, Storage and Analysis*, Austin, TX., 2015.

- Emerson, J. W., Hsu, A., Levy, M. A., Sherbinin, A. de, Mara, V., Esty, D. C. and Jaiteh, M.: 2012 Environmental Performance Index and Pilot Trend Environmental Performance Index., 2012.
- Fan, S.-M.: Modeling of observed mineral dust aerosols in the arctic and the impact on winter season low-level clouds, *J. Geophys. Res. Atmos.*, 118(19), 11,111-161,174, doi:10.1002/jgrd.50842, 2013.
- Fast, J. D., Gustafson, W. I., Easter, R. C., Zaveri, R. A., Barnard, J. C., Chapman, E. G., Grell, G. A. and Peckham, S. E.: Evolution of ozone, particulates, and aerosol direct radiative forcing in the vicinity of Houston using a fully coupled meteorology-chemistry-aerosol model, *J. Geophys. Res. Atmos.*, 111(D21), n/a--n/a, doi:10.1029/2005JD006721, 2006.
- Flanner, M. G., Zender, C. S., Randerson, J. T. and Rasch, P. J.: Present-day climate forcing and response from black carbon in snow, *J. Geophys. Res.*, 112(D11), D11202, doi:10.1029/2006JD008003, 2007.
- Freitas, S. R., Longo, K. M., Chatfield, R., Latham, D., Silva Dias, M. A. F., Andreae, M. O., Prins, E., Santos, J. C., Gielow, R. and Carvalho, J. A.: Including the sub-grid scale plume rise of vegetation fires in low resolution atmospheric transport models, *Atmos. Chem. Phys.*, 7(13), 3385–3398, doi:10.5194/acp-7-3385-2007, 2007.
- Freitas, S. R., Longo, K. M., Trentmann, J. and Latham, D.: Technical Note: Sensitivity of 1-D smoke plume rise models to the inclusion of environmental wind drag, *Atmos. Chem. Phys.*, 10(2), 585–594, doi:10.5194/acp-10-585-2010, 2010.
- Fuelberg, H. E., Harrigan, D. L. and Sessions, W.: A meteorological overview of the ARCTAS 2008 mission, *Atmos. Chem. Phys.*, 10(2), 817–842, doi:10.5194/acp-10-817-2010, 2010.
- Garrett, T. J., ZHAO, C. and NOVELLI, P. C.: Assessing the relative contributions of transport efficiency and scavenging to seasonal variability in Arctic aerosol, *Tellus B*, 62(3), 190–196, doi:10.1111/j.1600-0889.2010.00453.x, 2010.
- Ginoux, P., Chin, M., Tegen, I., Prospero, J. M., Holben, B., Dubovik, O. and Lin, S.-J.: Sources and distributions of dust aerosols simulated with the GOCART model, *J. Geophys. Res.*, 106(D17), 20255, doi:10.1029/2000jd000053, 2001.
- Ginoux, P., Prospero, J. M., Gill, T. E., Hsu, N. C. and Zhao, M.: Global-scale attribution of anthropogenic and natural dust sources and their emission rates based on MODIS Deep Blue aerosol products, *Rev. Geophys.*, 50(3), n/a--n/a, doi:10.1029/2012RG000388, 2012.
- Gong, S. L.: A parameterization of sea-salt aerosol source function for sub- and super-micron particles, *Glob. Biogeochem. Cycles*, 17(4), n/a-n/a, doi:10.1029/2003gb002079, 2003.
- Grell, G., Freitas, S. R., Stuefer, M. and Fast, J.: Inclusion of biomass burning in WRF-Chem: impact of wildfires on weather forecasts, *Atmos. Chem. Phys.*, 11(11), 5289–5303, doi:10.5194/acp-11-5289-2011, 2011.

- Grell, G. A., Peckham, S. E., Schmitz, R., McKeen, S. A., Frost, G., Skamarock, W. C. and Eder, B.: Fully coupled “online” chemistry within the WRF model, *Atmos. Environ.*, 39(37), 6957–6975, doi:10.1016/j.atmosenv.2005.04.027, 2005.
- Groot Zwaaftink, C. D., Arnalds, O., Dagsson-Waldhauserova, P., Eckhardt, S., Prospero, J. M. and Stohl, A.: Temporal and spatial variability of Icelandic dust emission and atmospheric transport, *Atmos. Chem. Phys. Discuss.*, 2017, 1–23, doi:10.5194/acp-2017-290, 2017.
- Guttikunda, S. K.: Impacts of Asian megacity emissions on regional air quality during spring 2001, *J. Geophys. Res.*, 110(D20), doi:10.1029/2004jd004921, 2005.
- Hand, J. L., Schichtel, B. A., Malm, W. C. and Pitchford, M. L.: Particulate sulfate ion concentration and SO₂ emission trends in the United States from the early 1990s through 2010, *Atmos. Chem. Phys.*, 12(21), 10353–10365, doi:10.5194/acp-12-10353-2012, 2012.
- Hansen, J. and Nazarenko, L.: Soot climate forcing via snow and ice albedos, *Proc. Natl Acad. Sci. USA*, 101, 423–428 [online] Available from: <http://dx.doi.org/10.1073/pnas.2237157100>, 2004.
- Haywood, J. M. and Ramaswamy, V.: Global sensitivity studies of the direct radiative forcing due to anthropogenic sulfate and black carbon aerosols, *J. Geophys. Res.*, 103, 6043–6058 [online] Available from: <http://dx.doi.org/10.1029/97JD03426>, 1998.
- Heidam, N. Z., Christensen, J., Wåhlin, P. and Skov, H.: Arctic atmospheric contaminants in NE Greenland: levels, variations, origins, transport, transformations and trends 1990-2001., *Sci. Total Environ.*, 331(1–3), 5–28, doi:10.1016/j.scitotenv.2004.03.033, 2004.
- Hirdman, D., Sodemann, H., Eckhardt, S., Burkhardt, J. F., Jefferson, A., Mefford, T., Quinn, P. K., Sharma, S., Ström, J. and Stohl, A.: Source identification of short-lived air pollutants in the Arctic using statistical analysis of measurement data and particle dispersion model output, *Atmos. Chem. Phys.*, 10(2), 669–693, doi:10.5194/acp-10-669-2010, 2010.
- Hsu, N. C., Tsay, S.-C., King, M. D. and Herman, J. R.: Aerosol Properties Over Bright-Reflecting Source Regions, *IEEE Trans. Geosci. Remote Sens.*, 42(3), 557–569, doi:10.1109/tgrs.2004.824067, 2004.
- Hsu, N. C., Tsay, S.-C., King, M. D. and Herman, J. R.: Deep Blue Retrievals of Asian Aerosol Properties During ACE-Asia, *IEEE Trans. Geosci. Remote Sens.*, 44(11), 3180–3195, doi:10.1109/tgrs.2006.879540, 2006.
- HTAP: Hemispheric Transport of Air Pollution 2010 (Executive Summary)., 2010.
- Huang, L., Gong, S. L., Jia, C. Q. and Lavoué, D.: Importance of deposition processes in simulating the seasonality of the Arctic black carbon aerosol, *J. Geophys. Res.*, 115(D17), D17207, doi:10.1029/2009JD013478, 2010.

- Huang, M., Carmichael, G. R., Spak, S. N., Adhikary, B., Kulkarni, S., Cheng, Y., Wei, C., Tang, Y., D'Allura, a., Wennberg, P. O., Huey, G. L., Dibb, J. E., Jimenez, J. L., Cubison, M. J., Weinheimer, a. J., Kaduwela, a., Cai, C., Wong, M., Bradley Pierce, R., Al-Saadi, J. a., Streets, D. G. and Zhang, Q.: Multi-scale modeling study of the source contributions to near-surface ozone and sulfur oxides levels over California during the ARCTAS-CARB period, *Atmos. Chem. Phys.*, 11(7), 3173–3194, doi:10.5194/acp-11-3173-2011, 2011.
- Huang, M., Carmichael, G. R., Kulkarni, S., Streets, D. G., Lu, Z., Zhang, Q., Pierce, R. B., Kondo, Y., Jimenez, J. L., Cubison, M. J., Anderson, B. and Wisthaler, A.: Sectoral and geographical contributions to summertime continental United States (CONUS) black carbon spatial distributions, *Atmos. Environ.*, 51(3), 165–174, doi:10.1016/j.atmosenv.2012.01.021, 2012.
- Hubanks, P. A., King, M. A., Platnick, S. and Pincus, R.: MODIS atmosphere L3 gridded product algorithm theoretical basis document, ATBD-MOD-30, (December), 2008.
- Jacob, D.: Introduction to Atmospheric Chemistry, 0th Editio., Princeton University Press., 1999.
- Jacob, D. J., Crawford, J. H., Maring, H., Clarke, a. D., Dibb, J. E., Emmons, L. K., Ferrare, R. a., Hostetler, C. a., Russell, P. B., Singh, H. B., Thompson, a. M., Shaw, G. E., McCauley, E., Pederson, J. R. and Fisher, J. a.: The Arctic Research of the Composition of the Troposphere from Aircraft and Satellites (ARCTAS) mission: design, execution, and first results, *Atmos. Chem. Phys.*, 10(11), 5191–5212, doi:10.5194/acp-10-5191-2010, 2010.
- Jacobson, M. Z.: Climate response of fossil fuel and biofuel soot, accounting for soot's feedback to snow and sea ice albedo and emissivity, *J. Geophys. Res.*, 109(D21), D21201, doi:10.1029/2004JD004945, 2004.
- Jiao, C., Flanner, M. G., Balkanski, Y., Bauer, S. E., Bellouin, N., Berntsen, T. K., Bian, H., Carslaw, K. S., Chin, M., De Luca, N., Diehl, T., Ghan, S. J., Iversen, T., Kirkevåg, a., Koch, D., Liu, X., Mann, G. W., Penner, J. E., Pitari, G., Schulz, M., Seland, Ø., Skeie, R. B., Steenrod, S. D., Stier, P., Takemura, T., Tsigaridis, K., van Noije, T., Yun, Y. and Zhang, K.: An AeroCom assessment of black carbon in Arctic snow and sea ice, *Atmos. Chem. Phys.*, 14(5), 2399–2417, doi:10.5194/acp-14-2399-2014, 2014.
- Johnsen, P., Straka, M., Shapiro, M., Norton, A. and Galarneau, T.: Petascale WRF simulation of hurricane sandy: Deployment of NCSA's cray XE6 blue waters, in High Performance Computing, Networking, Storage and Analysis (SC), 2013 International Conference for, pp. 1–7, IEEE., 2013.
- Klemm, M.: Intel ® VTune™ Amplifier XE and Intel ® MPI, 2011.
- Klonecki, A., Hess, P., Emmons, L., Smith, L., Orlando, J. and Blake, D.: Seasonal changes in the transport of pollutants into the Arctic troposphere-model study, *J. Geophys. Res. Atmos.*, 108(D4), n/a-n/a, doi:10.1029/2002JD002199, 2003.

- Koch, D. and Hansen, J.: Distant origins of Arctic black carbon: A Goddard Institute for Space Studies ModelE experiment, *J. Geophys. Res.*, 110(D4), D04204, doi:10.1029/2004JD005296, 2005.
- Koch, D., Bond, T. C., Streets, D., Unger, N. and van der Werf, G. R.: Global impacts of aerosols from particular source regions and sectors, *J. Geophys. Res.*, 112(D2), D02205, doi:10.1029/2005JD007024, 2007.
- Koch, D., Menon, S., Del Genio, A., Ruedy, R., Alienov, I. and Schmidt, G. A.: Distinguishing Aerosol Impacts on Climate over the Past Century, *J. Clim.*, 22(10), 2659–2677, doi:10.1175/2008JCLI2573.1, 2009a.
- Koch, D., Schulz, M., Kinne, S., McNaughton, C., Spackman, J. R., Balkanski, Y., Bauer, S., Bernsten, T., Bond, T. C., Boucher, O., Chin, M., Clarke, A., De Luca, N., Dentener, F., Diehl, T., Dubovik, O., Easter, R., Fahey, D. W., Feichter, J., Fillmore, D., Freitag, S., Ghan, S., Ginoux, P., Gong, S., Horowitz, L., Iversen, T., Kirkevåg, A., Klimont, Z., Kondo, Y., Krol, M., Liu, X., Miller, R., Montanaro, V., Moteki, N., Myhre, G., Penner, J. E., Perlwitz, J., Pitari, G., Reddy, S., Sahu, L., Sakamoto, H., Schuster, G., Schwarz, J. P., Seland, Ø., Stier, P., Takegawa, N., Takemura, T., Textor, C., van Aardenne, J. A. and Zhao, Y.: Evaluation of black carbon estimations in global aerosol models, *Atmos. Chem. Phys.*, 9(22), 9001–9026, doi:10.5194/acp-9-9001-2009, 2009b.
- Kruse, C. G., Del Vento, D., Monturo, R., Lubin, M. and McMillan, S.: Evaluation of WRF scaling to several thousand cores on yellowstone Supercomputer, in *FRCRC HPC symposium*, Laramie, WY., 2013.
- Kulkarni, S.: Assessment of source-receptor relationships of aerosols: an integrated forward and backward modeling approach, 2009.
- Kulkarni, S., Sobhani, N., Miller-Schulze, J. P., Shafer, M. M., Schauer, J. J., Solomon, P. A., Saide, P. E., Spak, S. N., Cheng, Y. F., Denier van der Gon, H. A. C., Lu, Z., Streets, D. G., Janssens-Maenhout, G., Wiedinmyer, C., Lantz, J., Artamonova, M., Chen, B., Imashev, S., Sverdlik, L., Deminter, J. T., Adhikary, B., D’Allura, A., Wei, C. and Carmichael, G. R.: Source sector and region contributions to BC and PM_{2.5} in Central Asia, *Atmos. Chem. Phys.*, 15(4), 1683–1705, doi:10.5194/acp-15-1683-2015, 2015.
- Kurata, G., Carmichael, G. R., Streets, D. G., Kitada, T., Tang, Y., Woo, J.-H. and Thongboonchoo, N.: Relationships between emission sources and air mass characteristics in East Asia during the TRACE-P period, *Atmos. Environ.*, 38(40), 6977–6987, doi:10.1016/j.atmosenv.2004.05.062, 2004.
- Law, K. S. and Stohl, A.: Arctic air pollution: origins and impacts., *Science*, 315(5818), 1537–40, doi:10.1126/science.1137695, 2007.

- Levy, R. C., Remer, L. A., Mattoo, S., Vermote, E. F. and Kaufman, Y. J.: Second-generation operational algorithm: Retrieval of aerosol properties over land from inversion of Moderate Resolution Imaging Spectroradiometer spectral reflectance, *J. Geophys. Res. Atmos.*, 112(D13), n/a-n/a, doi:10.1029/2006jd007811, 2007.
- Lim, S. S., Vos, T., Flaxman, A. D., Danaei, G., Shibuya, K., Adair-Rohani, H., Amann, M., Anderson, H. R., Andrews, K. G., Aryee, M., Atkinson, C., Bacchus, L. J., Bahalim, A. N., Balakrishnan, K., Balmes, J., Barker-Collo, S., Baxter, A., Bell, M. L., Blore, J. D., Blyth, F., Bonner, C., Borges, G., Bourne, R., Boussinesq, M., Brauer, M., Brooks, P., Bruce, N. G., Brunekreef, B., Bryan-Hancock, C., Bucello, C., Buchbinder, R., Bull, F., Burnett, R. T., Byers, T. E., Calabria, B., Carapetis, J., Carnahan, E., Chafe, Z., Charlson, F., Chen, H., Chen, J. S., Cheng, A. T.-A., Child, J. C., Cohen, A., Colson, K. E., Cowie, B. C., Darby, S., Darling, S., Davis, A., Degenhardt, L., Dentener, F., Des Jarlais, D. C., Devries, K., Dherani, M., Ding, E. L., Dorsey, E. R., Driscoll, T., Edmond, K., Ali, S. E., Engell, R. E., Erwin, P. J., Fahimi, S., Falder, G., Farzadfar, F., Ferrari, A., Finucane, M. M., Flaxman, S., Fowkes, F. G. R., Freedman, G., Freeman, M. K., Gakidou, E., Ghosh, S., Giovannucci, E., Gmel, G., Graham, K., Grainger, R., Grant, B., Gunnell, D., Gutierrez, H. R., Hall, W., Hoek, H. W., Hogan, A., Hosgood, H. D., Hoy, D., Hu, H., Hubbell, B. J., Hutchings, S. J., Ibeanusi, S. E., Jacklyn, G. L., Jasrasaria, R., Jonas, J. B., Kan, H., Kanis, J. A., Kassebaum, N., Kawakami, N., Khang, Y.-H., Khatibzadeh, S., Khoo, J.-P., Kok, C., et al.: A comparative risk assessment of burden of disease and injury attributable to 67 risk factors and risk factor clusters in 21 regions, 1990-2010: a systematic analysis for the Global Burden of Disease Study 2010., *Lancet*, 380(9859), 2224–60, doi:10.1016/S0140-6736(12)61766-8, 2012.
- Lindlan, K. A., Cuny, J., Malony, A. D., Shende, S., Mohr, B., Rivenburgh, R. and Rasmussen, C.: A tool framework for static and dynamic analysis of object-oriented software with templates, in *Supercomputing, ACM/IEEE 2000 Conference*, p. 49, IEEE., 2000.
- Liu, D., Quennehen, B., Darbyshire, E., Allan, J. D., Williams, P. I., Taylor, J. W., Bauguitte, S. J.-B., Flynn, M. J., Lowe, D., Gallagher, M. W., Bower, K. N., Choularton, T. W. and Coe, H.: The importance of Asia as a source of black carbon to the European Arctic during springtime 2013, *Atmos. Chem. Phys.*, 15(20), 11537–11555, doi:10.5194/acp-15-11537-2015, 2015.
- Liu, J., Mauzerall, D. L., Horowitz, L. W., Ginoux, P. and Fiore, A. M.: Evaluating inter-continental transport of fine aerosols: (1) Methodology, global aerosol distribution and optical depth, *Atmos. Environ.*, 43(28), 4327–4338, doi:10.1016/j.atmosenv.2009.03.054, 2009.
- Liu, J., Fan, S., Horowitz, L. W. and Levy, H.: Evaluation of factors controlling long-range transport of black carbon to the Arctic, *J. Geophys. Res.*, 116(D4), D04307, doi:10.1029/2010JD015145, 2011.

- Lu, Z., Streets, D. G., Zhang, Q., Wang, S., Carmichael, G. R., Cheng, Y. F., Wei, C., Chin, M., Diehl, T. and Tan, Q.: Sulfur dioxide emissions in China and sulfur trends in East Asia since 2000, *Atmos. Chem. Phys.*, 10, 6311–6331, doi:10.5194/acp-10-6311-2010, 2010.
- Lu, Z., Zhang, Q. and Streets, D. G.: Sulfur dioxide and primary carbonaceous aerosol emissions in China and India, 1996–2010, *Atmos. Chem. Phys.*, 11(18), 9839–9864, doi:10.5194/acp-11-9839-2011, 2011.
- Martín, M. J., Parada, M. and Doallo, R.: High Performance Air Pollution Simulation Using OpenMP, *J. Supercomput.*, 28(3), 311–321, doi:10.1023/B:SUPE.0000022102.00315.41, 2004.
- McNaughton, C. S., Clarke, a. D., Freitag, S., Kapustin, V. N., Kondo, Y., Moteki, N., Sahu, L., Takegawa, N., Schwarz, J. P., Spackman, J. R., Watts, L., Diskin, G., Podolske, J., Holloway, J. S., Wisthaler, a., Mikoviny, T., de Gouw, J., Warneke, C., Jimenez, J., Cubison, M., Howell, S. G., Middlebrook, a., Bahreini, R., Anderson, B. E., Winstead, E., Thornhill, K. L., Lack, D., Cozic, J. and Brock, C. a.: Absorbing aerosol in the troposphere of the Western Arctic during the 2008 ARCTAS/ARCPAC airborne field campaigns, *Atmos. Chem. Phys.*, 11(15), 7561–7582, doi:10.5194/acp-11-7561-2011, 2011.
- Meinander, O., Kazadzis, S., Arola, A., Riihelä, A., Räisänen, P., Kivi, R., Kontu, A., Kouznetsov, R., Sofiev, M., Svensson, J., Suokanerva, H., Aaltonen, V., Manninen, T., Roujean, J.-L. and Hautecoeur, O.: Spectral albedo of seasonal snow during intensive melt period at Sodankylä, beyond the Arctic Circle, *Atmos. Chem. Phys.*, 13(7), 3793–3810, doi:10.5194/acp-13-3793-2013, 2013.
- Michalakes, J. and Gill, D.: WRF Software: Code and Parallel Programming, WRF Users Tutor., 2016.
- Michalakes, J. and Vachharajani, M.: GPU Acceleration of Scalar Advection, [online] Available from: http://www2.mmm.ucar.edu/wrf/WG2/GPU/Scalar_Advect.htm, n.d.
- Michalakes, J., Dudhia, J., Gill, D., Henderson, T., Klemp, J., Skamarock, W. and Wang, W.: The weather research and forecast model: software architecture and performance Authors, *Use High Perform. Comput. Meteorol.*, doi:10.1142/9789812701831_0012, 2005.
- Mielikainen, J., Huang, B. and Huang, A. H.-L.: Intel Xeon Phi accelerated Weather Research and Forecasting (WRF) Goddard microphysics scheme, *Geosci. Model Dev. Discuss.*, 2014, 8941–8973, doi:10.5194/gmdd-7-8941-2014, 2014.
- Miller-Schulze, J. P., Shafer, M. M., Schauer, J. J., Solomon, P. A., Lantz, J., Artamonova, M., Chen, B., Imashev, S., Sverdluk, L., Carmichael, G. R. and Deminter, J. T.: Characteristics of fine particle carbonaceous aerosol at two remote sites in Central Asia, *Atmos. Environ.*, 45(38), 6955–6964, doi:10.1016/j.atmosenv.2011.09.026, 2011.

- Naik Bhadreshbhai, M. and Thomas, A. K.: Optimizaiton of Weather Model, *Int. J. Recent Innov. Trends Comput. Commun.*, 4(5), 2016.
- Painter, T. H., Barrett, A. P., Landry, C. C., Neff, J. C., Cassidy, M. P., Lawrence, C. R., McBride, K. E. and Farmer, G. L.: Impact of disturbed desert soils on duration of mountain snow cover, *Geophys. Res. Lett.*, 34(12), n/a--n/a, doi:10.1029/2007GL030284, 2007.
- Painter, T. H., Bryant, A. C. and Skiles, S. M.: Radiative forcing by light absorbing impurities in snow from MODIS surface reflectance data, *Geophys. Res. Lett.*, 39(17), n/a--n/a, doi:10.1029/2012GL052457, 2012.
- Parada, M., Martín, M. J. and Doallo, R.: High performance air pollution simulation using OpenMP, in *Parallel Processing Workshops, 2002. Proceedings. International Conference on*, pp. 391–397, IEEE., 2002.
- Paterson, W. S. B.: The Physics of Glaciers, *Earth Surf. Process. Landforms*, 21(10), 980–981, doi:10.1002/(SICI)1096-9837(199610)21:10<980::AID-ESP586>3.0.CO;2-G, 1994.
- Pope, C. A., Ezzati, M. and Dockery, D. W.: Fine-Particulate Air Pollution and Life Expectancy in the United States, *N. Engl. J. Med.*, 360(4), 376–386, doi:10.1056/NEJMsa0805646, 2009.
- Powers, J. G., Klemp, J. B., Skamarock, W. C., Davis, C. A., Dudhia, J., Gill, D. O., Coen, J. L., Gochis, D. J., Ahmadov, R., Peckham, S. E., Grell, G. A., Michalakes, J., Trahan, S., Benjamin, S. G., Alexander, C. R., Dimego, G. J., Wang, W., Schwartz, C. S., Romine, G. S., Liu, Z., Snyder, C., Chen, F., Barlage, M. J., Yu, W. and Duda, M. G.: The Weather Research and Forecasting (WRF) Model: Overview, System Efforts, and Future Directions, *Bull. Am. Meteorol. Soc.*, doi:10.1175/BAMS-D-15-00308.1, 2017.
- Qi, L., Li, Q., Li, Y. and He, C.: Factors controlling black carbon distribution in the Arctic, *Atmos. Chem. Phys.*, 17(2), 1037–1059, doi:10.5194/acp-17-1037-2017, 2017a.
- Qi, L., Li, Q., Henze, D. K., Tseng, H.-L. and He, C.: Sources of Springtime Surface Black Carbon in the Arctic: An Adjoint Analysis, *Atmos. Chem. Phys. Discuss.*, 2017, 1–32, doi:10.5194/acp-2016-1112, 2017b.
- Qian, Y., Yasunari, T. J., Doherty, S. J., Flanner, M. G., Lau, W. K. M., Ming, J., Wang, H., Wang, M., Warren, S. G. and Zhang, R.: Light-absorbing particles in snow and ice: Measurement and modeling of climatic and hydrological impact, *Adv. Atmos. Sci.*, 32(1), 64–91, doi:10.1007/s00376-014-0010-0, 2014.
- Quinn, P. K., Miller, T. L., Bates, T. S. and Shaw, G. E.: A 3-year record of simultaneously measured aerosol chemical and optical properties at Barrow , Alaska, , 107, 2002.
- Quinn, P. K., Shaw, G., ANDREWS, E., DUTTON, E. G., RUOHO-AIROLA, T. and GONG, S. L.: Arctic haze: current trends and knowledge gaps, *Tellus B*, 59(1), 99–114, doi:10.1111/j.1600-0889.2006.00238.x, 2007.

- Quinn, P. K., Bates, T. S., Baum, E., Doubleday, N., Fiore, A. M., Flanner, M., Fridlind, A., Garrett, T. J., Koch, D., Menon, S., Shindell, D., Stohl, A. and Warren, S. G.: Short-lived pollutants in the Arctic: their climate impact and possible mitigation strategies, *Atmos. Chem. Phys.*, 8(6), 1723–1735, doi:10.5194/acp-8-1723-2008, 2008.
- Ramanathan, V. and Carmichael, G.: Global and regional climate changes due to black carbon, *Nat. Geosci.*, 1(4), 221–227, doi:10.1038/ngeo156, 2008.
- Ramanathan, V., Crutzen, P. J., Kiehl, J. T. and Rosenfeld, D.: Aerosols, climate, and the hydrological cycle, *Science* (80-.), 294(5549), 2119–2124, 2001.
- Remer, L. A., Kaufman, Y. J., Tanré, D., Mattoo, S., Chu, D. A., Martins, J. V, Li, R.-R., Ichoku, C., Levy, R. C., Kleidman, R. G., Eck, T. F., Vermote, E. and Holben, B. N.: The MODIS Aerosol Algorithm, Products, and Validation, *J. Atmos. Sci.*, 62(4), 947–973, doi:10.1175/jas3385.1, 2005.
- Scott, L. R., Clark, T. and Bagheri, B.: *Scientific Parallel Computing*, Princeton University Press., 2005.
- Screen, J. A. and Simmonds, I.: The central role of diminishing sea ice in recent Arctic temperature amplification, *Nature*, 464(7293), 1334–1337 [online] Available from: <http://dx.doi.org/10.1038/nature09051>, 2010.
- Sharma, S., Ishizawa, M., Chan, D., Lavoué, D., Andrews, E., Eleftheriadis, K. and Maksyutov, S.: 16-year simulation of Arctic black carbon: Transport, source contribution, and sensitivity analysis on deposition, *J. Geophys. Res. Atmos.*, 118(2), 943–964, doi:10.1029/2012JD017774, 2013a.
- Sharma, S., Ogren, J. A., Jefferson, A., Eleftheriadis, K., Chan, E., Quinn, P. K. and Burkhart, J. F.: Equivalent Black Carbon in the Arctic, , (Figure 1), 2013b.
- Sharma, S., Leaitch, W. R., Huang, L., Veber, D., Kolonjari, F., Zhang, W., Hanna, S. J., Bertram, A. K. and Ogren, J. A.: An Evaluation of three methods for measuring black carbon at Alert, Canada, *Atmos. Chem. Phys. Discuss.*, 2017, 1–42, doi:10.5194/acp-2017-339, 2017.
- Shende, S. S. and Malony, A. D.: The TAU parallel performance system, *Int. J. High Perform. Comput. Appl.*, 20(2), 287–311, 2006.
- Shindell, D., Kuylenstierna, Johan C. I. Vignati, E., Dingenen, R. van, Amann, M., Klimont, Z., Anenberg, S. C., Muller, N., Janssens-Maenhout, G., Raes, F., Schwartz, J., Faluvegi, G., Pozzoli, L., Kupianen, K., Hoglund-Isaksson, L., Emberson, L., Streets, D., Ramanathan, V., Hicks, K., Oanh, N. T. K., Milly, G., Williams, M., Demkine, V. and Fowler, D.: Simultaneously mitigating near-term climate change and improving human health and food security, *Science* (80-.), 335(January), 183–189, 2012.

- Shindell, D. T., Chin, M., Dentener, F., Doherty, R. M., Faluvegi, G., Fiore, a. M., Hess, P., Koch, D. M., MacKenzie, I. a., Sanderson, M. G., Schultz, M. G., Schulz, M., Stevenson, D. S., Teich, H., Textor, C., Wild, O., Bergmann, D. J., Bey, I., Bian, H., Cuvelier, C., Duncan, B. N., Folberth, G., Horowitz, L. W., Jonson, J., Kaminski, J. W., Marmor, E., Park, R., Pringle, K. J., Schroeder, S., Szopa, S., Takemura, T., Zeng, G., Keating, T. J. and Zuber, a.: A multi-model assessment of pollution transport to the Arctic, *Atmos. Chem. Phys.*, 8(17), 5353–5372, doi:10.5194/acp-8-5353-2008, 2008.
- Sinha, P. R., Kondo, Y., Koike, M., Ogren, J. A., Jefferson, A., Barrett, T. E., Sheesley, R. J., Ohata, S., Moteki, N., Coe, H., Liu, D., Irwin, M., Tunved, P., Quinn, P. K. and Zhao, Y.: Evaluation of ground-based black carbon measurements by filter-based photometers at two Arctic sites, *J. Geophys. Res. Atmos.*, 122(6), 3544–3572, doi:10.1002/2016JD025843, 2017.
- Skamarock, W. C.: Positive-Definite and Monotonic Limiters for Unrestricted-Time-Step Transport Schemes, *Mon. Weather Rev.*, 134(8), 2241–2250, doi:10.1175/MWR3170.1, 2006.
- Skamarock, W. C. and Weisman, M. L.: The Impact of Positive-Definite Moisture Transport on NWP Precipitation Forecasts, *Mon. Weather Rev.*, 137(1), 488–494, doi:10.1175/2008MWR2583.1, 2009.
- Skamarock, W. C., Klemp, J. B., Dudhia, J., Gill, D. O., Barker, D. M., Duda, M. G., Huang, X.-Y., Wang, W. and Powers, J. G.: A Description of the Advanced Research WRF Version 3., NCAR Technical Note NCAR/TN-475+STR., 2008.
- Skiles, S. M., Painter, T. H., Deems, J. S., Bryant, A. C. and Landry, C. C.: Dust radiative forcing in snow of the Upper Colorado River Basin: 2. Interannual variability in radiative forcing and snowmelt rates, *Water Resour. Res.*, 48(7), n/a--n/a, doi:10.1029/2012WR011986, 2012.
- Solomon, S., Forster, P., Ramanswamy, V. and Solomon, S.: Climate Change 2007: The Physical Science Basis [mdash] Contribution of Working Group I to the Fourth Assessment Report of the Intergovernmental Panel on Climate Change, 2007.
- Stier, P., Schutgens, N. A. J., Bellouin, N., Bian, H., Boucher, O., Chin, M., Ghan, S., Huneus, N., Kinne, S., Lin, G., Ma, X., Myhre, G., Penner, J. E., Randles, C. A., Samset, B., Schulz, M., Takemura, T., Yu, F., Yu, H. and Zhou, C.: Host model uncertainties in aerosol radiative forcing estimates: results from the AeroCom Prescribed intercomparison study, *Atmos. Chem. Phys.*, 13(6), 3245–3270, doi:10.5194/acp-13-3245-2013, 2013.
- Stocker, T.: Climate change 2013: the physical science basis: Working Group I contribution to the Fifth assessment report of the Intergovernmental Panel on Climate Change, Cambridge University Press., 2014.
- Stohl, A.: Characteristics of atmospheric transport into the Arctic troposphere, *J. Geophys. Res.*, 111(D11), D11306, doi:10.1029/2005JD006888, 2006.

- Stohl, A., Hittenberger, M. and Wotawa, G.: Validation of the lagrangian particle dispersion model FLEXPART against large-scale tracer experiment data, *Atmos. Environ.*, 32(24), 4245–4264, doi:[http://dx.doi.org/10.1016/S1352-2310\(98\)00184-8](http://dx.doi.org/10.1016/S1352-2310(98)00184-8), 1998.
- Stohl, A., Klimont, Z., Eckhardt, S., Kupiainen, K., Shevchenko, V. P., Kopeikin, V. M. and Novigatsky, A. N.: Black carbon in the Arctic: the underestimated role of gas flaring and residential combustion emissions, *Atmos. Chem. Phys.*, 13(17), 8833–8855, doi:10.5194/acp-13-8833-2013, 2013.
- Stohl, a., Andrews, E., Burkhardt, J. F., Forster, C., Herber, a., Hoch, S. W., Kowal, D., Lunder, C., Mefford, T., Ogren, J. a., Sharma, S., Spichtinger, N., Stebel, K., Stone, R., Ström, J., Tørseth, K., Wehrli, C. and Yttri, K. E.: Pan-Arctic enhancements of light absorbing aerosol concentrations due to North American boreal forest fires during summer 2004, *J. Geophys. Res. Atmos.*, 111, 1–20, doi:10.1029/2006JD007216, 2006.
- Streets, D. G., Yan, F., Chin, M., Diehl, T., Mahowald, N., Schultz, M., Wild, M., Wu, Y. and Yu, C.: Anthropogenic and natural contributions to regional trends in aerosol optical depth, 1980–2006, *J. Geophys. Res. Atmos.*, 114(D10), n/a--n/a, doi:10.1029/2008JD011624, 2009.
- Supalov, A., Semin, A., Dahnken, C. and Klemm, M.: *Optimizing HPC Applications with Intel Cluster Tools: Hunting Petaflops*, Apress, Berkely, CA, USA., 2014.
- Thuburn, J.: Multidimensional Flux-Limited Advection Schemes, *J. Comput. Phys.*, 123(1), 74–83, doi:<http://dx.doi.org/10.1006/jcph.1996.0006>, 1996.
- UNEP: *Framework Convention on Environmental Protection for Sustainable Development in Central Asia*, Reg. Resour. Cent. Asia Pacific, 2006.
- UNEP and WMO: *Integrated Assessment of Black Carbon and Tropospheric Ozone: Summary for Decision Makers.*, 2011.
- Uno, I., Satake, S., Carmichael, G. R., Tang, Y., Wang, Z., Takemura, T., Sugimoto, N., Shimizu, A., Murayama, T., Cahill, T. A., Cliff, S., Uematsu, M., Ohta, S., Quinn, P. K. and Bates, T. S.: Numerical study of Asian dust transport during the springtime of 2001 simulated with the Chemical Weather Forecasting System (CFORS) model, *J. Geophys. Res.*, 109(D19), n/a-n/a, doi:10.1029/2003jd004222, 2004.
- Visschedijk, A., Denier van der Gon, H., Droge, R. and van der Brugh, H. .: *A European high resolution and size-differentiated emission inventory for elemental and organic carbon for the year 2005*, TNO, 2009.
- Wang, H., Skamarock, W. C. and Feingold, G.: Evaluation of Scalar Advection Schemes in the Advanced Research WRF Model Using Large-Eddy Simulations of Aerosol–Cloud Interactions, *Mon. Weather Rev.*, 137(8), 2547–2558, doi:10.1175/2009MWR2820.1, 2009.

- Wang, Q., Jacob, D. J., Fisher, J. a., Mao, J., Leibensperger, E. M., Carouge, C. C., Le Sager, P., Kondo, Y., Jimenez, J. L., Cubison, M. J. and Doherty, S. J.: Sources of carbonaceous aerosols and deposited black carbon in the Arctic in winter-spring: implications for radiative forcing, *Atmos. Chem. Phys.*, 11(23), 12453–12473, doi:10.5194/acp-11-12453-2011, 2011.
- Wang, W., Bruyère, C., Duda, M., Dudhia, J., Gill, D., Kavulich, M., Keene, K., Chen, M., Lin, H.-C., Michalakes, J., Rizvi, S., Zhang, X., Berner, J., Ha, S. and Fossell, K.: WRF ARW Version 3 Modeling System User's Guide, [online] Available from: http://www2.mmm.ucar.edu/wrf/users/docs/user_guide_V3.9/ARWUsersGuideV3.9.pdf, 2017.
- Warneke, C., Bahreini, R., Brioude, J., Brock, C. A., de Gouw, J. A., Fahey, D. W., Froyd, K. D., Holloway, J. S., Middlebrook, A., Miller, L., Montzka, S., Murphy, D. M., Peischl, J., Ryerson, T. B., Schwarz, J. P., Spackman, J. R. and Veres, P.: Biomass burning in Siberia and Kazakhstan as an important source for haze over the Alaskan Arctic in April 2008, *Geophys. Res. Lett.*, 36(2), n/a--n/a, doi:10.1029/2008GL036194, 2009.
- Warren, S. G.: Can black carbon in snow be detected by remote sensing?, *J. Geophys. Res. Atmos.*, 118(2), 779–786, doi:10.1029/2012JD018476, 2013.
- Wesely, M. L. and Hicks, B. B.: A review of the current status of knowledge on dry deposition, *Atmos. Environ.*, 34(12–14), 2261–2282, doi:10.1016/s1352-2310(99)00467-7, 2000.
- Whish-Wilson, P.: The Aral Sea environmental health crisis The Desiccation of the Aral Sea Health in the Aral Sea region, , 1(2), 29–34, 2002.
- WHO: Ambient air pollution: a global assessment of exposure and burden of disease, World Health Organization, Geneva. [online] Available from: <http://apps.who.int/iris/handle/10665/250141>, 2016.
- Wicker, L. J. and Skamarock, W. C.: Time-Splitting Methods for Elastic Models Using Forward Time Schemes, *Mon. Weather Rev.*, 130(8), 2088–2097, doi:10.1175/1520-0493(2002)130<2088:TSMFEM>2.0.CO;2, 2002.
- Wiedinmyer, C., Akagi, S. K., Yokelson, R. J., Emmons, L. K., Al-Saadi, J. A., Orlando, J. J. and Soja, A. J.: The Fire INventory from NCAR (FINN): a high resolution global model to estimate the emissions from open burning, *Geosci. Model Dev.*, 4(3), 625–641, doi:10.5194/gmd-4-625-2011, 2011.
- Wiedinmyer, C., Yokelson, R. J. and Gullett, B. K.: Global Emissions of Trace Gases, Particulate Matter, and Hazardous Air Pollutants from Open Burning of Domestic Waste, *Environ. Sci. Technol.*, 48(16), 9523–9530, doi:10.1021/es502250z, 2014.
- Wiscombe, W. J. and Warren, S. G.: A Model for the Spectral Albedo of Snow. I: Pure Snow, *J. Atmos. Sci.*, 37(12), 2712–2733, doi:10.1175/1520-0469(1980)037<2712:AMFTSA>2.0.CO;2, 1980.

- Xu, J., Martin, R. V, Morrow, A., Sharma, S., Huang, L., Leaitch, W. R., Burkart, J., Schulz, H., Zanatta, M., Willis, M. D., Henze, D. K., Lee, C. J., Herber, A. B. and Abbatt, J. P. D.: Source attribution of Arctic black carbon constrained by aircraft and surface measurements, *Atmos. Chem. Phys. Discuss.*, 2017, 1–45, doi:10.5194/acp-2017-236, 2017.
- Yienger, J. J., Galanter, M., Holloway, T. A., Phadnis, M. J., Guttikunda, S. K., Carmichael, G. R., Moxim, W. J. and Levy, H.: The episodic nature of air pollution transport from Asia to North America, *J. Geophys. Res.*, 105(D22), 26931, doi:10.1029/2000JD900309, 2000.
- Zhang, Q., Streets, D. G., Carmichael, G. R., He, K. B., Huo, H., Kannari, A., Klimont, Z., Park, I. S., Reddy, S., Fu, J. S., Chen, D., Duan, L., Lei, Y., Wang, L. T. and Yao, Z. L.: Asian emissions in 2006 for the NASA INTEX-B mission, *Atmos. Chem. Phys.*, 9(14), 5131–5153, doi:10.5194/acp-9-5131-2009, 2009.